Aromatization of Oxygenates over Zeolite Catalysts

Aromatisering van Zuurstofhoudende Verbindingen met Zeoliet Katalysatoren

(met een samenvatting in het Nederlands)

Proefschrift

ter verkrijging van de graad van doctor aan de
Universiteit Utrecht
op gezag van de
rector magnificus, prof.dr. H.R.B.M. Kummeling,
ingevolge het besluit van het college voor promoties
in het openbaar te verdedigen op

maandag 24 augustus 2020 des middags te 4.15 uur

door

Beatriz Luna Murillo

geboren op 27 januari 1992 te Barcelona, Spanje

Promotoren:

Prof. dr. ir. B.M. Weckhuysen

Prof. dr. P.C.A. Bruijnincx

This PhD Thesis was accomplished with financial support from the Netherlands Center for Multiscale Catalytic Energy Conversion (MCEC), the Netherlands Research Council (*NWO*) Gravitation Program, funded by the Ministry of Education, Culture and Science of the government of the Netherlands.

"*Las cosas podían haber sucedido de cualquier otra manera y, sin embargo, sucedieron así*"

Miguel Delibes (1920-2010)

A mi familia. También va por ti, papá.

Author: Beatriz Luna Murillo
Title: Aromatization of Oxygenates over Zeolite Catalysts
Cover design: thisilustrations.com
ISBN: 978-94-6416-040-6
Printed by: Ridderprint | www.ridderprint.nl

Table of Contents

Chapter 1 Introduction

1.1. Zeolites and their Use as Catalysts

Zeolites are crystalline aluminosilicates, characterized by a porous network with cages and channels of (sub)nanometer dimensions. The main composition of a zeolite-like material follows the formula: $xM_{2/n}O{\bullet}xAl_2O_3{\bullet}ySiO_2{\bullet}wH_2O$, where M is a cation, n the cation valence, and *w* corresponds to the water molecules contained within the zeolite material. The main building blocks of zeolites are tetrahedral silicon oxide fragments, which by sharing an oxygen atom form a three-dimensional network. If other cations than silicon are present during synthesis, an isomorphic substitution can take place, which is the replacement of an atom in a solid crystalline material without altering its crystalline structure. The most common replacements for silicon are either aluminum, phosphor or transition metal ions with a +2 or +3 oxidation state (i.e., Fe^{3+})[1–4]. If a zeolite framework is only composed of SiO_4 fragments, the overall charge of the framework is neutral. However, replacement of Si^{4+} by another atom, such as Al^{3+}, results in a charge imbalance and the negatively charged framework needs an extra-framework cation to compensate the overall charge. When this charge of the framework is compensated by a proton, Brønsted acid sites are formed, as illustrated in Figure 1.1b. Brønsted acid sites are considered to be the main active sites in zeolite-based materials when it comes to catalytic activity[2]. On the contrary, when the charge is balanced by an alkali or metal cation, this results in the formation of a Lewis acid site. Al^{3+} as an extra-framework cation can also form Lewis acid sites.

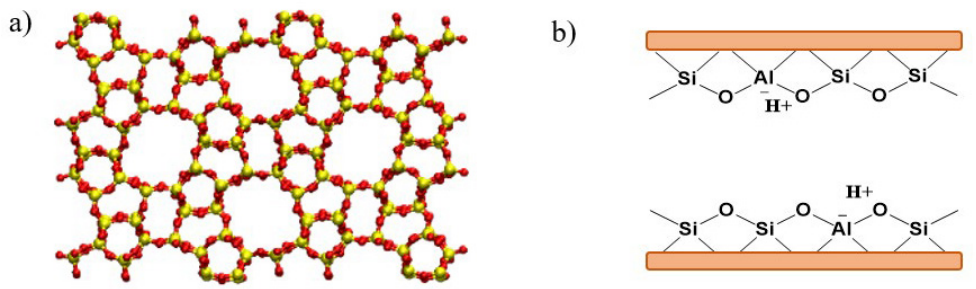

Figure 1.1. (a) Schematic of a 2-D representation of zeolite ZSM-5, possessing a MFI framework with yellow representing Si^{4+} or Al^{3+} ions and red representing O^{2-} ions, and (b) schematic description of a Brønsted acid site inside the zeolite framework, showing how the negatively charged framework is neutralized by a proton.

Zeolites come in many different topologies varying in pore and channel architecture. The International Zeolite Association (IZA), founded in 1973, has registered more than 250

framework types in its database[6]. An example of the structure and pore network of the industrially important zeolite ZSM-5 is given in Figure 1.1a. The MFI framework structure of ZSM-5 is characterized by two types of 10-membered ring channel structures (10-MRs); a sinusoidal and a straight channel. The dimensions of these channels, shown in Figure 1.2, range from 4.5 to 6.0 Å. Together, their highly crystalline structures, well-defined micropore network and their tunable acidic properties make zeolites very well suited for widespread uses in different commercial applications as detergents, adsorbents or catalysts[7], the latter in particular in the petrochemical industry[2].

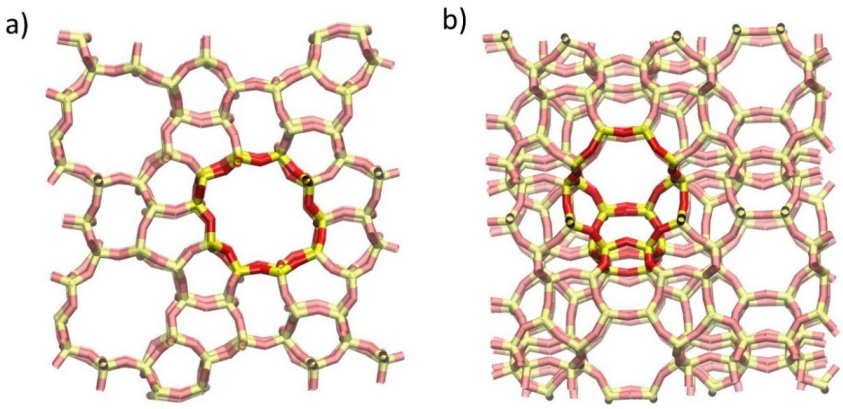

Figure 1.2. 3-D images of zeolite ZSM-5 with the MFI framework structure with 10-membered rings (10-MRs), highlighting the (a) straight channels and (b) sinusoidal channels when viewed along the [010] and [100] directions, respectively. Color labeling is identical to Figure 1.1.

Zeolite materials can be divided in synthetic zeolites, which account for 40% of the overall use, and natural zeolites (60%). The main manufacturers of synthetic zeolites are UOP (Honeywell), CECA (Arkema) and BASF, while the main manufacturers of zeolites specifically used for catalysis are Albemarle, BASF and W.R. Grace. The worldwide zeolite market represented more than 29 billion USD in 2016, and is expected to further grow with up to 3% annually in the next coming years due to increasing global demand for detergents, adsorbents and catalysts[7].

Zeolites are considered to be excellent catalysts for many different types of chemical conversions. Their high thermal stability allows their use under harsh conditions such as those encountered in, for example, the fluid catalytic cracking (FCC) process. Furthermore, a proper choice of zeolite topology can elicit high selectivity to certain products when the material is used as catalyst for chemical conversion, a property known as shape-selectivity. ZSM-5, for

example, is widely used as catalyst for its combination of shape selectivity and isomerization activity, e.g. to obtain branched additives for gasoline[8]. In addition, this material is also widely known to efficiently catalyze the production of Benzene-Toluene-Xylene (BTX) and small olefins from methanol[9].

Like many catalyst systems, the catalytic performance of zeolites also suffers from deactivation, however, for example by active site poisoning, pore blockage, framework deterioration or structure collapse, all compromising catalytic activity. Processes that expose the zeolite to a feedstock with a high metal content (metal poisoning), high temperature H_2O (steaming) or one that produces a large amount of carbon deposits (coking) are, for example, well-known to lead to loss of activity[5].

Zeolites are also often endowed with bifunctionality, e.g. by the addition of an active metal phase. Such zeolite-supported metal catalysts comprise another family of industrially important catalysts. Indeed, the incorporation of metal and metal oxides, such as Pt and Cu oxide clusters, leads to the formation of new active sites within the zeolite framework conferring redox properties, such as hydrogenation-dehydrogenation activity, to these acidic materials[10]. There are different approaches to introduce metals into the zeolite; either such metal sites can be part of the framework, i.e. via the mentioned isomorphic substitution, or be extra-framework, usually located in the micropores and cavities of the zeolite as metallic clusters or cations[9]. Either way, the catalytic performance of the zeolites can be tuned to serve a wide variety of chemical processes[11].

1.2. Biomass Valorization: Catalytic Fast Pyrolysis Technology

Present challenges, in particular climate change, motivate the replacement of the commonly used fossil resources, such as natural gas, coal and crude oil, by renewable and more sustainable feedstocks, such as biomass or municipal waste, for the production of transportation fuels and chemicals. Sustainably resourced biomass is an attractive resource capable of providing renewable energy, fuels and chemicals. Indeed, lignocellulosic biomass, e.g. residues from agriculture, forestry or dedicated energy crops, is the most abundant and renewable carbon resource on earth[12]. The acidic zeolite ZSM-5 is also heavily studied for the conversion of such lignocellulosic biomass and lignocellulose-derived oxygenates to produce liquid fuel and chemicals, e.g. via the so-called catalytic fast pyrolysis process. Zeolite ZSM-5 turns out to be particularly suited for this process due to its high ability to simultaneously perform cracking, deoxygenation, dehydration and aromatization reactions[13–15].

Lignocellulosic biomass is mainly composed of three biopolymers: cellulose, hemicellulose and lignin. Figure 1.3 shows the chemical structure of these three biopolymers. The content of each fraction within plant material varies enormously, depending e.g. plant type, but typically is in the order of ~ 40-50 % cellulose, ~ 30% hemicellulose and ~ 20-30% lignin[16]. To properly convert biomass into value-added products, such as useful chemicals or building blocks, (bio)chemical, thermal and catalytic treatments need to be carried out to properly isolate, upgrade and transform all its components[17].

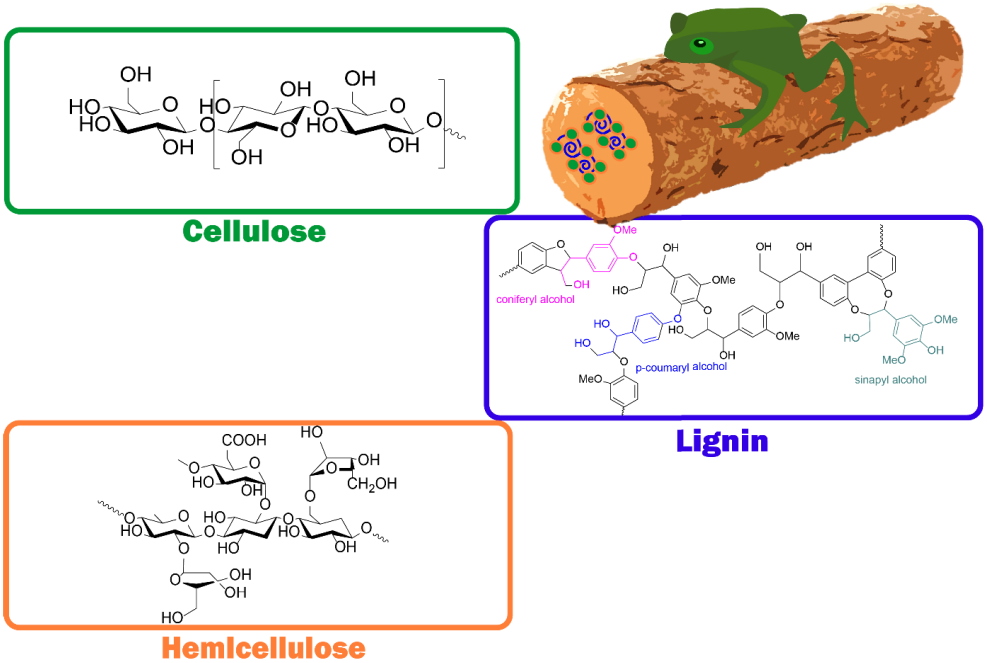

Figure 1.3. Schematic representation of the three main biopolymers, namely cellulose, hemicellulose and lignin, present in lignocellulosic biomass, including their chemical structures.

Thermochemical processes, that can upgrade biomass into value-added products, include gasification, liquefaction and pyrolysis. Depending on the residence time of the biomass in the reactor, the heating rate and the reaction temperatures, different types of reaction products can be obtained. If biomass is gasified by direct combustion, mainly synthesis gas (i.e., a mixture of CO and H_2) is produced, a useful source of carbon that can be further converted into fuels and platform compounds, e.g. via the Fischer-Tropsch synthesis process[18,19]. Thermal upgrading of biomass at moderate temperatures, short residence times and atmospheric pressure is known as pyrolysis[13]. Biomass pyrolysis is particularly attractive as high-quality liquid-phase

and gas-phase reaction products can be obtained with much lower oxygen content compared to other processes[20]. For example, the product distribution obtained during biomass pyrolysis can be controlled by changing the applied heating rate. The so-called fast pyrolysis takes place when short residence times and fast heating rates are applied, thus enhancing the yield to liquid-phase products (i.e., pyrolysis oil). Fast pyrolysis is the most economically feasible technology to upgrade biomass into valuable products due to its relatively low operational costs[21]. The pyrolysis oil obtained is a complex liquid, however, composed of many oxygenated compounds, including phenols, ketones and aldehydes, next to water. Its highly varied composition makes its direct transformation into biofuels or bio-chemicals challenging, as the bio-oil is unstable when stored. The high oxygen content, chemical instability, and high water content causes operating problems, such as corrosion and catalyst deactivation. The bio-oil is, nevertheless, an interesting alternative feedstock for renewable value-added products due to its lower sulfur and nitrogen content, when compared to conventional petroleum-derived feedstocks, such as vacuum-gas oil (VGO)[17]. To allow the use of bio-derived pyrolysis oils in current industrial infrastructure, e.g. as replacement of VGO oil, there is a need to first and foremost reduce the oxygen content of the bio-oil before it can be further processed and transformed into value-added chemicals. An interesting strategy that favors the removal of oxygen during the conversion of bio-oil into valuable chemicals is by catalytic fast pyrolysis.

Catalytic fast pyrolysis (CFP) is a modification of thermal fast pyrolysis and makes use of a catalyst to upgrade the biomass by a chemo-catalytic process in addition to thermal conversion to produce fuels and platform compounds. The most used catalysts for CFP are acidic zeolite-based materials[22–24]. The use of zeolites as catalyst during CFP ensures effective oxygen removal and catalytic conversion of the biomass feed into higher quality bio-oil[25]. It is noteworthy to mention that in CFP there are two different approaches that can be used for the upgrading of biomass into chemicals and fuels. These approaches are named *in-situ* and *ex-situ* CFP. In the *in-situ* CFP process, raw biomass is pyrolyzed and subsequently cracked in the same reactor in the presence of a catalyst, while in the *ex-situ* CFP process, raw biomass is first pyrolyzed in a separate reactor (i.e., a pyrolyzer) and subsequently, the pyrolysis vapors formed are fed into a second reactor, which contains a catalyst[26]. In the first method, raw biomass is directly mixed at high temperature with the catalysts material in the same reactor, resulting in almost instantaneous catalyst deactivation. In contrast, for the *ex-situ* CFP method the catalyst is separated from the harsh conditions and complex chemical matrix present in the pyrolyzer unit and only the vapors formed, which include non-condensable gases, are fed to the catalytic

reactor leading to a more optimum catalyst performance as catalyst lifetime improves. More desired reaction products are thus formed, as function of the process conditions chosen, resulting in a bio-oil pyrolysis fraction composed of light and heavy hydrocarbons. Nevertheless, as in ex situ CFP, there are still several challenges that require attention, such as the low carbon yields and still relatively rapid catalyst deactivation[13,27].

Bio-derived olefins and aromatics are often targeted as products in biomass CFP, given that they are highly valuable platform compounds with multiple uses. The development of catalyst materials to show improved performance during the CFP of biomass towards these product categories is therefore a topic of special interest. Several research groups have explored and investigated different zeolite topologies (i.e., MFI, BEA, FAU and MOR) for CFP[13], of which, zeolite ZSM-5 has received special attention as the size of its pores and channels enables high selectivity to aromatics and small olefins. The benefit of using zeolites as catalysts is that deoxygenation can easily take place at the Brønsted acid sites (BAS) without the need for hydrogen to be present. However, efficiency is limited by the often too low hydrocarbon yields, primarily because of the strong BAS-induced rapid formation of coke deposits. As mentioned in section 1.1, acidity and pore architecture in zeolites determine their product selectivity. Therefore, it is expected that an optimal zeolite catalyst for the upgrading of bio-oil needs to have sufficiently large pores and mild enough BAS to allow biomass-derived molecules to enter the zeolite pores and undergo the required chemical transformations to form the desired products, while at the same time avoiding unwanted side reactions (e.g., oligomerization and coking).

As also mentioned above, bio-oil is composed of a complex mixture of oxygenates. Consequently, elucidating the reactivity and related transformation of each group of oxygenates into the target chemical compounds is expected to be very challenging when feeds of such complexity are used directly. Therefore, in many cases, the transformation of single bio-derived compounds to model key components present in the bio-oil, have been used to improve our understanding of bio-oil deoxygenation in CFP[28–32]. In addition to the use of single biomass-derived compounds as model compounds for bio-oil upgrading, such compounds can also be regarded as (isolated) intermediate platform molecules in their own right. The further, downstream conversion of these oxygenate platform molecules, regardless of their means of production, into renewable aromatics and olefins using zeolites as catalysts is therefore also of particular interest[31,33,34]. Such efforts are the topic of the next section.

1.3. Catalytic Fast Pyrolysis of Bio-derived Furans

An important class of platform molecules that can be obtained via various routes from biomass, are the sugar-derived furans. In addition to understanding their chemistry under whole biomass CFP conditions as discussed above, the development of chemical conversion routes to further convert these bio-derived platform compounds into commodity chemicals is crucial since they also foster biomass valorization[31,37].

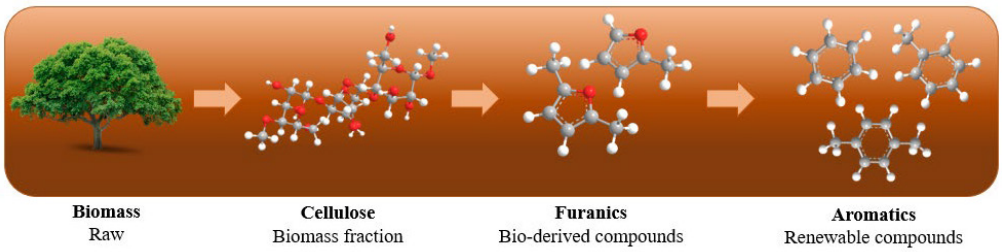

Figure 1.4. Schematic representation of the different transformations that need to take place to form renewable aromatics from raw biomass via catalytic fast pyrolysis (CFP) technology using zeolite HZSM-5 as catalyst.

Pyrolysis of cellulose and/or hemicellulose produces levoglucosan and other anhydrosugars, which can be further converted into smaller oxygenated compounds, such as aldehydes, ketones or furans, together with CO, CO_2 and char[38,39]. Furans are known to constitute a significant fraction of the oxygenates in the bio-oil produced from cellulose pyrolysis. Furan derivatives can also be produced via other routes, e.g. via sugar dehydration optionally coupled with hydrogenation/decarbonylation and are thus, widely considered as key sugar-derived platform molecules. As schematically illustrated in Figure 1.4, these furans in the biomass pyrolysis vapors can be converted into aromatics by acid catalysis[40–42]. For example, Huber *et al.* investigated the conversion of different furan derivatives (e.g., furan (F), 2,5-dimethylfuran (DMF), 2-methylfuran (MF) and 5-hydroxymethylfurfural) into alkylated mono-aromatics using zeolite ZSM-5-based catalysts[43]. Next to the targeted aromatics, these experiments also produced CO, CO_2, H_2O and coke (composed of oxygenated oligomers and graphite-like coke)[44,45]. Usually, furan aromatization primarily yields benzene and toluene, trace amounts of xylenes (usually *p*-xylene), olefins as well as coke deposits. It is known that polycyclic aromatic coke is usually formed from condensation or oligomerization reactions of monocyclic aromatics. Although the reaction mechanism for the formation of aromatics from furan derivatives is assumed to involve a hydrocarbon pool mechanism, the intermediates formed

within the zeolite pores responsible for the formation of aromatics and coke are still largely unknown. Studying the conversion of furans as model or platform compounds, can help to unravel the complex mechanisms that operate under biomass CFP conditions within the zeolite network and can aid in the development of more efficient means of conversions when these furans are considered as platform molecules as such.

The properties of pristine ZSM-5 zeolite catalysts are not necessarily optimal for the targeted furan to aromatics conversion and post-synthetic modifications need to be applied to tailor properties such as acidity, porosity or (de)hydrogenation activity. The latter can be tuned by the incorporation of metal promoter, such as Ga, Mo or Zn[46–50]. In previous reports, the addition of such metals greatly improved the aromatization efficiency of the ZSM-5 materials when hydrocarbons were used as feedstock[3,51,52]. In such bifunctional systems, the metal (oxide) sites promote hydrocarbon dehydrogenation by favoring C-H bonds activation, while with Brønsted acid sites from the zeolite material mostly favor hydrogen transfer, cracking, dehydration and isomerization reactions, thus ensuring the high selectivity towards aromatics. Furthermore, recent investigations revealed that if the metals are confined within the pores and channels of zeolites (i.e., as metal nanoparticles or single metal atoms), the size of the reaction intermediates can be restricted by the dimension of the micropores, yielding even higher aromatization rates[55,56]. This synergistic effect between the metal (oxide) promoters (i.e., Pt, Zn, Mo or Ga) and the Brønsted acid sites, illustrated in Figure 1.5, can also be exploited to enhance the selectivity towards aromatics with oxygenated feedstock[53,54].

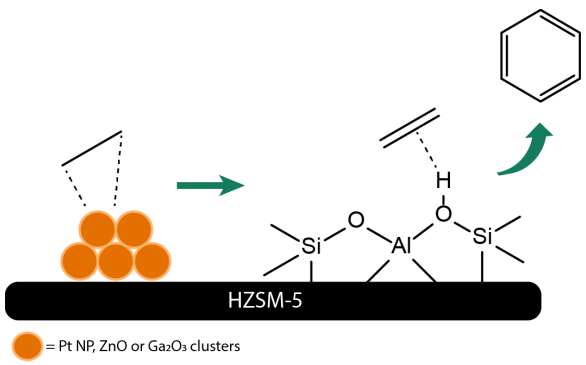

Figure 1.5. Schematic of the possible synergistic effects taking place during the aromatization of hydrocarbons over zeolite HZSM-5, loaded with metal (oxide) promotors.

For example, several investigations performed by Cheng *et al.* demonstrated that the presence of Ga boosted aromatics yields during the conversion of MF and DMF over HZSM-5[45,57,58]. In

addition to an enhancement of aromatization rates, some metal supported ZSM-5 zeolites also improved carbon yields by suppressing deactivation through coking[59]. To the best of our knowledge, other dehydrogenation metals for the aromatization of furan derivatives have not been explored yet, showing the importance of further developments in this field. Thus, the topic of using dehydrogenation metal promoted ZSM-5 to convert oxygenated compounds, furans in particular, into aromatics will be further explored in this PhD Thesis.

As discussed above, coking within the zeolite pores and channels during the conversion of feedstock compounds can be reduced by the incorporation of metal sites into the ZSM-5 zeolite[60]. The formation of complex and heavy condensed carbon deposits is known to be the result of hydrocarbon oligomerization and condensation reactions not only at the Brønsted acid sites, but also due to thermal consendation[61,62]. Coke formation then impacts performance by acid site and pore blockage[41,63,64]. Also in furan upgrading, coking is a major drawback for its practical operation, since it occurs very rapidly at the zeolite pores and channels[40]. This process is schematically displayed in Figure 1.6 for zeolite ZSM-5.

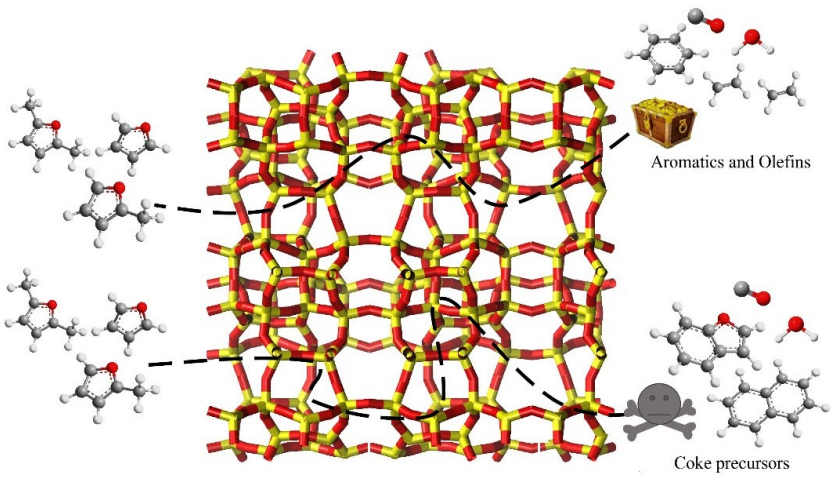

Figure 1.6. Schematic of the possible reaction products (e.g., aromatics, olefins and coke precursors) produced during the catalytic fast pyrolysis (CFP) of furan-type molecules when using zeolite ZSM-5 as catalyst.

It has been previously proposed that the conversion of furan over HZSM-5 zeolites follows a hydrocarbon pool (HCP) mechanism, in analogy to the well-known Methanol-to-Hydrocarbons (MTH) process for the conversion of methanol into light olefins and aromatics. In such a hydrocarbon pool mechanism, carbon loses its identity and two different types of coke are

formed at different stages[40,71–73]. At low temperatures, condensation and rearrangements take place and oligomers called “soft coke” are obtained. When high temperatures are applied, hydrogen-transfer and hydrogenation-dehydrogenation reactions occur giving polyaromatics, called “hard coke”. These species consist of highly condensed species that are retained within the zeolite micropores, thereby directly affecting catalytic activity[64].

Typical analytical methods used to determine the nature and chemical composition of coke deposits are e.g. thermogravimetric analysis (TGA), Fourier transform-infrared (FT-IR) spectroscopy, Raman spectroscopy, UV/Vis diffuse reflectance (DR) spectroscopy and ^{13}C and ^{1}H magic angle spinning (MAS) solid-state nuclear magnetic resonance (ssNMR)[67,74]. The location and distribution of carbon deposits inside the zeolite-based catalyst is a more complex task, although techniques, such as temperature programmed oxidation (TPO) with online mass spectrometry (MS), physisorption methods and confocal fluorescence microscopy (CFM) can be used for that purpose[75–77]. To investigate if coke deposits are trapped species within the intra-zeolitic framework structure, a total dilution of the catalyst matrix in hydrofluoric acid solution is usually performed. However, this latter technique may alter the chemical structure of the carbonaceous deposits extracted, as this strong acid is capable of converting some of the coke deposits into other hydrocarbon products. While these analytical techniques do provide some insight into the molecular composition of the hydrocarbon compounds retained within the catalyst, identification of the actual composition of coke deposits is still a very challenging task to accomplish. Despite of the many efforts, the definite mechanism of coke formation from furan derivates has not been described yet in great detail. Consequently, we stress here the necessity to use *in-situ* and *operando* spectroscopic methods to identify reaction intermediates to elucidate the reaction pathways to form the target molecules as well as carbon deposits.

1.4. Scope and Outline of the PhD Thesis

This PhD Thesis aims to explore and optimize the catalytic production of renewable building blocks, such as aromatics and olefins, from furan derivatives. To do so, we focus our investigation on the catalytic upgrading of lignocellulosic biomass and bio-derived furans as platform molecules into aromatics, with a special emphasis on the zeolite-catalyzed aromatization of these furans to BTX, as important platform molecules. Diverse catalyst compositions and reaction conditions were explored in combination with a variety of analytical

methods to get better insights into the catalytic performance as well as the mechanisms governing the aromatization of bio-derived furan derivatives.

Indeed, a more consistent molecular understanding of the catalytic process can be achieved by combining catalyst and process modification with *in-situ* and *ex-situ* spectroscopic characterization techniques. Moreover, analysis under *operando* conditions facilitates the identification of precursors leading to the formation of aromatics and coke. At last, by combining the aforementioned approaches, this PhD Thesis aims to give a more detailed picture of the reaction pathways taking place within the zeolite pores during the catalytic aromatization of furan, including a study aimed at determining the causes of catalyst deactivation, as function of the furan derivatives and catalytic system tested. The effect of modifying the Si/Al ratio when incorporating mesopores, or when using metallic and non-metallic promotors within the zeolite has also been investigated, as both approaches directly influence the number and type of Lewis and Brønsted acid sites present and consequently, the overall catalytic performance. Furthermore, this PhD Thesis shows the applications of established analytical and spectroscopic methods to new processes such as the Furan-to-Aromatics (FTA) process. The use of *operando* UV/Vis spectroscopy, or the investigation of dealumination in a ZSM-5-based catalyst after the CFP of biomass by ^{27}Al ssNMR will allow us to bridge the gap between the catalytic performance observed during experiments with powdered catalysts used at the lab scale and industrially used zeolite ZSM-5-based catalyst bodies used at the bench scale.

In **Part A** of this PhD Thesis, the Furan-to-Aromatics process is studied by *operando* UV/Vis DRS with online mass spectrometry (MS). The use of UV/Vis DRS provided insight into the reaction intermediates formed, conjugated systems anticipated to exhibit π-π* transitions observable by this technique. With online MS, an analysis of the reaction products and by-products formed during reaction showed us the formation of olefins and BTX aromatics was taking place. This state-of-the-art analytical approach allowed us to identify the main intermediates formed during the aromatization of furan derivatives, such as monoenyl and dienyl or arenium ions, and how these evolve to carbon deposits causing eventually catalyst deactivation. In addition, modifications of the benchmark zeolite HZSM-5 catalyst with non-metallic and metallic promotors were carried out to study their influence on the aromatization of furan derivatives. The synthesized catalyst materials were characterized in depth before and after reaction to elucidate the main active sites and their role in the aromatization reaction. Catalytic testing was performed in a custom-made reactor specially design to allow co-feeding

experiments during the aromatization of diverse furan derivatives. Moreover, the structural and chemical changes in the catalyst materials after deactivation and regeneration are discussed.

Chapter 2 describes an *operando* UV/Vis DRS-MS study of the aromatization of the biomass-derived furan derivatives F, DMF and MF over zeolite HZSM-5 catalysts with different Si/Al ratios and porosity. Identification of reaction intermediates, such as benzofuran, by means of *in-situ* and *ex-situ* spectroscopy together with the use of *a posteriori* analytical methods, allowed us to put forward a mechanistic proposal for the aromatization of these furan derivatives. Further *ex-situ* catalyst characterization performed after reaction provided insight into any changes in the catalyst structure and the overall catalytic (deactivation) process.

Chapter 3 presents an extended investigation about phosphorus-modified ZSM-5 zeolites by combining a large array of characterization techniques, such as ^{27}Al, ^{31}P and ^{29}Si solid-state (ss) nuclear magnetic resonance (NMR), Fourier transform-infrared (FT-IR) spectroscopy, and temperature programmed desorption (TPD) of NH_3 among other methods. Insight in the catalytic activity and structural information about the phosphorus species formed after impregnation are provided. Catalytic performance measurements during the aromatization of DMF and MF for different times-on-stream (TOS) are also described. In addition, the influence of ethylene co-feeding was studied during the catalytic conversion of DMF and MF.

In **Chapter 4** HZSM-5 zeolites impregnated with gallium are reported, materials showing a synergistic interaction between Ga and H^+ sites from zeolite ZSM-5 in the co-aromatization of DMF with ethylene. The incorporation of Ga sites into the zeolite structure boosted the amount of Lewis acid sites, which are known to favor dehydrogenation and aromatization reactions. By using *ex-situ* and *in-situ* bulk and (micro)spectroscopic characterization techniques, such as confocal fluorescence microscopy (CFM), UV/Vis DRS and X-ray photoelectron spectroscopy (XPS), insights in the Ga location and speciation together with catalyst performance of the bifunctional Ga/HZSM-5 catalyst system during the aromatization of DMF with ethylene were given.

Chapter 5 describes the aromatization of DMF with ethylene using Zn-promoted HZSM-5 zeolites as catalyst materials. This chapter is divided in two different sections in which we describe the synthesis and characterization of the Zn/ZSM-5 catalyst followed by the subsequent catalytic testing to better understand the role of ethylene co-feeding during the aromatization of DMF when Zn promotors are present. Based on the prior UV/Vis spectroscopic data obtained under *operando* conditions, together with the *ex-situ* FT-IR

spectroscopy and TPD measurements on the Zn catalysts, a mechanism for DMF aromatization with ethylene is also proposed.

In **Part B** of the PhD thesis, the CFP process of biomass performed in a bench scale reactor where pine wood vapors are used as feedstock (*ex-situ* CFP) is explored. In order to investigate the effect of each bio-polymer present in biomass, upgrading of cellulose is performed as well. In all these processes, technical ZSM-5-based catalyst extrudates are used as catalysts.

In **Chapter 6** various lab-scale characterization methods, used in the previous chapters, were employed to investigate the technical Al_2O_3-bound zeolite HZSM-5-based catalyst. Properties of the isolated components and the technical catalyst extrudates were carefully investigated to understand any repercussions of the extrusion process on catalytic performance. Characterization techniques, such as ^{27}Al ssNMR, NH_3-TPD, FT-IR and X-ray diffraction (XRD), are employed to gain new insights about the possible chemical and physical changes that occur upon scale-up to the technical catalyst material. Moreover, the performance of the zeolite ZSM-5-based catalyst composites was investigated for the *ex-situ* CFP of biomass and cellulose in a bench-scale reactor. In addition, an extensive catalyst characterization on the spent and regenerated catalysts was carried out to gain new insights into the nature and location of coke species within the catalyst composites formed after the *ex-situ* CFP of pine wood and cellulose. Using this holistic approach, we have investigated the aromatization and deactivation rate that each bio-polymer has on the zeolite ZSM-5-based catalyst extrudates.

Chapter 7 provides a summary of the main results and conclusions of this PhD Thesis together with some future perspectives, which provides suggestions for future research. The thesis ends with a summary on the main implications of this research work for industry and our society as a whole.

1.5. References

(1) Corma, A. Inorganic Solid Acids and Their Use in Acid-Catalyzed Hydrocarbon Reactions. *Chem. Rev.* **1995**, *95*, 559–614. https://doi.org/10.1021/cr00035a006.

(2) Vogt, E. T. C.; Whiting, G. T.; Dutta Chowdhury, A.; Weckhuysen, B. M. Zeolites and Zeotypes for Oil and Gas Conversion. *Adv. Catal.* 1st ed.; Elsevier, Amsterdam, **2015**; *58*, 143-314 https://doi.org/10.1016/bs.acat.2015.10.001.

(3) Weitkamp, J. Zeolites and Catalysis. *Solid State Ionics* **2000**, *131*, 175–188.

https://doi.org/10.1016/S0167-2738(00)00632-9.

(4) Byrappa, K.; Kumar, B. V. S. Characterization of Zeolites by Infrared Spectroscopy. *Asian J. Chem.* **2007**, *19*, 4933–4935. https://doi.org/10.1016/S1387-1811(98)80021-8.

(5) Guisnet, M.; Magnoux, P. Coking and Deactivation of Zeolites. *Appl. Catal.* **1989**, *54* , 1–27. https://doi.org/10.1016/s0166-9834(00)82350-7.

(6) International Zeolite Association (IZA) Database Copyright © 2017 http://www.iza-structure.org/databases/ (accessed Feb 24, 2020).

(7) *Zeolite Market Size, Share & Trends Analysis Report By Product, By Application (Catalysts, Detergent Builders), By Region (North America, Europe, Asia Pacific, CSA, MEA), And Segment Forecasts, 2012 - 2022*; 2018. https://doi.org/978-1-68038-601-1.

(8) Bellussi, G.; Carati, A.; Millini, R. Industrial Potential of Zeolites. Zeolites and Catalysis: Synthesis, Reactions and Applications, Eds. J. Cejka, A. Corma, S. Zones **2010**; Wiley-VCH, Weinhem, 449-491. https://doi.org/10.1002/9783527630295.ch16.

(9) Climent, M. J.; Corma, A.; Iborra, S. Zeolites as Catalysts for the Synthesis of Fine Chemicals, *Zeolites and Catalysis: Synthesis, Reactions and Applications*, Eds. J. Cejka, A. Corma, S. Zones, **2010**, Wiley-VCH, Weinheim, 775-826.https://doi.org/10.1002/9783527630295.ch25.

(10) Tatsumi, T. Metals in Zeolites for Oxidation Catalysis. *Zeolites and Catalysis: Synthesis, Reactions and Applications*, Eds. J. Cejka, A. Corma, S. Zones, **2010**, Wiley-VCH, Weinheim, 713-743. https://doi.org/10.1002/9783527630295.ch23.

(11) Kubička, D.; Kikhtyanin, O. Opportunities for Zeolites in Biomass Upgrading—Lessons from the Refining and Petrochemical Industry. *Catal. Today* **2015**, *243*, 10–22. https://doi.org/10.1016/j.cattod.2014.07.043.

(12) Bridgwater, A. V. Renewable Fuels and Chemicals by Thermal Processing of Biomass. *Chem. Eng. J.* **2003**, *91*, 87–102. https://doi.org/10.1016/S1385-8947(02)00142-0.

(13) Huber, G. W.; Iborra, S.; Corma, A. Synthesis of Transportation Fuels from Biomass: Chemistry, Catalysts, and Engineering. *Chem. Rev.* **2006**, *106*, 4044–4098. https://doi.org/10.1021/cr068360d.

(14) Das, A.; Rahimi, A.; Ulbrich, A.; Alherech, M.; Motagamwala, A. H.; Bhalla, A.; Da Costa Sousa, L.; Balan, V.; Dumesic, J. A.; Hegg, E. L.; et al. Lignin Conversion to Low-Molecular-Weight Aromatics via an Aerobic Oxidation-Hydrolysis Sequence: Comparison of Different Lignin Sources. *ACS Sustain. Chem. Eng.* **2018**, *6*, 3367–3374. https://doi.org/10.1021/acssuschemeng.7b03541.

(15) Zhang, H.; Zheng, J.; Xiao, R.; Jia, Y.; Shen, D.; Jin, B.; Xiao, G. Study on Pyrolysis of Pine Sawdust with Solid Base and Acid Mixed Catalysts by Thermogravimetry-Fourier Transform Infrared Spectroscopy and Pyrolysis-Gas Chromatography/Mass Spectrometry. *Energy and Fuels* **2014**, *28*, 4294–4299. https://doi.org/10.1021/ef500176w.

(16) Liu, C.; Wang, H.; Karim, A. M.; Sun, J.; Wang, Y. Catalytic Fast Pyrolysis of Lignocellulosic Biomass. *Chem. Soc. Rev.* **2014**, *43*, 7594–7623. https://doi.org/10.1039/C3CS60414D.

(17) Corma, A.; Huber, G. W.; Sauvanaud, L.; O'Connor, P. Processing Biomass-Derived Oxygenates in the Oil Refinery: Catalytic Cracking (FCC) Reaction Pathways and Role of Catalyst. *J. Catal.* **2007**, *247*, 307–327. https://doi.org/10.1016/j.jcat.2007.01.023.

(18) Prasertcharoensuk, P.; Bull, S. J.; Phan, A. N. Gasification of Waste Biomass for Hydrogen Production: Effects of Pyrolysis Parameters. *Renew. Energy* **2019**, *143*, 112–120. https://doi.org/10.1016/j.renene.2019.05.009.

(19) Davda, R. R.; Shabaker, J. W.; Huber, G. W.; Cortright, R. D.; Dumesic, J. A. A Review of Catalytic Issues and Process Conditions for Renewable Hydrogen and Alkanes by Aqueous-Phase Reforming of Oxygenated Hydrocarbons over Supported Metal Catalysts. *Appl. Catal. B Environ.* **2005**, *56*, 171–186. https://doi.org/10.1016/j.apcatb.2004.04.027.

(20) Huber, G. W.; O'Connor, P.; Corma, A. Processing Biomass in Conventional Oil Refineries: Production of High Quality Diesel by Hydrotreating Vegetable Oils in Heavy Vacuum Oil Mixtures. *Appl. Catal. A Gen.* **2007**, *329*, 120–129. https://doi.org/10.1016/j.apcata.2007.07.002.

(21) Goyal, H. B.; Seal, D.; Saxena, R. C. Bio-Fuels from Thermochemical Conversion of Renewable Resources: A Review. *Renew. Sustain. Energy Rev.* **2008**, *12*, 504–517.

https://doi.org/10.1016/j.rser.2006.07.014.

(22) Vitolo, S.; Bresci, B.; Seggiani, M.; Gallo, M. G. Catalytic Upgrading of Pyrolytic Oils over HZSM-5 Zeolite: Behaviour of the Catalyst When Used in Repeated Upgrading-Regenerating Cycles. *Fuel* **2001**, *80*, 17–26. https://doi.org/10.1016/S0016-2361(00)00063-6.

(23) Yung, M. M.; Starace, A. K.; Griffin, M. B.; Wells, J. D.; Patalano, R. E.; Smith, K. R.; Schaidle, J. A. Restoring ZSM-5 Performance for Catalytic Fast Pyrolysis of Biomass: Effect of Regeneration Temperature. *Catal. Today* **2019**, *323*, 76-85. https://doi.org/10.1016/j.cattod.2018.06.025

(24) Park, H. J.; Heo, H. S.; Jeon, J. K.; Kim, J.; Ryoo, R.; Jeong, K. E.; Park, Y. K. Highly Valuable Chemicals Production from Catalytic Upgrading of Radiata Pine Sawdust-Derived Pyrolytic Vapors over Mesoporous MFI Zeolites. *Appl. Catal. B Environ.* **2010**, *95*, 365–373. https://doi.org/10.1016/j.apcatb.2010.01.015.

(25) Valle, B.; Gayubo, A. G.; Alonso, A.; Aguayo, A. T.; Bilbao, J. Hydrothermally Stable HZSM-5 Zeolite Catalysts for the Transformation of Crude Bio-Oil into Hydrocarbons. *Appl. Catal. B Environ.* **2010**, *100*, 318–327. https://doi.org/10.1016/j.apcatb.2010.08.008.

(26) Jae, J.; Coolman, R.; Mountziaris, T. J.; Huber, G. W. Catalytic Fast Pyrolysis of Lignocellulosic Biomass in a Process Development Unit with Continual Catalyst Addition and Removal. *Chem. Eng. Sci.* **2014**, *108*, 33–46. https://doi.org/10.1016/j.ces.2013.12.023.

(27) Giannakopoulou, K.; Lukas, M.; Vasiliev, A.; Brunner, C.; Schnitzer, H. Conversion of Rapeseed Cake into Bio-Fuel in a Batch Reactor: Effect of Catalytic Vapor Upgrading. *Microporous Mesoporous Mater.* **2010**, *128*, 126–135. https://doi.org/10.1016/j.micromeso.2009.08.022.

(28) Gayubo, A. G.; Aguayo, A. T.; Atutxa, A.; Aguado, R.; Olazar, M.; Bilbao, J. Transformation of Oxygenate Components of Biomass Pyrolysis Oil on a HZSM-5 Zeolite. II. Aldehydes, Ketones, and Acids. *Ind. Eng. Chem. Res.* **2004**, *43*, 2619–2626. https://doi.org/10.1021/ie030792g.

(29) Prasomsri, T.; To, A. T.; Crossley, S.; Alvarez, W. E.; Resasco, D. E. Catalytic

Conversion of Anisole over HY and HZSM-5 Zeolites in the Presence of Different Hydrocarbon Mixtures. *Appl. Catal. B Environ.* **2011**, *106*, 204–211. https://doi.org/10.1016/j.apcatb.2011.05.026.

(30) Bertero, M.; Sedran, U. Upgrading of Bio-Oils over Equilibrium FCC Catalysts. Contribution from Alcohols, Phenols and Aromatic Ethers. *Catal. Today* **2013**, *212*, 10–15. https://doi.org/10.1016/j.cattod.2013.03.016.

(31) Mentzel, U. V.; Holm, M. S. Utilization of Biomass: Conversion of Model Compounds to Hydrocarbons over Zeolite H-ZSM-5. *Appl. Catal. A Gen.* **2011**, *396*, 59–67. https://doi.org/10.1016/j.apcata.2011.01.040.

(32) Gayubo, A. G.; Aguayo, A. T.; Atutxa, A.; Valle, B.; Bilbao, J. Undesired Components in the Transformation of Biomass Pyrolysis Oil into Hydrocarbons on an HZSM-5 Zeolite Catalyst. *J. Chem. Technol. Biotechnol.* **2005**, *80*, 1244–1251. https://doi.org/10.1002/jctb.1316.

(33) Lange, J. P.; Van Der Heide, E.; Van Buijtenen, J.; Price, R. Furfural-A Promising Platform for Lignocellulosic Biofuels. *ChemSusChem* **2012**, *5*, 150–166. https://doi.org/10.1002/cssc.201100648.

(34) Du, S.; Gamliel, D. P.; Valla, J. A.; Bollas, G. M. The Effect of ZSM-5 Catalyst Support in Catalytic Pyrolysis of Biomass and Compounds Abundant in Pyrolysis Bio-Oils. *J. Anal. Appl. Pyrolysis* **2016**, *122*, 7–12. https://doi.org/10.1016/j.jaap.2016.11.002.

(35) Rezaei, P. S.; Shafaghat, H.; Daud, W. M. A. W. Production of Green Aromatics and Olefins by Catalytic Cracking of Oxygenate Compounds Derived from Biomass Pyrolysis: A Review. *Appl. Catal. A Gen.* **2014**, *469*, 490–511. https://doi.org/10.1016/j.apcata.2013.09.036.

(36) Zakzeski, J.; Bruijnincx, P. C. A.; Jongerius, A. L.; Weckhuysen, B. M. The Catalytic Valorization of Ligning for the Production of Renewable Chemicals. *Chem. Rev.* **2010**, *110*, 3552–3599. https://doi.org/10.1021/cr900354u.

(37) Graça, I.; Ribeiro, F. R.; Cerqueira, H. S.; Lam, Y. L.; de Almeida, M. B. B. Catalytic Cracking of Mixtures of Model Bio-Oil Compounds and Gasoil. *Appl. Catal. B Environ.* **2009**, *90*, 556–563. https://doi.org/10.1016/j.apcatb.2009.04.010.

(38) Alonso, D. M.; Wettstein, S. G.; Dumesic, J. A. Bimetallic Catalysts for Upgrading of Biomass to Fuels and Chemicals. *Chem. Soc. Rev.* **2012**, *41*, 8075–8098. https://doi.org/10.1039/c2cs35188a.

(39) Lin, Y.; Cho, J.; Tompsett, G. A.; Westmoreland, P. R.; Huber, G. W. Kinetics and Mechanism of Cellulose Pyrolysis. *J. Phys. Chem. C* **2009**, *113*, 20097–20107. https://doi.org/10.1021/jp906702p.

(40) Cheng, Y. T.; Huber, G. W. Chemistry of Furan Conversion into Aromatics and Olefins over HZSM-5: A Model Biomass Conversion Reaction. *ACS Catal.* **2011**, *1*, 611–628. https://doi.org/10.1021/cs200103j.

(41) Gou, J.; Wang, Z.; Li, C.; Qi, X.; Vattipalli, V.; Cheng, Y.-T.; Conner, W. C.; Dauenhauer, P. J.; Mountziaris, T. J.; Fan, W.; et al. The Effect of ZSM-5 Mesoporotsity and Morphology on the Catalytic Fast Pyrolysis of Furan. *Green Chem.* **2017**, *19*, 286–297. https://doi.org/10.1039/c7gc01395g.

(42) Song, S.; Wu, G.; Dai, W.; Guan, N.; Li, L. Diels-Alder and Dehydration Reactions of Furan Derivatives with Ethylene Catalyzed by Liquid Brønsted Acids and Lewis Acids. *J. Mol. Catal. A Chem.* **2016**, *420*, 134–141. https://doi.org/10.1016/j.molcata.2016.04.023.

(43) Cheng, Y.-T.; Huber, G. W. Production of Targeted Aromatics by Using Diels–Alder Classes of Reactions with Furans and Olefins over ZSM-5. *Green Chem.* **2012**, *14*, 3114–3125. https://doi.org/10.1039/c2gc35767d.

(44) Carlson, T. R.; Cheng, Y.-T.; Jae, J.; Huber, G. W. Production of Green Aromatics and Olefins by Catalytic Fast Pyrolysis of Wood Sawdust. *Energy Environ. Sci.* **2011**, *4*, 145–161. https://doi.org/10.1039/C0EE00341G.

(45) Cheng, Y. T.; Jae, J.; Shi, J.; Fan, W.; Huber, G. W. Production of Renewable Aromatic Compounds by Catalytic Fast Pyrolysis of Lignocellulosic Biomass with Bifunctional Ga/ZSM-5 Catalysts. *Angew. Chem. Int. Ed.* **2012**, *51*, 1387–1390. https://doi.org/10.1002/anie.201107390.

(46) Tshabalala, T. E.; Scurrell, M. S. Aromatization of n-Hexane over Ga, Mo and Zn Modified H-ZSM-5 Zeolite Catalysts. *Catal. Commun.* **2015**, *72*, 49–52. https://doi.org/10.1016/j.catcom.2015.06.022.

(47) Liu, R.; Zhu, H.; Wu, Z.; Qin, Z.; Fan, W.; Wang, J. Aromatization of Propane over Ga-Modified ZSM-5 Catalysts. *Ranliao Huaxue Xuebao* **2015**, *43*, 961–969. https://doi.org/10.1016/S1872-5813(15)30027-X.

(48) Leth, K. T.; Rovik, A. K.; Holm, M. S.; Brorson, M.; Jakobsen, H. J.; Skibsted, J.; Christensen, C. H. Synthesis and Characterization of Conventional and Mesoporous Ga-MFI for Ethane Dehydrogenation. *Appl. Catal. A Gen.* **2008**, *348*, 257–265. https://doi.org/10.1016/j.apcata.2008.07.003.

(49) Shao, C.-T.; Lang, W.-Z.; Yan, X.; Guo, Y.-J. Catalytic Performance of Gallium Oxide Based-Catalysts for the Propane Dehydrogenation Reaction: Effects of Support and Loading Amount. *RSC Adv.* **2017**, *7*, 4710–4723. https://doi.org/10.1039/C6RA27204E.

(50) Tamiyakul, S.; Ubolcharoen, W.; Tungasmita, D. N.; Jongpatiwut, S. Conversion of Glycerol to Aromatic Hydrocarbons over Zn-Promoted HZSM-5 Catalysts. *Catal. Today* **2015**, *256*, 325–335. https://doi.org/10.1016/j.cattod.2014.12.030.

(51) Sigmund, M. Shape-Selective Catalysis in Zeolites. *Zeolites* **1984**, *4*, 202–213.

(52) Wang, C.; Zhang, L.; Huang, X.; Zhu, Y.; Li, G.; Gu, Q.; Chen, J.; Ma, L.; Li, X.; He, Q.; et al. Maximizing Sinusoidal Channels of HZSM-5 for High Shape-Selectivity to *p*-Xylene. *Nat. Commun.* **2019**, *10*, 1–8. https://doi.org/10.1038/s41467-019-12285-4.

(53) Corma, A. State of the Art and Future Challenges of Zeolites as Catalysts. *J. Catal.* **2003**, *216*, 298–312. https://doi.org/10.1016/S0021-9517(02)00132-X.

(54) Lok, C. M.; Van Doorn, J.; Aranda Almansa, G. Promoted ZSM-5 Catalysts for the Production of Bio-Aromatics, a Review. *Renew. Sustain. Energy Rev.* **2019**, *113*, 109248. https://doi.org/10.1016/j.rser.2019.109248.

(55) Samanta, A.; Bai, X.; Robinson, B.; Chen, H.; Hu, J. Conversion of Light Alkane to Value-Added Chemicals over ZSM-5/Metal Promoted Catalysts. *Ind. Eng. Chem. Res.* **2017**, *56*, 11006–11012. https://doi.org/10.1021/acs.iecr.7b02095.

(56) Pidko, E. A.; Kazansky, V. B.; Hensen, E. J. M.; van Santen, R. A. A Comprehensive Density Functional Theory Study of Ethane Dehydrogenation over Reduced Extra-Framework Gallium Species in ZSM-5 Zeolite. *J. Catal.* **2006**, *240*, 73–84. https://doi.org/10.1016/j.jcat.2006.03.011.

(57) Cheng, Y. T.; Wang, Z.; Gilbert, C. J.; Fan, W.; Huber, G. W. Production of *p*-Xylene from Biomass by Catalytic Fast Pyrolysis Using ZSM-5 Catalysts with Reduced Pore Openings. *Angew. Chem. Int. Ed.* **2012**, *51*, 11097–11100. https://doi.org/10.1002/anie.201205230.

(58) French, R.; Czernik, S. Catalytic Pyrolysis of Biomass for Biofuels Production. *Fuel Process. Technol.* **2010**, *91*, 25–32. https://doi.org/10.1016/j.fuproc.2009.08.011.

(59) Espindola, J. S.; Gilbert, C. J.; Perez-Lopez, O. W.; Trierweiler, J. O.; Huber, G. W. Conversion of Furan over Gallium and Zinc Promoted ZSM-5: The Effect of Metal and Acid Sites. *Fuel Process. Technol.* **2020**, *201*, 106319. https://doi.org/10.1016/j.fuproc.2019.106319.

(60) Collett, C. H.; McGregor, J. Things Go Better with Coke: The Beneficial Role of Carbonaceous Deposits in Heterogeneous Catalysis. *Catal. Sci. Technol.* **2016**, *6*, 363–378. https://doi.org/10.1039/c5cy01236h.

(61) Guisnet, M.; Magnoux, P. Fundamental Description of Deactivation and Regeneration of Acid Zeolites. *Studies in Surface Science and Catalysis*. 1994, 53–68. https://doi.org/10.1016/S0167-2991(08)62729-9.

(62) Guisnet, M.; Magnoux, P.; Martin, D. Catalyst Deactivation, Proceedings of the 7th International Symposium. *Stud. Surf. Sci. Catal.* **1997**, *111*, 1–19. https://doi.org/10.1016/S0167-2991(97)80138-3.

(63) Du, S.; Gamliel, D. P.; Giotto, M. V.; Valla, J. A.; Bollas, G. M. Coke Formation of Model Compounds Relevant to Pyrolysis Bio-Oil over ZSM-5. *Appl. Catal. A Gen.* **2016**, *513*, 67–81. https://doi.org/10.1016/j.apcata.2015.12.022.

(64) Guisnet, M.; Magnoux, P. Organic Chemistry of Coke Formation. *Appl. Catal. A Gen.* **2001**, *212*, 83–96. https://doi.org/10.1016/S0926-860X(00)00845-0.

(65) Vogt, E. T. C.; Weckhuysen, B. M. Fluid Catalytic Cracking: Recent Developments on the Grand Old Lady of Zeolite Catalysis. *Chem. Soc. Rev.* **2015**, *44*, 7342–7370. https://doi.org/10.1039/C5CS00376H.

(66) Shao, S.; Zhang, H.; Xiao, R.; Li, X.; Cai, Y. Controlled Regeneration of ZSM-5 Catalysts in the Combined Oxygen and Steam Atmosphere Used for Catalytic Pyrolysis

of Biomass-Derivates. *Energy Convers. Manag.* **2018**, *155*, 175–181. https://doi.org/10.1016/j.enconman.2017.10.062.

(67) Guisnet, M.; Costa, L.; Ribeiro, F. R. Prevention of Zeolite Deactivation by Coking. *J. Mol. Catal. A Chem.* **2009**, *305*, 69–83. https://doi.org/10.1016/j.molcata.2008.11.012.

(68) Yun, J. H.; Lobo, R. F. Catalytic Dehydrogenation of Propane over Iron-Silicate Zeolites. *J. Catal.* **2014**, *312*, 263–270. https://doi.org/10.1016/j.jcat.2014.02.007.

(69) Shpiro, E. S.; Shevchenko, D. P.; Dmitriev, E. V.; Tkachenko, O. P.; Minachev, K. M. Platinum Promoting Effects in Pt/Ga Zeolite Catalysts of Lower Alkane Aromatization. II. The Catalytic Properties in n-Butane Aromatization, Formation of the Catalytically Active Sites and Reaction Mechanism. *Appl. Catal. A, Gen.* **1994**, *107*, 165–180. https://doi.org/10.1016/0926-860X(94)85153-0.

(70) Hensen, E. J. M.; Pidko, E. A.; Rane, N.; Van Santen, R. A. Water-Promoted Hydrocarbon Activation Catalyzed by Binuclear Gallium Sites in ZSM-5 Zeolite. *Angew. Chem. Int. Ed.* **2007**, *46*, 7273–7276. https://doi.org/10.1002/anie.200702463.

(71) Zhang, H.; Shao, S.; Xiao, R.; Shen, D.; Zeng, J. Characterization of Coke Deposition in the Catalytic Fast Pyrolysis of Biomass Derivates. *Energy and Fuels* **2014**, *28*, 52–57. https://doi.org/10.1021/ef401458y.

(72) Valle, B.; Castaño, P.; Olazar, M.; Bilbao, J.; Gayubo, A. G. Deactivating Species in the Transformation of Crude Bio-Oil with Methanol into Hydrocarbons on a HZSM-5 Catalyst. *J. Catal.* **2012**, *285*, 304–314. https://doi.org/10.1016/j.jcat.2011.10.004.

(73) Yarulina, I.; Chowdhury, A. D.; Meirer, F.; Weckhuysen, B. M.; Gascon, J. Recent Trends and Fundamental Insights in the Methanol-to-Hydrocarbons Process. *Nat. Catal.* **2018**, *1*, 398–411. https://doi.org/10.1038/s41929-018-0078-5.

(74) Chowdhury, A. D.; Houben, K.; Whiting, G. T.; Mokhtar, M.; Asiri, A. M.; Al-Thabaiti, S. A.; Basahel, S. N.; Baldus, M.; Weckhuysen, B. M. Initial Carbon–Carbon Bond Formation during the Early Stages of the Methanol-to-Olefin Process Proven by Zeolite-Trapped Acetate and Methyl Acetate. *Angew. Chem. Int. Ed.* **2016**, *55*, 15840–15845. https://doi.org/10.1002/anie.201608643.

(75) Nordvang, E. C.; Borodina, E.; Ruiz-Martínez, J.; Fehrmann, R.; Weckhuysen, B. M.

Effects of Coke Deposits on the Catalytic Performance of Large Zeolite H-ZSM-5 Crystals during Alcohol-to-Hydrocarbon Reactions as Investigated by a Combination of Optical Spectroscopy and Microscopy. *Chem. Eur. J.* **2015**, *21*, 17324–17335. https://doi.org/10.1002/chem.201503136.

(76) Sánchez, B.; Gross, M. S.; Dalla Costa, B. O.; Querini, C. A. Coke Analysis by Temperature-Programmed Oxidation: Morphology Characterization. *Appl. Catal. A Gen.* **2009**, *364*, 35–41. https://doi.org/10.1016/j.apcata.2009.05.018.

(77) Verkleij, S. P.; Whiting, G. T.; Esclapez, S. P.; Mertens, M. M.; Bons, A.-J.; Burgers, M.; Weckhuysen, B. M. *Operando* Micro-Spectroscopy on ZSM-5 Containing Extrudates during the Oligomerization of 1-Hexene. *Catal. Sci. Technol.* **2018**, *8*, 2175–2185. https://doi.org/10.1039/C7CY02460F.

PART A

Chapter 2 *Operando* UV/Vis Diffuse Reflectance Spectroscopy of the Catalytic Aromatization of Bio-based Furans over HZSM-5 Zeolites

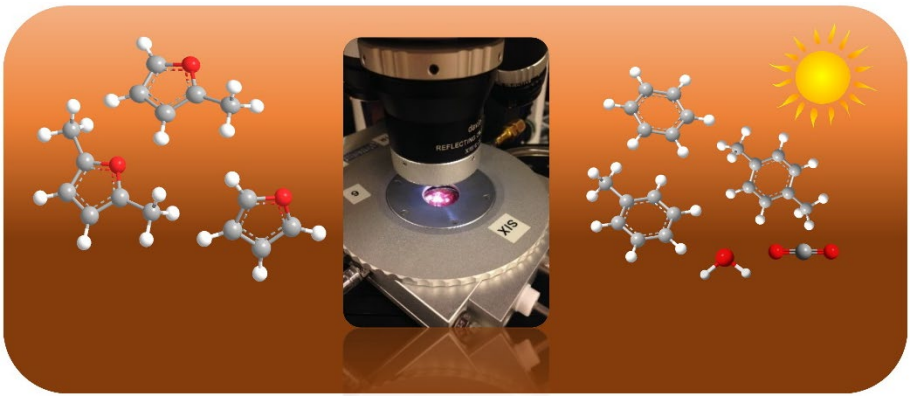

Abstract

The production of renewable platform compounds, such as aromatics and/or olefins, from biomass-derived furans via catalytic fast pyrolysis (CFP) technology is recently receiving increased attention. However, the low carbon selectivity and rapid catalyst deactivation hampers commercialization of this process. To improve the overall efficiency of this chemical process, detailed mechanistic insight at the level of the catalyst is needed, which can be obtained from *operando* spectroscopic studies. *Operando* UV/Vis Diffuse Reflectance Spectroscopy (DRS) coupled with online Mass Spectrometry (MS) allowed us to monitor the catalytic aromatization of bio-based furans over different HZSM-5 zeolites. Based on the time-resolved UV/Vis DRS profiles and online MS signals in which benzene, toluene and small olefins were detected, we propose that furan derivatives follow a mechanistic pathway similar to the well-established dual-cycle (alkene/arene) hydrocarbon pool mechanism (HCP) operating in the Methanol-to-Hydrocarbon conversion (MTH). Furthermore, UV/Vis DRS showed that the size of the active carbocations formed at the early stages of the reaction depends on the acidity and porosity of the catalyst, and that the active species formed during the conversion of furan, 2-methylfuran and 2,5-dimethylfuran displayed a red shift relative to the number of methyl groups of each starting reagent, implying that the size of the active species formed during the reaction as function of time on stream will depend on them. Nevertheless, the main mechanism of formation turned out to follow the same pathway independent of the type of furan derivatives and zeolite Si/Al ratio used.

2.1 Introduction

As discussed in Chapter 1, bio-oils are complex liquids with a high oxygen content (up to 40% depending on the origin of the biomass), which can, for example, be obtained from the (catalytic) pyrolysis of lignocellulosic biomass and can thereafter be upgraded into commodity chemicals and fuels[1,2]. The main fractions of lignocellulosic biomass are lignin, hemicellulose and cellulose. Char, non-condensable gases as well as pyrolysis vapors are obtained once solid biomass is converted within a catalytic fast pyrolysis (CFP) reactor. The chemical composition of the pyrolysis vapors formed mainly consists of a mixture of oxygenates[3]. For example, furans are directly obtained from the dehydration of cellulose and hemicellulose and can make up ~ 15% wt. of the bio-oil vapor fraction[2,4,5]. Given their relative abundance and ease of formation, furans are often considered as promising bio-derived intermediates that can be further upgraded into value-added chemicals[6–8]. This upgrading process is schematically illustrated in Figure 2.1.

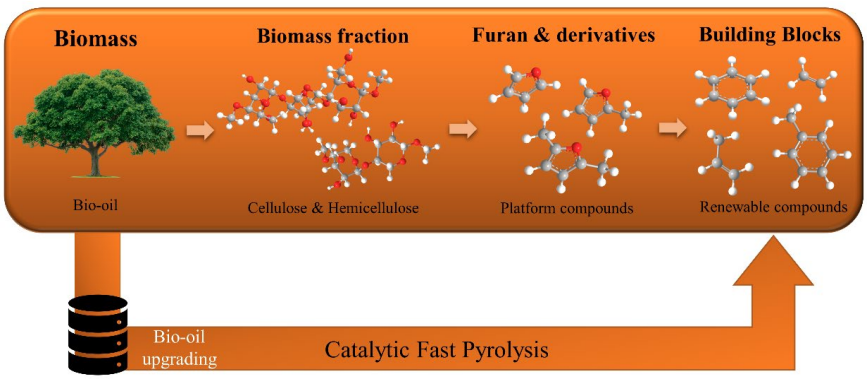

Figure 2.1. Schematic representation of the different chemical transformations that need to take place to form renewable olefins or aromatics from raw biomass, either through bio-derived platform compounds (e.g. furans) or in a single step via catalytic fast pyrolysis (CFP).

CFP is one of the most investigated processes to convert biomass into chemical building blocks, such as olefins and aromatics[9]. The upgrading of biomass to platform molecules often involves the use of acidic zeolites, being HZSM-5 zeolites the most commonly used, due to their strong dehydration and deoxygenation capabilities[10,11]. However, already at the very early stages of the conversion process, carbon deposits form, which ultimately lead to catalyst deactivation. In addition to bio-oil upgrading, the CFP of bio-derived, pure furans to produce aromatics, olefins, and bio-fuels over HZSM-5 zeolites has also been investigated. The conversion of bio-derived furans has gained increasing relevance due to the various routes by which they can be

catalytically converted into building blocks and their abundance within the bio-oil feed[12,13]. Thus, the conversion of bio-derived furans became a potential route to enhance biomass valorization [14]. In the last decade, several investigations focused on improving the performance of HZSM-5 zeolites during the catalytic conversion of bio-derived oxygenates by boosting the yield towards aromatics, while at the same time decreasing the degree of catalyst deactivation[15–17]. Modification of the acidic properties by incorporating metal promotors has become a common practice, modulating the density of strong Brønsted acid sites in the catalyst, sites considered detrimental as they promote catalyst deactivation[13,16,18,19]. This catalytic technology is usually able to convert these class of bio-based oxygenates into aromatics and olefins over HZSM-5 zeolites by effectively removing oxygen via decarboxylation, decarbonylation and dehydration reactions[20]. However, despite the many studies performed there is still a lack of mechanistic understanding of the reaction pathways taking place, which hampers further development of this approach. As is more common for the production of hydrocarbons via the well-known Methanol-to-Hydrocarbons (MTH), Methanol-to-Olefins (MTO)[21] and Methanol-to-Aromatics (MTA)[22,23] technologies, detailed insight into the diverse mechanistic pathways allowed for the design of improved and more efficient zeolite-based catalysts. Analogously, improved insights into the mechanistic pathways governing furan conversion should facilitate the development of new or improved catalyst formulations.

A first important contribution to the elucidation of the reaction mechanism of converting furans into aromatics was reported by Grandmaison *et al.*[6]. They detected benzofuran both within the coke deposits and as a reaction product. Later on, Huber *et al.*, further investigated the conversion of furan on zeolite HZSM-5 revealing that benzofuran was also a major reaction product during the conversion of furan and suggested that this chemical originates from Diels-Alder cycloaddition reactions[15,24]. Moreover, these authors also provided further insight into the deactivation pathways, thereby suggesting that benzofuran is considered both a deactivation precursor and a reaction intermediate since they revealed that its direct conversion can yield both benzene and CO[15]. Among others, highly condensed coke species, such as indene, naphthalene and their alkylated derivatives, were also detected during their experiments. These findings are illustrated in Figure 2.2.

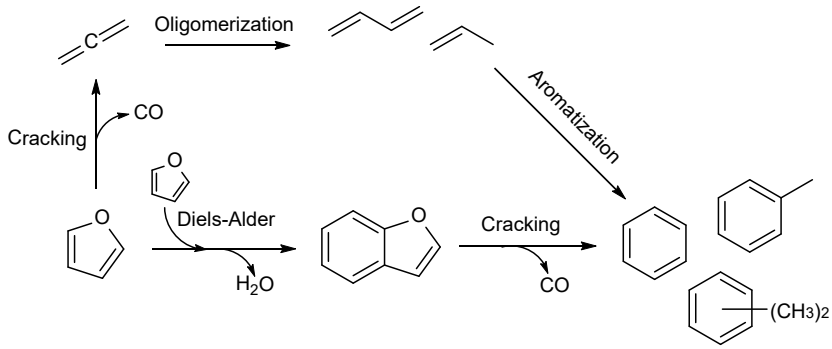

Figure 2.2. Reaction steps, as proposed by Cheng *et al.*, during the conversion of furan over a HZSM-5 zeolite as catalyst. Adapted from reference[15,16,25].

Operando spectroscopy could provide further insight into the mechanism, e.g. into benzofuran formation and its role during the aromatization of furan, and the eventual path of catalyst deactivation due to coke formation. Here, inspiration can be taken from mechanistic studies on the related, heavily investigated MTH, MTO and MTA processes[26,27]. Dahl and co-workers have proposed that the MTH process follows a so-called Hydrocarbon Pool (HCP)[28] mechanism, for which the formation of products occurs in a "pool" inside the zeolite pores/channels in which carbon loses its identity. Recently performed time-resolved *operando* UV/Vis spectroscopy experiments[29–31] coupled with other *ex-situ* (spectroscopic) characterization techniques allowed the identification of both adsorbed cationic and neutral species located inside the zeolite domains, based on the detection of reactions intermediates[32,33] and trapped coke deposits[34–37]. The latest investigations converged on the so-called dual-cycle mechanism[21], which was initially suggested by Olsbye *et al.*. This mechanism comprises two independent and competing alkene and arene-based cycles that run within the intra-zeolitic framework and are responsible for the formation of olefins and aromatics[38] (Figure 2.3). In this particular case, it is believed that further condensation of the generated aromatics eventually causes coke formation and thus, catalyst deactivation.

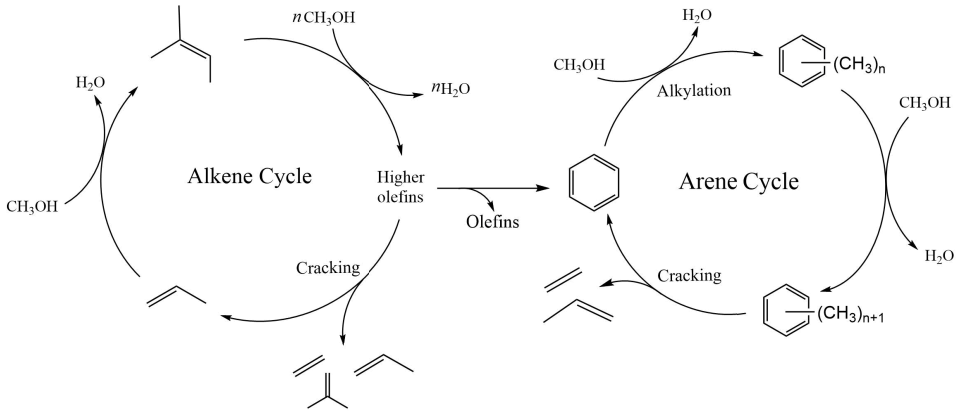

Figure 2.3. Dual-cycle mechanism proposed for the Methanol-to-Hydrocarbons (MTH) process. Adapted from reference[38].

First-of-its-kind studies suggested that furans are converted[39] at the catalytic active sites of zeolite HZSM-5 by a series of oligomerization, alkylation, decarbonylation and dehydration reactions, thereby producing aromatics, CO, CO_2, H_2O and coke deposits[7,13,15]. Nevertheless, the lack of spectroscopic and more specifically, *in-situ* or *operando* evidences for these mechanistic assumptions, warrants an in-depth *operando* spectroscopy study of the Furan-to-Aromatics (FTA) process.

Interestingly, recent studies on the aromatization mechanism of furan and 2,5-dimethylfuran over HZSM-5 proposed that the acid-catalyzed conversion of furan derivatives, after protonation of the furan ring, involves a series of ring opening, isomerization and tautomerization reactions. These reactions ultimately lead to decarbonylation and dehydration to give both olefins and aromatics[40]. These results were based on a combined temperature programmed reduction (TPR) and Fourier transform-infrared (FT-IR) spectroscopy study of furan derivatives at low temperatures (i.e., below the temperature of the formation of aromatics, 300 – 600 °C). However, how these observations translate to the typical high temperature reaction conditions remains to be demonstrated. In addition, it is noteworthy that porosity and acid density of the zeolite-based catalysts are crucial parameters that need to be optimized since they determine the type of reaction product formed and the extent of coke formation. To overcome this issue, hierarchical zeolites were proposed as a potential solution[41–43], since they are known to elongate catalyst life-time in a wide variety of processes. Simple post-synthetic methods, such as alkaline treatment, can created zeolite mesoporosity[44].

The above-mentioned efforts to propose a detailed mechanistic pathway for the formation of aromatics have yet to be complemented with a detailed *operando* spectroscopic study under realistic reaction conditions. In this Chapter, we report mechanistic investigations under such conditions using an *operando* approach using a combination of UV/Vis DRS approach and online Mass Spectrometry (MS). More specifically, the catalytic conversion of furan (F), 2-methylfuran (MF) and 2,5-dimethylfuran (DMF) over zeolite HZSM-5 catalysts with different Si/Al ratios and porosity have been studied in a time-resolved manner with the aim to obtain new insights on the aromatization of furan derivatives obtained during the CFP process.

2.2 Experimental Part

2.2.1 Catalyst Preparation and Chemicals

For this study, two ZSM-5 zeolites with Si/Al ratios of 15 and 40 were used. The H^+ form of the catalyst materials was obtained after calcination of two commercial (NH_4^+)ZSM-5 zeolites, namely CBV 8014 (NH_4^+ form zeolite with a Si/Al=40) and CBV 3024E (NH_4^+ form zeolite with a Si/Al=15), at 550 °C for 5 h in air. The materials are further labelled as H15 and H40. Hierarchical zeolites were prepared following an alkaline treatment described elsewhere[45]. Zeolites (in their H-form) were stirred in 0.2 M NaOH solution at 65 °C for 30 min. Then, to obtain the materials in their H^+ form the treated sample was stirred in 200 ml 0.1 M NH_4NO_3 aqueous solution, with the aqueous solution being refreshed two times after 15 h. Subsequently, samples were filtered off, dried and calcined at 550 for 5 h. The hierarchical samples obtained were labelled as H15-A and H40-A. Furan (>99%, Sigma Aldrich), 2-methylfuran (99%, Sigma Aldrich) and 2,5-dimethylfuran (98+%, Alfa Aesar) were used without any treatment.

2.2.2 Catalyst Characterization and Testing

X-ray diffraction (XRD) patterns were obtained using a Bruker-AXS D2 Phaser powder X-ray diffractometer in Bragg-Brentano mode equipped with a Lynxeye detector. The radiation used was a CoK_α (λ = 1.79026 Å) source. The XRD patterns were collected in the 2θ range from 5° to 50° at a scanning speed of 0.02 °/min and an acquisition time of 1 s per step.

Surface area and porosity of the synthesized catalysts were determined by Ar physisorption using a Micrometric TriStar II plus Analyzer at -196 °C. Before the experiments, all samples were degassed under a N_2 flow at 300 °C for 16 h to remove any physisorbed impurities. The micropore volume and the surface area were determined by the *t*-plot method and the Brunauer-Emmett-Teller (BET) theory, respectively. External surface area was determined by subtraction of the micropore volume area from the BET surface area.

Silicon and aluminum were determined by elemental analysis using an inductively coupled plasma-optical emission spectrometer (ICP-OES) analyzer. The experiments were performed at Mikroanalytisches laboratorium Kolbe in Oberhauser, Germany. Prior to analysis, all the samples were digested in special acid solutions.

Temperature programmed desorption (TPD) analyses with NH_3 as probe molecule were recorded in a Micromeritics AutoChem II 2920 to determine both the strength and number of acid sites of the materials. 100 mg of sample was placed on the chamber and pre-treated up to 600 °C under a He flow. The chamber was cooled down and kept at 100 °C before to start the NH_3 dossing. A 25 ml/min flow of 10% NH_3 in He was fed into the chamber using a pulse-wise manner until saturation. Afterwards, the temperature was ramped to 600 °C with a heating rate of 10 °C/min and kept at that temperature for 25 min more.

For pyridine Fourier transform-infrared (FT-IR) spectroscopy measurements, the samples were grounded and pressed into thin self-supported wafers (~ 25 mg sample). The wafers were placed in a sealed FT-IR cell equipped with a vacuum system and a heating system. The wafers were pre-treated under vacuum (~10^{-5} mbar) at 550 °C for 2 h to remove all adsorbates, then was cooled down to 40 °C where pyridine vapor was introduced into the cell for 30 min until complete saturation. The weakly adsorbed pyridine was removed by evacuation for 20 min. Afterwards, the temperature was ramped from 40 to 150 °C at 2.5 °C/min and kept at 150 °C for 30 min, after which a FT-IR spectrum was recorded. As described elsewhere[46], this procedure allows to determine the amount of Lewis and Bronsted acid sites. Afterwards, the temperature was ramped up to 550 °C with a heating rate of 2.5 °C/min and kept at that temperature for 2 h min to remove all pyridine from the sample. All FT-IR spectra were recorded between 4000-1000 cm^{-1} using a Perkin-Elmer System 2000 FT-IR instrument.

Thermogravimetric analyses (TGA) were performed with a Perkin Elmer TGA8000 analyzer hyphenated with a Hiden HPR-20 Mass Spectrometer (TGA-MS) to analyze the amount and nature of the coke deposits formed in the spent catalyst. Prior to starting the measurements, 10

mg of spent sample was pre-dried under N_2 at 120 °C. Subsequently, the spent sample was submitted to 80 ml/min Ar flow and a heating ramp of 10 °C/min from 120 °C to 700 °C was applied. The CO_2 and H_2O MS signals (with m/z 44 and 18, respectively) were recorded during all analyses.

Hydrofluoric (HF) leaching experiments were carried out to extract the retained hydrocarbons from the spent catalysts. 30 mg of spent catalyst were added to a solution of 48% HF (ACS reagent, Sigma-Aldrich) and stirred for 30 min. The organic compounds were then extracted from the aqueous solution with 3 x 1 ml CH_2Cl_2. The combined extracted organics in CH_2Cl_2 were injected in an advanced gas chromatography (GC) system, more specifically a 2D GC×GC-MS instrument. The 2D GC×GC-MS (1st column: VF-5MS 30 m, 0.25 mm ID, df 0.25 µm; 2nd column: VF-17MS, 2.5 m, 0.15 mm ID, df 0.15 µm) data acquisition was performed with a Shimadzu GCMS-QP2010 Ultra instrument equipped with a Zoex ZX1 cryogenic modulator (LN2). The modulation time was 7 s with a jet flow 6 L/min. The column was stabilized at 40 °C for 5 min and ramped up to 280 °C at 2.5 °C/min. The injection port was at 270 °C and the interface temperature was 300 °C. Injection was 1 µl in split mode (50 split rate). The modulation applied for the comprehensive GC×GC analysis was a hot jet pulse at 100 °C (375 ms) every 7000 ms. The mass range analyzed was 45-500 m/z at 20000 amu/s scan speed. The 2D chromatograms were processed with GC Image software (Zoex).

Operando UV/Vis Diffuse Reflectance Spectroscopy (DRS) experiments were performed in a quartz-window reactor (FTIR600, Linkam Scientific Instruments) at 500 °C during 30 min. The setup was equipped with a UV/Vis AvaSpec-2048L spectrometer and an AvaLight DH-S-BAL light source, as outlined in Figure 2.4. The UV/Vis DRS probe sends the light to the sample through six illumination fibers, while the reflection is measured by one read fiber located in the center of the probe. 55 mg fresh catalyst was pelletized and introduced inside the reactor. Before performing the reaction, the catalyst was activated at 500 °C under an O_2 flow for 90 min and then was cooled to reaction temperature under N_2 flow. The different reagents were fed into the reactor by using N_2 as carrier gas through a gas bubbler at a weight hourly space velocity (WHSV) of 1 h^{-1} under atmospheric pressure. The reaction products were analyzed using an online OmniStar GSD 320 O3 (Pfeiffer) mass spectrometer (MS) equipped with a Faraday detector.

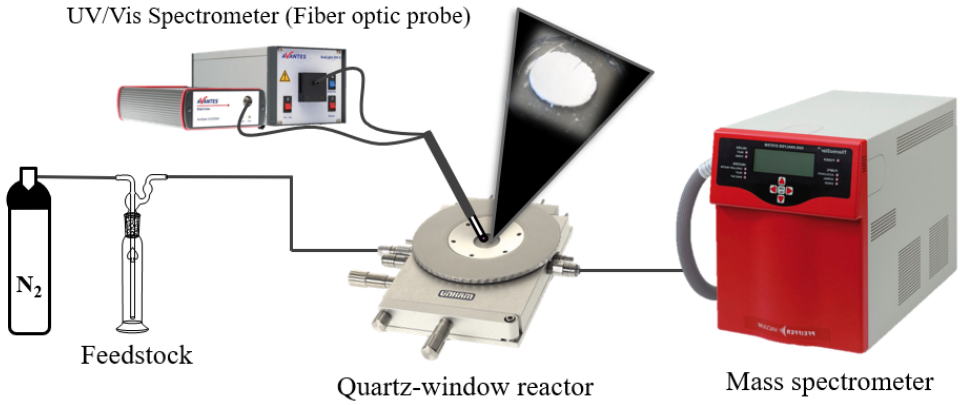

Figure 2.4. Schematic representation and related illustrations of the *operando* UV/Vis diffuse reflectance spectroscopy (DRS) setup used for studying the aromatization of furan derivatives. The reagents and reaction products are analyzed by an online mass spectrometer (MS).

2.3 Results

2.3.1 Bulk Catalyst Characterization

The crystallinity of the two pristine HZSM-5 zeolites H15 and H40 under study was investigated by X-ray diffraction (XRD) (Figure 2.5a), with the typical reflections for MFI zeolite crystals being observed for both materials. The most characteristic reflections are (101) at 9.2°, (200) at 10.2°, (111) at 10.5°, (332) at 26.9°, (051) at 27.2°, (151) at 27.6°, and (133) at 28.4°, which were assigned from the Powder Diffraction File (PDF) database. For the hierarchical zeolites, obtained after applying an alkaline treatment, a small shift was observed for both H15-A and H40-A. H40-A showed a small shift in the position of reflections towards higher values. In terms of crystallinity, no major changes were observed. However, the 9.2° peak for H40-A sample shows a relatively lower intensity, indicating that the available microporosity system has decreased. Ar physisorption measurements of H40 show a larger surface area and pore volume compared to the H15 sample (Table 2.1), as seen before for other materials with high Si/Al ratio[47]. After applying the alkaline treatment, the total micropore volume of both H15-A and H40-A materials decreased, while the total pore volume increased indicating the formation of mesopores in the system. Furthermore, the lower Si/Al ratio values confirm the increase in the density of Brønsted acid sites.

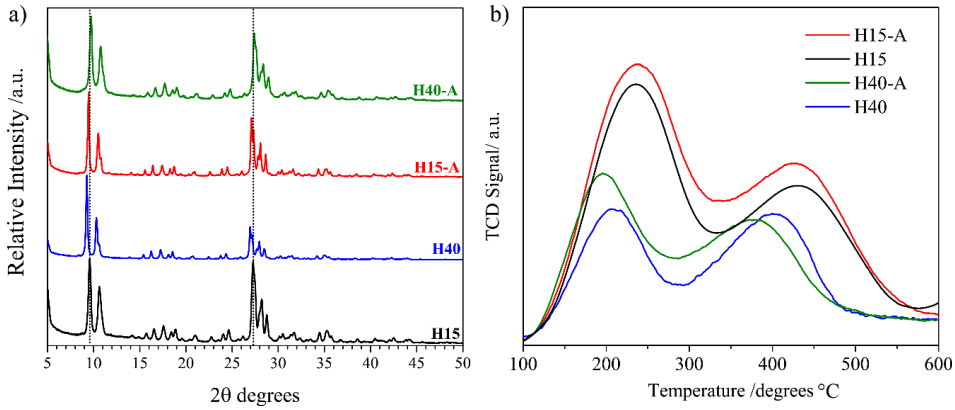

Figure 2.5. (a) X-ray diffractograms (XRD) and (b) NH_3-temperature programmed desorption (NH_3-TPD) profiles of the pristine H15 and H40 samples, as well as the alkaline-treated H15-A and H40-A samples.

Table 2.1. Overview of the physicochemical data of the four zeolite-based catalysts used in this study, as determined by (a) inductively coupled plasma-optical emission spectroscopy (ICP-OES) and (b) Ar physisorption at -196 °C.

Materials	**Si/Al ratio**[a]	**BET Surface Area** $m^2\ g^{-1}$	**(Micro)Pore Volume** $cm^3\ g^{-1}$	**Total Pore Volume** $cm^3\ g^{-1}$	**Micropore Area** $m^2\ g^{-1}$	**External Surface Area** $m^2\ g^{-1}$
H15	16	407	0.12	0.14	379	28
H40	39	453	0.14	0.23	388	65
H15-A	11	389	0.11	0.19	324	70
H40-A	27	475	0.10	0.39	288	187

The total amount and type of acid sites of the zeolite-based catalysts were measured by NH_3-TPD and pyridine FT-IR spectroscopy. The NH_3-TPD profiles are displayed in Figure 2.5b, showing two desorption peaks for all samples, corresponding to weak and strong acid sites. The NH_3-TPD profile for H15 compared to that one for H40 revealed a higher amount of strong acid sites, as expected due to the lower Si/Al ratio. Upon desilication, however, the NH_3-TPD profiles showed an overall increase of the number acid sites, especially of the weak acid sites, which is summarized in Table 2.2, confirming an overall increase in the acidity of the alkaline treated samples. Moreover, the strength of the weak and strong acid sites for the H40-A sample

shifted to lower temperatures, something which is not really expected or observed before in literature.

Table 2.2. Overview of the acidity data of the four zeolite-based catalysts used in this study, as determined by [a]NH_3-temperature programmed desorption (TPD) and [b]Pyridine Fourier transform-infrared (FT-IR) spectroscopy.

Materials	Amount of acid sites[a] μmol g^{-1}_{cat}	Weak acid sites[a] °C	Strong acid sites[a] °C	Lewis acid sites[b] μmol g^{-1}_{cat}	Bronsted acid sites[b] μmol g^{-1}_{cat}	Accessibility Index (ACI)[48]
H15	940	238	434	100	363	0.50
H40	400	209	403	32	195	0.56
H15-A	1050	230	413	128	350	0.45
H40-A	590	188	365	51	108	0.26

After adsorption of pyridine onto the zeolite-based catalysts, Brønsted acid sites (BAS) and Lewis acid sites (LAS) were determined with FT-IR spectroscopy and the obtained data are summarized in Table 2.2, while the spectroscopic data are shown in Figures 2.6 and 2.7 for the pristine and alkaline-treated samples, respectively.

The FT-IR band located at ~ 1490 cm^{-1} is assigned to the interaction of pyridine with both Lewis and Brønsted acid sites. The FT-IR bands at ~ 1600 cm^{-1} correspond to H-bonded pyridine on zeolite silanol groups, while the vibrations of the pyridinium ion and physisorbed pyridine can be observed from 1600 cm^{-1} to 1637 cm^{-1} and at ~ 1440-1445 cm^{-1}, respectively. Regarding the OH stretch region (ranging from 3500 to 3700 cm^{-1}), there are some changes taking place upon the addition of pyridine. More specifically, there is a decrease in the band intensity related to external silanol groups (3743-3746 cm^{-1}) and OH Brønsted acid sites (3608-3610 cm^{-1}), as shown in Figures 2.6a and Figure 2.6c.

Interestingly, the H15 zeolite sample shows the highest amount of BAS and LAS (Figure 2.6b), in accordance with the NH_3-TPD results. The slight discrepancy between the results on acidity obtained by NH_3-TPD and pyridine FT-IR spectroscopy, also observed in previous studies, is most probably related to two factors; the size of the probe molecule used for each of the acidity measurements, and the temperature difference between each experiments, since NH_3-TPD

experiments are recorded from 100 °C to 550 °C, while the pyridine probed FT-IR spectroscopy experiments underestimate the amount of acid sites since are calculated after recording a spectrum at 150 °C (i.e., the weaker acid sites were removed)[51–53].

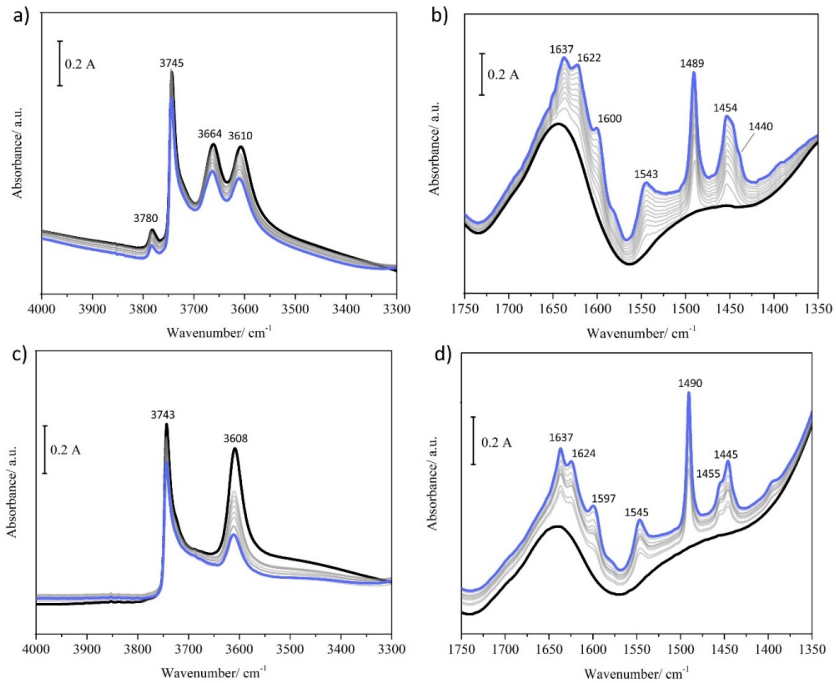

Figure 2.6. Fourier transform-infrared (FT-IR) spectra taken during pyridine adsorption at 30 °C until saturation of the pristine H15 (a-b) and H40 (c-d) samples. The **black** spectrum corresponds to the fresh materials after drying under high vacuum at 550 °C for 2 h and the **blue** spectrum corresponds to the same materials after saturation with pyridine.

For a more accurate evaluation on the determination of the acid sites by pyridine FT-IR spectroscopy, the accessibility index (ACI) was calculated[48,49]. This value correlates the detected acid sites by the pyridine probe with the total number of acid sites (i.e., as determined by NH_3-TPD). As tabulated in Table 2.2, the ACI for the two hierarchical zeolites under study decreased compared to the corresponding pristine zeolites, which is especially pronounced for the H40-A sample. As previously reported[54,55], alkaline treatments might cause a decrease in both the amount and accessibility of the acid sites due to a partial dealumination (thereby decreasing the amount of framework aluminum), leading to EFAl formation. This implies that the alkaline treatment conditions applied in this work for the synthesis of the H40-A sample

was not optimal suggesting that a milder treatment needs to be applied to create mesoporosity without reducing the accessibility/amount of acid sites.

For the FT-IR spectra of the hierarchical zeolites shown in Figure 2.7, the bridging hydroxyl band assigned to BAS (located at ~ 3610 cm^{-1}) of H15-A zeolite sample showed a relative increase respect to the external silanol band (located at ~ 3745 cm^{-1}) compared to the pristine zeolite samples[49] (Figure 2.7a). This observation suggests that there is a higher number of BAS present in the H15-A sample relative to the parent H15 sample. In addition, two extra FT-IR bands (3664 and 3780 cm^{-1}) corresponding to OH groups from extra-framework aluminum (EFAl) can be observed for the H15-A when compared to the pristine H15[49,50]. In the case of the H40-A sample, the intensity of the bridging hydroxyl band (Figure 2.7c) decreased with respect to that observed for the parent H40 sample, thereby confirming our working hypothesis mentioned above: BAS sites are less accessible for pyridine after desilication. Overall, upon pyridine adsorption onto the H15-A and H40-A samples (Figures 2.7b and 2.7d), almost no differences in terms of wavenumber shift ($\Delta\nu$) were observed with respect to their parent versions, suggesting that a slight increase in acidity was observed, while preserving the structural integrity of the zeolite framework.

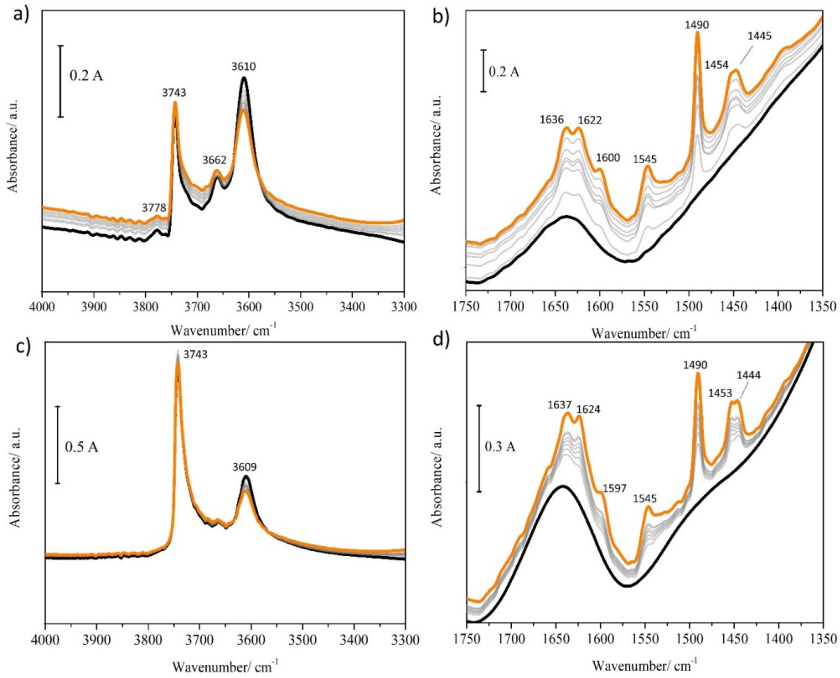

Figure 2.7. Fourier transform-infrared (FT-IR) spectra taken during pyridine adsorption at 30 °C until saturation of the alkaline treated H15-A (a-b) and H40-A (c-d) samples. The **black** spectrum corresponds to the fresh materials after drying under high vacuum at 550 °C for 2 h and the **orange** spectrum corresponds to the same materials after saturation with pyridine.

2.3.2 *Operando* UV/Vis Diffuse Reflectance Spectroscopy

Previous studies on the mechanisms of reaction and deactivation of the MTH, MTO and MTA processes showed that carbenium ion intermediates are formed within the zeolite pores, and these species serve as precursors for the formation of olefins and aromatics[19,56]. In some cases, these adsorbed cations may also grow into larger species and can eventually be retained inside the zeolite pores causing catalyst deactivation[56]. All these species can be observed by UV/Vis DRS due to the presence of π-π* and n- π* transitions, which appear in the UV/Vis region of the electromagnetic spectrum. The exact presence of these electronic transitions depends on both the charge and size of the organic molecules with the following general rule of thumb: the larger the conjugated nature of the alkenyl carbenium species, the higher the λ_{max} of the absorption band related to this species. Early studies performed by Kiricsi *et al.* on the characterization by UV/Vis and FT-IR of carbenium ions in acidic zeolites demonstrated that

the presence of diverse substituents in the intermediates formed had a direct influence in the wavelength of absorption. For example, more alkyl substituents led to a larger red shift[56]. Chowdhury *et al.* also observed a similar trend during the alkylation of benzene. They observed a red shift in wavelength, but when increasing the electron-donating character of the substituents. By increasing the electron-donating character of the alkyl groups attached to the reaction intermediates formed inside the zeolite, the λ_{max} of these hydrocarbon species appeared at higher wavelengths in UV/Vis[57].

In this work, we have applied time-resolved *operando* UV/Vis DRS spectroscopy to investigate hydrocarbon formation at 500 °C during furan (F), 2-methylfuran (MF) and 2,5-dimethylfuran (DMF) aromatization within the parent and hierarchical HZSM-5 zeolites. The spectroscopic data obtained are shown in Figure 2.8 and 2.9. As the aim was to work under *operando* conditions, the experimental conditions were chosen such that they fall within the kinetic regime favorable for the production of aromatics[58]. As seen previously[40,57], the tested furan derivatives, differing in the number of methyl groups, showed different band intensities and positions.

Based on the state of the art, understanding of the mechanism on the MTH process, as well as the conversion of related oxygenates over zeolite catalysts[21], we propose that the catalytic conversion of furans to olefins and aromatics is governed by a pathway similar to the MTH pathway. Initially, and independently of the feedstock used, the catalytic reactions taking place on the BAS sites of a zeolite are known to proceed via the formation of carbenium ions[59–62], the formation of which involves the protonation of the substrate in the zeolite pores followed by a subsequent propagation stage (i.e., ring-opening, cracking, dehydration, decarbonylation, oligomerization or cyclization).

An overview of the general assignments of the different UV/Vis absorption bands observed is given in Table 2.3. At the very early stages of the aromatization of the furan derivatives three main absorption bands appear, which are ascribed to three diverse functional groups: i) a first group of absorption bands arise at 256-265 nm, which correspond to π-π* transitions of neutral aromatics formed (including furans)[57,59]; ii) a second group of absorption bands are observed at 323-334 nm, which correspond to the formation of monoenyl carbenium ions, which are considered the active species within the alkene cycle[33,56,63], and iii) the last, and most intense group of absorption bands, appear between 398-414 nm, which most probably correspond to dienyl carbenium/arenium ions (and a part of the arene cycle)[33,56,59]. Thus, with the

experimental detection of aromatics (i.e., neutral and cationic species), we confirm that we are working under *operando* conditions. Subsequently, these active species undergo hydrogen transfer and alkylation reactions yielding olefins and aromatics as reaction products. After the reaction evolves further, the formation of a broad absorption band, which arises at 573-692 nm (depending on the furan derivative and zeolite catalyst used) is assigned to the so-called charged π-zeolite-aromatic complexes and large neutral polyaromatic species (coke precursors)[64].

Table 2.3. Summary of the UV/Vis absorption bands, as measured with diffuse reflectance spectroscopy (DRS), observed during the aromatization of furan derivatives over zeolites.

UV/Vis Absorption bands, λ /nm	**Absorbance**	**Species assigned**	**Reference**
250-270	Strong	Neutral (alkylated) aromatics/ Furans	59,65,66
300-400	Weak	Monoenyl carbenium ions	56,59,63
400-500	Strong	Dienyl carbenium and arenium ions	57,63
>500	Weak	π-interaction of zeolite-aromatic complexes/ neutral coke species	56,57

It is important to note that trienyl carbenium ions (461-552 nm) were only observed when using the H40 sample[64], indicating that their formation is possible but restricted by the zeolite pore size. Their detection is in line with the observed change in the color of the catalyst (from yellow/red to grey/black), indicative of catalyst deactivation[15,31]. The red shift observed for each absorption band depended on the furan derivatives used and correlated with the extent of methylation of the furan, with more electron donating groups stabilizing the zeolite-trapped carbocations more effectively[40,57,59]. Another remarkable aspect of the absorption bands observed for almost all reactants is that some of them shift as a function of increasing time-on-stream towards higher wavelengths and furthermore increase in intensity, indicating the gradual growth of the π-systems and an increase in abundance of those species inside the zeolite channels. At the end of the reaction, some more pronounced absorption bands located around 550 and 600 nm were detected, which correspond to highly condensed coke species (as is very noticeable in Figure 2.8b).

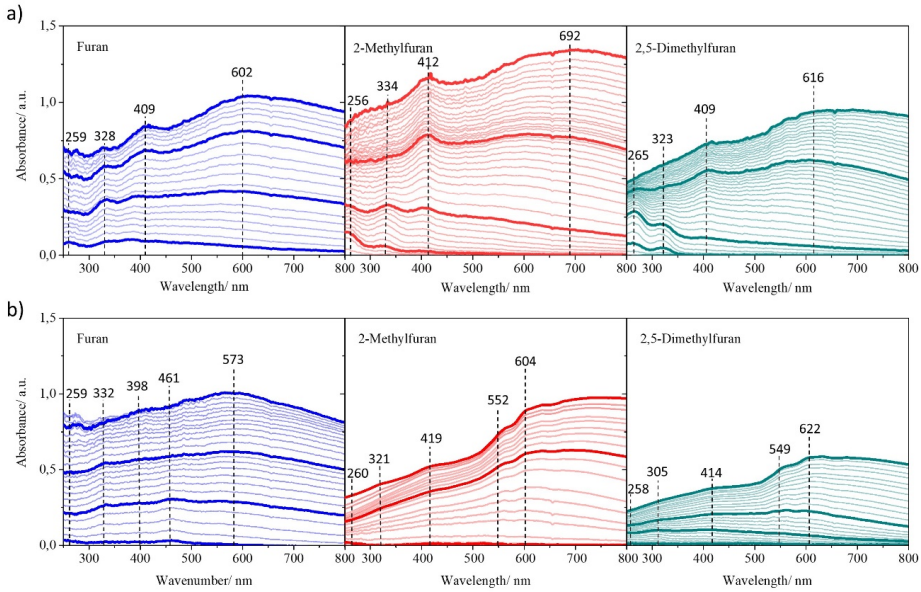

Figure 2.8. *Operando* UV/Vis diffuse reflectance (DR) spectra obtained (0-5 min) during the conversion of furan, 2-methylfuran and 2,5-dimethylfuran when using (a) H15 and (b) H40 as catalyst materials. Reaction Conditions: $T_{reaction}$ = 500 °C for 30 min with $WHSV_F = WHSV_{MF} = WHSV_{DMF} = 1\ h^{-1}$.

The UV/Vis absorption bands detected with the HZSM-5 zeolites in the Furans-to-Aromatics (FTA) process resemble those seen in the MTH process[21]. This suggests that although the carbon sources are different, the main active species are similar[67,68]. Despite the difference in reaction temperature between both processes (MTH vs. FTA), several active/intermediate species, such as monoenyl and arenium carbenium ions, detected during the MTH were also present and evolved similarly during furan conversion[69,70]. These similarities and the fact that both olefins and aromatics are formed during FTA, support the proposal that dual olefinic and aromatic cycles are being propagated within the HZSM-5 zeolite pores[69,71].

Aromatics formation occurred faster with H15 than with H40, as indicated by the mainly well-resolved and pronounced absorption bands. These main bands, corresponding to neutral and charged aromatic species (256-265 nm) appear upon adsorption, protonation and reaction of the furan derivatives. This is also seen in the online MS data (Figures 2.10a and 2.11a) with more benzene, toluene and traces of xylenes being detected. With increasing time-on-stream and rather rapidly, further transformations take place giving rise to the presence of carbenium ions, which result in the formation of absorption bands located at 323-334 nm and 409-412 nm[57]. Unexpectedly, together with the absorption band at 602-692 nm, the (combination) band at 409-

412 nm developed into one of the most intense absorption bands when using the H15 sample. When comparing different catalyst materials with the same feedstock, the difference in the amount of strong acid sites (more specifically the BAS) between H15 and H40 seems to be linked to the differences in the UV/Vis DRS spectra[56,57], which becomes more apparent when a less reactive furan derivative is being used as feedstock. In short, these results demonstrated that the higher the number of BAS, the easier the reaction intermediates (e.g., monoenyl and enyl carbenium ions) can be visualized by UV/Vis. We suggest that this might be related to the acid strength of the respective BAS in the H15 samples. Regarding feedstock reactivity, the lack of well-resolved UV/Vis bands observed in some spectra is in line with the increasing furan derivatives reactivity used. These observations suggest that for highly active feedstocks, such as furan, faster adsorption, cracking (e.g., formation of carbenium ions), cyclization and desorption reactions occur simultaneously than with less reactive reagents, such as DMF.

The hierarchical H15-A and H40-A zeolites (Figure 2.9) showed several differences in FTA when compared to the parent H15 and H40 zeolites. First, the overall and relative intensity of the bands are lower than the UV/Vis spectra obtained from the parent zeolites. Regarding the most pronounced UV/Vis bands, there is a competing growth observed for the bands at 319-336 nm and 390-416 nm, the latter being the predominant one at the later reaction stages together with the coke deposits bands (above 500 nm). This indicates that the ratio of large to small active species is lower than when using smaller pore size systems. In this case, we have two factors that influence that, the larger pore system and the higher acidity, suggesting that the pore system is also key and are responsible for the size of the active species formed, as reported in previously[69]. Second, a slight blue shift for some of the absorption bands is seen (specially for bands above 500 nm). Even though these catalysts have increased mesoporosity, access to the zeolite channels is partially limited, as indicated by the accessibility values (ACI) for the hierarchical zeolites discussed above (see Table 2.2). The lower ratio of larger to smaller active species would be in line with this[21,70].

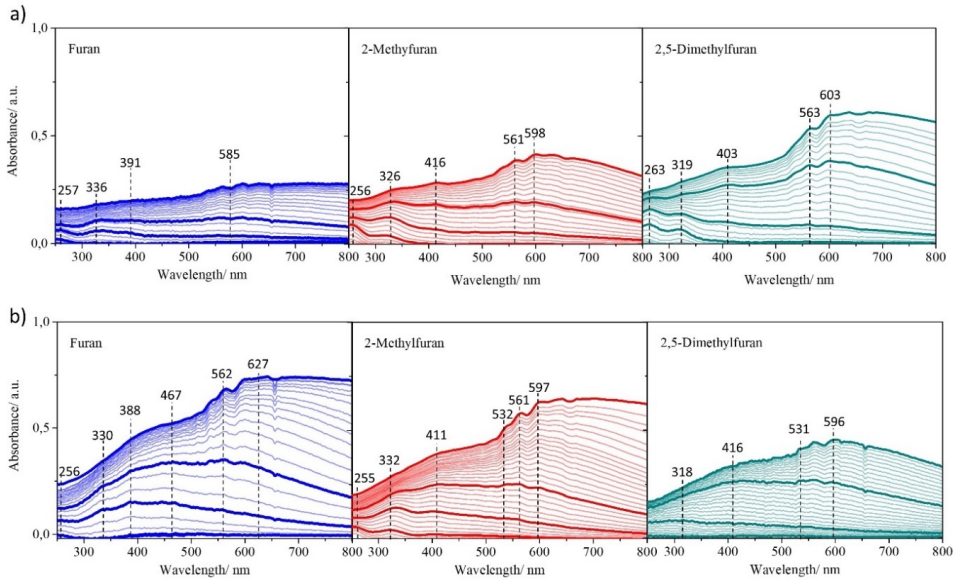

Figure 2.9. *Operando* UV/Vis diffuse reflectance (DR) spectra obtained (0-5 min) during the conversion of furan, 2-methylfuran and 2,5-dimethylfuran when using (a) H15-A and (b) H40-A as catalysts. Reaction Conditions: $T_{reaction}$ = 500 °C for 30 min with $WHSV_F = WHSV_{MF} = WHSV_{DMF} = 1\ h^{-1}$.

In summary, all UV/Vis DR spectra recorded expectedly showed a trend of formation of smaller to larger species as function of time-on-stream. Initially, smaller active species are formed which seem to evolve to larger species via oligomerization and aromatization reactions. At longer reaction times, broad band emerged above 500 nm, corresponding to the formation of polyaromatic coke deposits in and on the catalyst. The most well-resolved UV/Vis spectra were mostly obtained when using the H15 and H15-A zeolite as catalysts. Especially at early reaction stages, well-resolved bands around ~ 250, 330 and 400 nm are observed, with, in some cases, the latter prevailing even at longer reaction times (see Figure 2.8a).

In Figures 2.10 and 2.11 the MS data monitored during 30 min of reaction over H15 and H15-A is shown, providing qualitative trends on product formation and catalyst stability. As general observations, for all catalyst after normalization, different conversions were attained for each furan derivatives at the same WHSV values. The reactivity of the furan derivatives employed as feedstock is as follows: F >> MF > DMF (Figure 2.9d). Indeed, furan shows strong chemisorption on the Brønsted active sites of the HZSM-5 zeolite[40]. Cheng *et al*. demonstrated also its high reactivity since, even at room temperature, furan is able to be converted into oligomers[15]. The more rapid deactivation seen with F in comparison with MF and DMF is also

thought to be directly related to this higher (unselective) reactivity. As a result, a pronounced steep slope was displayed for the furan MS signal after 15 min time on stream. The main mono-aromatics detected were benzene (m/z = 78) and toluene (m/z = 91), while just trace amounts of xylenes (m/z = 106) were detected. The highest amount of benzene and toluene was observed during furan aromatization after 20 min time-on-stream. Olefins (ethylene (m/z = 26), allene (m/z = 40)), CO_2 (m/z = 44) and H_2O (m/z = 18) were the main detected products, with more CO_2 being formed than water, suggesting that the predominant pathway of deoxygenation is via decarboxylation. In addition, It is noteworthy to remark that for all furan derivatives the CO_2 MS signal appeared at the same reaction time and followed as the MS signal for BTX, suggesting that deoxygenation mainly occurs via decarboxylation reactions, as observed in previous works[15,40]. The CO mass signal (m/z = 28) could not be monitored as function of time, as it overlaps with the MS signal of N_2 (carrier gas). A time delay (dead time) of roughly 5 to 10 min in the MS data (depending on the furan derivative employed) is caused due to the time the compounds take to reach the MS analyzer from the reactor cell, since different gas flows were used to have the same WHSV for all the reagents. Only with furan as substrate, benzene and toluene production increased up to a steady state, which later on starts to decrease, as did aromatics formation in general (see Figure 2.10a). For all the reactions, species larger than mono-aromatics (such as naphthalene and benzofuran) were not detected. If formed, they may not have reached the MS analyzer, since the outlet of the reactor setup was not heat-traced.

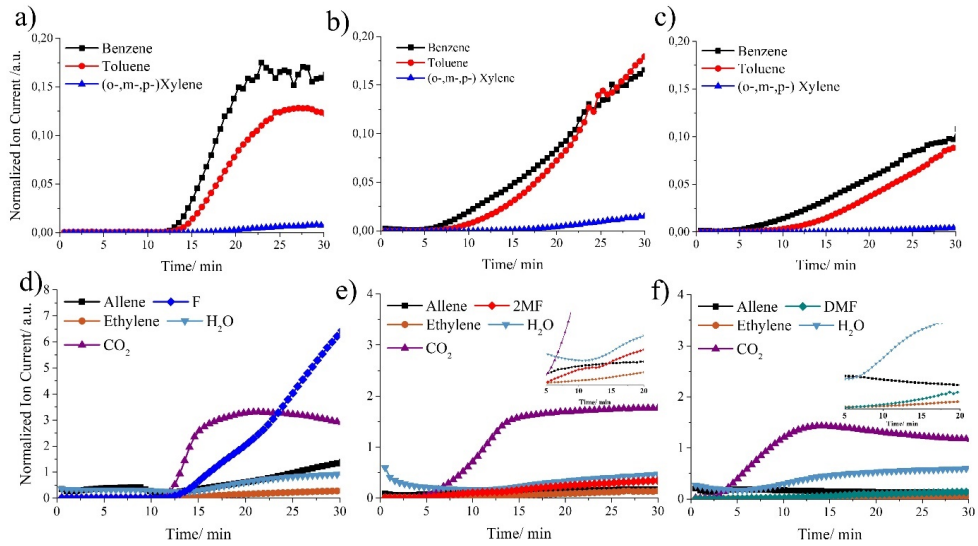

Figure 2.10. Time-resolved mass spectrometry (MS) data monitored during the aromatization of furan (m/z = 68) (a and d), 2-methylfuran (m/z = 82) (b and e) and 2,5-dimethylfuran (m/z = 96) (c and f) when using H15 zeolite as catalyst. The MS signals of all ion currents have been normalized by one of the N_2 fragmentation ions (14 m/z), which was used as carrier gas. Insets from 5 to 20 min reaction time for the Figure 2.10e and 2.10f are shown in the top-right of each figure.

In addition, the intense MS signals for CO_2 and H_2O could be due to a contribution from part of the coke deposits in and on the catalyst, which are being desorbed from the catalyst surface as the reaction proceeds, as suggested by other authors[72,73]. Formation of allene and ethylene occurs simultaneously with the formation of aromatics. However, while aromatics formation decreased during the conversion of furan, allene and ethylene signals reach a quasi-steady state followed by a slight increase before 30 min reaction. This increase in the detection of low olefins might suggest a decrease of the aromatization rates due to the partial deactivation of the strong BAS within the zeolite, in line with previous studies[59,74]. Based on the MTH dual-cycle mechanism, once the arene cycle starts slowing down its propagation, the reaction rate to olefins should start increasing, since they are competing cycles running simultaneously in the intra-zeolitic framework. At prolonged reaction times, the formation of carbon deposits is unavoidable, and the pore blockage is detrimental for the formation of aromatics. Unfortunately, UV/Vis spectra cannot confirm the above, as highly condensed coke species rapidly dominate the spectra, already at very early reaction stages. This precludes one to

distinguish if the formation of olefins (from monoenyl or dienyl carbenium ions) is predominantly occurring over the formation of arenium ions (see Table 2.3).

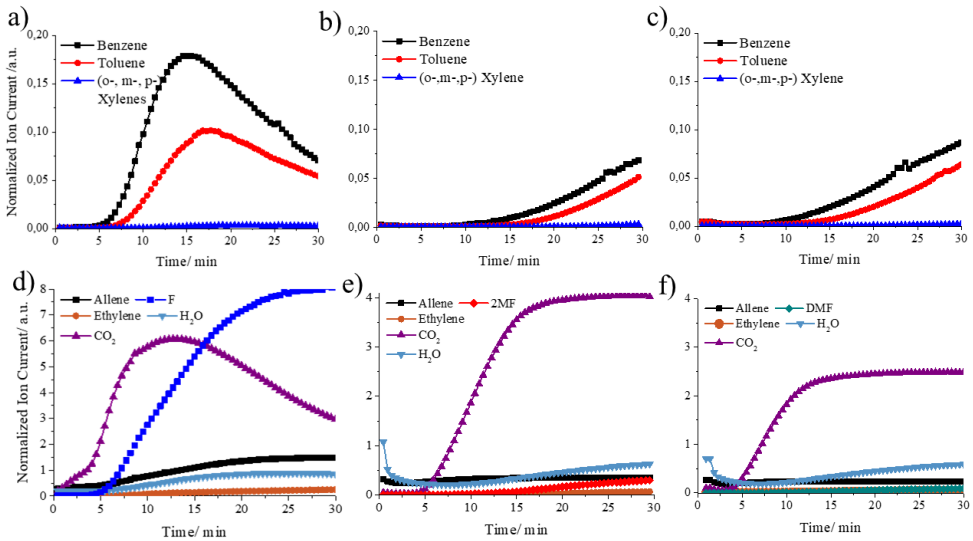

Figure 2.11. Time-resolved online mass spectrometry (MS) data monitored during the aromatization of furan (m/z = 68) (a and d), 2-methylfuran (m/z = 82) (b and e) and 2,5-dimethylfuran (m/z = 96) (c and f) when using H15-A zeolite as catalyst. The MS signals of all ion currents have been normalized by one of the N_2 fragmentation ions (14 m/z), which was used as carrier gas.

With H15-A zeolite (Figure 2.11a), due to its higher acidity, furan conversion was higher, the aromatics formed faster and the catalyst deactivated faster than with H15. Overall, despite the faster aromatization, the incorporation of mesopores in H15 therefore did not, as anticipated, seem to either lower the rate of deactivation or favor selectivity to aromatics. Benzene and toluene were detected as mono-aromatics, but xylenes were hardly formed. In addition, over time, allene and ethylene MS signals are slightly higher than with the parent H15 zeolite, in accordance with the rapid decrease in aromatics production. Furthermore, slightly more CO_2 is formed than when using the parent H15 zeolite catalysts, also in line with the faster formation of aromatics.

The MS results for the aromatization of furan derivatives over the parent H40 and the hierarchical H40-A zeolites as catalyst are shown in Figure 2.12 and 2.13, respectively. In this case, the slightly larger pore size and lower acidity of the H40 zeolites, as demonstrated by Ar physisorption and NH_3-TPD, yielded less aromatics in comparison to the H15 zeolite catalysts

in almost all cases. Benzene and toluene are predominantly observed when using furan as reactant and H40 as catalyst. During the aromatization of the other furan derivatives, MF and DMF, benzene and toluene amounts did not plateau as when F was used as reagent, which indicates that the aromatic cycle continues propagating almost in parallel with the olefinic cycle, since some olefins were also observed at the same reaction times (insets in Figure 2.12e and Figure 2.12f).

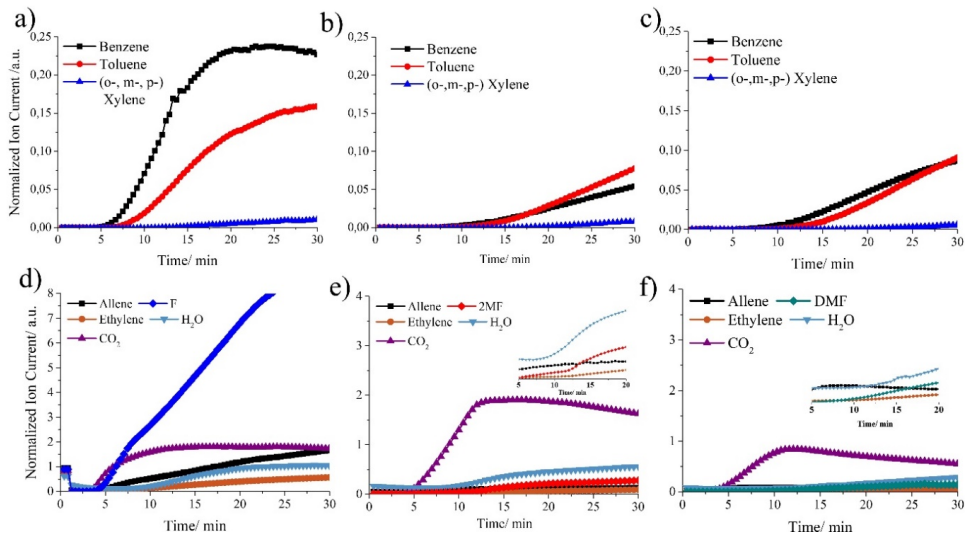

Figure 2.12. Time-resolved online mass spectrometry (MS) data monitored during the aromatization of furan (m/z = 68) (a and d), 2-methylfuran (m/z = 82) (b and e) and 2,5-dimethylfuran (m/z = 96) (c and f) when using H40 zeolite as catalyst. The MS signals of all ion currents have been normalized by one of the N_2 fragmentation ions (14 m/z), which was used as carrier gas. Insets from 5 to 20 min reaction time for the 2.12e and 2.12f figures are shown in the top-right of each figure.

Regarding the formation of allene and ethylene, similar trends are seen as for the two H15 catalysts. The hierarchical zeolite catalyst again showed a fast decrease in the benzene and toluene signals during the conversion of furan (Figure 2.12a), which start decreasing after 20 and 25 min reaction, respectively. The higher acid density and larger pores favor the faster production and subsequent condensation and oligomerization of the aromatics formed, which are known to be precursors to coke species[75,76]. Furthermore, large pores can accommodate larger coke species, thus promoting a more rapid deactivation of the catalyst.

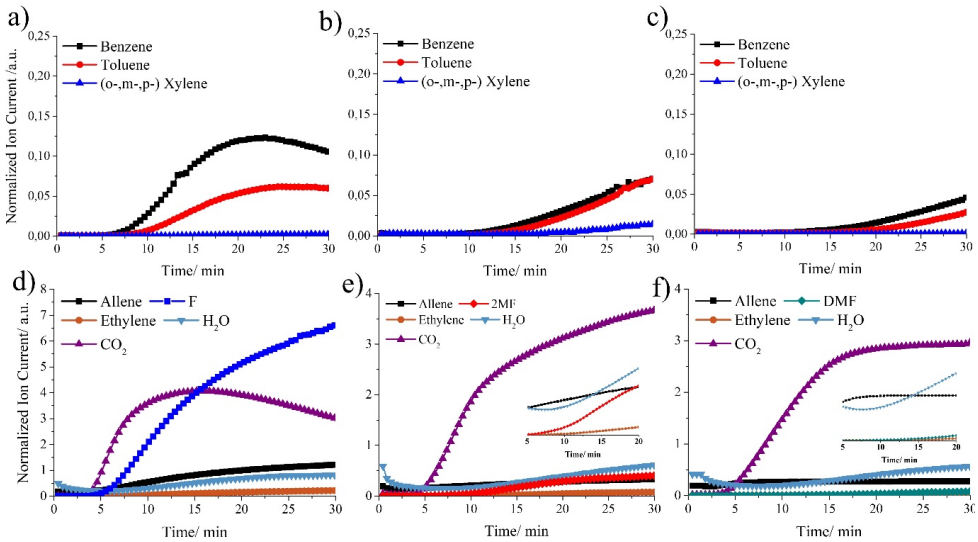

Figure 2.13. Time-resolved online mass spectrometry (MS) data monitored during the aromatization of furan (m/z = 68) (a and d), 2-methylfuran (m/z = 82) (b and e) and 2,5-dimethylfuran (m/z = 96) (c and f) when using H40-A zeolite as catalyst. The MS signals of all ion currents have been normalized by one of the N_2 fragmentation ions (14 m/z), which was used as carrier gas. Insets from 5 to 20 min reaction time for the 2.13e and 2.13f Figures are shown in the top-right of each figure.

2.3.3 Analysis of Carbon Deposits

To further elucidate the amount and nature of the carbon deposits formed, those catalysts showing the fastest deactivation (after 30 min reaction) have been analyzed after reaction with thermogravimetric analysis with online mass spectrometry (TGA-MS) and 2D gas chromatography with mass spectrometry (2D GC×GC-MS).

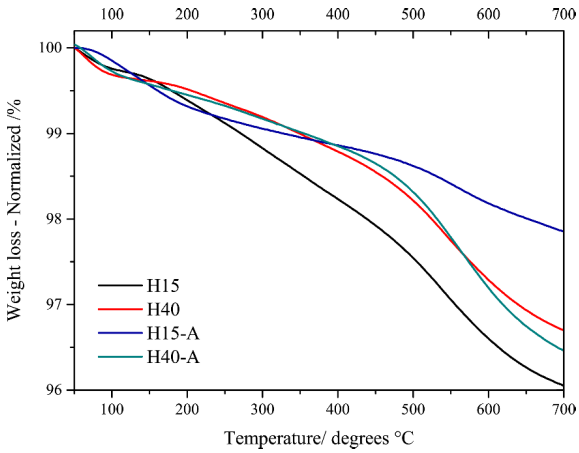

Figure 2.14. Thermogravimetric analyses (TGA) of spent HZSM-5 zeolite-based catalysts after furan aromatization at 500 °C for 30 min.

The TGA profiles of all samples, shown in Figure 2.14, show that the removal of carbon deposits was not complete at 700 °C, with the remainder likely being the so-called hard graphite-like coke deposits[77]. Soft and hard coke are known to be observed at low temperatures (150-400 °C) and high temperatures (400-600 °C), respectively[76].

In Table 2.4, a summary of the different weight losses calculated at the different stages (drying and calcination) during the TGA analysis is shown. Strikingly, although the catalytic MS results showed that H15-A deactivated faster, TGA analyses showed that the H15-A spent catalyst had the lowest amount of carbon deposits after 30 min of reaction (3.6%). The catalyst weight loss during the drying step (performed at 120 °C for 20 min) was ~ 1-1.5 wt. % for the H15 sample, while a lower weight loss was displayed for the H40 sample. The presence of mesopores in the system was only favorable for the H15 catalysts, since a lower formation of coke was observed at high temperatures (i.e., hard coke). For H40-A, a higher amount of coke was formed relative to its H40 counterpart sample[58].

Table 2.4. Normalized weight losses, as obtained with thermogravimetric analysis (TGA), from the spent catalysts after performing furan aromatization for 30 min at 500 °C.

Catalyst	Weight loss during drying (30 – 120 °C), in wt. %	Weight loss during calcination (50 – 700 °C), in wt. %	Total weight loss in wt. %
H15	1.1	4	5.1
H15-A	1.6	2	3.6
H40	0.6	3.3	3.9
H40-A	1	3.5	4.5

The evolution of H_2O and CO_2 were monitored with TGA-MS under Ar atmosphere. The corresponding online MS data for H_2O and CO are shown in Figure 2.15a and 2.15b, respectively, for both the drying and the calcination steps. The sharp H_2O signal after 10 min showed the water released during drying. Upon calcination, we have observed an increase in H_2O desorption followed by a plateau (after 70 min), indicating that water desorption has ceased and most of the carbon deposits burnt off at low temperature are oxygenated organic compounds (which we assume to be soft coke). The online MS results for CO also showed that its mainly detected during the drying step and at low temperatures (below 350 °C). These results suggest that oxygenated compounds are present within the carbon deposits retained in the spent catalysts. While at higher calcination temperatures, mass loss is more due to decomposition of aromatic compounds, lean or deficient in oxygen, given the lower signal for CO and H_2O. This observation is in accordance with what has been previously proposed in literature[78]. More specifically, it indicates that the formation of carbonaceous deposits at low temperatures involves mainly condensation and rearrangement steps, which implies that these hydrocarbons deposits are generally (oxygenated) oligomers from the reactant. The high temperature coke is generally poly-aromatic in nature, its formation involving also hydrogen transfer reactions and dehydrogenation steps on the acid sites.

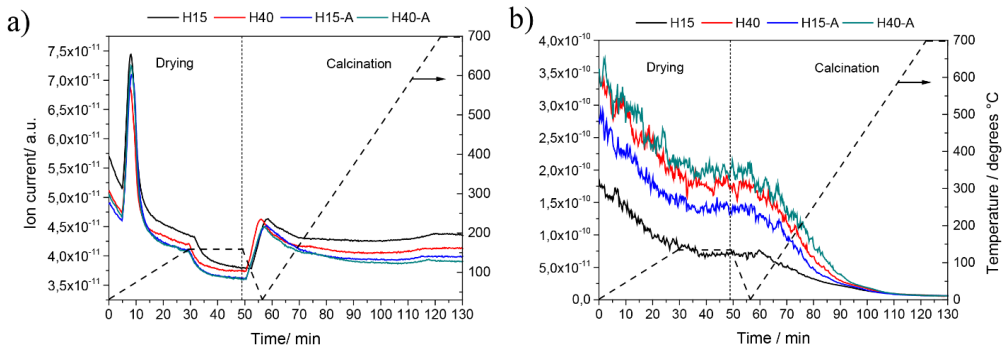

Figure 2.15. Monitored online mass spectrometry (MS) signals of (a) H_2O (m/z = 18) and CO (m/z = 29) during the thermogravimetric analysis (TGA) measurements of four spent HZSM-5 zeolite samples under study.

To further identify the hydrocarbons trapped inside the spent catalyst materials, extraction of the retained hydrocarbons from the spent HZSM-5 zeolite catalyst after the conversion of MF at 500 ºC was performed by HF leaching[64]. This approach allowed us to gain insights about the possible reaction intermediates and coke precursors formed during the aromatization of MF. This substrate/catalyst combination was chosen because it showed a high MS signal to benzene and toluene and a lower rate of deactivation (see Figure 2.12). After the HF leaching experiment, the dichloromethane soluble organic compounds were analyzed by 2D GC×GC-MS. In Figure 2.16 the 2D chromatogram with the assignment of the most relevant peaks at 500 °C is shown.

The most abundant compounds retained in the spent catalyst were oxygenated compounds, such as furan derivatives, phenol and methylated benzofurans. Elucidating the compounds at higher retention times (which can be found in the top-right of the chromatograms) was challenging as the data base available for those compounds was limited and the MS library suggestions seemed to be misleading. One of the most abundant species detected in the chromatogram were methylated benzofurans, which is in accordance to the findings reported by Huber *et al.*[15]. That methylated benzofurans instead of benzofuran were observed is because MF was used instead of F as starting reagent.

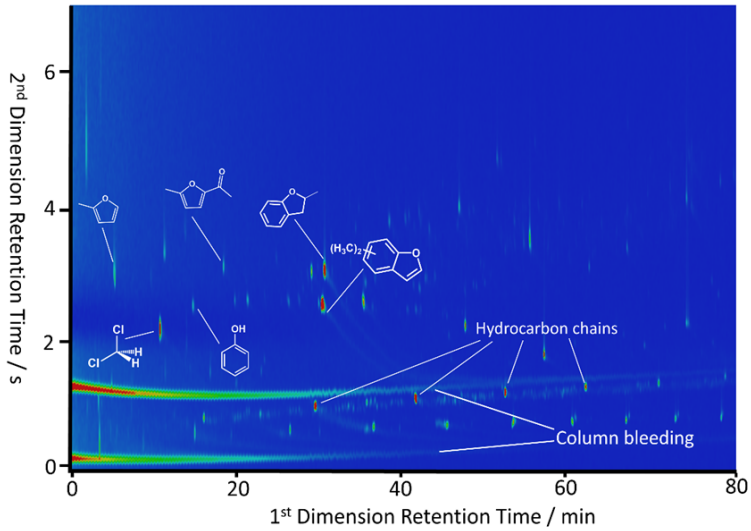

Figure 2.16. 2D GCxGC obtained after the injection of the organic phase extracted (in CH_2Cl_2) after the HF leaching of the spent catalyst (i.e., H40 zeolite) obtained during the aromatization of MF at 500 °C for 30 min.

At low retention times, oxygenated compounds, such as furan derivatives and phenol, were also identified, in addition to methylated benzofurans. Different linear hydrocarbon chains were observed, again showing that at such high temperatures, 500 °C, both cracking and aromatization reactions take place[15,79].

The detection of methylated benzofurans in the spent catalysts, prompted us to study the role of these compounds further by testing benzofuran as feedstock on a fresh H40 zeolite. In previous works, Huber *et al.* proposed that benzofuran was one of the main products formed at low reaction temperatures during the conversion of furan. Furthermore, it was suggested that benzofuran was possibly a reaction intermediate to aromatics since it was also detected at higher reaction temperatures, but up-to-date, little evidences has been presented to confirm this hypothesis[58].

In Figure 2.17a, the UV/Vis DR spectrum of benzofuran at RT after its addition to the zeolite material is shown. The main absorption bands were assigned as follows: the sharp bands at ~ 271 and ~ 280 nm correspond to the absorption of neutral benzofuran, and therefore, we assume that bands centered at ~ 397, ~ 480 and ~ 615 nm correspond to (protonated) benzofuran interacting and possibly being already converted within the zeolite framework[80]. These UV/Vis absorption bands detected at RT are in line with some of the UV/Vis bands observed during the

conversion of MF at 500 °C, as shown in Figure 2.8a. Although benzofuran was not monitored by MS, these results indicate that benzofuran is one of the main compounds formed (and trapped) within the intra-zeolitic structure of H40 zeolite catalyst at these reaction conditions.

To corroborate our hypothesis, benzofuran was then tested as feed at 500 °C over the H40 zeolite catalyst. The MS signals obtained during the conversion of benzofuran are shown in Figure 2.17b, 2.17c and 2.17d.

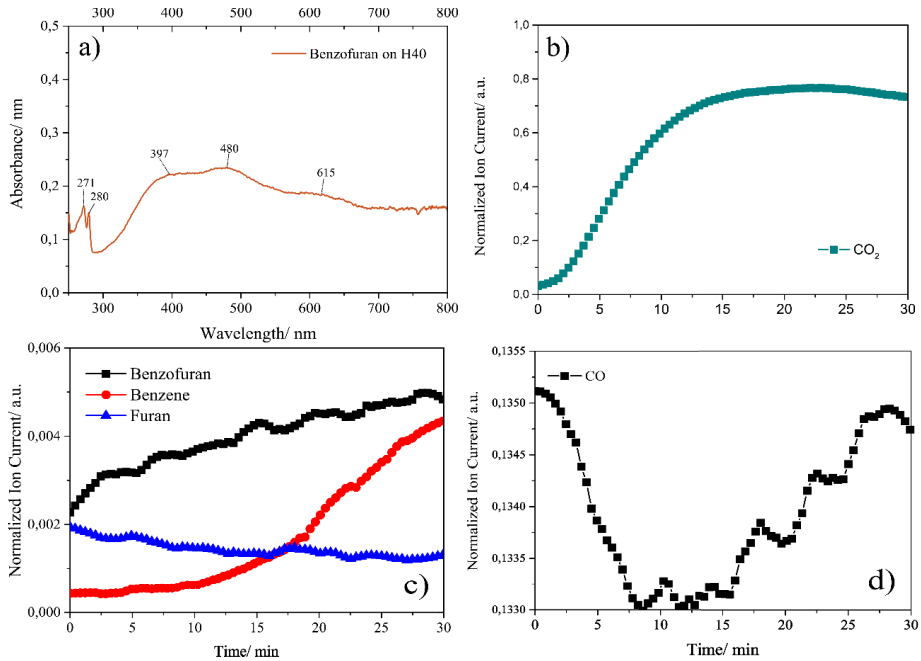

Figure 2.17. (a) UV/Vis diffuse reflectance (DR) spectrum recorded at RT from H40 zeolite 30 s after the addition of benzofuran; (b) CO_2 mass spectrometry (MS) signal (m/z = 44), (c) benzofuran, benzene and furan, and (d) CO MS signal (m/z = 29) monitored during the conversion of benzofuran at 500 °C for 30 min at H40 zeolite as catalyst. Reaction Conditions: $T_{bubbler\ saturator}$ =105 °C with a N_2 flow = 10 ml/min at 500 °C for 30 min (55 mg catalyst).

As the reaction evolves over time, after 15 min, the signal of benzene (Figure 2.17c) increases as function of time. Simultaneously, the CO signal (Figure 2.17d) increases as well, indicating that benzene is being formed during the conversion of benzofuran by decarbonylation. This, suggests that benzofuran (or methylated benzofuran in case of MF aromatization) could be a possible reaction intermediate, in line with the proposal of Huber and co-workers that

benzofuran is formed and is part of the hydrocarbon pool[58,80]. Furthermore, it remains as a coke precursor, as the GC×GC-MS data revealed.

2.4. Discussion

The UV/Vis DRS data and online MS data of the different zeolite/substrate combinations under study show how the ratio of olefins to aromatics produced is determined by the starting reagent, the density of acid sites and the porosity of the zeolite used. UV/Vis DR spectra showed a fast aromatization rate for low Si/Al ratio zeolites, when converting highly reactive furan derivatives. For example, with H15 as catalyst and furan as starting reagent, the formation of aromatics occurs very fast, as indicated by the pronounced rise of the absorption band located at ~ 400-410 nm that corresponds to dienylic and arenium ions active species. Subsequently, the absorption bands above 500 nm, indicating the formation of coke deposits, dominate all the spectra after 5 min of reaction. Formation of olefins can be monitored by the rise of absorption bands between 300 and 400 nm, i.e. monoenylic species. It can be observed that there is a competing growth between the absorption bands corresponding to monoenylic species (~ 320-340 nm) and those corresponding to dienylic or arenium active species (~400-410 nm), with the latter dominating the later stages of the catalytic reaction. With H15, monoenylic species (~ 300-320 nm) are only observed at early reaction stages, because, as the reaction evolves, the broad and predominant absorption band corresponding to the formation of coke overlaps with other absorption bands, hampering the monitoring of the less intense absorption. Thus, defining a ratio between dienylic or arenium species, and monoenylic species is a challenging task when using these highly active catalysts. What can be extracted from the UV/Vis results is that the formation of aromatics dominates over the formation of olefins when using H15 zeolite as catalyst, based on the larger and pronounced absorption band at ~ 400-410 nm. When using H40 as catalyst, the absorption band at ~ 400-410 nm is less pronounced at the early stages of the reaction, indicating that the relative ratio between dienyl or arenium species and monoenyl species, i.e., aromatics and olefins, is lower than when using H15 as catalyst. This is ascribed to its lower acidity (Si/Al = 40), compared to the H15. Remarkable differences were observed also depending on the number of alkyl substituents of the furan derivatives. The higher the number of substituents, the more red-shifted the absorption wavelength formed for species of the same nature, such as non-substituted or substituted arenium ions. As for the hierarchical systems, a small blue shift of the absorption bands was observed, suggesting that smaller active

species are formed with these hierarchical zeolites (see Figure 2.9a and 2.9b). This is counterintuitive but in line with the measured accessibility indices.

Moreover, by monitoring the formation of BTX and small olefins by mass spectrometry (MS), we studied if the aromatic cycle was indeed propagating more than the olefinic cycle. Firstly, in the UV/Vis DR spectra monoenyl and dienyl carbenium species are already detected at the very early reaction stages. Secondly, the subsequent increase in the formation of dienyl and/or arenium ions over time suggests that these species are being predominantly formed over the initially formed monoenyl ions. This correlates with the early formation of allene and ethylene, observed at early reaction times, after which, at around 10-15 min reaction time, aromatics start to be formed (~ 400-410 nm), suggesting that aromatics are formed from cyclization of olefins at the BAS. When using less acidic and larger pore size zeolites, for example, H40-A zeolite, the aromatic and olefinic cycles were observed to run *quasi* in parallel, as indicated by the very similar intensity of the UV/Vis absorption bands for the monoenyl, and dienyl/arenium species. This observation was as well displayed by the MS data, wherein lower MS signals for BTX were detected compared to more acidic catalysts such as H15, indicating that to favor the propagation of the arene cycle over the olefinic cycle, a high density of strong acid sites is needed.

It has been previously suggested that after protonation of the furan ring ring opening takes place yielding linear alkenes containing oxygen as alcohol or carbonyl groups[40,80]. These (oxygenated) active species could undergo a series of elementary steps; cracking, methylation, deoxygenation (dehydration or decarboxylation), hydrogen transfer and aromatization[15,21] to rapidly form monoenyl carbenium ions which can further deoxygenate by decarbonylation/decarboxylation or dehydration (Figure 2.18). Based on our UV/Vis experiments, we can speculate that the first elementary steps are furan ring protonation followed by cracking and decarboxylation to form small olefins (monoenyl ions). Subsequently, aromatics (arenium ions) are rapidly being formed from monoenyl cations, which after further condensation with other active species form the so-called polyaromatic coke species, causing catalyst deactivation, as indicated by the broad band at ~ 600 nm. It is worth remembering that all these steps take place at the available BAS of the zeolite.

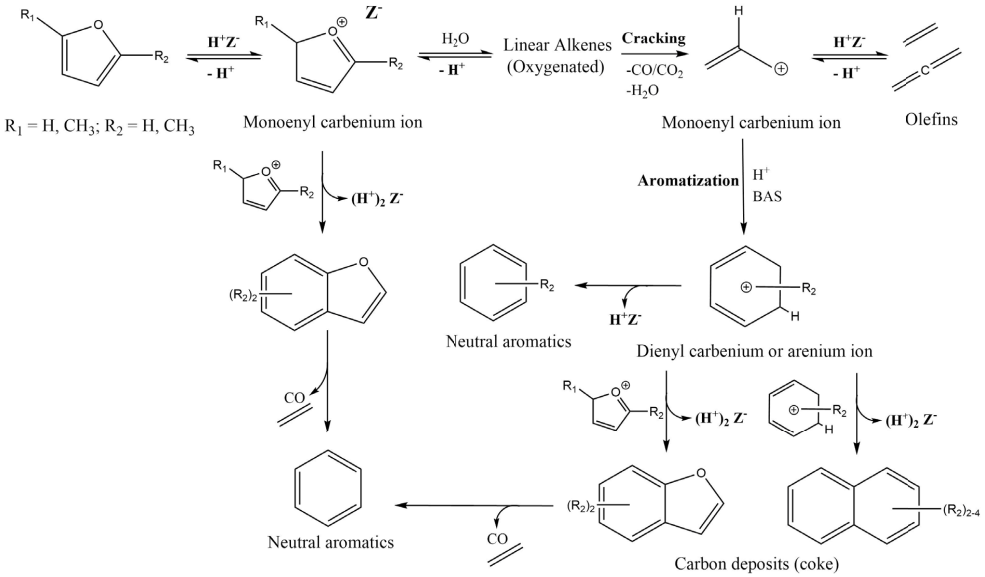

Figure 2.18. Proposed reaction pathways taking place during the aromatization of furan derivatives using HZSM-5 zeolites as catalysts. $H^+ Z^-$ represent the restoration of a BAS in the HZSM-5 zeolite. $(H^+)_2 Z^-$ represents that two BAS are restored.

When the amount of strong BAS decreases and the accessibility within the zeolite pores decreases as a result of coke buildup, aromatics production decreases and the monoenyl carbenium ions, formed after cracking at the BAS, desorb and yield mostly olefins instead. At this stage, the alkene cycle is promoted over the aromatic cycle. In Figure 2.19, an adaptation from the original dual-cycle mechanism for the MTH reaction is given for the aromatization of furan derivatives[69], in line with the intermediates and products detected by UV/Vis and MS, respectively. In this mechanism, benzofuran can be part of the alkene and arene cycle since it can form olefins and furan by cracking/decomposition but also aromatics by decarbonylation. Furthermore, we also consider it a coke precursor, been identified as a one of the trapped carbon species within the spent catalysts.

.

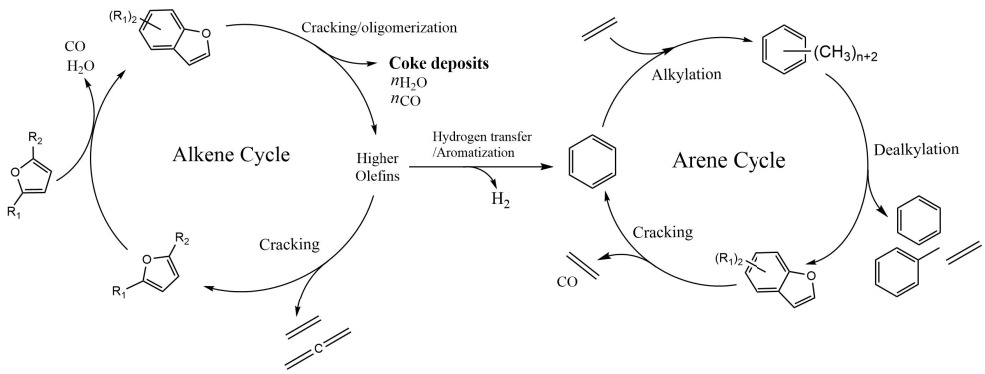

Figure 2.19. Proposed dual-cycle mechanism taking place in the ZSM-5 zeolite pores during the conversion of Furan-to-Aromatics (FTA) process.

2.5. Conclusions

In this Chapter, we have presented an *operando* UV/Vis diffuse reflectance spectroscopy study to monitor the evolution of reaction intermediates and related coke precursors in the aromatization of bio-based furan derivatives, such as furan, 2-methylfuran, 2,5-dimethylfuran. For this purpose, two different sets of HZSM-5 zeolite catalysts were tested, differing in their Si/Al ratio and porosity, thereby revealing that pore size, Brønsted and Lewis acidity; and accessibility are key parameters that determine both the type/size of active species formed and thus, the final product distribution.

With operando UV/Vis DRS it was possible to identify the formation of monoenyl followed by the formation of dienyl/arenium ions within the zeolite channels of zeolite HZSM-5. Regarding the feedstocks used, a red shift in the UV/Vis DR spectra is observed when increasing the number of alkyl substituents of the furan rings, indicating that larger species are formed. In contrast, in this case, the use of mesoporous systems gave blue shifted bands, indicating the formation of smaller hydrocarbon species. The evolution of the UV/Vis spectra over time revealed that small olefins are formed first, followed by the formation of aromatics, in line with the related online MS data recorded. Taken together, the data also supports the proposal of two catalytic cycles running in parallel, such as the olefinic and arene cycles, similar to the current dual-cycle mechanism proposed for the HZSM-5 catalyzed MTH process. Analysis of the spent catalysts by different bulk characterization methods showed that relatively high amounts of (methylated)benzofuran are formed during MF conversion, confirming Huber´s proposal on the

role of benzofuran; both a reaction intermediate and a coke precursor. Since furan derivatives are already small aromatics species, we have adapted the dual-cycle mechanism accordingly as outlined in Figure 2.19. Olefins can be formed by cracking and decarbonylation/decarboxylation reactions, while aromatics can be formed by aromatization of olefins or decarbonylation of benzofuran

.

2.6. Acknowledgements

Dustin Eekhof (Utrecht University, UU) and Katarina Stanciakova (UU) are thanked for helping during the development of the experimental work. Dennie Wezendonk (UU) is acknowledged for performing the TGA-MS experiments, while Pascal Wijten (UU) is thanked for helping with the 2D GC×GC-MS analyses.

2.7. References

(1) Bridgwater, A. V. Renewable Fuels and Chemicals by Thermal Processing of Biomass. *Chem. Eng. J.* **2003**, *91*, 87–102. https://doi.org/10.1016/S1385-8947(02)00142-0.

(2) Huber, G. W.; Iborra, S.; Corma, A. Synthesis of Transportation Fuels from Biomass: Chemistry, Catalysts, and Engineering. *Chem. Rev.* **2006**, *106*, 4044–4098. https://doi.org/10.1021/cr068360d.

(3) Goyal, H. B.; Seal, D.; Saxena, R. C. Bio-Fuels from Thermochemical Conversion of Renewable Resources: A Review. *Renew. Sustain. Energy Rev.* **2008**, *12*, 504–517. https://doi.org/10.1016/j.rser.2006.07.014.

(4) Wei, Y.; Lei, H.; Wang, L.; Zhu, L.; Zhang, X.; Liu, Y.; Chen, S.; Ahring, B. Liquid-Liquid Extraction of Biomass Pyrolysis Bio-Oil. *Energy and Fuels* **2014**, *28*, 1207–1212. https://doi.org/10.1021/ef402490s.

(5) Bertero, M.; De La Puente, G.; Sedran, U. Fuels from Bio-Oils: Bio-Oil Production from Different Residual Sources, Characterization and Thermal Conditioning. *Fuel* **2012**, *95*, 263–271. https://doi.org/10.1016/j.fuel.2011.08.041.

(6) Grandmaison, J. L.; Chantal, P. D.; Kaliaguine, S. C. Conversion of Furanic Compounds over H-ZSM-5 Zeolite. *Fuel* **1990**, *69*, 1058–1061. https://doi.org/10.1016/0016-

2361(90)90020-Q.

(7) Foster, A. J.; Jae, J.; Cheng, Y. T.; Huber, G. W.; Lobo, R. F. Optimizing the Aromatic Yield and Distribution from Catalytic Fast Pyrolysis of Biomass over ZSM-5. *Appl. Catal. A Gen.* **2012**, *423–424*, 154–161. https://doi.org/10.1016/j.apcata.2012.02.030.

(8) Climent, M. J.; Corma, A.; Iborra, S. Conversion of Biomass Platform Molecules into Fuel Additives and Liquid Hydrocarbon Fuels. *Green Chem.* **2014**, *16*, 516–547. https://doi.org/10.1039/C3GC41492B.

(9) Corma, A.; Huber, G. W.; Sauvanaud, L.; O'Connor, P. Processing Biomass-Derived Oxygenates in the Oil Refinery: Catalytic Cracking (FCC) Reaction Pathways and Role of Catalyst. *J. Catal.* **2007**, *247*, 307–327. https://doi.org/10.1016/j.jcat.2007.01.023.

(10) Corma, A.; Corresa, E.; Mathieu, Y.; Sauvanaud, L.; Al-Bogami, S.; Al-Ghrami, M. S.; Bourane, A. Crude Oil to Chemicals: Light Olefins from Crude Oil. *Catal. Sci. Technol.* **2017**, *7*, 12–46. https://doi.org/10.1039/c6cy01886f.

(11) Huber, G. W.; Corma, A. Synergies between Bio- and Oil Refineries for the Production of Fuels from Biomass. *Angew. Chemie - Int. Ed.* **2007**, *46*, 7184–7201. https://doi.org/10.1002/anie.200604504.

(12) Lange, J. P.; Van Der Heide, E.; Van Buijtenen, J.; Price, R. Furfural-A Promising Platform for Lignocellulosic Biofuels. *ChemSusChem* **2012**, *5*, 150–166. https://doi.org/10.1002/cssc.201100648.

(13) Carlson, T. R.; Cheng, Y. T.; Jae, J.; Huber, G. W. Production of Green Aromatics and Olefins by Catalytic Fast Pyrolysis of Wood Sawdust. *Energy Environ. Sci.* **2011**, *4*, 145–161. https://doi.org/10.1039/c0ee00341g.

(14) Wang, Z.; Huang, J. Production of Biofuels and Chemicals with Bifunctional Catalysts. *Biofuels and Biorefineries*, Eds. Fang Z.; Smith Jr. R. L.; Li H. **2017**, Springer, Singapore, 99-135. https://doi.org/10.1007/978-981-10-51137-1.

(15) Cheng, Y. T.; Huber, G. W. Chemistry of Furan Conversion into Aromatics and Olefins over HZSM-5: A Model Biomass Conversion Reaction. *ACS Catal.* **2011**, *1*, 611–628. https://doi.org/10.1021/cs200103j.

(16) Cheng, Y. T.; Jae, J.; Shi, J.; Fan, W.; Huber, G. W. Production of Renewable Aromatic

Compounds by Catalytic Fast Pyrolysis of Lignocellulosic Biomass with Bifunctional Ga/ZSM-5 Catalysts. *Angew. Chem. Int. Ed.* **2012**, *51*, 1387–1390. https://doi.org/10.1002/anie.201107390.

(17) Zhang, B.; Zhong, Z.; Xie, Q.; Chen, P.; Ruan, R. Reducing Coke Formation in the Catalytic Fast Pyrolysis of Bio-Derived Furan with Surface Modified HZSM-5 Catalysts. *RSC Adv.* **2015**, *5* , 56286–56292. https://doi.org/10.1039/c5ra08827e.

(18) Zheng, Y.; Wang, F.; Yang, X.; Huang, Y.; Liu, C.; Zheng, Z.; Gu, J. Study on Aromatics Production via the Catalytic Pyrolysis Vapor Upgrading of Biomass Using Metal-Loaded Modified H-ZSM-5. *J. Anal. Appl. Pyrolysis* **2017**, *126*, 169–179. https://doi.org/10.1016/j.jaap.2017.06.011.

(19) Vogt, E. T. C.; Whiting, G. T.; Dutta Chowdhury, A.; Weckhuysen, B. M. Zeolites and Zeotypes for Oil and Gas Conversion. *Adv. Catal.* 1st ed.; Elsevier, Amsterdam, **2015**; *58*, 143-314 https://doi.org/10.1016/bs.acat.2015.10.001.

(20) Rezaei, P. S.; Shafaghat, H.; Daud, W. M. A. W. Production of Green Aromatics and Olefins by Catalytic Cracking of Oxygenate Compounds Derived from Biomass Pyrolysis: A Review. *Appl. Catal. A Gen.* **2014**, *469*, 490–511. https://doi.org/10.1016/j.apcata.2013.09.036.

(21) Yarulina, I.; Chowdhury, A. D.; Meirer, F.; Weckhuysen, B. M.; Gascon, J. Recent Trends and Fundamental Insights in the Methanol-to-Hydrocarbons Process. *Nat. Catal.* **2018**, *1*, 398–411. https://doi.org/10.1038/s41929-018-0078-5.

(22) Gao, J.; Zheng, Y.; Jehng, J.-M.; Tang, Y.; Wachs, I. E.; Podkolzin, S. G. Identification of Molybdenum Oxide Nanostructures on Zeolites for Natural Gas Conversion. *Science* **2015**, *348*, 686–690. https://doi.org/10.1126/science.aaa7048.

(23) Majhi, S.; Mohanty, P.; Wang, H.; Pant, K. K. Direct Conversion of Natural Gas to Higher Hydrocarbons: A Review. *J. Energy Chem.* **2013**, *22*, 543–554. https://doi.org/10.1016/S2095-4956(13)60071-6.

(24) Cheng, Y. T.; Huber, G. W. Production of Targeted Aromatics by Using Diels-Alder Classes of Reactions with Furans and Olefins over ZSM-5. *Green Chem.* **2012**, *14*, 3114–3125. https://doi.org/10.1039/c2gc35767d.

(25) Settle, A. E.; Berstis, L.; Rorrer, N. A.; Roman-Leshkóv, Y.; Beckham, G. T.; Richards, R. M.; Vardon, D. R. Heterogeneous Diels–Alder Catalysis for Biomass-Derived Aromatic Compounds. *Green Chem.* **2017**, *19*, 3468–3492. https://doi.org/10.1039/C7GC00992E.

(26) Svelle, S.; Joensen, F.; Nerlov, J.; Olsbye, U.; Lillerud, K. P.; Kolboe, S.; Bjørgen, M. Conversion of Methanol into Hydrocarbons over Zeolite H-ZSM-5: Ethene Formation Is Mechanistically Separated from the Formation of Higher Alkenes. *J. Am. Chem. Soc.* **2006**, *128*, 14770–14771. https://doi.org/10.1021/ja065810a.

(27) Lesthaeghe, D.; De Sterck, B.; Van Speybroeck, V.; Marin, G. B.; Waroquier, M. Zeolite Shape-Selectivity in the Gem-Methylation of Aromatic Hydrocarbons. *Angew. Chem. Int. Ed.* **2007**, *46*, 1311–1314. https://doi.org/10.1002/anie.200604309.

(28) Dahl, I. M.; Kolboe, S. On the Reaction Mechanism for Propene Formation in the MTO Reaction over SAPO-34. *Catal. Lett.* **1993**, *20*, 329–336. https://doi.org/10.1007/BF00769305.

(29) Qian, Q.; Vogt, C.; Mokhtar, M.; Asiri, A. M.; Al-Thabaiti, S. A.; Basahel, S. N.; Ruiz-Martínez, J.; Weckhuysen, B. M. Combined Operando UV/Vis/IR Spectroscopy Reveals the Role of Methoxy and Aromatic Species during the Methanol-to-Olefins Reaction over H-SAPO-34. *ChemCatChem* **2014**, *6*, 3396–3408. https://doi.org/10.1002/cctc.201402714.

(30) Iglesias-Juez, A.; Beale, A. M.; Maaijen, K.; Weng, T. C.; Glatzel, P.; Weckhuysen, B. M. A Combined in Situ Time-Resolved UV/Vis, Raman and High-Energy Resolution X-Ray Absorption Spectroscopy Study on the Deactivation Behavior of Pt and PtSn Propane Dehydrogenation Catalysts under Industrial Reaction Conditions. *J. Catal.* **2010**, *276*, 268–279. https://doi.org/10.1016/j.jcat.2010.09.018.

(31) Hemelsoet, K.; Qian, Q.; De Meyer, T.; De Wispelaere, K.; De Sterck, B.; Weckhuysen, B. M.; Waroquier, M.; Van Speybroeck, V. Identification of Intermediates in Zeolite-Catalyzed Reactions by in Situ UV/Vis Microspectroscopy and a Complementary Set of Molecular Simulations. *Chem. Eur. J.* **2013**, *19*, 16595–16606. https://doi.org/10.1002/chem.201301965.

(32) VanSpeybroeck, V.; Hemelsoet, K.; DeWispelaere, K.; Qian, Q.; VanderMynsbrugge,

J.; DeSterck, B.; Weckhuysen, B. M.; Waroquier, M. Mechanistic Studies on Chabazite-Type Methanol-to-Olefin Catalysts: Insights from Time-Resolved UV/Vis Microspectroscopy Combined with Theoretical Simulations. *ChemCatChem* **2013**, *5*, 173–184. https://doi.org/10.1002/cctc.201200580.

(33) Chowdhury, A. D.; Houben, K.; Whiting, G. T.; Mokhtar, M.; Asiri, A. M.; Al-Thabaiti, S. A.; Basahel, S. N.; Baldus, M.; Weckhuysen, B. M. Initial Carbon–Carbon Bond Formation during the Early Stages of the Methanol-to-Olefin Process Proven by Zeolite-Trapped Acetate and Methyl Acetate. *Angew. Chem. Int. Ed.* **2016**, *55*, 15840–15845. https://doi.org/10.1002/anie.201608643.

(34) Chen, D.; Moljord, K.; Holmen, A. A Methanol to Olefins Review: Diffusion, Coke Formation and Deactivation on SAPO Type Catalysts. *Microporous Mesoporous Mater.* **2012**, *164*, 239–250. https://doi.org/10.1016/j.micromeso.2012.06.046.

(35) Mores, D.; Kornatowski, J.; Olsbye, U.; Weckhuysen, B. M. Coke Formation during the Methanol-to-Olefin Conversion: In Situ Microspectroscopy on Individual H-ZSM-5 Crystals with Different Brønsted Acidity. *Chem. Eur. J.* **2011**, *17*, 2874–2884. https://doi.org/10.1002/chem.201002624.

(36) Bleken, F. L.; Barbera, K.; Bonino, F.; Olsbye, U.; Lillerud, K. P.; Bordiga, S.; Beato, P.; Janssens, T. V. W.; Svelle, S. Catalyst Deactivation by Coke Formation in Microporous and Desilicated Zeolite H-ZSM-5 during the Conversion of Methanol to Hydrocarbons. *J. Catal.* **2013**, *307*, 62–73. https://doi.org/10.1016/j.jcat.2013.07.004.

(37) Rojo-Gama, D.; Signorile, M.; Bonino, F.; Bordiga, S.; Olsbye, U.; Lillerud, K. P.; Beato, P.; Svelle, S. Structure–Deactivation Relationships in Zeolites during the Methanol–to-Hydrocarbons Reaction: Complementary Assessments of the Coke Content. *J. Catal.* **2017**, *351*, 33–48. https://doi.org/10.1016/j.jcat.2017.04.015.

(38) Olsbye, U.; Svelle, S.; Bjrgen, M.; Beato, P.; Janssens, T. V. W.; Joensen, F.; Bordiga, S.; Lillerud, K. P. Conversion of Methanol to Hydrocarbons: How Zeolite Cavity and Pore Size Controls Product Selectivity. *Angew. Chem. Int. Ed.* **2012**, *51*, 5810–5831. https://doi.org/10.1002/anie.201103657.

(39) Carlson, T. R.; Jae, J.; Lin, Y. C.; Tompsett, G. A.; Huber, G. W. Catalytic Fast Pyrolysis of Glucose with HZSM-5: The Combined Homogeneous and Heterogeneous Reactions.

J. Catal. **2010**, *270*, 110–124. https://doi.org/10.1016/j.jcat.2009.12.013.

(40) Uslamin, E. A.; Kosinov, N. A.; Pidko, E. A.; Hensen, E. J. M. Catalytic Conversion of Furanic Compounds over Ga-Modified ZSM-5 Zeolites as a Route to Biomass-Derived Aromatics. *Green Chem.* **2018**, *20*, 3818–3827. https://doi.org/10.1039/C8GC01528G.

(41) Hernando, H.; Hernández-Giménez, A. M.; Ochoa-Hernández, C.; Bruijnincx, P. C. A.; Houben, K.; Baldus, M.; Pizarro, P.; Coronado, J. M.; Fermoso, J.; Čejka, J.; et al. Engineering the Acidity and Accessibility of the Zeolite ZSM-5 for Efficient Bio-Oil Upgrading in Catalytic Pyrolysis of Lignocellulose. *Green Chem.* **2018**, *20*, 3499–3511. https://doi.org/10.1039/c8gc01722k.

(42) Mehlhorn, D.; Valiullin, R.; Kärger, J.; Cho, K.; Ryoo, R. Exploring the Hierarchy of Transport Phenomena in Hierarchical Pore Systems by NMR Diffusion Measurement. *Microporous Mesoporous Mater.* **2012**, *164*, 273–279. https://doi.org/10.1016/j.micromeso.2012.06.049.

(43) Qiao, K.; Shi, X.; Zhou, F.; Chen, H.; Fu, J.; Ma, H.; Huang, H. Catalytic Fast Pyrolysis of Cellulose in a Microreactor System Using Hierarchical Zsm-5 Zeolites Treated with Various Alkalis. *Appl. Catal. A Gen.* **2017**, *547*, 274–282. https://doi.org/10.1016/j.apcata.2017.07.034.

(44) Puertolas, B.; Veses, A.; Callen, M. S.; Mitchell, S.; Garcia, T.; Perez-Ramirez, J. Porosity-Acidity Interplay in Hierarchical ZSM-5 Zeolites for Pyrolysis Oil Valorization to Aromatics. *ChemSusChem* **2015**, *8*, 3283–3293. https://doi.org/10.1002/cssc.201500685.

(45) Groen, J. C.; Peffer, L. A. A.; Moulijn, J. A.; Pérez-Ramírez, J. Mesoporosity Development in ZSM-5 Zeolite upon Optimized Desilication Conditions in Alkaline Medium. *Colloids Surfaces A Physicochem. Eng. Asp.* **2004**, *241*, 53–58. https://doi.org/10.1016/j.colsurfa.2004.04.012.

(46) Emeis, C. A. Determination of Integrated Molar Extinction Coefficients for Infrared Absorption Bands of Pyridine Adsorbed on Solid Acid Catalysts. *J. Catal.* **1993**, *141*, 347–354.

(47) Milina, M.; Mitchell, S.; Michels, N. L.; Kenvin, J.; Pérez-Ramírez, J. Interdependence between Porosity, Acidity, and Catalytic Performance in Hierarchical ZSM-5 Zeolites

Prepared by Post-Synthetic Modification. *J. Catal.* **2013**, *308*, 398–407. https://doi.org/10.1016/j.jcat.2013.08.020.

(48) Verboekend, D.; Pérez-Ramírez, J. Design of Hierarchical Zeolite Catalysts by Desilication. *Catal. Sci. Technol.* **2011**, *1*, 879–890. https://doi.org/10.1039/c1cy00150g.

(49) Bordiga, S.; Lamberti, C.; Bonino, F.; Travert, A.; Thibault-Starzyk, F. Probing Zeolites by Vibrational Spectroscopies. *Chem. Soc. Rev.* **2015**, *44*, 7262–7341. https://doi.org/10.1039/C5CS00396B.

(50) Thibault-Staruk, F.; Francoise, M. *Characterization of Solid Materials and Heterogeneous Catalysts*; Che, M., Védrine, J. C., Eds.; Wiley-VCH, Weinheim, **2012**, 1-48. https://doi.org/10.1002/9783527645329.

(51) Deutschmann, O.; Knözinger, H.; Kochloefl, K.; Turek, T. Heterogeneous Catalysis and Solid Catalysts. In *Ullmann's Encyclopedia of Industrial Chemistry*; Wiley-VCH Weinheim, **2009**. https://doi.org/10.1002/14356007.a05_313.pub2.

(52) Boronat, M.; Corma, A. What Is Measured When Measuring Acidity in Zeolites with Probe Molecules? *ACS Catal.* **2019**, *9*, 1539–1548. https://doi.org/10.1021/acscatal.8b04317.

(53) Jin, F.; Li, Y. A FTIR and TPD Examination of the Distributive Properties of Acid Sites on ZSM-5 Zeolite with Pyridine as a Probe Molecule. *Catal. Today* **2009**, *145*, 101–107. https://doi.org/10.1016/j.cattod.2008.06.007.

(54) Jin, F.; Tian, Y.; Li, Y. Effect of Alkaline Treatment on the Catalytic Performance of ZSM-5 Catalyst in Pyridine and Picolines Synthesis. *Ind. Eng. Chem. Res.* **2009**, *48*, 1873–1879. https://doi.org/10.1021/ie8014457.

(55) Ahmed, M. H. M.; Muraza, O.; Al-Amer, A. M.; Miyake, K.; Nishiyama, N. Development of Hierarchical EU-1 Zeolite by Sequential Alkaline and Acid Treatments for Selective Dimethyl Ether to Propylene (DTP). *Appl. Catal. A Gen.* **2015**, *497*, 127–134. https://doi.org/10.1016/j.apcata.2015.03.011.

(56) Kiricsi, I.; Förster, H.; Tasi, G.; Nagy, J. B. Generation, Characterization, and Transformations of Unsaturated Carbenium Ions in Zeolites. *Chem. Rev.* **1999**, *99*, 2085–

2114. https://doi.org/10.1021/cr9600767.

(57) Chowdhury, A. D.; Houben, K.; Whiting, G. T.; Chung, S.-H.; Baldus, M.; Weckhuysen, B. M. Electrophilic Aromatic Substitution over Zeolites Generates Wheland-Type Reaction Intermediates. *Nat. Catal.* **2018**, *1*, 23–31. https://doi.org/10.1038/s41929-017-0002-4.

(58) Cheng, Y.-T.; Huber, G. W. Chemistry of Furan Conversion into Aromatics and Olefins over HZSM-5: A Model Biomass Conversion Reaction. *ACS Catal.* **2011**, *1*, 611–628. https://doi.org/10.1021/cs200103j.

(59) Yang, S.; Kondo, J. N.; Domen, K. Formation of Alkenyl Carbenium Ions by Adsorption of Cyclic Precursors on Zeolites. *Catal. Today* **2002**, *73*, 113–125. https://doi.org/10.1016/S0920-5861(01)00504-1.

(60) Pidko, E. A.; Hensen, E. J. M.; Van Santen, R. A. Dehydrogenation of Light Alkanes over Isolated Gallyl Ions in Ga/ZSM-5 Zeolites. *J. Phys. Chem. C* **2007**, *111*, 13068–13075. https://doi.org/10.1021/jp072110z.

(61) Kumbhalkar, M. D.; Buchanan, J. S.; Huber, G. W.; Dumesic, J. A. Ring Opening of Biomass-Derived Cyclic Ethers to Dienes over Silica/Alumina. *ACS Catal.* **2017**, *7*, 5248–5256. https://doi.org/10.1021/acscatal.7b01436.

(62) Verkleij, S. P.; Whiting, G. T.; Esclapez, S. P.; Mertens, M. M.; Bons, A.-J.; Burgers, M.; Weckhuysen, B. M. *Operando* Micro-Spectroscopy on ZSM-5 Containing Extrudates during the Oligomerization of 1-Hexene. *Catal. Sci. Technol.* **2018**, *8*, 2175–2185. https://doi.org/10.1039/C7CY02460F.

(63) Yang, S.; Kondo, J. N.; Domen, K. Formation of Stable Alkenyl Carbenium Ions in High Yield by Adsorption of 1-Methylcyclopentene on Zeolite Y at Low Temperature. *Chem. Commun.* **2001**, *1*, 2008–2009. https://doi.org/10.1039/b106450a.

(64) Goetze, J.; Meirer, F.; Yarulina, I.; Gascon, J.; Kapteijn, F.; Ruiz-Martínez, J.; Weckhuysen, B. M. Insights into the Activity and Deactivation of the Methanol-to-Olefins Process over Different Small-Pore Zeolites As Studied with Operando UV-Vis Spectroscopy. *ACS Catal.* **2017**, *7*, 4033–4046. https://doi.org/10.1021/acscatal.6b03677.

(65) Spoto, G. .; Geobaldo, F. .; Bordiga, S. .; Lamberti, C. .; Scarano, D. .; Zecchina, A. . Heterocycles Oligomerization in Acidic Zeolites: A UV-Visible and IR Study. *Top. Catal.* **1999**, *8*, 279–292. https://doi.org/10.1023/A:1019137900710.

(66) Jiang, Y.; Wang, W.; Marthala, V. R. R.; Huang, J.; Sulikowski, B.; Hunger, M. Effect of Organic Impurities on the Hydrocarbon Formation via the Decomposition of Surface Methoxy Groups on Acidic Zeolite Catalysts. *J. Catal.* **2006**, *238*, 21–27. https://doi.org/10.1016/j.jcat.2005.11.029.

(67) Abubakar, S. M.; Marcus, D. M.; Lee, J. C.; Ehresmann, J. O.; Chen, C. Y.; Kletnieks, P. W.; Guenther, D. R.; Hayman, M. J.; Pavlova, M.; Nicholas, J. B.; et al. Structural and Mechanistic Investigation of a Phosphate-Modified HZSM-5 Catalyst for Methanol Conversion. *Langmuir* **2006**, *22*, 4846–4852. https://doi.org/10.1021/la0534367.

(68) Song, W.; Marcus, D. M.; Fu, H.; Ehresmann, J. O.; Haw, J. F. An Oft-Studied Reaction That May Never Have Been: Direct Catalytic Conversion of Methanol or Dimethyl Ether to Hydrocarbons on the Solid Acids HZSM-5 or HSAPO-34. *J. Am. Chem. Soc.* **2002**, *124*, 3844–3845. https://doi.org/10.1021/ja016499u.

(69) Ilias, S.; Bhan, A. Mechanism of the Catalytic Conversion of Methanol to Hydrocarbons. *ACS Catal.* **2013**, *3*, 18–31. https://doi.org/10.1021/cs3006583.

(70) Olsbye, U.; Svelle, S.; Lillerud, K. P.; Wei, Z. H.; Chen, Y. Y.; Li, J. F.; Wang, J. G.; Fan, W. B. The Formation and Degradation of Active Species during Methanol Conversion over Protonated Zeotype Catalysts. *Chem. Soc. Rev.* **2015**, *44*, 7155–7176. https://doi.org/10.1039/c5cs00304k.

(71) Ilias, S.; Khare, R.; Malek, A.; Bhan, A. A Descriptor for the Relative Propagation of the Aromatic- and Olefin-Based Cycles in Methanol-to-Hydrocarbons Conversion on H-ZSM-5. *J. Catal.* **2013**, *303*, 135–140. https://doi.org/10.1016/j.jcat.2013.03.021.

(72) Müller, S.; Liu, Y.; Vishnuvarthan, M.; Sun, X.; Van Veen, A. C.; Haller, G. L.; Sanchez-Sanchez, M.; Lercher, J. A. Coke Formation and Deactivation Pathways on H-ZSM-5 in the Conversion of Methanol to Olefins. *J. Catal.* **2015**, *325*, 48–59. https://doi.org/10.1016/j.jcat.2015.02.013.

(73) Liu, Z.; Dong, X.; Liu, X.; Han, Y. Oxygen-Containing Coke Species in Zeolite-Catalyzed Conversion of Methanol to Hydrocarbons. *Catal. Sci. Technol.* **2016**, *6*, 8157–

8165. https://doi.org/10.1039/c6cy01463a.

(74) Dejaifve, P.; Védrine, J. C.; Bolis, V.; Van Hooff, J. H. C.; Derouane, E. G. The Reaction Pathways to Aromatic Hydrocarbons from Conversion of Methanol and Olefins on H-ZSM-5 Zeolite. **1979**, *24*, 286–303.

(75) Uslamin, E. A.; Kosinov, N.; Filonenko, G. A.; Mezari, B.; Pidko, E.; Hensen, E. J. M. Co-Aromatization of Furan and Methanol over ZSM-5—A Pathway to Bio-Aromatics. *ACS Catal.* **2019**, *9*, 8547–8554. https://doi.org/10.1021/acscatal.9b02259.

(76) Zhang, H.; Shao, S.; Xiao, R.; Shen, D.; Zeng, J. Characterization of Coke Deposition in the Catalytic Fast Pyrolysis of Biomass Derivates. *Energy and Fuels* **2014**, *28*, 52–57. https://doi.org/10.1021/ef401458y.

(77) Fanchiang, W. L.; Lin, Y. C. Catalytic Fast Pyrolysis of Furfural over H-ZSM-5 and Zn/H-ZSM-5 Catalysts. *Appl. Catal. A Gen.* **2012**, *419–420*, 102–110. https://doi.org/10.1016/j.apcata.2012.01.017.

(78) Wang, Y.; Mourant, D.; Hu, X.; Zhang, S.; Lievens, C.; Li, C. Z. Formation of Coke during the Pyrolysis of Bio-Oil. *Fuel* **2013**, *108*, 439–444. https://doi.org/10.1016/j.fuel.2012.11.052.

(79) Green, S. K.; Patet, R. E.; Nikbin, N.; Williams, C. L.; Chang, C. C.; Yu, J.; Gorte, R. J.; Caratzoulas, S.; Fan, W.; Vlachos, D. G.; et al. Diels-Alder Cycloaddition of 2-Methylfuran and Ethylene for Renewable Toluene. *Appl. Catal. B Environ.* **2016**, *180*, 487–496. https://doi.org/10.1016/j.apcatb.2015.06.044.

(80) Vaitheeswaran, S.; Green, S. K.; Dauenhauer, P.; Auerbach, S. M. On the Way to Biofuels from Furan: Discriminating Diels-Alder and Ring-Opening Mechanisms. *ACS Catal.* **2013**, *3*, 2012–2019. https://doi.org/10.1021/cs4003904.

Chapter 3 Phosphorus-promoted HZSM-5 Zeolite Catalysts for the Aromatization of Biomass-derived Furan Derivatives

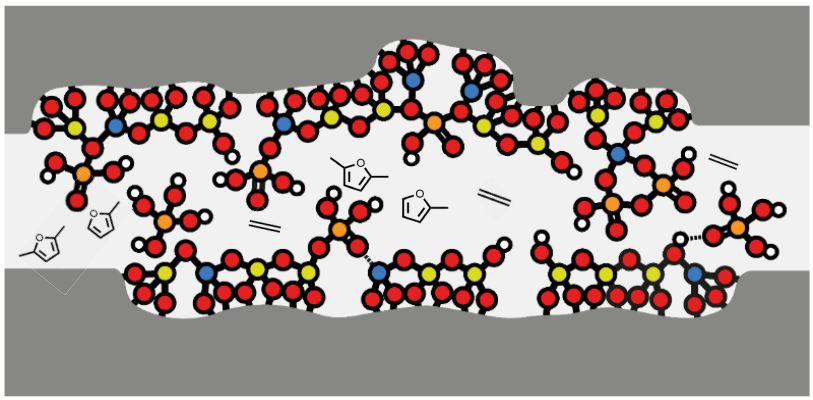

This Chapter is based on the following publication: B. Luna-Murillo, D. Waard, A. Lucini Paioni, M. Baldus, P.C.A. Bruijnincx, B.M. Weckhuysen, Structure-Performance Relationships for the Aromatization of Furan Derivatives over Phosphorus-modified ZSM-5 Zeolites, *in preparation.*

Abstract

The aromatization of both 2-methylfuran (MF) and 2,5-dimethylfuran (DMF) was studied over phosphorus-modified HZSM-5 zeolites. Phosphorus was added to tune the acidity and surface area of the zeolites and influence their reactivity. Advanced characterization techniques, such as FT-IR spectroscopy with pyridine as probe molecule and, ^{27}Al, ^{29}Si, ^{31}P MAS, 2D ^{27}Al MQ-MAS solid-state NMR (ssNMR) spectroscopy were used to elucidate the phosphorus – zeolite interactions. The FT-IR and ^{27}Al NMR spectra revealed the formation of AlPO species at higher weight loadings. Furthermore, ^{31}P ssNMR showed a wide range of other free and condensed phosphorus compounds. These species could be partly removed by washing, a post-synthesis treatment that improved the acidity, accessibility and as a result, performance of the materials. The PHZSM-5 catalyst was tested in the aromatization of DMF and MF, with the lower phosphorus loaded materials giving better yields than the HZSM-5 benchmark catalyst. The washed 2 wt. % PHZSM-5 catalyst showed an improved selectivity towards (di)alkylated aromatics in the aromatization of MF and an increase in xylenes selectivity when DMF was used as substrate. More non-condensable gases were observed when ethylene was added during MF and DMF aromatization over PHZSM-5 zeolites. While co-feeding ethylene with MF slightly improved toluene selectivity (from 20% to 25% selectivity when using 2 wt. % PHZSM-5 zeolite catalyst). P addition resulted in improved selectivity to (mono)alkylated aromatics only at low loadings (>2 wt. %). A low P loading also influenced loss of activity through deactivation in the MF aromatization reaction. Phosphorus loadings should thus, be carefully controlled during catalyst optimization for the aromatization of furan derivatives.

3.1 Introduction

Nowadays, the production of chemical building blocks such as olefins or benzene, toluene, and xylene (BTX) is performed by steam cracking of naphtha. However, due to the ongoing concerns about climate change, alternative and more sustainable routes are being explored in order to find alternatives to common fossil route. One way that has been widely investigated, and one of topics of this PhD Thesis, is the upgrading of bio-derived feedstock to chemical building blocks over acidic zeolites as catalysts.

As we introduced in previous Chapters, furan derivatives can be obtained from sugars such as xylose or glucose[1–4]. Zeolite-catalyzed aromatization is then one of the most investigated routes for further valorization of these furan derivatives, yielding aromatics such as BTX[5–7]. Previous investigations revealed that Brønsted acid sites present in HZSM-5 zeolites catalyze furan conversion towards BTX, but this process is known to suffer from rapid deactivation by coke buildup and low carbon selectivities[5,8]. In general, the most often suggested route to form aromatics from furans is via decarbonylation/decarboxylation followed by a carbon rearrangement or by addition of another carbon source, such as olefins, which can either be formed by cracking of the furan ring or added via co-feeding[3,9,10]. The formation of aromatics through the latter route is proposed to proceed via Diels-Alder cycloaddition[11], a [4+2] addition reaction that yields aromatics after dehydration of the diene and dienophile adduct (Figure 3.1). Corma and co-workers proposed this reaction mechanism to be taking place during various gas-phase biomass acid-catalyzed reactions involving zeolites as catalysts[11,12]. Later investigations carried by Carlson *et al.* revealed the effect of co-feeding different olefins (i.e., propylene and, ethylene), which resulted in improved BTX selectivity, especially for alkylated aromatics[13]. Furthermore, they demonstrated how co-feeding of olefins such as ethylene or propylene, considerably improved the H/C_{eff} ratio (Hydrogen/Carbon effective ratio) and thus, the production to aromatics[14].

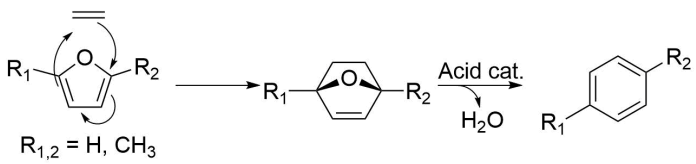

Figure 3.1. Schematic representation of the Diels-Alder cycloaddition when co-feeding furan derivatives with olefins.

The conversion of Furan-to-Aromatics (FTA) in presence of olefins in the gas phase is usually catalyzed by the combination of Lewis acid sites (LAS) and Brønsted acid sites (BAS) present in the HZSM-5 zeolite materials[5,14–17]. These latter sites are known to favor the final dehydration step[18,19]. However, a high number of BAS (e.g. as a result of a low Si/Al ratio) are known to not only favor aromatization, but also catalyst coking. Besides the high rate of side reactions, the considerably large amount of water produced during the reaction is detrimental for the structural integrity of the zeolite, as under these conditions the removal of framework aluminum by steaming is promoted[20]. To improve carbon selectivity as well as catalyst stability, further investigations in catalyst design for the FTA process are needed.

A common and easy practice to improve the catalytic performance of HZSM-5 zeolites is by means of post-synthesis modification. The addition of promotors directly modifies the chemical properties of the zeolite, allowing to improve their catalytic performance. A well-known practice for improving zeolite catalyst performance is by the addition of phosphorus species, which is known to significantly improve catalyst lifetime by preventing aluminum leaching from the framework[21,22]. Furthermore, van der Bij *et al.* reported that phosphatation can result in an improved catalytic performance for HZSM-5 zeolites depending on the synthesis method applied. In addition, depending on the phosphorus loadings used, key physicochemical properties such as acidity and accessibility are known to be directly affected[23]. Moreover, impregnation of phosphorus can be used for a controlled dealumination, a process known to be strictly dependent on the phosphorus loading and post-synthetic method employed[24].

The most common technique for the incorporation of phosphorus on HZSM-5 zeolites is by wetness or incipient-wetness impregnation of a phosphorus precursor, such as orthophosphoric acid (H_3PO_4)[22]. It is noteworthy to remark that the use of phosphoric acid as precursor indirectly favors dealumination due to the very low pH ~0-1 used.

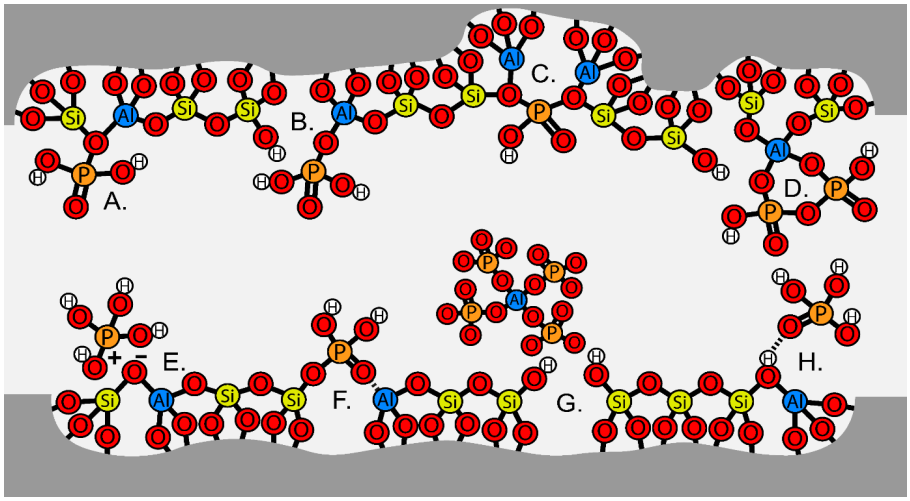

Figure 3.2. Proposed zeolite-phosphate interactions from: (a.) Keading *et al.*[25], (b.) Zhuang *et al.*[26] (c.) Xue *et al.*[27], (d.) van der Bij *et al.*[23], (e.) Blasco *et al.*[21] (f.) Lercher *et al.*[28], (g.) Caro *et al.*[29], (h.) Abubakar *et al.*[30].

After synthesis, the phosphorus species are found to be mostly distributed over the surface of the zeolite. This is especially the case at high weight loadings (>5% phosphorus), at which most of the phosphorus is deposited on the external surface of the zeolite[29,31]. The addition of phosphorus results in the interaction of monomeric phosphorus species with Si and Al sites from the zeolite, with the phosphorus preferentially binding to the aluminum sites on the zeolite, as was demonstrated in previous studies[32]. Although the origin of the phosphorus-zeolite interactions still remains under debate, several researchers proposed various phosphorus species that might be formed within the zeolite domains. Several interactions were proposed, such as the incorporation of phosphates into the structure (see phosphorus species a, b, c, d, and f from Figure 3.2), or electrostatic interactions between the phosphate species and the zeolitic framework, as shown in Figure 3.2e or by hydrogen bonding as shown in Figure 3.2h. Formation of Si-O-P bonds are proposed but their formation seems to be thermodynamically unlikely due to drastic hydrothermal treatments need to be applied to favor their formation[33–36]. Protonation of the phosphorus species via the acid sites present in the zeolite framework (Figure 3.2e) was also proposed, by Blasco *et al.*[21], who suggested that such phosphorus binding to a Brønsted acid site creates "neutralized" aluminum atoms. This phosphorus cationic formation is highly favorable in zeolites with a high Al content, as this protonated phosphorus species stabilizes another near BAS acid site by stabilizing the "non-neutralized" second aluminum atom. This model assumes then assumes a close proximity of acid sites within the

framework. Phosphorus is also known to dealuminate the zeolite structure by forming either aluminum phosphate phases (AlPO) (Figure 3.2g), or partially dislodging aluminum from the framework by monodentate phosphate (Figure 3.2b) or bidentate phosphates species (Figure 3.2d). In previous works by van der Bij *et al*., formation of the so-called SAPO interfaces within the zeolite structure such as $(SiO)_2Al(O_2P(OR)_2)$ or $(SiO)_2Al(O_2P_2O_2(OR)_3)$ were also proposed, where R is either a phosphate or a polyphosphoric species[23,31]. Besides the direct attachment of phosphorus to the framework, the formation of larger condensed phosphates can also take place thereby decreasing pore volume. Up to some extent, such induced pore narrowing of the zeolite framework can result in reaction with improved shape-selectivity, as seen in the production of *p*-xylene over *m*- or *o*-xylene[14,37,38]. Despite the partial dislodging of the aluminum from the framework, these phosphorus interactions (i.e. Figure 3.2b) favor aluminum sites to be kept within the zeolite framework during steaming conditions, because they prevent the Si-O-Al bond of being broken. Moreover, phosphorus impregnation leads to a decrease in strong acid sites, while the amount of weak acid sites increases slightly with increased phosphorus loading[39,40]. It is also noteworthy to mention that P deposition is a reversible process and that the original acid sites and pore volume can be regenerated if no calcination is applied after impregnation[41,42]. Thus, to promote the formation of strong and irreversible phosphorus-zeolite interactions a subsequent calcination step after the wetness impregnation step is strictly necessary. Nevertheless, despite all the available literature on phosphorus-modified HZSM-5 zeolites, there is still scarce knowledge about the catalytically active sites and speciation of phosphorus zeolites.

Previous reports on the effect of phosphorus addition to HZSM-5 zeolite demonstrated that the formation of phosphorus-zeolite adducts removes BAS by partial dislodging Al sites from the framework[43]. In contrast, the adduct formed stabilizes the zeolitic framework providing also a lower acid concentration compared to the unmodified zeolite. Not only because of the removal of the original BAS but because of the presence of protons from the phosphate species[44]. The high concentration of BAS within the HZSM-5 zeolites promotes the formation of side and uncontrolled reactions during furan aromatization, resulting in a broad distribution of products and a low carbon selectivity, e.g. as a result of excessive coking[5]. Furthermore, the use of phosphorus as promotor during the conversion of Methanol-to-Olefins (MTO) enhanced selectivity by reducing coking[45]. Therefore, given the large amount of H_2O produced within our system, incorporation of phosphorus is expected to have a similar effect as in the MTO process. The introduction of phosphorus as promotor known to improve zeolite catalysts´

lifetime and reduce coking, is then again anticipated to benefit the FTA process[36]. Additionally, the physicochemical (i.e., a decrease in BAS/LAS acidity and accessibility) changes induced within the intra-zeolitic domains upon the incorporation of the phosphorus will result in a modified performance because of the decrease of BAS. By reducing the extent of side reactions, we expect to improve the selectivity to BTX.

In this Chapter, we have investigated phosphorous-modified HZSM-5 zeolites in furan aromatization, combining catalyst synthesis, characterization and testing. We synthesized a variety of phosphorous-modified HZSM-5 zeolite catalysts by wetness impregnation[46], using H_3PO_4 as phosphorus precursor. Extensive characterization employing different spectroscopic techniques provided further insight into the most abundant and catalytically active phosphorus species formed after phosphatation. The aromatization of 2-methylfuran (MF) and 2,5-dimethylfuran (DMF) was studied with and without ethylene co-feeding. Investigations on the presence of phosphorus in ZSM-5 zeolites is believed to facilitate aromatization or/and co-aromatization process via Diels-Alder cycloadditions by reducing coking and improving catalyst hydrothermal stability.

3.2 Experimental Part

3.2.1 Catalyst Preparation and Reagents

Phosphorus-modified HZSM-5 zeolites were prepared by wetness impregnation of a commercial zeolite (CBV 3024E, Si/Al = 15) using H_3PO_4 as phosphatation agent, similarly as described in ref.[46]. Firstly, the H-form was obtained after calcination of the commercial (NH_4^+)ZSM-5 zeolite at 550 °C for 5 h under air. Next, 40 ml solution containing the H_3PO_4 precursor was prepared (from 0.04 to 0.22 ml H_3PO_4 in demi-water to obtain from 1 to 5 wt. % phosphorus content). 2 g H-form zeolite was added to the H_3PO_4 prepared solution and stirred for 15 min reaching a pH = ~2. Subsequently, the solvent was evaporated under vacuum, and samples were dried and calcined at 550 °C for 3 h. The samples obtained were labelled as *x*PH15; were *x* denotes the percentage of phosphor loaded, which ranged from 1 to 5 wt. %. A second batch of samples was subjected to an extra washing and calcination step to remove any excess of phosphor deposited on the materials. W_C-*x*PH15 samples were obtained from the *x*PH15 samples after washing with 20 ml demi-water, vacuum filtration, drying overnight at

120 °C and calcination at 550 °C for 3 h. W- xPH15 samples were only washed a second time and not again calcined.

Commercially available H_3PO_4 solution (85 wt. %, Sigma-Aldrich) was used to prepare the phosphorus precursor. 2-methylfuran (99%, Sigma Aldrich) and 2,5-dimethylfuran (98+%, Alfa Aesar) were used without any treatment. Ethylene was purchased and directly used from a steel cylinder without further treatment (> 99.95% purity, Linde).

3.2.2 Catalyst Characterization

X-ray diffraction (XRD) patterns were recorded on a Bruker-AXS D2 Phaser powder X-ray diffractometer in Bragg-Brentano mode equipped with a Lynxeye detector. The radiation used was a CoKα (λ = 1.79026 Å) source. XRD patterns were collected in the 2θ range from 5° to 50° at a scanning speed of 0.02 °/min and an acquisition time of 1 s per step.

The specific surface area and porosity of the zeolite materials were determined by Ar physisorption using a Micrometric TriStar Analyzer. Before the experiments were performed, all samples were degassed under a N_2 flow at 300 °C for 16 h to remove any physiosorbed impurities. The micropore volume and the surface area were determined by the *t*-plot method and the Brunauer-Emmett-Teller (BET) theory, respectively. External surface area was determined by subtraction of the micropore volume area from the BET surface area.

Silicon, aluminum and phosphor were determined by elemental analysis using an Inductively Coupled Plasma-Optical Emission Spectrometer (ICP-OES) analyzer. The experiments were performed at Mikroanalytisches laboratorium Kolbe in Oberhauser, Germany. Prior to analysis, all the samples were digested in special acid solutions.

Temperature programmed desorption (TPD) analyses with NH_3 as probe molecule were recorded with a Micromeritics AutoChem II 2920 instrument to determine the strength and number of acid sites of the zeolite-based materials. 100 mg of sample was placed on the chamber and pre-treated up to 550 °C under a He flow. The chamber was cooled down and kept at 100 °C before to start the dosing of NH_3. A 25 ml/min flow of 10% NH_3 in He was fed into the chamber using a pulse wise manner until saturation. Afterwards, the temperature was ramped to 550 °C at 10 °C/min and kept at that temperature for 25 min more.

For the Fourier transform-infrared (FT-IR) spectroscopy measurements with pyridine as probe molecule, the samples were grounded and pressed into thin self-supported wafers (~ 25 mg sample). The wafers were placed in a sealed FT-IR cell equipped with a vacuum system and a heating system. The wafers were pre-treated under vacuum (~10^{-3} mbar) at 550 °C for 2 h to remove all adsorbates, then was cooled down to 40 °C where pyridine vapor was introduced into the cell for 30 min until complete saturation. The weakly adsorbed pyridine was removed by evacuation for 1 h. Afterwards, the temperature was ramped from 40 to 150 °C at 5 °C/min and kept at 150 °C for 30 min, after which a spectrum was recorded. As described elsewhere[47], this step is done to calculate the amount of Lewis acid sites (LAS) and Bronsted acid sites (BAS). In a next step, the temperature was ramped up to 550 °C to remove all pyridine from the sample. All spectra were recorded between 4000-1000 cm^{-1} using a Perkin-Elmer System 2000 instrument.

^{27}Al, ^{29}Si and ^{31}P magic angle spinning (MAS) solid-state (ss) nuclear magnetic resonance (NMR) experiments were performed at 11.7 T (500 MHz) on a Bruker Avance III spectrometer equipped with a 3.2 mm MAS probe. Spectra were recorded at ambient temperature and referencing was done externally to $Al(NO_3)_3$, tetramethylsilane (TMS) and NaP, respectively. For all the measurements the rotors were filled with the same amount of sample (~ 30 mg). A MAS of 16 kHz was applied for ^{27}Al and ^{31}P experiments, while a radiofrequency (RF) field of 50 kHz was used for the ^{27}Al $\pi/12$ pulse followed by 4.4 ms acquisition. An inter-scan delay of 1s was applied and 10240 scans were accumulated for [Z] and 2P[Z] samples, for W-2P[Z] and W_C-2P[Z] samples 4096 scans were used (where [Z] = H15). The spectra were processed with a line-broadening of 100 Hz. A zero-quantum (ZQ) filtered multiple-quantum magic angle spinning (MQ-MAS) pulse-sequence[48] was used to correlate the ^{27}Al isotropic chemical shift (F1) with the quadrupolar line-shape (F2). The excitation and conversion pulses were applied with a RF field of 50 kHz, instead for the soft, selective pulse following the Z-filter delay an RF field of 6.5 kHz was used. 2400 scans were accumulated using an inter-scan delay of 1 s. Acquisition times of 5 ms and 1 ms were used for the direct and indirect dimensions, respectively. MQ-MAS data were Fourier transformed and sheared, and 100 Hz line-broadening was applied in both dimensions. A RF field of 83 kHz, 12 ms acquisition time and 2048 scans were applied for the 1D ^{31}P spectra, with 5 s recycle delay and 88 kHz SPINAL-64[49] proton decoupling and 100 Hz line broadening for spectral processing.

For the ^{1}H-^{31}P cross-polarization (CP)[50] RF fields of 70 kHz and 57 kHz were used, respectively, and a 70% ramp, with CP contact time of 2 ms and 10 ms acquisition time. Using

88 kHz SPINAL-64 proton decoupling, 2048 scans were recorded with 1.5 s recycle delay and a line broadening of 100 Hz was applied for spectral processing.

For ^{29}Si ssNMR experiments a MAS frequency of 12 kHz was applied. 88 kHz SPINAL-64 proton decoupling and RF field of 54 kHz were used for ^{29}Si 1D spectra, recorded with 512 scans, 13 ms acquisition time and 80 s recycle delay, then processed with 50 Hz line broadening. All spectra were processed and analyzed using the Bruker software Topspin 3.5.

To verify that phosphorous pentoxide (P_4O_{10}) can be formed inside zeolite ZSM-5 channels, its adsorption energy was computed. As a zeolite model, purely siliceous version of ZSM-5, silicalite-1, with an orthorhombic unit cell and lattice parameters a = 20.090 Å, b = 19.738 Å and c= 13.142 Å was used. All geometries were optimized using periodic Density Functional Theory (DFT) calculations implemented within cp2k software[51]. Gaussian and plane waves approach (GPW)[52] with GTH pseudopotentials[53] and Perdew–Burke–Ernzerhof (PBE)[54] functional with Grimme dispersion correction (-D3)[55] were used. The accuracy of calculations was controlled using MOLOPT-TZVP basis set[56] and plane-wave cutoff of 700 Ry. Prior the geometry optimization phosphorous pentoxide was placed in its most favorable position, i.e. at the intersection of a- and b- channels[57]. The adsorption energy was computed as:

$$E_{ads} = E_{complex} - E_{zeolite} - E_{P_4O_{10}} ,$$

where $E_{complex}$ is the energy of the phosphorous pentoxide adsorbed in the zeolite framework, $E_{zeolite}$ is the energy of an empty zeolite and $E_{P_4O_{10}}$ is the energy of the phosphorous pentoxide in vacuum.

3.2.3 Catalyst Testing

The catalytic aromatization of 2-methylfuran (MF) and 2,5-dimethylfuran (DMF) with ethylene was performed in a custom-made reactor setup, as shown in Figure 3.3. For every catalytic test, ~ 55 mg catalyst was placed inside the reactor. All reagents and gases were fed into the reactor using calibrated mass-flow controllers (Bronkhorst). Activation of the catalyst was performed at the reaction temperature (500 °C) for 60 min under O_2/N_2 flow. Subsequently, the reactor was purged with N_2 for 30 min before starting the reaction. MF and DMF were fed into the reactor in gas phase using a bubbler saturator with Ar as carrier gas (2 ml/min at 30 °C) which was then added to N_2 flow (18 ml/min) obtaining a weight hourly space velocity

(WHSV) of respectively $WHSV_{MF}$ 1 h^{-1} and $WHSV_{DMF}$ 0.7 h^{-1}, in a total flow of 20 ml/min. For the ethylene co-feeding experiments, a calibrated mass-flow controller for ethylene (Bronkhorst) was used. The flows were set to obtain a volume (molar) ratio of 1:0.5 furan-to-ethylene with a 3.9% of either MF or DMF with respect to the total flow rate. Both reagents were also diluted by a N_2 carrier gas (16 ml/min) obtaining a total flow rate of 20 ml/min. The total products were analyzed using an online compact GC (Interscience) equipped with three 25 µl sample loops mounted on a six-way valve. The GC was equipped with three different columns and two different detectors; C1-C3 products were analyzed with a Rt-QBond column of 3 m length and 0.32 mm diameter equipped with a flame ionization detector (FID). C4-C8/aromatic products were analyzed on a MXT-5 column of 15 m length and 0.28 mm diameter equipped with a FID. Non-condensable gases, such as O_2, H_2, N_2 and CO_2, were analyzed with a Carboxen 1010 column of 10 m length and 0.32 mm diameter equipped with a thermal conductivity detector (TCD).

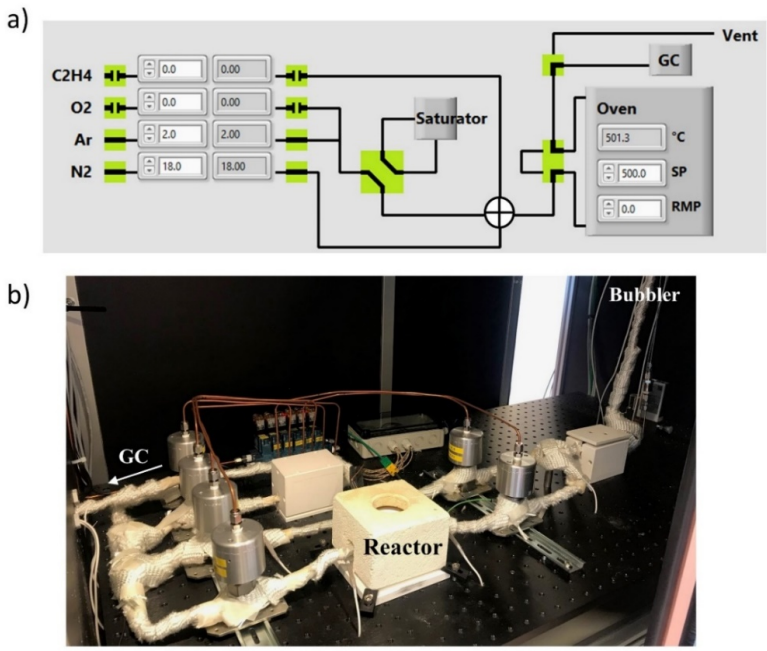

Figure 3.3. (a) Schematic obtained from the LabVIEW program used for running the reactions, depicting the setup configuration and (b) Picture of the setup used for the catalytic aromatization of 2-methylfuran (MF) and 2,5-dimethylfuran (DMF) in the absence and presence of ethylene over HZSM-5 zeolite-based catalysts.

The catalytic conversion, selectivity and yield (carbon-based) in the aromatization of MF and DMF (represented as A) with co-feeding of ethylene (represented as B) were calculated using the following equations[58]:

$$X_{A,B}(t = x) = \frac{n_{A,B}^{in} - n_{A,B}^{out}}{n_{A,B}^{in}} = 1 - \frac{n_{A,B}^{out}}{n_{A,B}^{in}} \quad \text{(eq. 3.1)}$$

$$S_P(t = x) = \frac{n_P^{out} - n_P^{in}}{n_{A,B}^{in} - n_{A,B}^{out}} \times \left|\frac{\mu_p}{\mu_{A,B}}\right| \quad \text{(eq. 3.2)}$$

$$Y_P(t = x) = \frac{n_P^{out} - n_P^{in}}{n_{A,B}^{in}} = X_{A,B} \times S_P; \quad \text{(eq. 3.3)}$$

where $n^{in}{}_{A,B}$ and $n^{out}{}_{A,B}$ represent number of moles of MF or DMF (A) and ethylene (B) entering the reactor and in the outlet, respectively. Selectivity for a product p at a time x = 125 min, μ_p and $\mu_{A,B}$ represent the number of carbons of a product p and of the starting reagents (DMF and ethylene), respectively.

For the selectivity, conversion and yield calculations of the co-feeding tests, ethylene was included in all the calculation together with either MF or DMF as starting reagent. MF or DMF and ethylene were both added to the carbon balance (calculated after 125 min).

3.3 Results and Discussion

3.3.1 Catalyst Characterization

Various phosphorus-modified HZSM-5 zeolites (PHZSM-5) were synthesized with different P loadings (1-5 wt. %) by the wetness impregnation method using H_3PO_4 as phosphatation precursor. In addition, samples that were subjected to an extra washing and calcination step, labelled as W_C-PH15 zeolites, were also investigated. The P-modified zeolitic materials were thoroughly characterized to gain insight into the location and type of phosphorus species formed and, ultimately, to correlate structure with performance in the furan aromatization reaction.

XRD experiments of the pristine and simply impregnated PHZSM-5 zeolites revealed that the MFI crystal structure remained almost unchanged, with all the characteristic reflections for an MFI structure being visible. The slight decrease of the diffraction peak intensity seen at low 2θ angles (Figure 3.4a) indicates filling of the pore system by phosphor species after phosphatation. Neither crystalline aluminum phosphate (AlPO) or silicon orthophosphate (SiPO) species were observed in the XRD patterns, suggesting that such species are not formed, at least not in detectable amounts[36].

Physisorption results revealed a linear decrease in surface area (Figure 3.4b) upon increasing phosphorus loading. The decrease in surface area was mostly the result of a decrease in microporous area, as the external surface area remained very similar (~55 m^2/g). This suggests that the deposition of phosphorus species occurred mostly within the micropores, in accordance with the XRD results (Figure 3.4c). Previously, van der Bij *et al.* proposed that the phosphorus species preferentially react with aluminum sites (mostly located within the pores) from the zeolite framework[59]. Upon additional washing and calcination of the PHZSM-5 samples, a considerable increase in BET area and micropore area was seen compared to the non-washed samples, suggesting that washing and calcination is indeed necessary to irreversible deposit the P species[60]. These larger surface area and porosity values reflect the better accessibility of the washed samples compared to the non-washed samples. Additional washing and calcination thus allowed most of the original surface area and porosity of the zeolite materials to be recovered, but as the values do not exceed the original values from the parent zeolite material, none of these steps is thought to induce major desilication or dealumination.

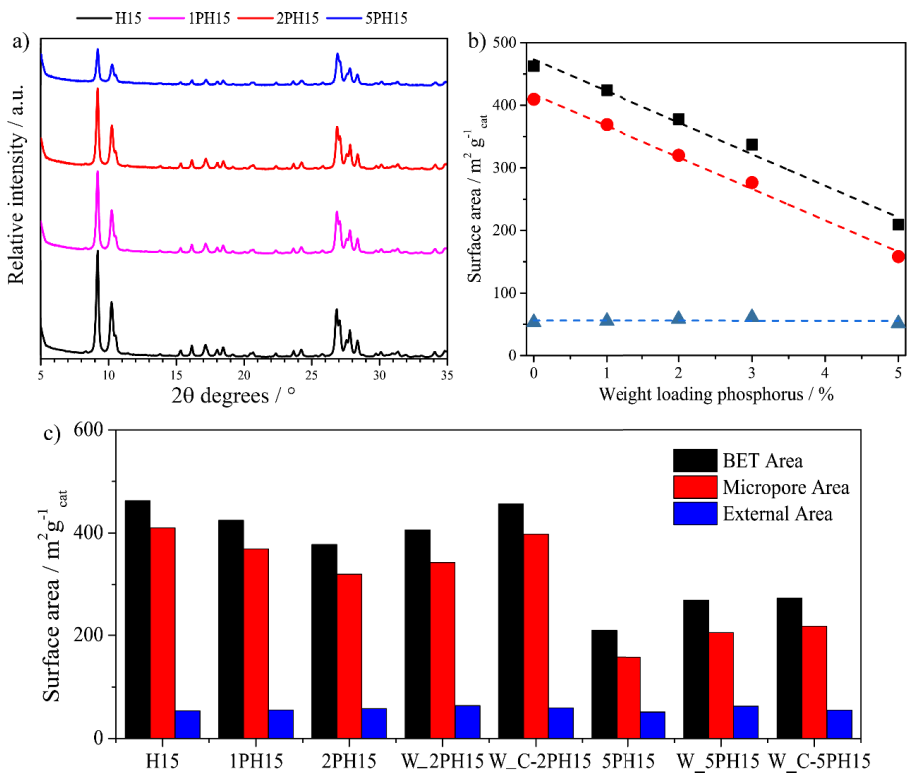

Figure 3.4. (a) X-ray diffraction (XRD) patterns of non-modified and phosphorus-modified HZSM-5 zeolite catalysts. (b) Surface area of the only impregnated PH15 samples and (c) micropore and external surface area obtained from Ar physisorption experiments for several only impregnated phosphorus PH15, washed, and washed and calcined PH15 zeolite samples.

The acidity of the non-modified and phosphorus-modified HZSM-5 zeolites was evaluated by a combination of NH_3-TPD and FT-IR spectroscopy with pyridine as probe molecule. The NH_3-TPD desorption profiles, shown in Figure 3.5a, revealed how by increasing the phosphorus content, the overall acidity gradually decreased (both in terms of the strength and number of the acid sites). High phosphorus loadings (i.e., 5 wt. %), resulted in a further decrease of the acidity as reflected by the broader distribution of weak acid sites and a low amount of strong acid sites. These results might suggest the formation of a new type of acid sites of medium acid strength. In the case of the washed samples (W_2PH15 and W_5PH15), an increase in acidity is observed especially for the strong acid sites, as also previously reported by Blasco *et al.*[21]. They demonstrated that washing with a polar solution could remove part of the phosphorus species leading to partial restoration of strong acidity, indicative of the phosphorus species interacting with the BAS in the first place. This result suggests that the phosphatation process

was partly reversible. The total amount of acid sites and the temperature maxima of the different NH_3-TPD peaks are summarized in Table 3.1.

FT-IR spectroscopy with pyridine as probe molecule allowed us to gain a better understanding of the main interactions between phosphorus species and the MFI structure. By employing pyridine as probe molecule together with FT-IR spectroscopy, BAS and LAS were determined[47]. In Figure 3.5b, the peaks corresponding to BAS (1545 cm^{-1}) and LAS (1455 cm^{-1}) after pyridine adsorption for different phosphorus zeolites are displayed[61]. Among the different washed and unwashed phosphorus samples, an increase in LAS and BAS can be observed, in line with the noted reversibility of the phosphatation process after washing and calcination[36,59]. The amounts of LAS and BAS, as summarized in Table 3.1, showed a decrease of BAS upon the incorporation of phosphorus while at low weight loadings (>1 wt. %), the number of BAS increased. Only for the washed and calcined W_C2PH15 zeolite sample, the number of BAS increased compared to the parent H15 zeolite. This suggests that two phenomena are taking place: the improved accessibility and a higher number of BAS are the result of a decrease of the BAS-P interactions. A similar trend is observed for the concentration of LAS, which increases slightly more after the washing and subsequent calcination steps. As mentioned in literature, a hydrothermal treatment of a HZSM-5 zeolite in the presence of phosphoric acid leads to bond breaking at the Si-O-Al sites, causing an increase in the degree of partial zeolite dealumination[36]. Despite of the differences in the number of acid sites obtained by each technique used to determine acidity, the acidity results obtained from pyridine probed FT-IR follow the same trends observed in the NH_3-TPD analyses.

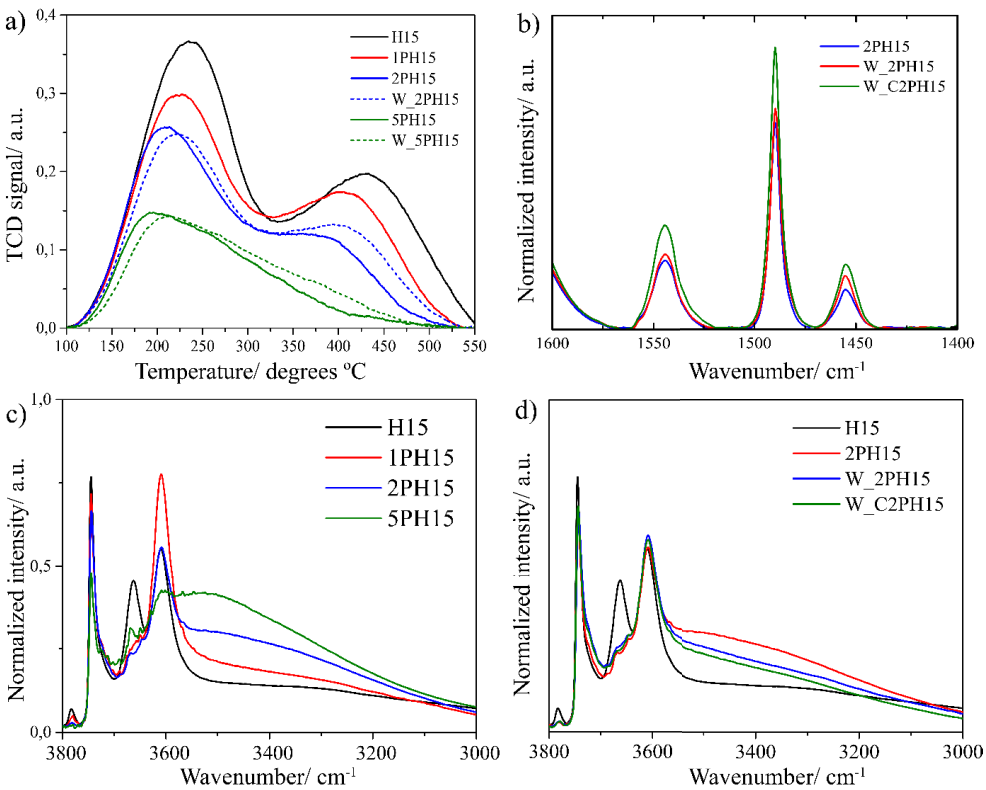

Figure 3.5. (a) Profiles obtained with temperature programmed desorption (TPD) with NH_3 as probe for different PHZSM-5 zeolites. Analysis of the number of acid sites (BAS and LAS) by (b) FT-IR spectroscopy with pyridine as probe for 2% phosphorus HZSM-5 zeolites before and after washing and calcination. The FT-IR vibrations from the silanol region of the different PHZSM-5 samples (c and d) after drying and activating them at 550 °C for 2 h under high vacuum.

The OH-stretching region (4000 cm^{-1}-3000 cm^{-1}) is considered of interest for evaluating the P-MFI interactions since noticeable, diagnostic differences can be observed (Figure 3.5c and 3.5d). The FT-IR spectrum of parent H15 zeolite shows the main characteristic vibrations; the band at 3610 cm^{-1} is assigned to bridging hydroxyls or Brønsted acid sites (BAS); 3660 and 3780 cm^{-1} to extra-framework aluminum (EFAl, Al-OH) and partially dealuminated aluminum species (Al(V)), respectively; and 3745 cm^{-1} is assigned to silanol groups on the external surface of the zeolite crystals. Upon incorporation of phosphorus, the overall intensities dropped within the hydroxyl region, while a new P-OH vibration was now detected at 3675 cm^{-1} in all phosphorous-modified samples, a band that shifted towards lower wavenumbers (3669 cm^{-1} for 5PH15 zeolite) with increasing phosphorus content[21,44]. The intensity decreases of the 3610 cm^{-}

[1] peak with increasing phosphorus loading indicates the decrease of the number of BAS. At high phosphorus loadings (i.e., 5 wt. %), the peak intensities corresponding to free EFAl and partial EFAl species decreased considerably, indicating the formation of AlPO species. After washing and calcining the 2PH15 sample, the overall peak intensities remained mostly unchanged except for the peak at 3610 cm^{-1} which increased slightly in intensity (Figure 3.5d). Thus, the W_ 2PH15 and W_C-2PH15 samples appear to have a higher acidity. In addition, these results suggest that the initial AlPO and phosphorus species located on the external silanol species present within the 2PH15 sample, remain intact after washing and calcination.

Table 3.1. Physicochemical properties of phosphorus-modified HZSM-5 zeolites investigated in this work.

	P content[a] wt. %	**Total acid sites[b]** µmol g^{-1}_{cat}	**Weak acid sites[b]** °C	**Strong acid sites[b]** °C	**Lewis acid sites[c]** µmol g^{-1}_{cat}	**Brønsted acid sites[c]** µmol g^{-1}_{cat}
H15	-	101	236	432	37	104
1PH15	1.04	71	225	404	45	118
2PH15	1.85	54	211	385	31	80
W_2PH15	1.29	55	224	402	35	89
W_C-2PH15	1.40	n.a.	n.a.	n.a.	43	116
5PH15	n.a.	27	195	-	10	34
W_5PH15	n.a.	29	212	-	19	60

For a better insight into the phosphorus-zeolite interactions, solid-state NMR experiments were carried out on a selection of phosphorus-modified zeolites. The ^{29}Si ssNMR spectra given in Figure 3.6a, show two peaks for all samples with maxima at -105 and -112 ppm, which correspond to Q^3 type Si species with framework aluminum ($Si(OSi)_3(OAl)$) and Q^4 ($Si(OSi)_4$) type sites, respectively[36,62]. The incorporation of phosphorus resulted in a decrease in intensity of the Q^3 peak, suggesting the direct formation of P-zeolite interactions with framework Al. A small decrease and shift towards lower chemical shifts was observed for the Q^4 peaks, which is attributed to a distortion in the tetrahedral silicon chemical environment due to the close proximity of phosphorus[36,63]. No Si-O-P interactions are expected for any of the samples, given the absence of the -214 ppm peak in the ^{29}Si ssNMR spectra (inset in Figure 3.6a).

In Figure 3.6b, the ^{27}Al MAS ssNMR spectra are shown. For the parent H15 zeolite, two main NMR peaks are observed; a peak at 55 ppm, which corresponds to tetrahedrally coordinated aluminum in the zeolite framework (TFAl), and another peak at 0 ppm, which corresponds to octahedrally coordinated extra-framework aluminum (EFAl)[62,64]. After the incorporation of phosphorus, the overall peak intensities for the Al(IV) and Al(VI) species decreased and new peaks at 40 and -10 ppm arose, which are assigned to distorted TFAl and AlPO species, respectively[26]. Washing and calcination steps resulted in a major decrease in intensity for all the NMR peaks, suggesting that the excess of phosphorus originally located in close proximity to TFAl sites and the AlPO species were partially removed.

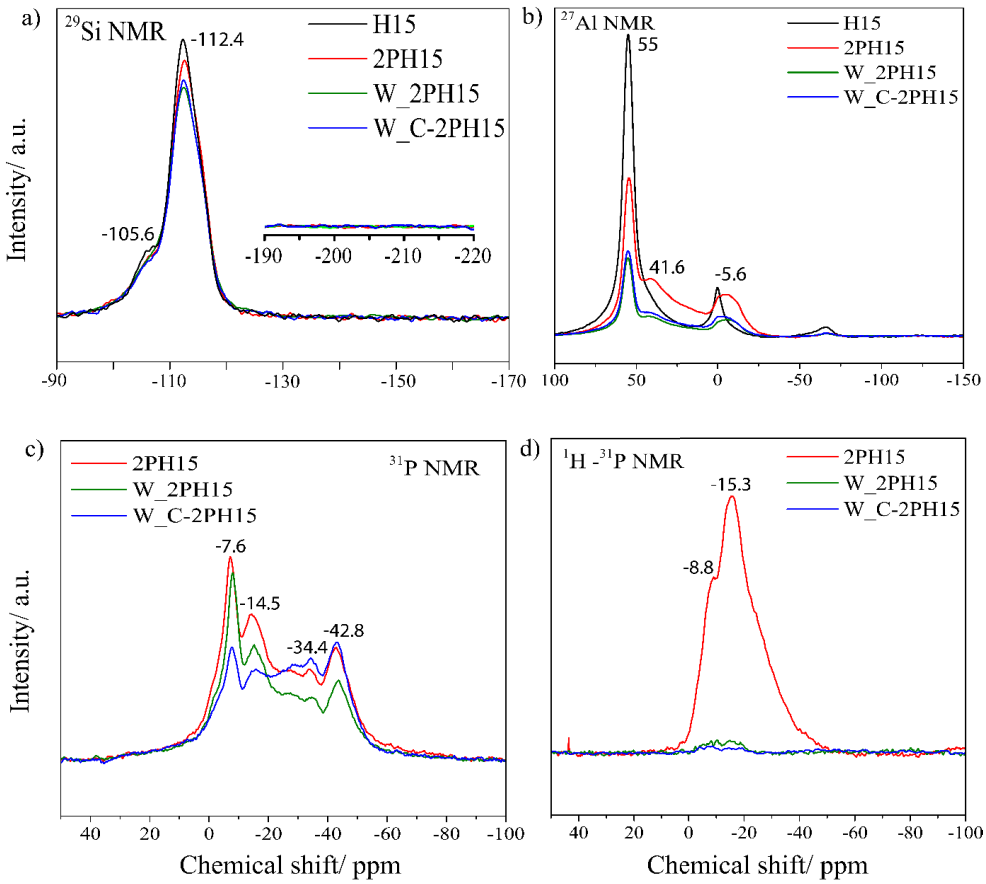

Figure 3.6. Solid-state (a) ^{29}Si nuclear magnetic resonance (NMR), (b) 1D ^{27}Al NMR, (c) ^{31}P NMR and cross polarization (CP) ^{1}H-^{31}P NMR spectra of 2PH15 zeolites as synthesized (red line), after washing (green line), and after calcination (blue line).

2D ^{27}Al MQ-MAS ssNMR spectra provided further insight into the Al interaction (Figure 3.7). Two symmetric NMR peaks, ascribed to tetra- and octahedral aluminum sites, are seen for all the samples under study. With the addition of 2 wt. % phosphorus to the system, (2P[Z], where [Z] = H15), a third NMR peak is observed, which corresponds to distorted TFAl species (40 ppm, 60ppm). This shift indicates a stronger quadrupolar environment, which arises from the presence of phosphorus next to the TFAl species in the zeolite. A shift is also observed for the O_h Al species due to the formation of AlPO species. Upon washing, no major differences in the ^{27}Al MQ-MAS NMR spectrum were observed, suggesting that the phosphorus species being washed out had almost no interaction with either O_h or T_d aluminum sites. However, after calcination, a major shift of the distorted TFAl species is seen (±35 ppm, 60 ppm), suggesting that the aluminum is influenced by a stronger quadrupole environment due to the increase of phosphorus in the vicinity. This stronger quadrupole environment results in a stronger interaction between phosphorus and the zeolite framework.

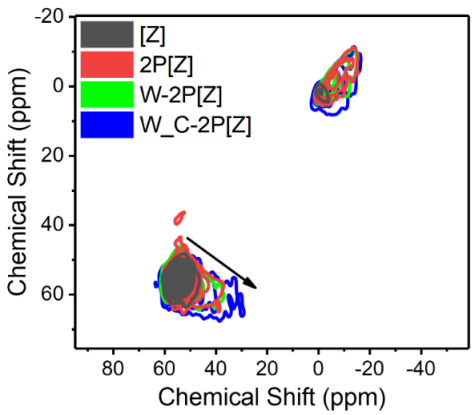

Figure 3.7. 2D ^{27}Al multi-quantum (MQ) magic angle spinning (MAS) nuclear magnetic resonance (NMR) spectra of fresh HZSM-5 (dark grey), 2% PHZSM-5 (red), and 2% PHZSM-5 washed (green) and calcined samples (blue).

The ^{31}P ssNMR spectra for the different phosphorous-modified zeolites are shown in Figure 3.6c. Various assignments can be found in the literature but the exact nature of the different P species contributing to the spectra is still under discussion. It is noteworthy to mention that the type and amount of species formed is strongly dependent on the synthesis method employed[65]. The ^{31}P chemical shifts values of different phosphorus species, together with their chemical structure, are depicted in Figure 3.8. A NMR peak at -7 ppm present in all NMR spectra is assigned to the end groups in pyrophosphate species[65], while a shoulder present at -1 ppm

corresponds to orthophosphoric acid groups[36]. The presence of larger phosphorus species, such as triphosphates or phosphorus pentoxide, can be confirmed by the NMR peaks at -14.5 ppm and -42.8, respectively. The former peak is assigned to middle chain phosphorus groups, while the latter peak is assigned to branched polyphosphates[36,65]. Within the -30 and -50 ppm region, different spectral assignments have been proposed in the literature[29,36,65,66]. For example, silicon phosphate species (i.e., silicon hydrogen orthophosphate or silicon hydrogen tripolyphosphate) proposed to appear at -35 ppm, however their presence cannot be assured from our experiments[36,65]. Tetrahedral phosphates[67] or phosphate ligands bound to aluminum[23,68] are observed at -29 ppm, while AlPO appear at -32 ppm[27]. ^{1}H-^{31}P CP ssNMR experiments of the 2PH15 sample show two peaks centered at -8.8 and -15.3 ppm, which are assigned to interactions of phosphate groups from polyphosphate species attached to Brønsted acid sites (Figure 3.6d). This confirms the interaction of a phosphorus species without direct binding to framework aluminum, which according to the model suggested by Caro *et. al*[29], the polyphosphate is protonated by the acid site.

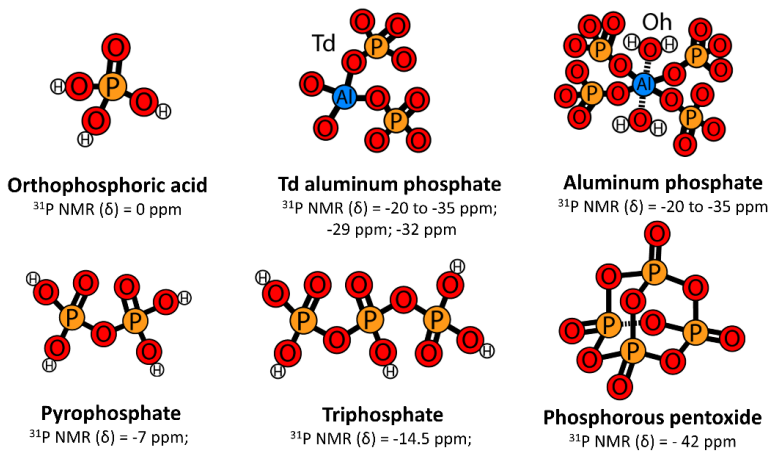

Figure 3.8. Representation of some phosphorus species (with their respective ^{31}P chemical shifts) formed after phosphatation of HZSM-5 zeolite. All assignments are based on different references.

Washing and calcination affected the phosphorous species present, as can be seen in the ^{31}P ssNMR spectra. After washing, the overall spectral intensity decreased, especially for small phosphate species such as pyrophosphate and triphosphate, species known to be soluble in water. Furthermore, the intensity of the NMR peak centered at -42.8 ppm, which corresponds to condensed polyphosphate species also decreased considerably. This decrease coincides with a simultaneous increase of a shoulder located at 0 ppm, which corresponds to phosphoric acid

species, indicating the removal due to hydrolysis of these condensed polyphosphate species to phosphoric acid species (Figure 3.6c). Previous investigations reported that highly condensed phosphates, such as phosphorus pentoxide or phosphorus trioxide, are known to be easily hydrolyzed in the presence of water, leading to monomeric orthophosphate species (Figure 3.9b)[69]. Strikingly, after calcination, the NMR peaks at -34.4 and -42.8 ppm have a slightly higher intensity comparable to those of the unwashed 2PH15 zeolite sample, suggesting that new phosphorus species attached to the zeolite framework have been formed during the extra hydrothermal treatment, as observed in the MQ-MAS NMR results. After the extra washing and subsequent calcination steps, a stronger interaction between phosphorus species and the zeolite framework is formed. However, smaller phosphorus species, such as orthophosphoric acid, pyrophosphate and triphosphate species appearing at 0 and -7.6 and -14.5 ppm decreased in intensity. These evidences suggest that part of these species are being removed from the intra-zeolitic framework allowing for a better accessibility. Very low intensity spectra resulted after ^{1}H-^{31}P CP ssNMR experiments of the washed and calcined samples. This prompt decrease in spectral intensity suggests that the interaction between Brønsted acid sites and phosphorus decreased, leading to a restoration of the BAS, observations that are in accordance with NH_3-TPD and pyridine FT-IR experiments.

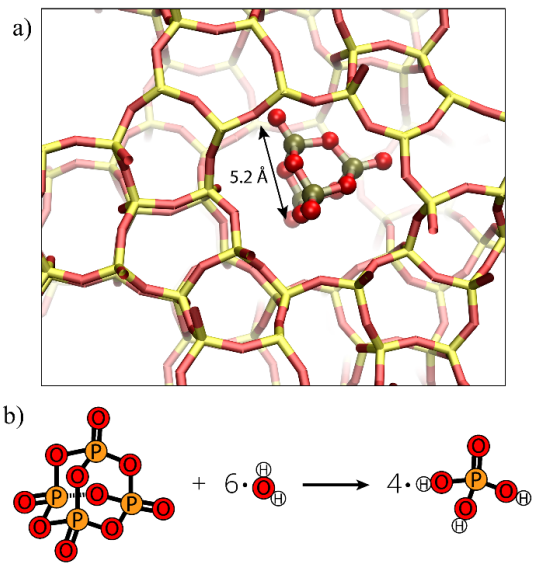

Figure 3.9. (a) Representation of the intersection of an MFI cluster with phosphorus pentoxide molecule as obtained by density functional theory (DFT) simulations. (b) Schematic representation of the exothermal hydrolysis (ΔH_r = -177 kJ/mol) of phosphorus pentoxide during the washing step.

Density functional theory (DFT) simulations allowed us to further investigate whether the presence and adsorption of phosphorus pentoxide species is possible within an MFI structure (Figure 3.9a). The adsorption of phosphorous pentoxide in silicalite-1 is a very exothermic process with adsorption energy of -169 kJ/mol. This suggests that phosphorous pentoxide can be easily formed inside the zeolite channels without steric constraints. To further support this hypothesis the ground state optimized geometries were used to estimate the phosphorus pentoxide dimensions. The molecule size was approximated by a sphere with a diameter equal to the distance between corner oxygen atoms (Figure 3.9a). The measured diameter was 5.2 Å which is about 1 Å less than the theoretically predicted maximum diameter of sphere that can be included within MFI zeolite (6.3 Å). Therefore, we can conclude that phosphorus pentoxide can be formed within the channels of zeolite ZSM-5, and it seems that it is one of the major phosphorus species present within the intra-zeolitic framework together with the phosphate aluminum bound species (bound to partially dislodged Al from framework and with extra-framework Al).

3.3.2 Catalyst Testing

Building on the work presented in Chapter 2 of this PhD Thesis, the aromatization of the furan derivatives MF and DMF was investigated using the PHZSM-5 zeolites as catalysts. The effect of ethylene co-feeding was also investigated to study the effect of phosphatation on catalyst performance, in particular BTX yield and selectivity.

Aromatization of MF under the reaction conditions specified in section 3.2.3 using phosphorus-modified HZSM-5 zeolites as catalysts yielded BTX as products with a higher selectivity to alkylated aromatics compared to the benchmark, unmodified HZSM-5. Conversion of MF over 125 min of reaction is shown for each catalyst in Figure 3.10a. Lower conversion was obtained for the W_C-2PH15 than for the H15 catalyst, while a similar deactivation rate was observed for both catalysts over time. The gradual drop in conversion of MF suggest a first order rate of deactivation. This rate of deactivation is similar for both catalysts, showing that the incorporation of phosphorus as promotor did not decrease deactivation.

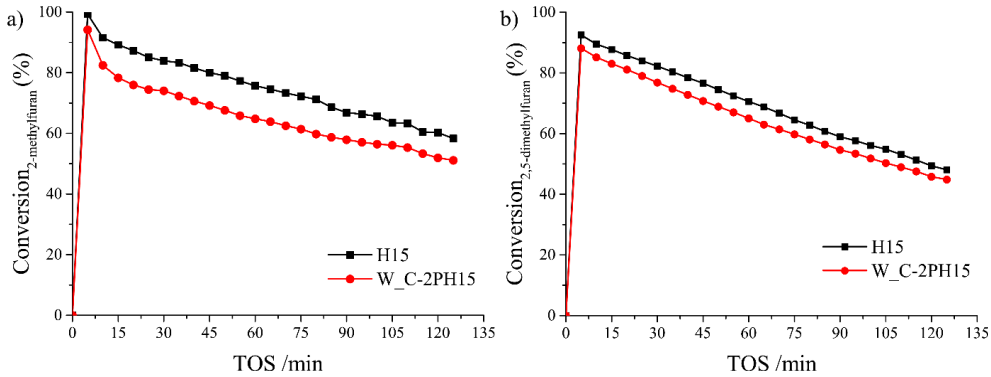

Figure 3.10. Conversion of (a) 2-methylfuran (MF) and (b) 2,5-dimethylfuran (DMF) only at different time-on-stream (TOS) at 500 °C using various HZSM-5 zeolites as catalysts.

The selectivity to mono-aromatics, determined at 75% conversion, was very similar for the H15 and W_C-2PH15 zeolite catalyst, ~ 40% BTX selectivity. The BTX distribution did show a difference between the two catalysts, however, with the latter being slightly more selective for alkylated aromatics such as toluene and xylenes, despite its lower acidity compared to the parent H15 zeolite (see Figure 3.11a).

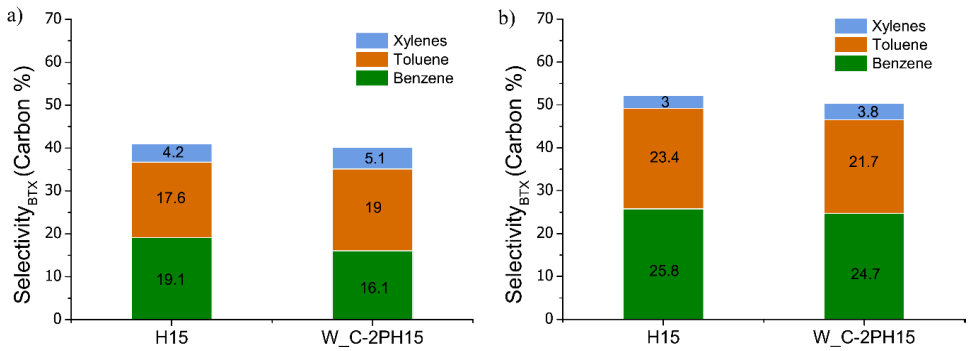

Figure 3.11. Selectivity towards Benzene-Toluene-Xylenes (BTX) obtained during the aromatization of (a) 2-methylfuran (MF), and (b) 2,5-dimethylfuran (DMF), at a conversion level of 75% for both reagents.

The obtained selectivities to benzene, toluene and xylenes in the conversion of MF and DMF using PHZSM-5 zeolites are depicted as function of time in Figure 3.12 and 3.13, respectively. BTX selectivity during the conversion of MF as function of time on stream is shown in Figure 3.12. Overall, a higher selectivity is displayed to alkylated aromatics by the W_C-2PH15

catalyst as function of time-on-stream (Figure 3.12b, 3.12c and 3.12d), while benzene selectivity is higher for the H15 catalyst up to 125 min reaction time (Figure 3.12a). After 90 min reaction, selectivity to toluene and *m*-/*p*-xylenes became similar to the selectivity given by the H15 catalyst, whilst the selectivity to *o*-xylene remained higher than when using pristine H15 zeolite catalysts. This higher selectivity towards alkylated aromatics and lower conversion obtained by W_C-2PH15 zeolite catalyst suggests that a combination of both lower BAS together with new medium strength acid sites formed by the incorporation of phosphorous is optimal for (di)alkylated aromatics production from MF.

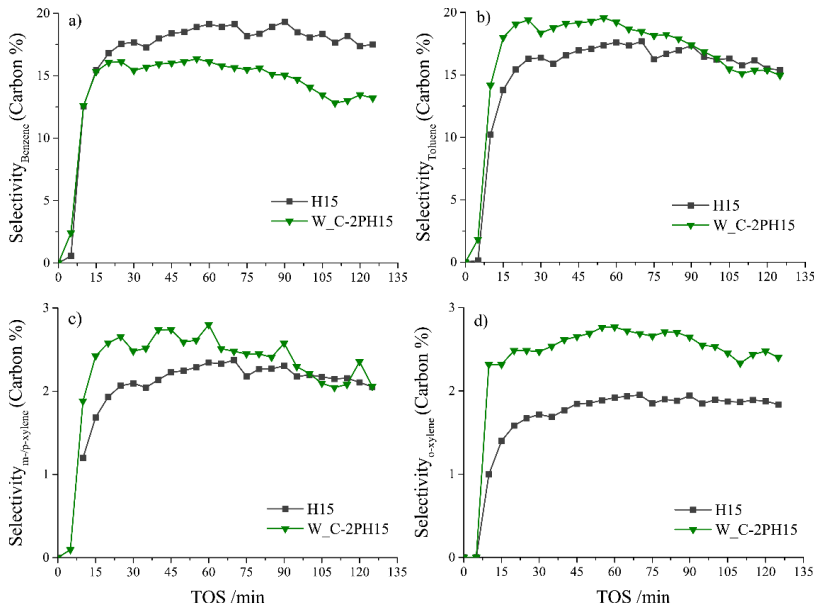

Figure 3.12. Selectivity toward (a) benzene, (b) toluene, (c) *m*-, *p*-xylene and (d) *o*-xylene obtained during the aromatization of 2-methylfuran (MF) for different time-on-stream (TOS) using H15 and W_C-2PH15 zeolites as catalysts at 500 °C for 125 min.

To further compare the catalytic performance of W_C-2PH15 and H15 zeolite catalysts, the aromatization of DMF was also investigated. As in the aromatization of MF, conversion of DMF is lower when using W_C-2PH15 than when using H15 as catalyst (Figure 3.10b). In this case, the gradual decrease in conversion again showed first order behavior. Deactivation to be similar for both catalysts under the same reaction conditions. Selectivity to BTX determined at 75% conversion shown in Figure 3.11b displayed the highest selectivity to BTX when using the H15 zeolite as catalyst (52.2% vs 50.2% for the W_C-2PH15 zeolite). Additionally, BTX selectivity for DMF differed from the one for MF. The selectivity to benzene and toluene with

W_C-2PH15 zeolite as catalyst was lower than with the benchmark catalyst as function of time-on-stream (Figure 3.13a and 3.13b). However, selectivity to xylenes (*m*-, *p*- and *o*-xylene), is higher for the W_C-2PH15 zeolite (Figure 3.13c and 3.13d). These differences in selectivity between MF and DMF conversion can be ascribed to the size and carbon number of each starting reagent. It is known from literature, that DMF is more prone to yield xylenes than MF[7]. Notably, the amount of propylene detected in the products outlet was qualitatively higher when using phosphorus-modified zeolites than when using H15 zeolite as catalyst, (the small olefins and non-condensable gases were not quantified).

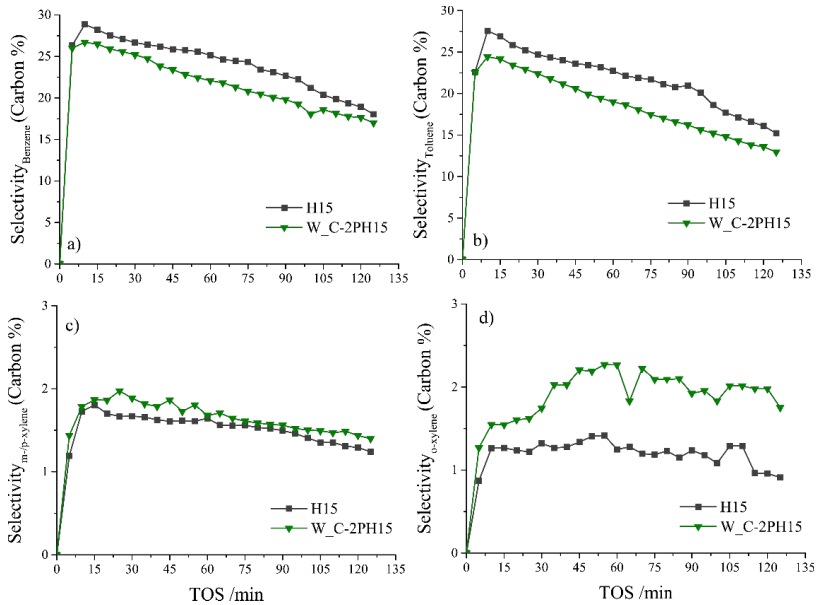

Figure 3.13. Selectivity towards (a) benzene, (b) toluene, (c) *m*-, *p*-xylene and (d) *o*-xylene obtained during the aromatization of 2,5-dimethylfuran (DMF) as different time-on-stream (TOS) using H15 and W_C-2PH15 zeolites as catalysts at 500 °C for 125 min.

To investigate if the aromatization performance can be further improved during the conversion of MF and DMF, ethylene co-feeding experiments were also performed. Previous investigations demonstrated that by co-feeding olefins production of alkylated aromatics can be boosted[9,70]. Conversion for MF is higher in presence of ethylene and the deactivation rate is slower for almost all cases (Figure 3.14a). Regarding the aromatization of DMF in presence of ethylene (Figure 3.14b), conversion of DMF is higher than during the conversion of DMF only for all catalysts used. Furthermore, the deactivation rate is slower, with conversion remaining above

70% for up to 125 min. During both MF and DMF conversion, the 2PH15 deactivation rate is slightly faster than for the other phosphorus-modified zeolites.

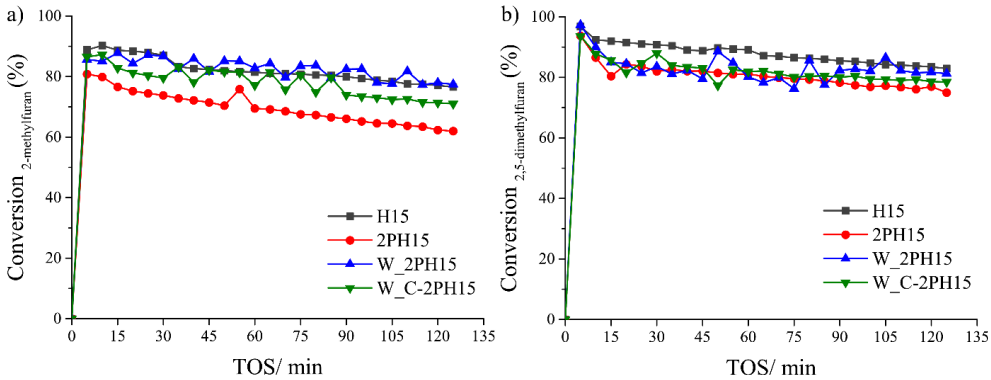

Figure 3.14. Conversion of (a) 2-methylfuran (MF) and (b) 2,5-dimethylfuran (DMF) with ethylene co-feeding at different time-on-stream (TOS) at 500 °C using various HZSM-5 zeolites as catalysts.

The highest selectivity to BTX during the aromatization of MF and ethylene (43%) was obtained with the H15 catalyst (Figure 3.15a). When comparing the different phosphorous-modified materials, the washed and calcined W_C-2PH15 catalyst gave the highest selectivity to BTX (33.3%). During MF aromatization in presence of ethylene, only xylenes selectivity is higher compared to the MF experiments without ethylene for all modified and non-modified PHZSM-5 zeolites. Total selectivity to BTX during the aromatization of DMF with ethylene co-fed (Figure 3.15b) was slightly higher (55%) than without ethylene (52.2%). Also, in this case, the highest BTX selectivity was exhibited by the H15 zeolite catalyst. Among the phosphorus-modified materials, washed W_2PH15 zeolite displayed the highest BTX selectivity (42.5%). The performance of the different phosphorus-modified zeolite catalysts (impregnated, washed, and washed and calcined) was therefore very similar in the aromatization of furan derivatives with ethylene co-feeding.

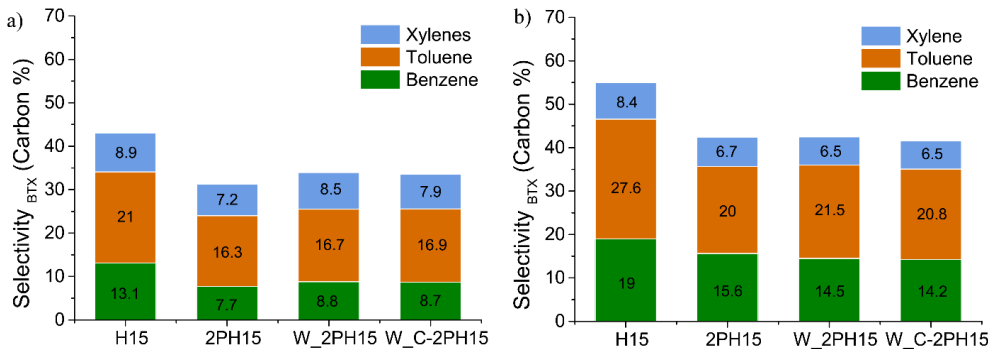

Figure 3.15. Selectivity to Benzene-Toluene-Xylenes (BTX) obtained during the conversion of (a) 2-methylfuran (MF) (at a conversion level of 80%) with ethylene co-feeding, and (b) 2,5-dimethylfuran (DMF) (at conversion level of 90%) with ethylene co-feeding.

Selectivity to BTX during the conversion of MF with the phosphorus-modified zeolites as catalysts (synthesized, washed, and calcined) is displayed in Figure 3.16 as a function of time. The highest selectivity to benzene (Figure 3.16a) was obtained when using the H15 zeolite catalyst, while slightly higher selectivity to toluene (Figure 3.16b) was given by 2PH15 at longer reaction times (75 min). Additionally, small olefins such as propylene, ethylene, and non-condensable gases such as methane, were detected in the outlet stream. Based on our work, the addition of phosphorus seems to be detrimental for the benzene selectivity during the aromatization of MF with ethylene co-feeding, possibly due to the low concentration of strong BAS. For toluene, we believe that the combination of reduced BAS concentration together with a stronger effect of confinement caused by the presence of condensed phosphorous species, are key parameters that enhance alkylation reactions. Selectivity to xylenes during co-feeding of ethylene was still better when using the parent H15 zeolite as catalyst (Figure 3.16c and 3.16d). That xylenes are produced less during the co-feeding experiments could suggest that the presence of phosphor hampers the formation of dialkylated aromatics due to severe confinement[19].

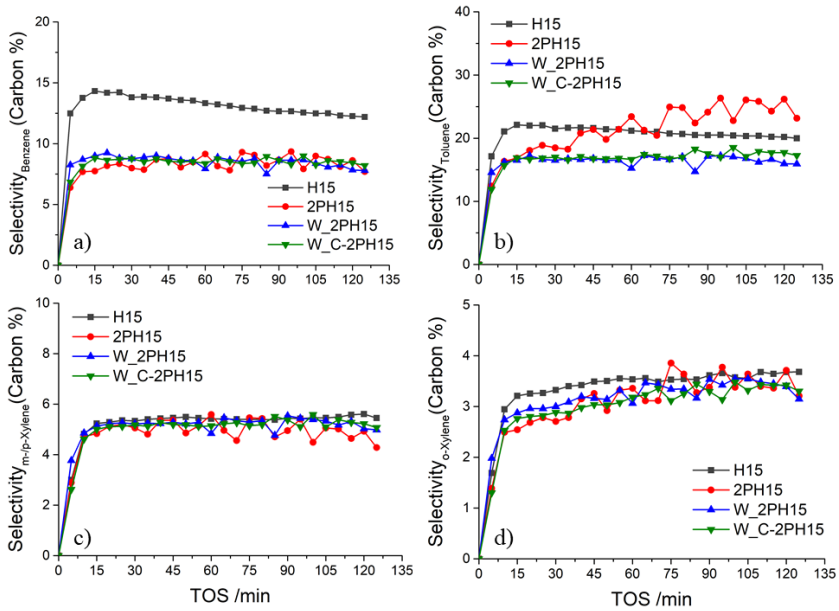

Figure 3.16. Selectivity towards (a) benzene, (b) toluene, (c) *m*-, *p*-xylene and (d) *o*-xylene at different time-on-stream (TOS) using various HZSM-5 zeolites as catalysts obtained during the conversion of 2-methylfuran (MF) with ethylene co-feeding at 500 °C.

During the aromatization of DMF with ethylene co-feeding, a similar trend was observed in BTX selectivity as when using MF and ethylene; the phosphorus-modified catalysts performed less well than the benchmark catalyst. Still xylenes selectivity is better when co-feeding ethylene, but H15 zeolite gave also the highest BTX selectivity during ethylene co-feeding, as shown in Figure 3.17, which shows BTX selectivity as function of time-on-stream. Seemingly, these investigations indicate that the performance of PHZSM-5 materials in gas phase aromatization while co-feeding ethylene is neither better or comparable to what has been proposed in literature for similar reaction processes in the liquid phase that used phosphorus as promotor in zeolite catalysts[19].

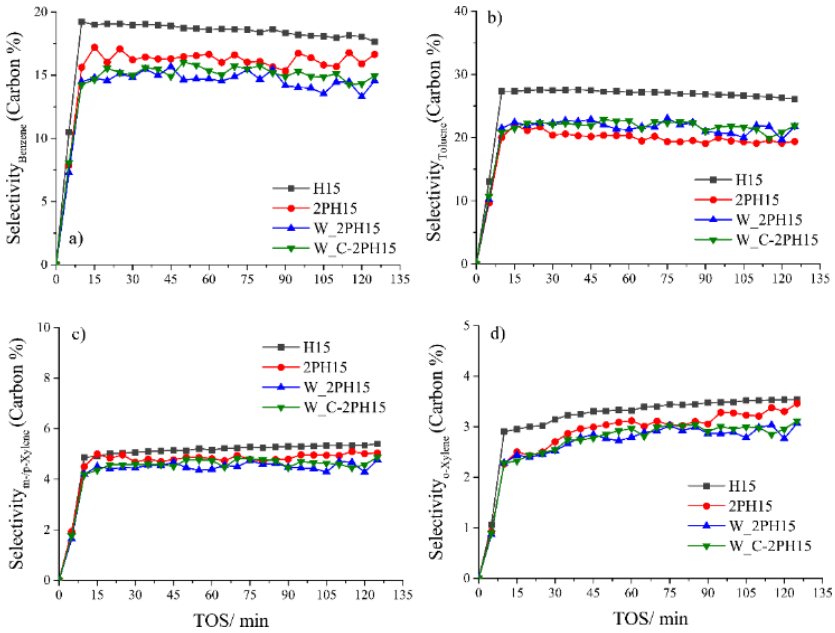

Figure 3.17. Selectivity towards (a) benzene, (b) toluene, (c) *m*-, *p*-xylene and (d) *o*-xylene at different time-on-stream (TOS) using various HZSM-5 zeolites as catalysts obtained during the conversion of 2,5-dimethylfuran (DMF) with ethylene co-feeding at 500 °C.

The carbon mass balances for the different PHZSM-5 zeolites, shown in Figure 3.18, were calculated after 125 min reaction of aromatization of both MF and DMF with ethylene co-feeding. BTX yields for the conversion of MF with ethylene were only better when using 2PH15 catalysts, and the lowest amount of coke deposits was observed with the W_2PH15 (13%) and W_C-2PH15 (15.2%) catalysts (Figure 3.18a). As previously mentioned, rather high amount of non-condensable gases were formed when using W_2PH15 and W_C-2PH15 catalysts when compared to the non-promoted H15 zeolite catalyst, which is in accordance to previous reports in literature[21,39,71,74], which the presence of phosphor is widely known to be an additive that favors cracking. For DMF (Figure 3.18b), a higher fraction of non-condensable gases was obtained with the phosphorous modified catalyst, especially for the W_2PH15 catalysts (36%).

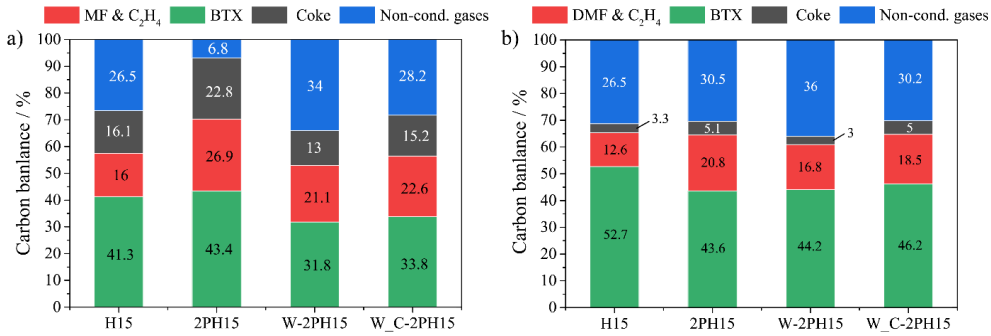

Figure 3.18. Carbon balance obtained after the conversion of (a) 2-methylfuran (MF) and (b) 2,5-dimethylfuran (DMF) with ethylene co-feeding at 500 °C after 125 min reaction.

Upon the introduction of phosphor in the HZSM-5 zeolites, overall BAS acidity decreased while with the subsequent extra washing and calcination steps, BAS acidity was partially restored. The strong dehydration character of phosphorus-promoted zeolites previously shown in the conversion of oxygenated compounds[40,71], led us to expect that these catalysts would also show improved performance during furan aromatization. However, when comparing their catalytic performance during the aromatization of MF and DMF only, the overall BTX selectivity obtained was lower when compared with the pristine H15 zeolite catalyst. Only, the selectivity to alkylated aromatics was higher when the washed and calcined W_C-2PH15 zeolite was used as catalyst. An even higher decrease in the aromatization rates was observed when using phosphorous-modified zeolites as catalysts during the co-feeding experiments. We believe that the presence of phosphorus species inside the zeolite channels together with the lower concentration of BAS even after the extra washing and calcination restoration, hampers aromatization, leading to enhanced production of propylene instead, as reported previously [39,72,73]. Furthermore, the partial blockage of the pores and channels of the zeolite by the phosphorus, as observed in the Ar physisorption experiments, possibly also contributes to the low aromatization rates.

3.4 Conclusions

A series of phosphorus-modified zeolites with different phosphorus loadings (1-5 wt. %) have been synthesized by the wetness impregnation method using H_3PO_4 as phosphorus precursor. Extra washing and calcination steps after the first hydrothermal treatment restores part of the acidity, confirming that phosphatation is partially reversible, as revealed by NH_3-TPD and FT-

IR spectroscopy with pyridine as probe molecule. Extensive characterization of the phosphorus-modified zeolite materials gave us insight into the phosphorus specialization and location within the intra-zeolitic framework. Crystallinity of the zeolite crystals remained unchanged upon the impregnation of phosphor, while porosity linearly decreased upon increasing P loading, indicating that the addition of phosphorus species occurred mainly into the micropores. Same was observed for acidity, especially for BAS, which also dropped upon increasing the P loading. The extra washing and calcination steps had a positive effect on acidity and accessibility. As demonstrated by the ssNMR experiments, upon washing and calcination, several phosphate species that were not directly interacting with the intra-zeolitic framework were removed, resulting in a larger accessibility and acidity, as shown in the ^{31}P MAS ssNMR spectra. These changes allowed for more acidic phosphorus-containing zeolites with a higher accessibility since the condensed and large phosphorus species, such as phosphorus pentoxide, were hydrolyzed and removed. Different phosphorus-zeolite interactions were also identified by ^{31}P ssNMR and ^{27}Al ssNMR. Species involving a partially dislodged aluminum site upon the incorporation of phosphorus or totally extra-framework phosphorus-aluminum species (AlPO) were also identified.

The catalytic performance of the phosphorous-promoted zeolites was explored in MF and DMF aromatization, and overall performance to BTX did not exceed the pristine H15 performance. Instead, the P promoted catalysts showed higher yields of non-condensable gases, such as propylene and ethylene. Only a slightly higher selectivity to (di)alkylated aromatics was seen for the W_C-2PH15 as catalyst compared to the benchmark H15 zeolite. Also, in the co-feeding experiments, the use of PHZSM-5 catalyst did not improve BTX formation. A smaller amount of coke was produced during the conversion of MF with ethylene co-feeding when using the W_2PH15 and W_C-2PH15 catalysts, while during DMF aromatization with ethylene co-feeding, a higher amount of non-condensable gases was obtained with the W_2PH15 catalysts after 125 min reaction. This suggests that the formation of aromatics from both MF and DMF with ethylene co-feeding does not proceed solely via a Diels-Alder cycloaddition mechanism. The phosphorus-modified zeolites thus showed enhanced alkylated aromatics formation during the aromatization of MF and DMF only, i.e. without ethylene co-feeding. According to literature and based on our results, the presence of phosphor increased cracking rates, as higher formation of non-condensable gases, such as propylene, ethylene and methane, were detected. This boosted the formation of alkylated aromatics. The anticipated positive effect of P-promotion seen in liquid phase catalytic conversions could thus not be translated to gas phase

furan aromatization. Further studies focused on the optimization of the phosphorus loading and speciation may still lead to improved catalyst performance.

3.5 Acknowledgements

Davey de Waard (Utrecht University, UU) is thanked for his contribution during the development of this project, while Alessandra Lucini Paioni (UU) is acknowledged for carrying out the solid-state NMR experiments. Furthermore, Katarina Stanciakova (UU) is thanked for performing the DFT simulations, while Dennie Wezendonk (UU) is acknowledged for performing the TGA-MS measurements.

3.6 References

(1) Alipour, S.; Omidvarborna, H.; Kim, D.-S. A Review on Synthesis of Alkoxymethyl Furfural, a Biofuel Candidate. *Renew. Sustain. Energy Rev.* **2017**, *71*, 908–926. https://doi.org/10.1016/J.RSER.2016.12.118.

(2) Lange, J.-P.; van der Heide, E.; van Buijtenen, J.; Price, R. Furfural-A Promising Platform for Lignocellulosic Biofuels. *ChemSusChem* **2012**, *5*, 150–166. https://doi.org/10.1002/cssc.201100648.

(3) Williams, C. L.; Chang, C. C.; Do, P.; Nikbin, N.; Caratzoulas, S.; Vlachos, D. G.; Lobo, R. F.; Fan, W.; Dauenhauer, P. J. Cycloaddition of Biomass-Derived Furans for Catalytic Production of Renewable *p*-Xylene. *ACS Catal.* **2012**, *2*, 935–939. https://doi.org/10.1021/cs300011a.

(4) Huang, R.; Qi, W.; Su, R.; He, Z. Integrating Enzymatic and Acid Catalysis to Convert Glucose into 5-Hydroxymethylfurfural. *Chem. Commun.* **2010**, *46*, 1115–1117. https://doi.org/10.1016/j.renene.2018.02.085.

(5) Cheng, Y.-T.; Huber, G. W. Chemistry of Furan Conversion into Aromatics and Olefins over HZSM-5: A Model Biomass Conversion Reaction. *ACS Catal.* **2011**, *1* , 611–628. https://doi.org/10.1021/cs200103j.

(6) Cheng, Y. T.; Wang, Z.; Gilbert, C. J.; Fan, W.; Huber, G. W. Production of *p*-Xylene

from Biomass by Catalytic Fast Pyrolysis Using ZSM-5 Catalysts with Reduced Pore Openings. *Angew. Chem. Int. Ed.* **2012**, *51*, 11097–11100. https://doi.org/10.1002/anie.201205230.

(7) Uslamin, E. A.; Kosinov, N. A.; Pidko, E. A.; Hensen, E. J. M. Catalytic Conversion of Furanic Compounds over Ga-Modified ZSM-5 Zeolites as a Route to Biomass-Derived Aromatics. *Green Chem.* **2018**, *20*, 3818–3827. https://doi.org/10.1039/C8GC01528G.

(8) Foster, A. J.; Jae, J.; Cheng, Y. T.; Huber, G. W.; Lobo, R. F. Optimizing the Aromatic Yield and Distribution from Catalytic Fast Pyrolysis of Biomass over ZSM-5. *Appl. Catal. A Gen.* **2012**, *423–424*, 154–161. https://doi.org/10.1016/j.apcata.2012.02.030.

(9) Cheng, Y.-T.; Huber, G. W. Production of Targeted Aromatics by Using Diels–Alder Classes of Reactions with Furans and Olefins over ZSM-5. *Green Chem.* **2012**, *14*, 3114–3125. https://doi.org/10.1039/c2gc35767d.

(10) Chang, C.-C.; Green, S. K.; Williams, C. L.; Dauenhauer, P. J.; Fan, W. Ultra-Selective Cycloaddition of Dimethylfuran for Renewable p-Xylene with H-BEA. *Green Chem.* **2014**, *16*, 585–588. https://doi.org/10.1039/C3GC40740C.

(11) Corma, A.; Huber, G. W.; Sauvanaud, L.; O'Connor, P. Processing Biomass-Derived Oxygenates in the Oil Refinery: Catalytic Cracking (FCC) Reaction Pathways and Role of Catalyst. *J. Catal.* **2007**, *247*, 307–327. https://doi.org/10.1016/j.jcat.2007.01.023.

(12) Huber, G. W.; Iborra, S.; Corma, A. Synthesis of Transportation Fuels from Biomass: Chemistry, Catalysts, and Engineering. *Chem. Rev.* **2006**, *106*, 4044–4098. https://doi.org/10.1021/cr068360d.

(13) Carlson, T. R.; Cheng, Y.-T.; Jae, J.; Huber, G. W. Production of Green Aromatics and Olefins by Catalytic Fast Pyrolysis of Wood Sawdust. *Energy Environ. Sci.* **2011**, *4*, 145–161. https://doi.org/10.1039/C0EE00341G.

(14) Cheng, Y. T.; Huber, G. W. Production of Targeted Aromatics by Using Diels-Alder Classes of Reactions with Furans and Olefins over ZSM-5. *Green Chem.* **2012**, *14*, 3114–3125. https://doi.org/10.1039/c2gc35767d.

(15) Gou, J.; Wang, Z.; Li, C.; Qi, X.; Vattipalli, V.; Cheng, Y.-T.; Conner, W. C.; Dauenhauer, P. J.; Mountziaris, T. J.; Fan, W.; et al. The Effect of ZSM-5 Mesoporotsity

and Morphology on the Catalytic Fast Pyrolysis of Furan. *Green Chem.* **2017**, *19*, 286–297. https://doi.org/10.1039/c7gc01395g.

(16) He, S.; Muizebelt, I.; Heeres, A.; Schenk, N. J.; Blees, R.; Heeres, H. J. Catalytic Pyrolysis of Crude Glycerol over Shaped ZSM-5 / Bentonite Catalysts for Bio-BTX Synthesis. *Appl. Catal. B Environ.* **2018**, *235*, 45–55. https://doi.org/10.1016/j.apcatb.2018.04.047.

(17) Climent, M. J.; Corma, A.; Iborra, S. Conversion of Biomass Platform Molecules into Fuel Additives and Liquid Hydrocarbon Fuels. *Green Chem.* **2014**, *16*, 516–547. https://doi.org/10.1039/C3GC41492B.

(18) Song, S.; Wu, G.; Dai, W.; Guan, N.; Li, L. Diels-Alder and Dehydration Reactions of Furan Derivatives with Ethylene Catalyzed by Liquid Brønsted Acids and Lewis Acids. *J. Mol. Catal. A Chem.* **2016**, *420*, 134–141. https://doi.org/10.1016/j.molcata.2016.04.023.

(19) Cho, H. J.; Ren, L.; Vattipalli, V.; Yeh, Y. H.; Gould, N.; Xu, B.; Gorte, R. J.; Lobo, R.; Dauenhauer, P. J.; Tsapatsis, M.; et al. Renewable *p*-Xylene from 2,5-Dimethylfuran and Ethylene Using Phosphorus-Containing Zeolite Catalysts. *ChemCatChem* **2017**, *9*, 398–402. https://doi.org/10.1002/cctc.201601294.

(20) Cruciani, G. Zeolites upon Heating: Factors Governing Their Thermal Stability and Structural Changes. *J. Phys. Chem. Solids* **2006**, *67*, 1973–1994. https://doi.org/10.1016/j.jpcs.2006.05.057.

(21) Blasco, T.; Corma, A.; Martínez-Triguero, J. Hydrothermal Stabilization of ZSM-5 Catalytic-Cracking Additives by Phosphorus Addition. *J. Catal.* **2006**, *237*, 267–277. https://doi.org/10.1016/j.jcat.2005.11.011.

(22) Lee, Y.-J.; Kim, J. M.; Bae, J. W.; Shin, C.-H.; Jun, K.-W. Phosphorus Induced Hydrothermal Stability and Enhanced Catalytic Activity of ZSM-5 in Methanol to DME Conversion. *Fuel* **2009**, *88*, 1915–1921. https://doi.org/10.1016/J.FUEL.2009.04.007.

(23) Van Der Bij, H. E.; Weckhuysen, B. M. Local Silico-Aluminophosphate Interfaces within Phosphated H-ZSM-5 Zeolites. *Phys. Chem. Chem. Phys.* **2014**, *16*, 9892–9903. https://doi.org/10.1039/c3cp54791d.

(24) Vogt, E. T. C.; Weckhuysen, B. M. Fluid Catalytic Cracking: Recent Developments on the Grand Old Lady of Zeolite Catalysis. *Chem. Soc. Rev.* **2015**, *44*, 7342–7370. https://doi.org/10.1039/C5CS00376H.

(25) Kaeding, W. W.; Butter, S. A. Production of Chemicals from Methanol: I. Low Molecular Weight Olefins. *J. Catal.* **1980**, *61*, 155–164. https://doi.org/10.1016/0021-9517(80)90351-6.

(26) Zhuang, J.; Ma, D.; Yang, G.; Yan, Z.; Liu, X.; Liu, X.; Han, X.; Bao, X.; Xie, P.; Liu, Z. Solid-State MAS NMR Studies on the Hydrothermal Stability of the Zeolite Catalysts for Residual Oil Selective Catalytic Cracking. *J. Catal.* **2004**, *228*, 234–242. https://doi.org/10.1016/j.jcat.2004.08.034.

(27) Xue, N.; Chen, X.; Nie, L.; Guo, X.; Ding, W.; Chen, Y.; Gu, M.; Xie, Z. Understanding the Enhancement of Catalytic Performance for Olefin Cracking: Hydrothermally Stable Acids in P/HZSM-5. *J. Catal.* **2007**, *248*, 20–28. https://doi.org/10.1016/J.JCAT.2007.02.022.

(28) Lercher, J. A.; Rumplmayr, G. Controlled Decrease of Acid Strength by Orthophosphoric Acid on ZSM5. *Appl. Catal.* **1986**, *25*, 215–222. https://doi.org/10.1016/S0166-9834(00)81239-7.

(29) Caro, J.; Bülow, M.; Derewinski, M.; Haber, J.; Hunger, M.; Kärger, J.; Pfeifer, H.; Storek, W.; Zibrowius, B. NMR and IR Studies of Zeolite H-ZSM-5 Modified with Orthophosphoric Acid. *J. Catal.* **1990**, *124*, 367–375. https://doi.org/10.1016/0021-9517(90)90185-M.

(30) Abubakar, S. M.; Marcus, D. M.; Lee, J. C.; Ehresmann, J. O.; Chen, C. Y.; Kletnieks, P. W.; Guenther, D. R.; Hayman, M. J.; Pavlova, M.; Nicholas, J. B.; Haw J. F. Structural and Mechanistic Investigation of a Phosphate-Modified HZSM-5 Catalyst for Methanol Conversion. *Langmuir* **2006**, *22*, 4846–4852. https://doi.org/10.1021/la0534367.

(31) Van Der Bij, H. E.; Aramburo, L. R.; Arstad, B.; Dynes, J. J.; Wang, J.; Weckhuysen, B. M. Phosphatation of Zeolite H-ZSM-5: A Combined Microscopy and Spectroscopy Study. *ChemPhysChem* **2014**, *15*, 283–292. https://doi.org/10.1002/cphc.201300910.

(32) Védrine, J. C.; Auroux, A.; Dejaifve, P.; Ducarme, V.; Hoser, H.; Zhou, S. Catalytic and Physical Properties of Phosphorus-Modified ZSM-5 Zeolite. *J. Catal.* **1982**, *73*, 147–

160. https://doi.org/10.1016/0021-9517(82)90089-6.

(33) Ashtekar, S.; Chilukuri, S. V. V; Chakrabarty, D. K. Small-Pore Molecular Sieves SAPO-34 and SAPO-44 with Chabazite Structure: A Study of Silicon Incorporation. *J. Phys. Chem* **1994**, *98*, 4878–4883.

(34) Deimund, M. A.; Harrison, L.; Lunn, J. D.; Liu, Y.; Malek, A.; Shayib, R.; Davis, M. E. Effect of Heteroatom Concentration in SSZ-13 on the Methanol-to-Olefins Reaction. *ACS Catal.* **2016**, *6*, 542–550. https://doi.org/10.1021/acscatal.5b01450.

(35) Sastre, G.; Lewis, D. W.; Richard, C.; Catlow, A. Modeling of Silicon Substitution in SAPO-5 and SAPO-34 Molecular Sieves. *J. Phys. Chem. B* **1997**, *101*, 5249–5262. https://doi.org/10.1021/jp963736k.

(36) Danisi, R. M.; Lucini Paioni, A.; Schmidt, J. E.; Houben, K.; Poplawsky, J. D.; Baldus, M.; Weckhuysen, B.; Vogt, E. T. C. Revealing Long- and Short-Range Structural Modifications within Phosphorus-Treated HZSM-5 Zeolites by Atom Probe Tomography, Nuclear Magnetic Resonance and Powder X-Ray Diffraction. *Phys. Chem. Chem. Phys.* **2018**, doi: 10.1039/C8CP03828G. https://doi.org/10.1039/C8CP03828G.

(37) Janardhan, H. L.; Shanbhag, G. V.; Halgeri, A. B. Shape-Selective Catalysis by Phosphate Modified ZSM-5: Generation of New Acid Sites with Pore Narrowing. *Appl. Catal. A Gen.* **2014**, *471*, 12–18. https://doi.org/10.1016/J.APCATA.2013.11.029.

(38) Lónyi, F.; Engelhardt, J.; Kalló, D. Para-Selectivity of Toluene Ethylation over ZSM-5 Catalysts. *Zeolites* **1991**, *11*, 169–177. https://doi.org/10.1016/0144-2449(91)80412-S.

(39) Song, Z.; Takahashi, A.; Nakamura, I.; Fujitani, T. Phosphorus-Modified ZSM-5 for Conversion of Ethanol to Propylene. *Appl. Catal. A Gen.* **2010**, *384*, 201–205. https://doi.org/10.1016/j.apcata.2010.06.035.

(40) Ramesh, K.; Jie, C.; Han, Y. F.; Borgna, A. Synthesis, Characterization, and Catalytic Activity of Phosphorus Modified H-ZSM-5 Catalysts in Selective Ethanol Dehydration. *Ind. Eng. Chem. Res.* **2010**, *49*, 4080–4090. https://doi.org/10.1021/ie901666f.

(41) Lischke, G.; Eckelt, R.; Jerschkewitz, H.-G.; Parlitz, B.; Schreier, E.; Storek, W.; Zibrowius, B.; Öhlmann, G. Spectroscopic and Physicochemical Characterization of P-Modified H-ZSM-5. *J. Catal.* **1991**, *132*, 229–243. https://doi.org/10.1016/0021-

9517(91)90259-7.

(42) Derewinski, M.; Sarv, P.; Sun, X.; Müller, S.; van Veen, A. C.; Lercher, J. A. Reversibility of the Modification of HZSM-5 with Phosphate Anions. *J. Phys. Chem. C* **2014**, *118*, 6122–6131. https://doi.org/10.1021/jp4053677.

(43) Vogt, E. T. C.; Whiting, G. T.; Dutta Chowdhury, A.; Weckhuysen, B. M. Zeolites and Zeotypes for Oil and Gas Conversion. *Adv. Catal.* 1st ed.; Elsevier, Amsterdam, **2015**; *58*, 143-314 https://doi.org/10.1016/bs.acat.2015.10.001.

(44) Xue, N.; Olindo, R.; Lercher, J. A. Impact of Forming and Modification with Phosphoric Acid on the Acid Sites of HZSM-5. *J. Phys. Chem. C* **2010**, *114*, 15763–15770. https://doi.org/10.1021/jp106621d.

(45) Jang, H. G.; Min, H. K.; Hong, S. B.; Seo, G. Tetramethylbenzenium Radical Cations as Major Active Intermediates of Methanol-to-Olefin Conversions over Phosphorous-Modified HZSM-5 Zeolites. *J. Catal.* **2013**, *299*, 240–248. https://doi.org/10.1016/j.jcat.2012.12.014.

(46) Li, J.; Ma, H.; Sun, Q.; Ying, W.; Fang, D. Effect of Iron and Phosphorus on HZSM-5 in Catalytic Cracking of 1-Butene. *Fuel Process. Technol.* **2015**, *134*, 32–38. https://doi.org/10.1016/j.fuproc.2014.11.026.

(47) Emeis, C. A. Determination of Integrated Molar Extinction Coefficients for Infrared Absorption Bands of Pyridine Adsorbed on Solid Acid Catalysts. *J. Catal.* **1993**, *141*, 347–354.

(48) Amoureux, J. P.; Fernandez, C.; Steuernagel, S. Z Filtering in MQMAS NMR. *J. Magn. Reson. - Ser. A* **1996**, *123*, 116–118. https://doi.org/10.1006/jmra.1996.0221.

(49) Fung, B. M.; Khitrin, A. K.; Ermolaev, K. An Improved Broadband Decoupling Sequence for Liquid Crystals and Solids. *J. Magn. Reson.* **2000**, *142*, 97–101. https://doi.org/10.1006/jmre.1999.1896.

(50) Pines, A.; Gibby, M. G.; Waugh, J. S. Proton-Enhanced NMR of Dilute Spins in Solids. *J. Chem. Phys.* **1973**, 569–590. https://doi.org/10.1063/1.1680061.

(51) Hutter, J.; Iannuzzi, M.; Schiffmann, F.; Vandevondele, J. Cp2k: Atomistic Simulations of Condensed Matter Systems. *Wiley Interdiscip. Rev. Comput. Mol. Sci.* **2014**, *4*, 15–

25. https://doi.org/10.1002/wcms.1159.

(52) Vandevondele, J.; Krack, M.; Mohamed, F.; Parrinello, M.; Chassaing, T.; Hutter, J. Quickstep: Fast and Accurate Density Functional Calculations Using a Mixed Gaussian and Plane Waves Approach. *Comput. Phys. Commun.* **2005**, *167*, 103–128. https://doi.org/10.1016/j.cpc.2004.12.014.

(53) Goedecker, S.; Teter, M. Separable Dual-Space Gaussian Pseudopotentials. *Phys. Rev. B - Condens. Matter Mater. Phys.* **1996**, *54*, 1703–1710. https://doi.org/10.1103/PhysRevB.54.1703.

(54) Perdew, J. P.; Burke, K.; Ernzerhof, M. Erratum: Generalized Gradient Approximation Made Simple. *Phys. Rev. Lett.* **1997**, *78*, 1396. https://doi.org/10.1103/PhysRevLett.78.1396.

(55) Grimme, S.; Antony, J.; Ehrlich, S.; Krieg, H. A Consistent and Accurate Ab Initio Parametrization of Density Functional Dispersion Correction (DFT-D) for the 94 Elements H-Pu. *J. Chem. Phys.* **2010**, *132*. https://doi.org/10.1063/1.3382344.

(56) VandeVondele, J.; Hutter, J. Gaussian Basis Sets for Accurate Calculations on Molecular Systems in Gas and Condensed Phases. *J. Chem. Phys.* **2007**, *127*. https://doi.org/10.1063/1.2770708.

(57) Foster, M. D.; Rivin, I.; Treacy, M. M. J.; Friedrichs, O. D. A Geometric Solution to the Largest-Free-Sphere Problem in Zeolite Frameworks. *Microporous Mesoporous Mater.* **2006**, *90*, 32–38. https://doi.org/10.1016/j.micromeso.2005.08.025.

(58) Hanefeld, U.; Lefferts, L. Catalysis: An Integrated Textbook for Students, Hanefeld, U., Lefferts, L., Eds.;Wiley-VCH.; Weinheim, **2018**, 1-370.

(59) van der Bij, H. E.; Weckhuysen, B. M. Phosphorus Promotion and Poisoning in Zeolite-Based Materials: Synthesis, Characterisation and Catalysis. *Chem. Soc. Rev.* **2015**, *44*, 7406–7428. https://doi.org/10.1039/C5CS00109A.

(60) Göhlich, M.; Reschetilowski, W.; Paasch, S. Spectroscopic Study of Phosphorus Modified H-ZSM-5. *Microporous Mesoporous Mater.* **2011**, *142*, 178–183. https://doi.org/10.1016/j.micromeso.2010.11.033.

(61) Jin, F.; Li, Y. A FTIR and TPD Examination of the Distributive Properties of Acid Sites

on ZSM-5 Zeolite with Pyridine as a Probe Molecule. *Catal. Today* **2009**, *145*, 101–107. https://doi.org/10.1016/j.cattod.2008.06.007.

(62) Mafra, L.; Vidal-Moya, J. A.; Blasco, T. Annual Reports on NMR Spectroscopy. *Structural Characterization of Zeolites by Advanced Solid State NMR Spectroscopic Methods*; Webb G. A. Ed.; Elsevier, **2012**; *77*, 1-362. https://doi.org/10.1016/B978-0-12-397020-6.00004-0.

(63) Clayden, N. J.; Esposito, S.; Pernice, P.; Aronne, A. Solid State ^{29}Si and ^{31}P NMR Study of Gel Derived Phosphosilicate Glasses. *J. Mater. Chem.* **2001**, *11*, 936–943. https://doi.org/10.1039/b004107f.

(64) Holzinger, J.; Beato, P.; Lundegaard, L. F.; Skibsted, J. Distribution of Aluminum over the Tetrahedral Sites in ZSM-5 Zeolites and Their Evolution after Steam Treatment. *J. Phys. Chem. C* **2018**, *122*, 15595–15613. https://doi.org/10.1021/acs.jpcc.8b05277.

(65) Damodaran, K.; Wiench, J. W.; Cabral de Menezes, S. M.; Lam, Y. L.; Trebosc, J.; Amoureux, J.-P.; Pruski, M. Modification of H-ZSM-5 Zeolites with Phosphorus. 2. Interaction between Phosphorus and Aluminum Studied by Solid-State NMR Spectroscopy. *Microporous Mesoporous Mater.* **2006**, *95*, 296–305. https://doi.org/10.1016/J.MICROMESO.2006.05.034.

(66) de Oliveira Lima, E. C.; Moita Neto, J. M.; Fujiwara, F. Y.; Galembeck, F. Aluminum Polyphosphate Thermoreversible Gels: A Study By ^{31}P And ^{27}Al NMR Spectroscopy. *J. Colloid Interface Sci.* **1995**, *176*, 388–396. https://doi.org/10.1006/JCIS.1995.9953.

(67) Jahn, E.; Müller, D.; Becker, K. Characterization of the Local Environment of Si Atoms Incorporated into $AlPO_4$-11 by Means of ^{27}Al, ^{31}P and ^{29}Si MAS n.m.r. Spectroscopy. *Zeolites* **1990**, *10*, 151–156. https://doi.org/10.1016/0144-2449(90)90038-S.

(68) Montagne, L.; Palavit, G.; Draoui, M. Mechanism of Polyphosphate Gel Formation in the Na_2O-Al_2O_3-P_2O_5 System. *J. Non. Cryst. Solids* **1993**, *155*, 115–121. https://doi.org/10.1016/0022-3093(93)91315-T.

(69) Trusell, F.; Diehl, H. Efficiency of Chemical Desiccants. *Anal. Chem.* **1963**, *35*, 674–677. https://doi.org/10.1021/ac60199a053.

(70) Cheng, Y. T.; Jae, J.; Shi, J.; Fan, W.; Huber, G. W. Production of Renewable Aromatic

Compounds by Catalytic Fast Pyrolysis of Lignocellulosic Biomass with Bifunctional Ga/ZSM-5 Catalysts. *Angew. Chem. Int. Ed.* **2012**, *51*, 1387–1390. https://doi.org/10.1002/anie.201107390.

(71) Feng, R.; Yan, X.; Hu, X.; Zhang, Y.; Wu, J.; Yan, Z. Phosphorus-Modified b-Axis Oriented Hierarchical ZSM-5 Zeolites for Enhancing Catalytic Performance in a Methanol to Propylene Reaction. *Appl. Catal. A Gen.* **2020**, *594*, 117464. https://doi.org/10.1016/j.apcata.2020.117464.

(72) Huangfu, J.; Mao, D.; Zhai, X.; Guo, Q. Remarkably Enhanced Stability of HZSM-5 Zeolite Co-Modified with Alkaline and Phosphorous for the Selective Conversion of Bio-Ethanol to Propylene. *Appl. Catal. A Gen.* **2016**, *520*, 99–104. https://doi.org/10.1016/j.apcata.2016.04.016.

(73) Van Der Bij, H. E.; Meirer, F.; Kalirai, S.; Wang, J.; Weckhuysen, B. M. Hexane Cracking over Steamed Phosphated Zeolite H-ZSM-5: Promotional Effect on Catalyst Performance and Stability. *Chem. Eur. J.* **2014**, *20*, 16922–16932. https://doi.org/10.1002/chem.201404924.

(74) Zhao, G.; Teng, J.; Xie, Z.; Jin, W.; Yang, W.; Chen, Q.; Tang, Y. Effect of Phosphorus on HZSM-5 Catalyst for C_4-Olefin Cracking Reactions to Produce Propylene. *J. Catal.* **2007**, *248*, 29–37. https://doi.org/10.1016/j.jcat.2007.02.027.

Chapter 4 Gallium-promoted HZSM-5 Zeolite Catalyst for the Aromatization of Biomass-derived Furan Derivatives

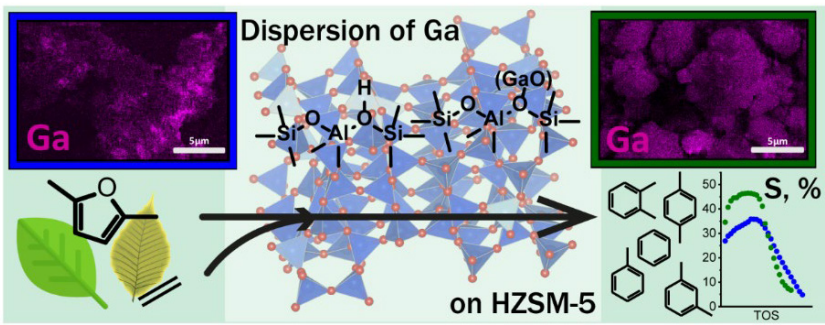

This Chapter is based on the following publication: E.A. Uslamin, B. Luna-Murillo, N.A. Kosinov, P.C.A. Bruijnincx, E.A. Pidko, B.M. Weckhuysen, E.J.M. Hensen, Gallium-promoted HZSM-5 Zeolites as Efficient Catalysts for the Aromatization of Biomass-derived Furans, *Chem. Eng. Sci.* **2019,** 198, 305-316.

Abstract

The development of novel technologies to convert renewable biomass feedstocks to fuels and chemicals is of increasing interest for making our chemical industry more sustainable. Plant biomass or its biomass-derived platform molecules are typically over-functionalized, requiring substantial modification to produce the chemicals currently demanded by industry. Furans compounds are intermediates in the catalytic fast pyrolysis of lignocellulosic biomass or sugar dehydration and can in principle be further converted to aromatics. While upgrading of furans by zeolite-catalyzed aromatization typically results in a large loss of carbon due to coke deposition, carbon laydown can be mitigated by the addition of ethylene and by the modification of the zeolite with Lewis acid Ga sites. In this Chapter, we investigate the influence of the Ga loading on the physicochemical properties of Ga-modified HZSM-5 zeolite and its performance in the gas-phase aromatization of 2,5-dimethylfuran with ethylene. Characterization of the morphological, textural and acidic properties were carried out to understand the role of Brønsted and Lewis acid sites on the catalytic reaction. We demonstrate a crucial role of the dispersion of Ga-species and the resulting Lewis acidity of the Ga/ZSM-5 catalysts; and show means how to control both parameters by adjusting the synthesis method.

4.1 Introduction

The potential of zeolite catalysts for the production of sustainable chemical building blocks from biomass has attracted widespread attention in the last decade[1–5]. Bio-based platform molecules are small molecules obtained preferably from lignocellulosic biomass that can be utilized as building blocks for higher-value chemicals and in this way help to introduce alternative, sustainable feedstock in the value chain of the chemical industry[6,7]. Deoxygenated furan derivatives, such as furan, 2-methylfuran and 2,5-dimethylfuran, together can be thought to constitute a class of such renewable platform molecules. These furan derivatives can be converted into light aromatic hydrocarbons, such as benzene, toluene, ethylbenzene and xylenes (further denoted as BTEX), for example by selective Diels-Alder addition with ethylene in the liquid phase[2,8,9]. Another route prominently investigated in recent years is catalytic fast pyrolysis (CFP) of raw biomass to bio-oil, with furans thought to play a crucial role in particular in the production of the aromatic components of the oil[10,11]. Carlson et al. proposed a reaction pathway for the CFP of cellulose over HZSM-5 catalysts involving dehydration of sugar fragments derived from cellulose to form anhydrosugars and then furans[12]. Further deoxygenation reactions of furans leads to aromatics, light olefins and coke[11]. Recently we demonstrated that methylated furans, namely 2-methylfuran and 2,5-dimethylfuran (2,5-dMF) poses significantly higher selectivity to aromatics comparable to furan[13]. Despite promising yield in the aromatization of furan derivatives compounds, the overall process remains problematic, primarily due to a low selectivity of valuable alkylated benzenes and strong catalyst deactivation.

In recent studies, Huber and co-workers discussed Diels-Alder pathways as a main reaction mechanism of furan aromatization when co-feeding small olefins[11,14]. Based on these insights, co-feeding of light dienophiles, such as ethylene and propylene, has been explored to enhance the reaction selectivity. The BTEX selectivity was indeed enhanced upon addition of ethylene, with the addition of olefins, especially propylene, additionally improving deoxygenation by dehydration, resulting in less carbon loss as CO_x[15]. Addition of Ga to ZSM-5 was demonstrated to improve the BTEX yield during furan aromatization and CFP of saw dust[14]. The authors speculated that Lewis acid Ga sites promote aromatics yields by increasing Diels-Alder reaction rates. However, the acidic and morphological properties of the catalysts used were not evaluated. To gain deeper understanding of the reaction mechanism and to design novel catalysts with high performance it is necessary to use well-defined materials.

Ga-promoted zeolites are well-known as effective catalysts for the aromatization of other feeds, such as alkanes, alkenes and methanol to aromatics[16–19]. Depending on the preparation method used, different Ga species can be obtained with the Ga/ZSM-5 system, strongly affecting catalyst performance in aromatization. The exact nature of the gallium species formed and desired for catalysis has long been the subject of investigation. The group of Hensen and Kazansky investigated Ga species in HZSM-5 by XANES and DRIFT spectroscopy[20–22], demonstrating that reduced Ga^+ species are formed in a H_2 atmosphere at elevated temperatures. It has also been established that such reducing conditions result in the migration of bulky Ga-oxides into the zeolite micropores and ion-exchange with protons[22]. Rane *et al.* observed that GaH_2^+ is less active for alkane dehydrogenation than Ga^+, while oxidized gallium species, present as GaO^+ or $Ga_2O_2^{2+}$, are the most active, requiring an oxygen source to prevent reduction of Ga^{3+} to Ga^+ [23,24]. These authors also observed that at high temperature Brønsted acid sites were regenerated with concomitant formation of Ga_2O_3 species. Kazansky *et al.* studied the adsorption of ethane over Ga_2O_3 clusters by DRIFT spectroscopy and observed that these non-cationic Ga oxide clusters can in fact also activate alkanes via dissociative adsorption[25]. While Brønsted acidic HZSM-5 catalyzes both cracking and dehydrogenation of alkanes[26], Ga-modified HZSM-5 generally show a preference for dehydrogenation to olefins and aromatization. High aromatization activity is achieved with bifunctional catalysis involving Ga species and Brønsted acid sites[27–29]. Pidko *et al.* demonstrated a significant enhancement of ethane dehydrogenation when Brønsted acid sites are in close proximity to Ga sites. Finally, Hensen *et al.* demonstrated that water addition positively affects alkane dehydrogenation by stabilization of the Ga-oxo cations[24]. Thus, depending on the preparation procedures and especially the reaction conditions different Ga species can be formed in the zeolite. In contrast to more defined model systems prepared via CVD of $GaCl_3$ or $Ga(CH_3)_3$, preparation of well-defined Ga modified zeolites by a simple insipient wetness impregnation method has not been systematically described yet.

In this Chapter, we have prepared a set of Ga-promoted HZSM-5 zeolites by wetness impregnation with $Ga(NO_3)_3$ followed by a reduction-oxidation procedure to increase the Ga dispersion. We show that the materials with designed acidic properties can be obtained. These catalysts were characterized in detail for their acidity, texture and morphology. By comparing these data to the catalytic performance in the co-aromatization of 2,5-dimethylfuran with ethylene, structure-performance relations are deduced, showing that Ga Lewis acid sites play an important role in this reaction.

4.2 Experimental Part

4.2.1 Catalyst Preparation

Ga/HZSM-5 catalysts were prepared via incipient wetness impregnation of a pristine HZSM-5 zeolite (Süd-Chemie, Si/Al = 13) with an aqueous solution of $Ga(NO_3)_3$ (Alfa Aesar, 99.9% metal based). As-prepared samples were first dried at 110 °C overnight and then calcined at 550 °C (heating ramp rate 2 °C/min) under static air atmosphere. Those samples are denoted as Ga(x) with x corresponding to Ga wt. % further in the text. Calcined samples were then treated in H_2 at 550 °C (heating rate 2 °C/min, 30% H_2 in Ar) for 7 h to enhance the metal dispersion. After reduction, the samples were exposed to O_2 at 150 °C (30 vol. % O_2 in Ar, 1 h). These samples after reduction – oxidation treatment are denoted as Ga(x)RO. Additionally a sample was prepared by physically mixing Ga_2O_3 (Alfa Aesar, 99.9% metal based) with a parent zeolite followed by calcination at 550 °C (heating ramp rate 2 °/min) and denoted as Ga(8)PM.

4.2.2 Catalyst Characterization

The elemental composition (Si/Al ratio and Ga content) of the zeolite catalysts was determined by inductively coupled plasma-optical emission spectroscopy (ICP-OES) (Spectro CIROS CCD ICP optical emission spectrometer with axial plasma viewing). Prior to analysis, the zeolite samples were dissolved in a 1:1:1 (by weight) mixture of HF (Merck, 40 % for trace analysis), HNO_3 (Merck, 65% for trace analysis) and H_2O (18.2 mQ·cm).

Scanning electron microscopy (SEM) and Energy Dispersive X-Ray analysis (EDX) were performed to determine the presence and morphology of gallium over the surface of the zeolites. Measurements were carried out with a FEI Helios Nanolab 600 FIB-SEM instrument at 15.0 kV acceleration voltage. Energy Dispersive Spectroscopy (EDS) was performed using a Silicon Drift Detector (SDD) X-MAX from Oxford Instruments coupled to the Helios Nanolab.

NH_3 temperature programmed desorption (TPD) experiments were carried out in a Micromeritics AutoChem II equipped with a TCD detector. Approximately 100 mg sample was placed in the reaction chamber and the sample was dried up at 600 °C in a He flow. Then, the chamber was cooled to 100 °C in a He flow and held at 100 °C for 2 h. A flow of 10 ml/min of

10 vol. % NH_3/He was fed into the chamber to saturate the sample with NH_3. Thereafter, the sample was kept at 100 °C in a He flow for 2 h, followed by heating to 600 °C at 10 °C/min.

Fourier transform-infrared (FT-IR) spectroscopy of adsorbed pyridine and carbon monoxide was carried out to probe the acid sites. Spectra were taken in the 4000 − 1000 cm^{-1} range using a Bruker Vertex 70v spectrometer. First, a zeolite sample was pressed into a self-supporting wafer (5 − 10 mg, diameter 13 mm) and then placed in an environmental transmittance IR cell. Samples were first pre-treated in a O_2/N_2 flow at 550 °C (heating rate 5 °C/min) to eliminate adsorbed species, followed by cooling in dynamic vacuum (~10^{-5} mbar). For pyridine adsorption experiments, the sample was exposed to an excess of pyridine at 150 °C. Spectra were then recorded at different temperatures (150 − 450 °C) under dynamic vacuum. Heating was done at a rate of 5 °C/min followed by a dwell of 1 h before recording a spectrum. For the quantification of Brønsted and Lewis acid sites the integral molar extinction coefficients (IMEC, *E*) of 0.73 cm/µmol and 1.11 cm/µmol respectively were used[30,31]. For the CO adsorption experiments, the cell was cooled with liquid nitrogen to a temperature of ~ -183 °C in dynamic vacuum. Small pulses of CO (10 µmol) were then admitted to the IR cell, whilst recording IR spectra. Prior to CO dosing the cell was pressurized with a few mbar of He to enhance thermal conductivity and eliminate possible temperature gradients.

In situ UV/Vis Diffuse Reflectance Spectroscopy (DRS) experiments were carried out in a Linkam FTIR600 *in situ* cell equipped with a temperature controller. All UV/Vis DRS spectra were collected using a AvaSpec-2048L spectrometer and a AvaLight DH-S-BAL fiber probe (Avantes). Samples were pressed over a quartz slide and 15 µl 4-fluorostyrene (99%, Sigma Aldrich) was added to the materials. Afterwards, they were heated to 120 °C while collecting UV/Vis DRS spectra to monitor oligomer formation over time.

Confocal fluorescence microscopy (CFM) measurements were carried out using a Nikon ECLIPS 90i upright confocal laser scanning fluorescence microscope equipped with a 100×0.73NA dry objective lens and a pinhole value of 1.2 au. Fluorescence microphotographs were collected using 488 nm and 561 nm laser lights. The emission was measured in a range of 510 − 670 nm when using 488 nm laser light and in a range of 580 − 700 nm when using 561 nm laser light by the A1R scanning head equipped with a spectral detection unit consisting of a diffraction grating and a 32-photomultiplier tube array. The catalysts were analyzed *in-situ* by CFM after staining the samples by 4-fluorostyrene oligomerization. All the materials were heated to 120 °C and held at that temperature for 5 min. Subsequently, 15 µl 4-fluorostyrene

was added and after 15 sec. the heating was turned off. After cooling to room temperature, the stained samples, these were illuminated by specific wavelength lasers causing the oligomeric species to fluoresce.

Zeolite crystallinity was evaluated by powder X-ray diffraction (XRD) method. XRD measurements were performed on a Bruker D2 powder diffraction system (Cu Kα radiation, scan speed 0.01° per step, 2θ range 5−60°). The relative crystallinity of samples normalized to a parent HZSM-5 was evaluated by comparing of the integral areas of the reflections (*Miller indices* in parentheses) at 23.1° (051), 23.3° (501), 23.7° (511), 24.0° (033), and 24.4° (313).

The texture of the zeolites was determined by Ar porosimetry, carried out at - 186 °C using a Micromeritics ASAP-2020 apparatus. The samples were degassed at 500 °C prior to measurements. The micropore volume was determined by the *t*-plot method in a thickness range from 3.5 to 4.5 Å.

X-ray Photoelectron Spectroscopy (XPS) spectra were taken using a Thermo Scientific K-alpha spectrometer equipped with a monochromatic Al Kα X-ray source and a 180° double-focusing hemispherical analyzer with a 128-channel detector.

4.2.3 Catalyst Testing

The catalytic aromatization of 2,5-dimethylfuran (2,5-dMF) in the presence of ethylene was carried out in a fixed bed quartz reactor. In a typical catalytic run, 0.5 g of the sieved catalyst fraction (250-500 µm) was placed into the reactor and held between quartz wool plugs. Calibrated thermal gas mass-flow controllers (Brooks) were used to feed the gases into the reactor. To feed 2,5-dMF a thermostated glass saturator was used. Reaction products were analyzed using online GC (Trace 1300, Thermo) and MS (Pfeiffer Omnistar GSD 301 T3) instruments. The gas flow from the reactor was sent directly to the GC injection system equipped with a 100 µl sample loop mounted on a 6-way valve. The MS capillary entrance was installed just below the reactor bed exit. The GC was equipped with two columns and detectors. A TCD detector with an RT-Q-Bond column (l. 20 m; i.d. 0.32 mm; d.f. 10 µm) was used for the analysis of the light fraction of the reaction products. Aromatics and other heavier products (including substituted naphthalenes) were analyzed on a Stabilwax-DB column (length 30 m; i. d. 0.25 mm; d. f. 0.25 µm) coupled with a FID. Identification of the compounds was done

based on the retention time compared to standards. The reaction selectivity, conversion and yield were calculated as:

$$x_i(t) = 1 - \frac{n_i^{out}}{n_i^{in}}; \quad \text{(eq. 4.1)}$$

$$s_k(t) = \frac{n_k^{out}}{n_i^{in} - n_i^{out}} * \left|\frac{\mu_i}{\mu_k}\right|; \quad \text{(eq. 4.2)}$$

$$X_\Sigma(C_{based}) = \sum_i \mu_i * \int_0^t (n_i^{in} - n_i^{out})dt; \quad \text{(eq. 4.3)}$$

$$S_k = \frac{\mu_k * \int_0^t n_k^{out} dt}{X_i}; \quad \text{(eq. 4.4)}$$

$$Y_k = \mu_k * \int_0^t n_k^{out} dt = S_k * X_i, \quad \text{(eq. 4.5)}$$

where (eq. 4.1) – conversion at *t*; (eq. 4.2) – C based selectivity to a product *k* at *t* where n_j – concentration of compound and μ_j – number of carbon atoms in k; (eq 4.3) – overall C based conversion at t; (eq. 4.4) – overall C based selectivity to a product k; (eq. 4.5) – overall C based yield of a product k. Cumulative (overall) parameters were calculated at t such that *x(t)* = 90%. Both ethylene and 2,5-dimethylfuran are included in the overall carbon balance.

4.3 Results and Discussion

4.3.1 Catalyst Characterization

As solvated Ga^{3+} ions are too large to enter the ZSM-5 micropores, the direct exchange of Brønsted acid sites (BAS) with Ga during wet impregnation is limited[32]. Therefore, wet impregnation leads to the predominant deposition of aggregated Ga-oxide on the external zeolite surface. A different, more effective method to substitute ZSM-5 BAS for Ga involves their gas phase reaction with volatile Ga compounds, such as $Ga(CH_3)_3$ or $GaCl_3$. However, this method is only applicable to prepare model catalyst systems at a small scale. A high degree of gallium-proton exchange can also be achieved by a high-temperature reductive treatment of a Ga/HZSM-5 zeolite sample prepared via conventional wet impregnation or wet ion-exchange methods. Reduction leads to the formation of mobile Ga_2O, which can migrate into the micropores and react with BAS. This procedure is sometimes called reductive solid-state ion

exchange. Subsequent oxidation in oxygen results in the formation of well-dispersed GaO^+ ions, which are considered catalytically active[2128]:

$$Ga_2O_3 + 2H_2 \rightarrow Ga_2O + 2\ H_2O,$$

$$Ga_2O + 2\ ZO^-\cdots H^+ \rightarrow 2\ ZO^-\cdots Ga^+ + H_2O,$$

$$2\ ZO^-\cdots Ga^+ + \tfrac{1}{2}\ O_2 \rightarrow 2\ ZO^-\cdots GaO^+.$$

A drawback of this approach is that repeated calcination and reductive treatments at 550 °C result in damage to the zeolite framework due to water formation. Moreover, volatile Ga species might be removed from the solid catalyst. Accordingly, we investigated the texture, structure and composition of Ga/ZSM-5 after the reductive treatment step followed by the re-oxidation. It should be noted though that the XRD patterns show that neither the presence of Ga nor the high-temperature reductive and oxidative treatments affected the crystal structure of zeolite, even for the highest Ga loading of 8 wt. % (Figure 4.2a). Quantification of the relative crystallinity confirms that the MFI framework remained intact (Table 4.1). The observed shift of the XRD reflections can be attributed to a slight increase of the zeolite unit cell dimensions, induced by the intra-zeolite Ga species[33].

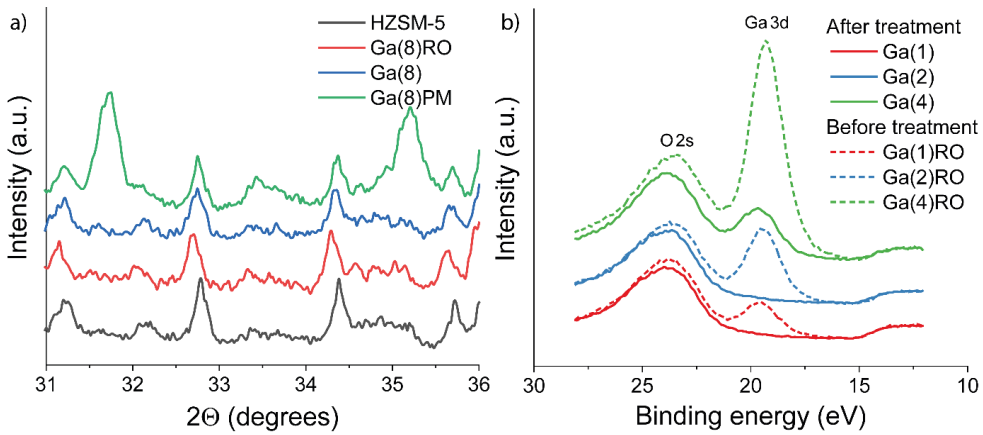

Figure 4.1. (a) X-ray diffraction (XRD) patterns of the parent HZSM-5, Ga(8)RO, Ga(8) and Ga(8)PM; (b) X-ray photoelectron spectroscopy (XPS) data of Ga(x)RO (dashed lines) and Ga(x) (solid lines).

The presence of a bulk gallium oxide phase (particles >30 nm) can be inferred from XRD reflections at 31.75° and 35.25° 2Θ[32]. Figure 4.2a shows that such bulk Ga_2O_3 reflexes are absent in the XRD patterns of the impregnated and treated catalysts, while they are apparent for

the physical mixture of Ga_2O_3 and ZSM-5. XPS analysis of the zeolite samples, which mainly probes the external surface of the crystals, shows how the reductive treatment affects the Ga distribution. After impregnation and calcination, a large amount of Ga-species was found to reside at the external surface (Figure 4.1b). Reduction resulted in the complete disappearance of the Ga 3d signal for Ga(1)RO and Ga(2)RO. This implies that most of the Ga-oxide has dispersed inside the zeolite pores during reduction. A Ga 3d signal remains for Ga(4)RO, showing that not all Ga can be dispersed inside the zeolite at a higher Ga content.

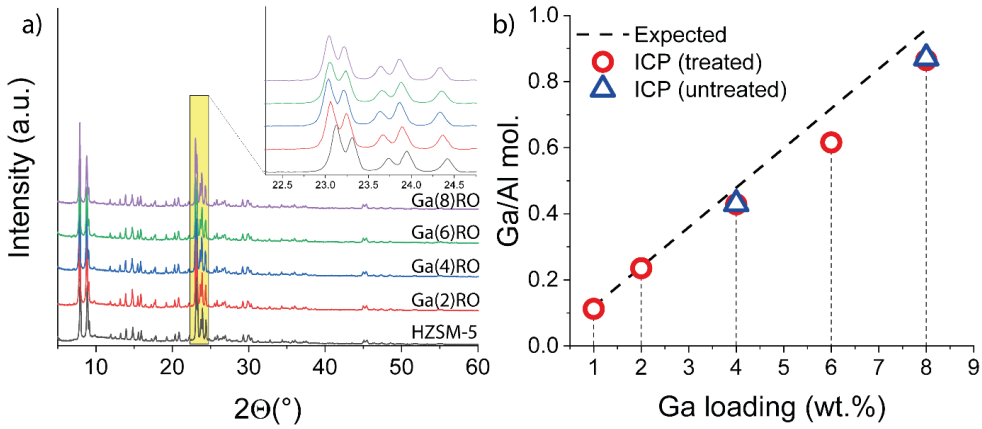

Figure 4.2. (a) X-ray diffraction (XRD) patterns of the Ga(x)RO samples and the pristine HZSM-5; (b) Ga loading, and actual Ga content based on elemental analysis data for Ga(x) and Ga(x)RO samples.

Elemental analysis showed that the total Ga loading does not change upon reductive treatment (Figure 4.2b), confirming that all Ga is retained by the zeolite during high-temperature reduction. Considering that Ga is not Visible in the XPS spectra of Ga(1)RO and Ga(2)RO, and just a 10% fraction of Ga remains on the surface for Ga(4)RO, it is clear that Ga is (nearly) quantitatively located inside the zeolite pores at loadings below 4%.

SEM-EDX was used to determine the presence and morphology of the Ga species over the surface of the promoted materials. In order to get an insight into the physical appearance and elemental composition of the Ga/HZSM-5 catalysts, SEM-EDX analysis was performed for the samples before and after reductive treatment. The micrographs of those samples and EDX mapping of the elements are shown in Figure 4.3.

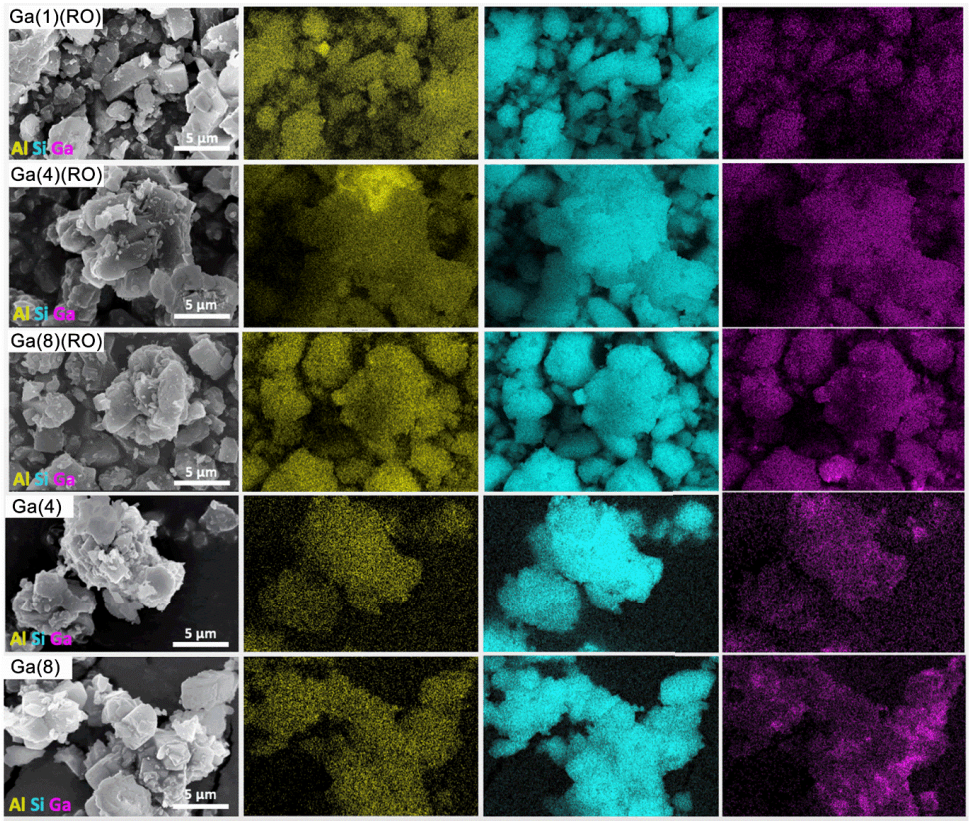

Figure 4.3. Scanning electron microscopy (SEM) image and energy dispersive X-ray (EDX) mapping (Al, Si, Ga) of Ga/ZSM-5 samples.

SEM images show that incorporation of Ga did not introduce any significant morphological changes in zeolite crystal habit. In line with expectation, EDX mapping showed the presence of Ga conglomerates for Ga(4) and Ga(8) samples. After the reductive treatment the distribution of Ga became significantly more homogeneous. Only Ga(8)RO contained measurable aggregates of Ga. The EDX data is thus in a good agreement with the XRD and XPS data reported above. It confirms the importance of the reductive treatment on the Ga distribution and indicates that, at a Ga loading higher than 4%, a larger fraction of Ga remains on the zeolite outer surface.

The acidity of the samples was probed by different methods. NH_3 desorption traces are shown in Figure 4.4, revealing the two main features typical for acidic zeolites. The low temperature desorption feature with a maximum at 220 – 230 °C (*l*-peak) is associated with ammonia adsorbed on weak acid sites or physically adsorbed ammonia. The feature at high temperature

(*h*-peak) is attributed to ammonia adsorption on strong acid sites[34,35]. Introduction of Ga led to significant changes in the NH_3 desorption traces. The *h*-peak became broader with the maximum shifting to lower temperature with increasing Ga loading. The broadening indicates that there are different acid sites associated with *h*-peak including strong Brønsted acid sites and Lewis acid sites. In contrast, the *l*-peak remains similar in shape and position. The ratio between *l*- and *h*-peaks decreases upon increasing Ga content. Introduction of Ga most likely decreases the number and strength of the remaining strong acid sites, which can be attributed to the partial exchange of Brønsted acid sites and formation of Ga-associated Lewis acid sites.

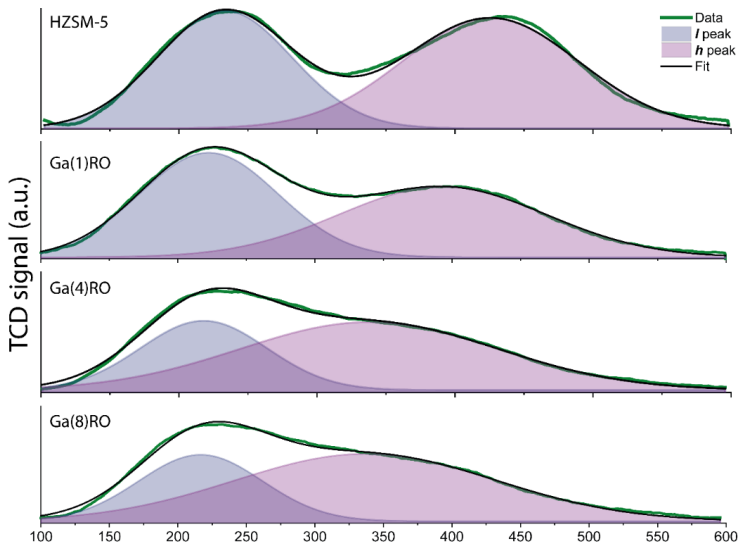

Figure 4.4. NH_3 temperature programmed desorption (TPD) profiles for HZSM-5 and Ga(x)RO zeolites.

The quantity, nature and strength of the acid sites was further characterized by FT-IR spectroscopy of adsorbed pyridine at 150 °C and CO at -196 °C. Analysis of the pyridine FT-IR spectra (Figure 4.5) shows that the exchange degree of Brønsted acid sites increases proportionally with Ga loading between 0 and 4 wt. %, before reaching a plateau. These data are supported by the EDX-mapping and XPS results, where we found that agglomerated Ga starts to form at a Ga loading above 4 wt. %. It is also important to note that the disappearance of BAS is accompanied by a proportional increase in Lewis acidity (Figure 4.5b). The stoichiometry implies that the composition of Ga species formed is different in the samples with different loading. At low Ga loading formation of $(Ga_2O)_{2x}^{2x+}$ can be anticipated while at higher

loading the ions with the composition $(GaO)_x^{x+}$ are the dominant species. These observations are in line with previously reported theoretical studies detailing the formation and self-organization of such multinuclear clusters, particularly $(Ga(\mu\text{-}O)_2Ga)^{2+}$ [36,37].

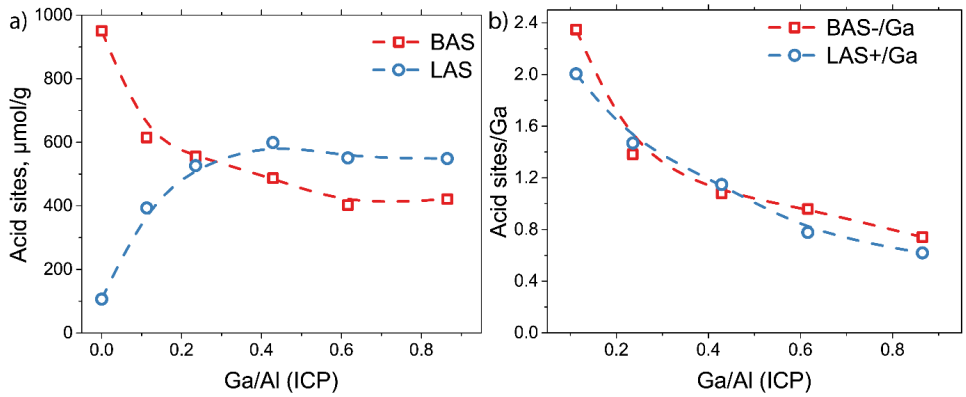

Figure 4.5. (a) Concentration of Lewis and Brønsted acid sites obtained from Fourier transform-infrared (FT-IR) pyridine adsorption; (b) Number of Brønsted acid sites (BAS) removed and Lewis acid sites (LAS) introduced normalized by amount of Ga deposited.

FT-IR analysis of adsorbed CO shows that the presence of Ga at exchange sites did not change the acid strength of the remaining BAS. The band positions related to bridging OH groups and CO adsorbed to this bridging OH group were similar for the parent HZSM-5 and the Ga(2)RO and Ga(4)RO samples (Figure 4.6). At low partial pressure of CO, only a band at 2174 cm^{-1} was observed in the CO stretching region, corresponding to ν(OH···CO). With increasing CO pressure, a band at 2140 cm^{-1} appeared, which is due to physisorbed CO. No bands are observed in the 2200 – 2300 cm^{-1} region, showing that reduced Ga species are absent after the re-oxidation treatment[21]. A summary of the acidity characterization results is given in Table 4.1.

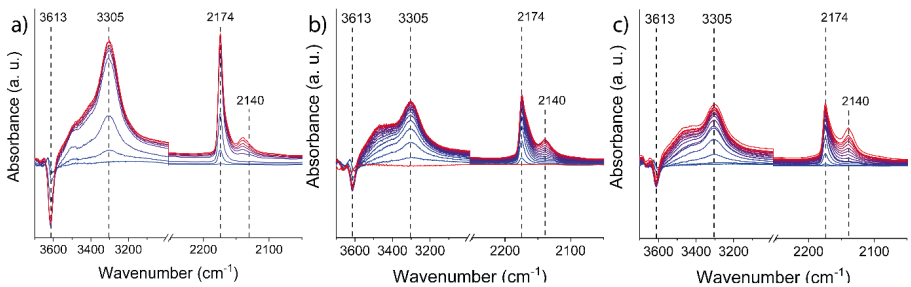

Figure 4.6. Fourier transform-infrared (FT-IR) spectra of CO adsorbed on Ga(x)RO samples under sequential dosing of CO at 77 K. (a) parent HZSM-5, (b) Ga(2)RO (c) Ga(4)RO.

Table 4.1. Summary of the physiochemical properties of the Ga/HZSM-5 materials under study.

Catalyst	HZSM-5	Ga(1)RO	Ga(2)RO	Ga(4)RO	Ga(6)RO	Ga(8)RO	Ga(4)	Ga(8)
Ga/Al[a]	0	0.11	0.23	0.43	0.62	0.86	0.43	0.87
NH_3 TPD total, mmol g^{-1}	1.0	0.81	0.86	1.08	n.d.	0.8	n.d.	n.d.
NH_3 TPD weak, °C	233	222	226	218	n.d.	216	n.d.	n.d.
NH_3 TPD weak, mmol g^{-1}	0.45	0.41	0.37	0.36	n.d.	0.26	n.d.	n.d.
NH_3 TPD strong, °C	426	393	378	338	n.d.	336	n.d.	n.d.
NH_3 TPD strong, mmol g^{-1}	0.55	0.40	0.48	0.72	n.d.	0.54	n.d.	n.d.
ν(OH·CO)[b], cm^{-1}	3305	3305	3305	3305	n.d.	3305	n.d.	n.d.
ν(CO·HO)[b], cm^{-1}	2174	2174	2174	2174	n.d.	2174	n.d.	n.d.
BAS/LAS[c], µmol g^{-1}[c]	950/107	614/393	556/526	487/599	402/551	421/548	n.d.	664/152
S_{total}, m^2 g^{-1}	321.3	349.2	331.3	292.5	275.4	292.2	235.1	274.4
S_{micro}, m^2 g^{-1}	281.8	307.9	280.8	219.0	251.0	269.1	233.7	248.8
$S_{external}$, m^2 g^{-1}	39.5	41.2	50.5	73.5	24.3	23.2	25.2	25.7
V_{micro}, cm^3 g^{-1}	0.11	0.12	0.11	0.10	0.10	0.11	0.08	0.09
Crystallinity[d]	1	n.d.	1.01	1.06	0.99	0.99	n.d.	n.d.

Measured by ICP; (b) CO adsorbed FT-IR (c) pyridine adsorbed FT-IR; (d) XRD.

As demonstrated by NH_3-TPD and FT-IR spectroscopy measurements, an increase of the Ga loading leads to a lower Brønsted acidity. To gain further insight into the nature and location of acid sites in the Ga-exchanged zeolites, these samples and the parent HZSM-5 reference were analyzed with *in situ* UV/Vis DR spectroscopy and fluorescence micro-spectroscopy using the BAS-catalyzed oligomerization of 4-fluorostyrene as a probe reaction. In previous works, reactivity and distribution of Brønsted acid sites of different porous zeolitic materials have been studied in combination with micro-spectroscopy techniques and acid-catalyzed oligomerization reactions[38,39]. 4-fluorostyrene oligomerization yields conjugated cyclic and linear dimeric carbocationic species as well as higher oligomeric carbocationic species, which serve as BAS-selective reporter molecules (Figure 4.7)[40,41]. Sprung and Weckhuysen observed that linear dimeric carbocations predominantly occupy straight MFI channels, while the cyclic carbocations can be formed either in the intersections or close to the external surface.

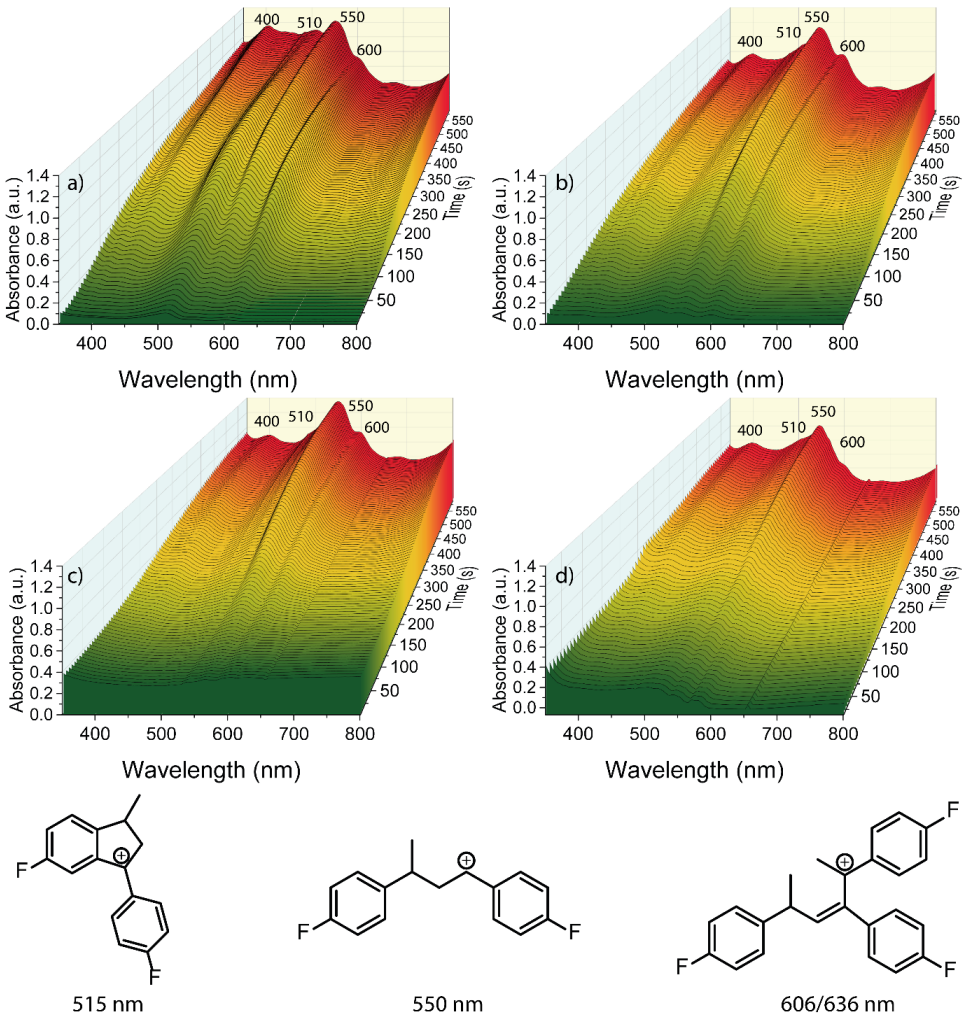

Figure 4.7. UV/Vis diffuse reflectance (DR) spectra recorded after the exposure of zeolites to 4-fluorostyrene at 25 °C followed by heating to 120 °C and the main oligomeric species formed with their expected absorption wavelengths (bottom) (a) HZSM-5; (b) Ga(2)RO; (c) Ga(4)RO and d) Ga(8)RO.

The data, given in Figure 4.7, show the linear dimeric carbocations, likely occupying the straight channels, to dominate the spectra, as indicated by the intense absorption band at 550 nm found for all catalysts. Modification of zeolite with Ga led to the suppressed formation of the cyclic dimeric (510-515 nm) and the higher oligomeric carbocations (600 nm), which are located in the intersections of the MFI framework and the zeolitic external surface, respectively. This implies a reduction in Brønsted acidity or hindered accessibility of the acid sites in these positions. The most noticeable decrease in intensity of the linear and cyclic dimeric

carbocations is observed between the parent ZSM-5 zeolite and the Ga(2)RO sample. A drop in intensity is only observed for the 600 nm absorption band of the Ga(8)RO catalyst, which is attributed to the large amount of Ga species agglomerated after the reduction step on the surface. This result is in line with the XPS and SEM analyses shown above. The absorption band around 400 nm decreases in intensity as well with increasing Ga loading. This band is assigned to the formation of methyl-substituted benzenium carbocationic species[42,43]. Furthermore, as shown in Figure 4.7, introduction of Ga into MFI also increased the onset temperature for the oligomerization reaction. Specifically, 4-fluorostyrene oligomerization over the HZSM-5 material (Figure 4.7a) already yielded the cyclic and linear carbocations after 50 s of reaction. In contrast, for Ga(8)RO (Figure 4.7d) the linear dimeric carbocation is detected only after 200 s of reaction, attributed to the lower BAS content and reduced accessibility, in line with the above reasonings.

For a more detailed visualization of the decrease in the formation of oligomeric species by increasing Ga content, absorption spectra of all samples at 300 s are shown in Figure 4.8a. It can be observed that an increase in the Ga loading leads to a decrease in the intensity of all the absorption bands. Furthermore, the 400, 510, 550 and 600 nm absorption bands have been plotted over time to see if there is any difference between the ratio of formation of the different oligomeric species (Figure 4.8b**,** 4.8c**,** 4.8d and 4.8e). The absorption difference between the linear and the cyclic carbocations is larger among HZSM-5 and Ga(4)RO, however for sample Ga(8)RO their difference in intensity is smaller revealing a significant reduction of BAS. Concerning the higher oligomeric carbocationic species, their difference in the absorption intensities between the linear carbocations increases as well. Both evidences indicate the decrease in the amount and strength of BAS, which are in line with the TPD data discussed above.

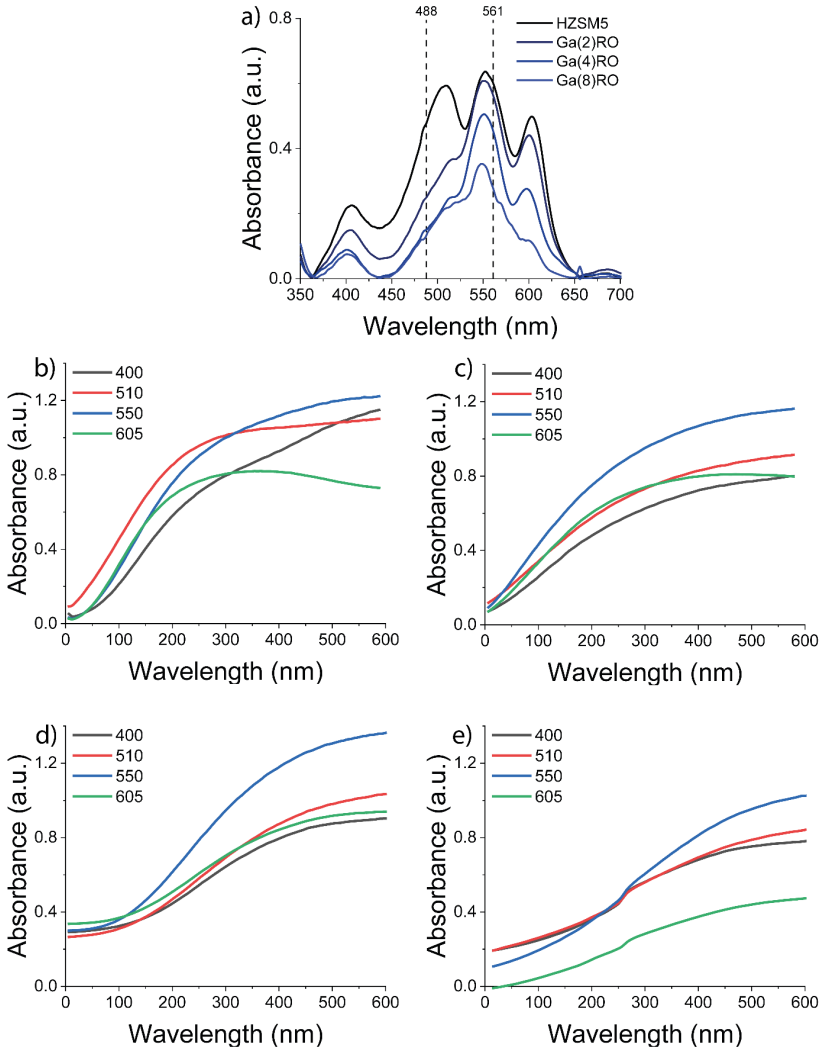

Figure 4.8. (a) UV/Vis DR spectra for the different catalyst materials after 300 s of reaction with 4-fluorostyrene, including the position of the two laser frequencies, used to excite the oligomeric species formed; Intensity plots of 400, 510, 550 and 600 nm absorption bands as a function of reaction time for: (b) Fresh HZSM-5, (c) Ga(2)RO, (d) Ga(4)RO and (e) Ga(8)RO.

The fluorescence microscopy images of the series of (Ga-exchanged) HZSM-5 catalysts stained with 4-fluorostyrene are shown in Figure 4.9. The images were taken after excitation with 488 nm and 561 nm wavelength lasers, respectively.

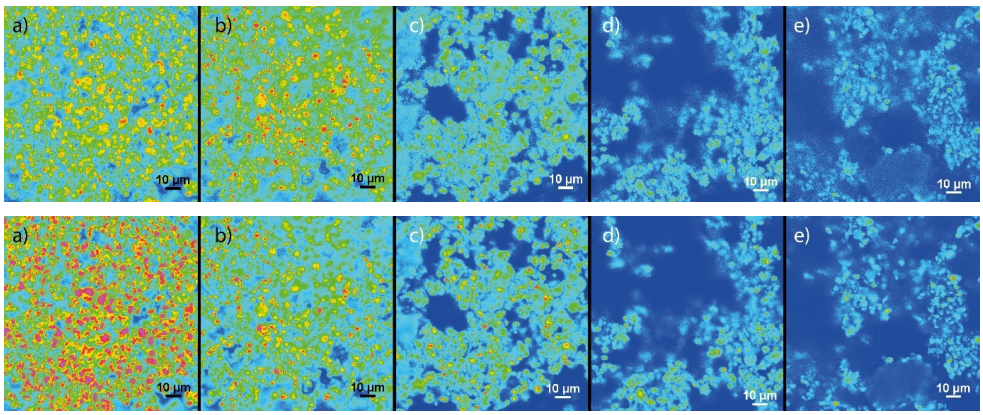

Figure 4.9. Fluorescence microscopy images taken from stained catalysts after irradiating them with a 488 nm (top) and 561 nm (bottom) wavelength laser; (a) Fresh HZSM-5, (b) Ga(2)RO, (c) Ga(4)RO, (d) Ga(6)RO and (e) Ga(8)RO.

After excitation with the 488 nm laser the predominant species excited are the cyclic dimeric carbocations and to a lower extent the linear dimeric carbocations. As Figure 4.9 shows, the fresh HZSM-5 sample expectedly gives the highest fluorescence intensity after excitation with the 488 nm laser followed by Ga(2)RO and Ga(4)RO samples. The overall fluorescence intensity decreases with increasing Ga loading, confirming that the density of BAS is reduced. Moreover, a rather consistent fluorescence intensity is displayed in all the CFM images revealing a homogeneous distribution of the Ga species in all the Ga-exchanged samples, as also shown in the SEM-EDX analyses shown above. Also, after excitation with the 561 nm wavelength laser, the parent ZSM-5 shows the highest fluorescence intensity. The main excited oligomeric species in this case are the linear dimeric carbocations and the larger oligomeric carbocations.

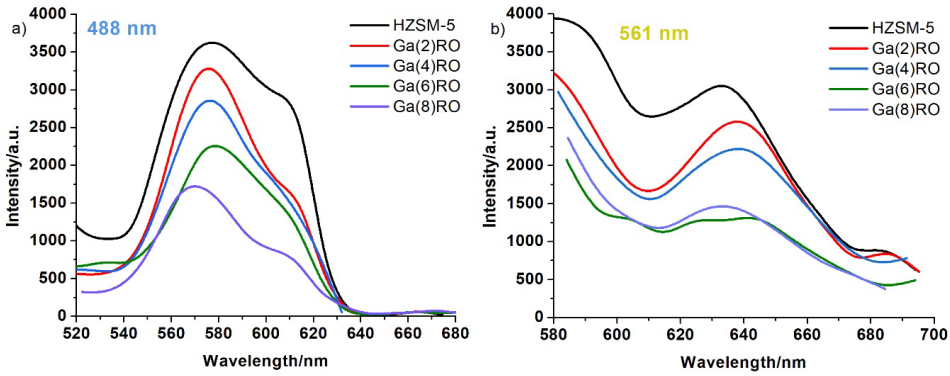

Figure 4.10. Emission spectra of each sample after excitation with (a) 488 nm and (b) 561 nm wavelength lasers.

For a more detailed analysis of the fluorescence microscopy measurements we also collected emission spectra, as shown in Figure 4.10**,** for each sample after excitation with 488 nm and 561 nm lasers. After excitation with the 488 nm laser, there is one broad shoulder at around 550 nm in the emission spectra, which corresponds to the cyclic dimeric carbocation, and two bands at around 570 nm and 610 nm in the emission spectra, corresponding to the linear dimeric carbocation emission bands. In turn, after excitation with the 561 nm laser there is a band around 630-640 nm, which can be attributed to the larger oligomeric carbocation. For both sets of spectra we can corroborate that fresh HZSM-5 displays the highest fluorescence intensity, reflecting also its higher reactivity in 4-fluorostyrene oligomerization.

4.3.2 Catalytic Activity Tests

To investigate the influence of Ga content and location on the catalytic performance, the different samples were used as catalysts in the co-aromatization reaction of 2,5-dMF with ethylene. We first verified that SiC, used as a diluent, was not active in this reaction in the 300 – 600 °C temperature regime (Figure 4.11), in line with an earlier study[44]. A silica reference was found to convert 2,5-dMF at temperatures of 400 °C. Full conversion was reached at 600 °C and above 500 °C, benzene and toluene formation was observed.

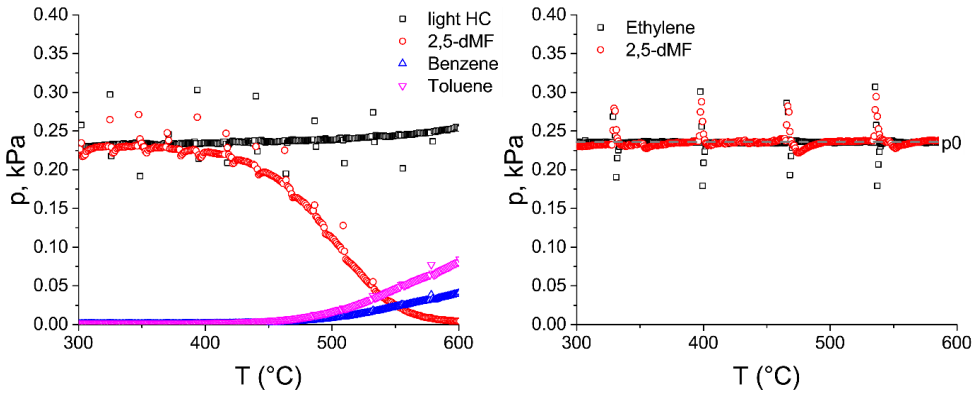

Figure 4.11. Temperature dependence of 2,5-dMF and ethylene conversion over SiO_2 (left) and SiC (right) as derived from the MS analysis. Observed spikes correspond to GC injections.

The low mass balance indicates that most 2,5-dimethylfuran is converted to coke at these high temperatures. Accordingly, we carried out the activity measurements of the zeolites at a temperature of 450 °C to avoid non-selective reactions at the external zeolite surface. Figure 4.13a shows that all catalysts possess a complete conversion of 2,5-dMF at the start of the reaction. After *ca.* 100 min, the catalysts undergo rapid deactivation. The major deoxygenation product is water for both Ga-modified and pristine zeolites (Figure 4.12).

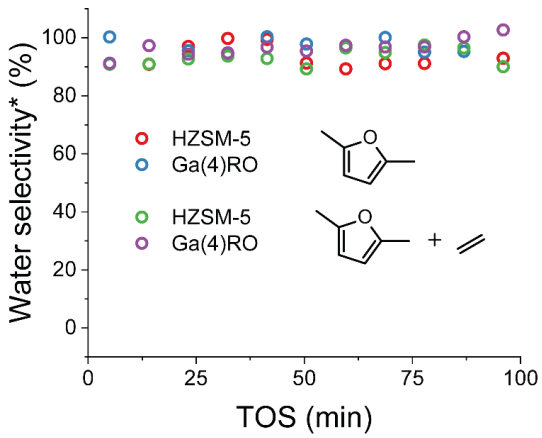

Figure 4.12. Deoxygenation selectivity towards water in the aromatization reaction of 2,5-dMF and 2,5-dMF with co-feeding of ethylene over HZSM-5 and 4% Ga(HT) catalysts. Conditions: T = 450 °C; p(2,5-dMF) = p(C_2H_4) = 0.2 kPa in 100 ml/min Ar.

Only trace amounts of CO_x and benzofuran were detected. The product distribution for the various catalysts are displayed in Figure 4.13b. The hydrocarbon products are aromatics, mainly benzene and toluene with small amounts of xylenes. The BTEX selectivity (Figure 4.13b) shows a considerable increase from *ca.* 25% on the pristine zeolite to 40% on Ga(2)RO. Further increase in Ga loading from 2 wt. % to 8 wt. % leads to an increase in BTEX selectivity of *ca.* 7 – 8%. The observed trends correlate well with the concentration of LAS as well as with removal of BAS.

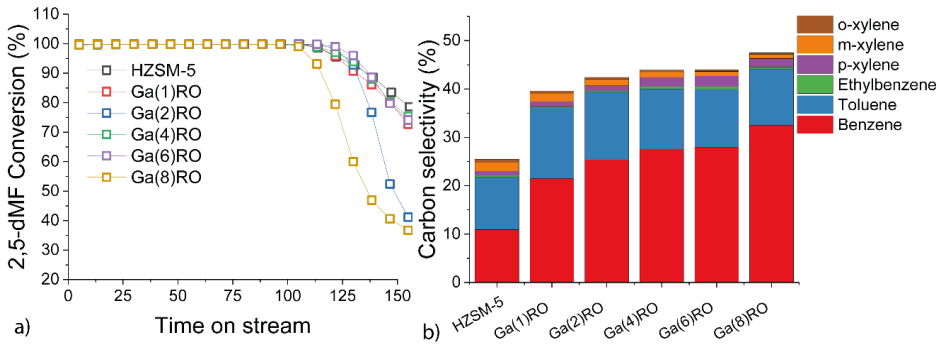

Figure 4.13. Conversion (a) of 2,5-dMF and selectivity (b) towards BTEX aromatics in the reaction of 2,5-dMF with ethylene. Conditions: T = 450 °C; p(2,5-dMF) = $p(C_2H_4)$ = 0.2 kPa in 100 ml/min Ar.

In addition, we found that the distribution of aromatic products changes with increasing the Ga loading. The overall carbon selectivity towards benzene and xylenes significantly increased, while the production of toluene stayed on almost the same level. This difference can be attributed to a change in the reaction mechanism due to the presence of Ga. Based on literature reports, we suspect that following reaction pathways might be facilitated by Ga species: (i) Diels-Alder coupling of 2,5-dMF and ethylene, (ii) enhanced aromatization of ethylene via hydrogen transfer reactions[45], and (iii) interaction of ethylene with some other reaction intermediates, for example (de)alkylation of aromatic or olefinic intermediates. To evaluate which of these pathways is important under our conditions, we investigated the behavior of ethylene in a more detailed way.

Figure 4.14a shows that ethylene is produced in the reaction of pure 2,5-dMF on both HZSM-5 and Ga(4)RO catalysts. It contributes about 10% and 5% to the overall carbon selectivity, respectively. No conversion of ethylene is observed when ethylene is co-fed with 2,5-dMF over pristine HZSM-5 catalysts. (Figure 4.14b) In contrast, Ga(4)RO catalysts shows 65%

conversion at the beginning of the reaction, which dropped in a linear manner to zero. Figure 4.15a and 4.15b shows the BTX selectivity as function of time-on-stream for HZSM-5 and Ga(4)RO, respectively. Conversion of pure ethylene over the HZSM-5 zeolite under the same reaction conditions is relatively low (<5%). Modification of the zeolite with Ga substantially improved the conversion up to 85% for Ga(4)RO, yielding mostly benzene and toluene in a nearly equimolar ratio (Figure 4.14c).

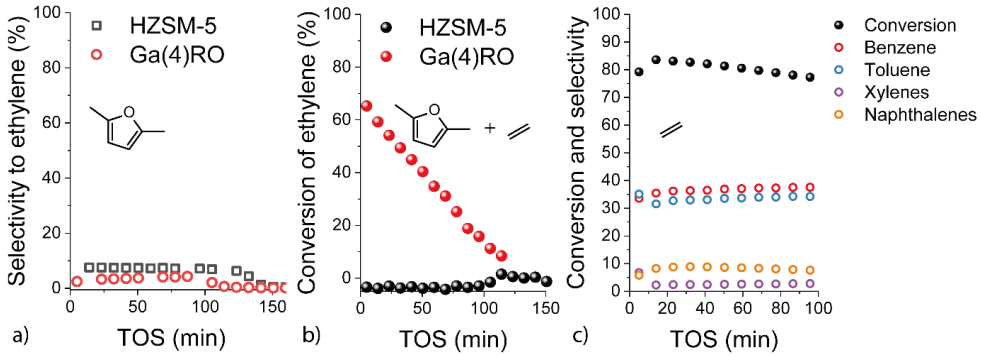

Figure 4.14. (a) Carbon selectivity to ethylene in the aromatization reaction of 2,5-dMF on HZSM-5 and Ga(4)RO; (b) carbon selectivity to ethylene in aromatization reaction of 2.5-dMF with ethylene on HZSM-5 and Ga(4)RO (c) conversion of pure ethylene on HZSM-5 and Ga(4)RO;. Conditions: T = 450 °C; p(2,5-dMF) = p(C_2H_4) = 0.2 kPa; in 100 ml/min Ar.

Interestingly, the conversion of ethylene which is co-fed with 2,5-dMF is close to zero on HZSM-5, indicating that the conversion of ethylene and the formation of ethylene from 2,5-dMF have nearly equal rates under our reaction conditions (Figure 4.14b). Considering that ethylene affected the product distribution (Figure 4.13), we infer that ethylene is involved in the further conversion of the primary products from 2,5-dMF conversion. However, the net conversion of ethylene is very low. A thermodynamic basis for similar effects observed during co-aromatization of alkanes with methane over zeolites has been earlier discussed[46,47]. When Ga is added to ZSM-5 zeolite, there is a net conversion rate of ethylene. However, as ethylene addition did not lead to a significant increase in xylenes selectivity (the principal product of Diels-Alder coupling of 2,5-dMF with ethylene is *p*-xylene), it is not likely that a Diels-Alder reaction of 2,5-dMF with ethylene is the predominant reaction by which ethylene is incorporated in the products.

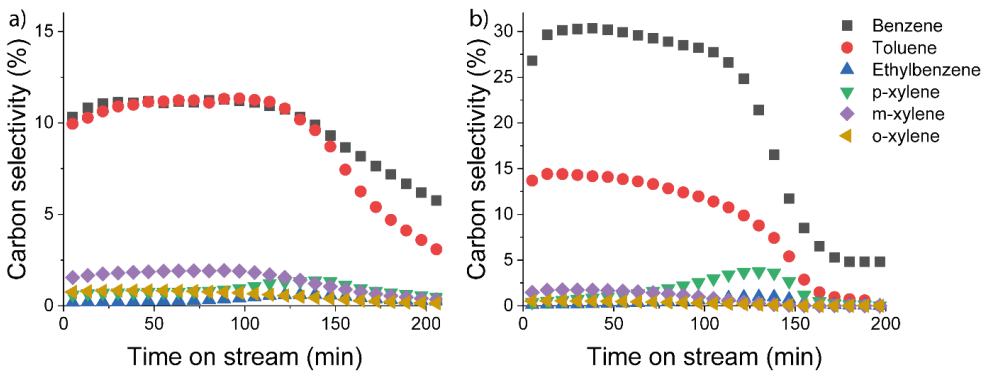

Figure 4.15. Distribution of BTEX aromatics as a function of time-on-stream in the reaction of ethylene with 2,5-dMF over (a) HZSM-5, and (b) Ga(4)RO . Conditions: T = 450 °C; p(2,5-dMF) = p(C_2H_4) = 0.2 kPa; in 100 ml/min Ar.

Finally, to evaluate catalyst stability we carried out 10 reaction-regeneration experiments (Figure 4.16). Intermediate regeneration was carried out at 550 °C (ramp rate 5 °C /min,) in 20% O_2 in Ar. Although water evolving during the reaction and regeneration might cause dealumination of the zeolite[48], the catalytic activity remained at the same level after 10 reaction-regeneration cycles. These results indicate that Ga/HZSM-5 is an active and stable catalyst for cyclic reaction-regeneration operation of co-aromatization of furans with ethylene.

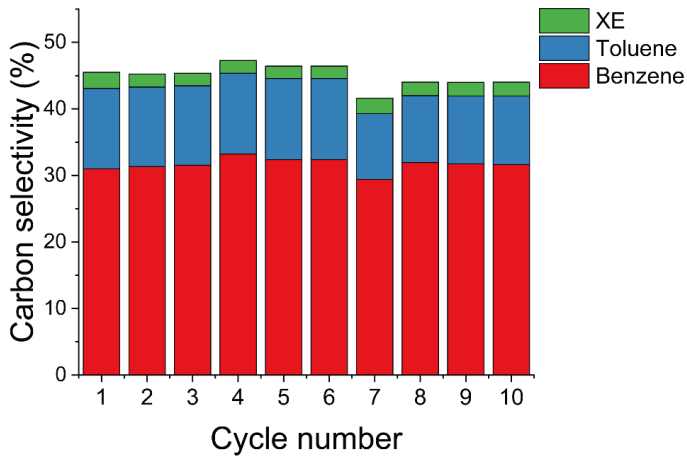

Figure 4.16. Aromatic selectivity under the sequential reaction regeneration cycles aromatization reaction of 2,5-dMF with co-feeding of ethylene on Ga(4)RO catalysts. Conditions: T = 450 °C; p(2,5-dMF) = p(C_2H_4) = 0.2 kPa in100 ml/min Ar

4.4 Conclusions

By applying a wide range of characterization methods, including SEM-EDX, XPS, NH_3-TPD, FT-IR and UV/Vis DRS and CFM, we showed that Ga-oxide clusters are abundantly present on the external surface of the HZSM-5 zeolite crystals after impregnation. Upon reduction and re-oxidation, these large agglomerates are dispersed into the zeolite micropores and nearly quantitatively exchanged as $(GaO)_x^{x+}$ species. A high dispersion and the absence of Ga-oxide on the external zeolite surface can be achieved in this manner, when the Ga loading is kept below 4 wt. %. The cationic Ga species substitute Brønsted acid sites, resulting in a lowering of the Brønsted acidity and an increase of the Lewis acidity of Ga/HZSM-5. The evaluation of these catalysts in the co-aromatization of 2,5-dMF with ethylene showed a positive role of Ga-promotion on the BTEX productivity. The role of ethylene is more complex in this reaction and cannot be attributed exclusively to Diels-Alder chemistry. Ethylene most likely participates in various alkylation and trans-alkylation reactions affecting the net reaction network. The BTEX selectivity increased proportionally to the concentration of exchanged GaO^+ sites, implying that Ga LAS play an important role in the reaction. Finally, we found that an optimized Ga(4)RO catalysts is stable during at least 10 reaction–regeneration cycles, proving the high stability of cationic Ga-oxo-species in Ga/HZSM-5.

4.5 Acknowledgements

Evgeny Uslamin (Eindhoven University of Technology) is acknowledged for his contribution in developing this work. Jochem Wijten (Utrecht University) is thanked for measuring SEM-EDX.

4.6 References

(1) Corma, A.; Huber, G.; Sauvanaud, L.; Oconnor, P. Processing Biomass-Derived Oxygenates in the Oil Refinery: Catalytic Cracking (FCC) Reaction Pathways and Role of Catalyst. *J. Catal.* **2007**, *247*, 307–327. https://doi.org/10.1016/j.jcat.2007.01.023.

(2) Williams, C. L.; Chang, C. C.; Do, P.; Nikbin, N.; Caratzoulas, S.; Vlachos, D. G.; Lobo, R. F.; Fan, W.; Dauenhauer, P. J. Cycloaddition of Biomass-Derived Furans for Catalytic Production of Renewable *p*-Xylene. *ACS Catal.* **2012**, *2*, 935–939.

https://doi.org/10.1021/cs300011a.

(3) Rezaei, P. S.; Shafaghat, H.; Daud, W. M. A. W. Production of Green Aromatics and Olefins by Catalytic Cracking of Oxygenate Compounds Derived from Biomass Pyrolysis: A Review. *Appl. Catal. A Gen.* **2014**, *469*, 490–511. https://doi.org/10.1016/j.apcata.2013.09.036.

(4) Kubička, D.; Kikhtyanin, O. Opportunities for Zeolites in Biomass Upgrading—Lessons from the Refining and Petrochemical Industry. *Catal. Today* **2015**, *243*, 10–22. https://doi.org/10.1016/j.cattod.2014.07.043.

(5) Graaff, W. N. P. Van Der; Pidko, E. A.; Hensen, E. J. M. Zeolite Catalysis for Biomass Conversion. In *Zeolites in Sustainable Chemistry: Synthesis, Characterization and Catalytic Applications*; Xiao, F.-S., Meng, X., Eds.; Green Chemistry and Sustainable Technology; Springer, Berlin, **2016**, 347–372. https://doi.org/10.1007/978-3-662-47395-5.

(6) Ennaert, T.; Van Aelst, J.; Dijkmans, J.; De Clercq, R.; Schutyser, W.; Dusselier, M.; Verboekend, D.; Sels, B. F. Potential and Challenges of Zeolite Chemistry in the Catalytic Conversion of Biomass. *Chem. Soc. Rev.* **2016**, *45*, 584–611. https://doi.org/10.1039/c5cs00859j.

(7) Sheldon, R. A. Green and Sustainable Manufacture of Chemicals from Biomass: State of the Art. *Green Chem.* **2014**, *16*, 950–963. https://doi.org/10.1039/C3GC41935E.

(8) Rohling, R. Y.; Uslamin, E.; Zijlstra, B.; Tranca, I. C.; Filot, I. A. W.; Hensen, E. J. M.; Pidko, E. A. An Active Alkali-Exchanged Faujasite Catalyst for p -Xylene Production via the One-Pot Diels–Alder Cycloaddition/Dehydration Reaction of 2,5-Dimethylfuran with Ethylene. *ACS Catal.* **2018**, *8*, 760–769. https://doi.org/10.1021/acscatal.7b03343.

(9) Settle, A. E.; Berstis, L.; Rorrer, N. A.; Roman-Leshkóv, Y.; Beckham, G. T.; Richards, R. M.; Vardon, D. R. Heterogeneous Diels–Alder Catalysis for Biomass-Derived Aromatic Compounds. *Green Chem.* **2017**, *19*, 3468–3492. https://doi.org/10.1039/C7GC00992E.

(10) Ramirez-Corredores, M. M. The Role of Catalysis for the Sustainable Production of Bio-fuels and Bio-chemicals; *Pathways and Mechanisms of Fast Pyrolysis.* Triantafyllidis K. S.; Lappas A. A.; Stöcker M.; Eds., Elsevier, **2013**; 161–216.

https://doi.org/10.1016/B978-0-444-56330-9.00006-1.

(11) Cheng, Y. T.; Huber, G. W. Chemistry of Furan Conversion into Aromatics and Olefins over HZSM-5: A Model Biomass Conversion Reaction. *ACS Catal.* **2011**, *1*, 611–628. https://doi.org/10.1021/cs200103j.

(12) Carlson, T. R.; Tompsett, G. A.; Conner, W. C.; Huber, G. W. Aromatic Production from Catalytic Fast Pyrolysis of Biomass-Derived Feedstocks. *Top. Catal.* **2009**, *52*, 241–252. https://doi.org/10.1007/s11244-008-9160-6.

(13) Uslamin, E. A.; Kosinov, N. A.; Pidko, E. A.; Hensen, E. J. M. Catalytic Conversion of Furanic Compounds over Ga-Modified ZSM-5 Zeolites as a Route to Biomass-Derived Aromatics. *Green Chem.* **2018**, *20*, 3818–3827. https://doi.org/10.1039/C8GC01528G.

(14) Cheng, Y. T.; Jae, J.; Shi, J.; Fan, W.; Huber, G. W. Production of Renewable Aromatic Compounds by Catalytic Fast Pyrolysis of Lignocellulosic Biomass with Bifunctional Ga/ZSM-5 Catalysts. *Angew. Chem. Int. Ed.* **2012**, *51*, 1387–1390. https://doi.org/10.1002/anie.201107390.

(15) Cheng, Y.-T.; Huber, G. W. Production of Targeted Aromatics by Using Diels–Alder Classes of Reactions with Furans and Olefins over ZSM-5. *Green Chem.* **2012**, *14*, 3114–3125. https://doi.org/10.1039/c2gc35767d.

(16) Hagen, A.; Roessner, F. Ethane to Aromatic Hydrocarbons: Past, Present, Future. *Catal. Rev.* **2000**, *42*, 403–437. https://doi.org/10.1081/CR-100101952.

(17) Bhan, A.; Delgass, W. N. Propane Aromatization over HZSM-5 and Ga/HZSM-5 Catalysts. *Catal. Rev. Sci. Eng.* **2008**, *50*, 19–151. https://doi.org/10.1080/01614940701804745.

(18) Qiu, P.; Lunsford, J.; Rosynek, M. Characterization of Ga/ZSM-5 for the Catalytic Aromatization of Dilute Ethylene Streams. *Catal. Lett.* **1998**, *52*, 37–42.

(19) Lalik, E.; Liu, X.; Klinowski, J. The Role of Gallium in the Catalytic Activity of Zeolite [Si, Ga]-ZSM-5 for Methanol Conversion. *J. Phys. Chem.* **1992**, *96*, 805–809. https://doi.org/10.1021/j100181a051.

(20) Hensen, E. J. M.; García-Sánchez, M.; Rane, N.; Magusin, P. C. M. M.; Liu, P. H.; Chao, K. J.; Van Santen, R. A. *In Situ* Ga K Edge XANES Study of the Activation of Ga/ZSM-5 Prepared by Chemical Vapor Deposition of Trimethylgallium. *Catal. Lett.* **2005**, *101*, 79–85. https://doi.org/10.1007/s10562-004-3753-x.

(21) Kazansky, V. B.; Subbotina, I. R.; van Santen, R. A.; Hensen, E. J. M. DRIFTS Study of the Chemical State of Modifying Gallium Ions in Reduced Ga/ZSM-5 Prepared by Impregnation. I. Observation of Gallium Hydrides and Application of CO Adsorption as Molecular Probe for Reduced Gallium Ions. *J. Catal.* **2004**, *227*, 263–269. https://doi.org/10.1016/j.jcat.2004.07.021.

(22) Kazansky, V. B.; Subbotina, I. R.; Van Santen, R. A.; Hensen, E. J. M. DRIFTS Study of the Nature and Chemical Reactivity of Gallium Ions in Ga/ZSM-5: II. Oxidation of Reduced Ga Species in ZSM-5 by Nitrous Oxide or Water. *J. Catal.* **2005**, *233*, 351–358. https://doi.org/10.1016/j.jcat.2005.05.004.

(23) Rane, N.; Overweg, A. R.; Kazansky, V. B.; van Santen, R. A.; Hensen, E. J. M. Characterization and Reactivity of Ga^+ and GaO^+ Cations in Zeolite ZSM-5. *J. Catal.* **2006**, *239*, 478–485. https://doi.org/10.1016/j.jcat.2006.03.004.

(24) Hensen, E. J. M.; Pidko, E. A.; Rane, N.; Van Santen, R. A. Water-Promoted Hydrocarbon Activation Catalyzed by Binuclear Gallium Sites in ZSM-5 Zeolite. *Angew. Chem. - Int. Ed.* **2007**, *46*, 7273–7276. https://doi.org/10.1002/anie.200702463.

(25) Kazansky, V. B.; Subbotina, I. R.; Pronin, A. A.; Schlögl, R.; Jentoft, F. C. Unusual Infrared Spectrum of Ethane Adsorbed by Gallium Oxide. *J. Phys. Chem. B* **2006**, *110*, 7975–7978. https://doi.org/10.1021/jp055793w.

(26) Van Bokhoven, J. A.; Williams, B. A.; Ji, W.; Koningsberger, D. C.; Kung, H. H.; Miller, J. T. Observation of a Compensation Relation for Monomolecular Alkane Cracking by Zeolites: The Dominant Role of Reactant Sorption. *J. Catal.* **2004**, *224*, 50–59. https://doi.org/10.1016/j.jcat.2004.02.003.

(27) Pidko, E. A.; Kazansky, V. B.; Hensen, E. J. M.; van Santen, R. A. A Comprehensive Density Functional Theory Study of Ethane Dehydrogenation over Reduced Extra-Framework Gallium Species in ZSM-5 Zeolite. *J. Catal.* **2006**, *240*, 73–84.

https://doi.org/10.1016/j.jcat.2006.03.011.

(28) Rane, N.; Kersbulck, M.; van Santen, R. A.; Hensen, E. J. M. Cracking of N-Heptane over Brønsted Acid Sites and Lewis Acid Ga Sites in ZSM-5 Zeolite. *Microporous Mesoporous Mater.* **2008**, *110*, 279–291. https://doi.org/10.1016/j.micromeso.2007.06.014.

(29) Caeiro, G.; Carvalho, R. H.; Wang, X.; Lemos, M. A. N. D. A.; Lemos, F.; Guisnet, M.; Ramôa Ribeiro, F. Activation of C2-C4 Alkanes over Acid and Bifunctional Zeolite Catalysts. *J. Mol. Catal. A Chem.* **2006**, *255*, 131–158. https://doi.org/10.1016/j.molcata.2006.03.068.

(30) Datka, J. Acidic Properties of Supported Niobium Oxide Catalysts: An Infrared Spectroscopy Investigation. *J. Catal.* **1992**, *135*, 186–199. https://doi.org/10.1016/0021-9517(92)90279-Q.

(31) Emeis, C. A. Determination of Integrated Molar Extintion Coefficients for Infrared Absorption Bands of Pyridine Adsorbed on Solid Acid Catalysts. *J. Catal.* **1993**,141, 347–354. https://doi.org/http://dx.doi.org/10.1006/jcat.1993.1145.

(32) Fricke, R.; Kosslick, H.; Lischke, G.; Richter, M. Incorporation of Gallium into Zeolites: Syntheses, Properties and Catalytic Application. *Chem. Rev.* **2000**, *100*, 2303–2405. https://doi.org/10.1021/cr9411637.

(33) Wu, E. L.; Lawton, S. L.; Olson, D. H.; Rohrman, A. C.; Kokotallo, G. T. ZSM-5-Type Materials. Factors Affecting Crystal Symmetry. *J. Phys. Chem.* **1979**, *83*, 2777–2781. https://doi.org/10.1021/j100484a019.

(34) Sandoval-Díaz, L. E.; González-Amaya, J. A.; Trujillo, C. A. General Aspects of Zeolite Acidity Characterization. *Microporous Mesoporous Mater.* **2015**, *215*, 229–243. https://doi.org/10.1016/j.micromeso.2015.04.038.

(35) Topsøe, N. Y.; Pedersen, K.; Derouane, E. G. Infrared and Temperature-Programmed Desorption Study of the Acidic Properties of ZSM-5-Type Zeolites. *J. Catal.* **1981**, *70*, 41–52. https://doi.org/10.1016/0021-9517(81)90315-8.

(36) Pidko, E. A.; Hensen, E. J. M.; van Santen, R. A. Self-Organization of Extraframework Cations in Zeolites. *Proc. R. Soc. A Math. Phys. Eng. Sci.* **2012**, *468*, 2070–2086.

https://doi.org/10.1098/rspa.2012.0057.

(37) Pidko, E. A.; van Santen, R.; Hensen, E. J. M. Multinuclear Gallium-Oxide Cations in High-Silica Zeolites. *Phys. Chem. Chem. Phys.* **2009**, *11*, 2794–2798. https://doi.org/10.1039/b905015a.

(38) Kox, M. H. F.; Stavitski, E.; Groen, J. C. C.; Pérez-Ramírez, J.; Kapteijn, F.; Weckhuysen, B. M. Visualizing the Crystal Structure and Locating the Catalytic Activity of Micro- and Mesoporous ZSM-5 Zeolite Crystals by Using In Situ Optical and Fluorescence Microscopy. *Chem. Eur. J.* **2008**, *14*, 1718–1725. https://doi.org/10.1002/chem.200701591.

(39) Aramburo, L. L. R. L.; Ruiz-Martínez, J.; Hofmann, J. P.; Weckhuysen, B. M. Imaging the Effect of a Hydrothermal Treatment on the Pore Accessibility and Acidity of Large ZSM-5 Zeolite Crystals by Selective Staining. *Catal. Sci. Technol.* **2013**, *3*, 1208–1214. https://doi.org/10.1039/c2cy20661g.

(40) Buurmans, I. L. C.; Ruiz-Martínez, J.; Vana Leeuwen, S. L.; Vana Dera Beek, D.; Bergwerff, J. A.; Knowles, W. V.; Vogt, E. T. C.; Weckhuysen, B. M. Staining of Fluid-Catalytic-Cracking Catalysts: Localising Brønsted Acidity within a Single Catalyst Particle. *Chem. Eur. J.* **2012**, *18*, 1094–1101. https://doi.org/10.1002/chem.201102949.

(41) Sprung, C.; Weckhuysen, B. M. Differences in the Location of Guest Molecules within Zeolite Pores as Revealed by Multilaser Excitation Confocal Fluorescence Microscopy: Which Molecule Is Where? *J. Am. Chem. Soc.* **2015**, *137*, 1916–1928. https://doi.org/10.1021/ja511381f.

(42) Bjørgen, M.; Bonino, F.; Kolboe, S.; Lillerud, K. P.; Zecchina, A.; Bordiga, S. Spectroscopic Evidence for a Persistent Benzenium Cation in Zeolite H-Beta. *J. Am. Chem. Soc.* **2003**, *125*, 15863–15868. https://doi.org/10.1021/ja037073d.

(43) Aramburo, L. R.; Karwacki, L.; Cubillas, P.; Asahina, S.; De Winter, D. A. M.; Drury, M. R.; Buurmans, I. L. C.; Stavitski, E.; Mores, D.; Daturi, M.; Bazin P.; Dumas P.; Thibault-Starzyk F.; Post J. A.; Anderson M. W.; Terasaki O.; Weckhuysen B.M.;. The Porosity, Acidity, and Reactivity of Dealuminated Zeolite ZSM-5 at the Single Particle Level: The Influence of the Zeolite Architecture. *Chem. Eur. J.* **2011**, *17*, 13773–13781. https://doi.org/10.1002/chem.201101361.

(44) Lifshitz, A.; Tamburu, C.; Shashua, R. Thermal Decomposition of 2,5-Dimethylfuran. Experimental Results and Computer Modeling. *J. Phys. Chem. A* **1998**, *102*, 10655–10670. https://doi.org/10.1021/jp982772b.

(45) Guisnet, M.; Gnep, N. S.; Alario, F. Aromatization of Short Chain Alkanes on Zeolite Catalysts. *Appl. Catal. A, Gen.* **1992**, *89*, 1–30. https://doi.org/10.1016/0926-860X(92)80075-N.

(46) Parmon, V. N. Catalysis and Non-Equilibrium Thermodynamics: Modern in Situ Studies and New Theoretical Approaches. *Catal. Today* **1999**, *51*, 435–456. https://doi.org/10.1016/S0920-5861(99)00032-2.

(47) Luzgin, M. V.; Rogov, V. A.; Arzumanov, S. S.; Toktarev, A. V.; Stepanov, A. G.; Parmon, V. N. Understanding Methane Aromatization on a Zn-Modified High-Silica Zeolite. *Angew. Chem. Int. Ed.* **2008**, *47*, 4559–4562. https://doi.org/10.1002/anie.200800317.

(48) Kosinov, N.; Coumans, F. J. A. G.; Li, G.; Uslamin, E.; Mezari, B.; Wijpkema, A. S. G.; Pidko, E. A.; Hensen, E. J. M. Stable Mo/HZSM-5 Methane Dehydroaromatization Catalysts Optimized for High-Temperature Calcination-Regeneration. *J. Catal.* **2017**, *346*, 125–133. https://doi.org/10.1016/j.jcat.2016.12.006.

Chapter 5 Zinc-promoted HZSM-5 Zeolite Catalysts for the Aromatization of Biomass-derived 2,5-Dimethylfuran with Ethylene

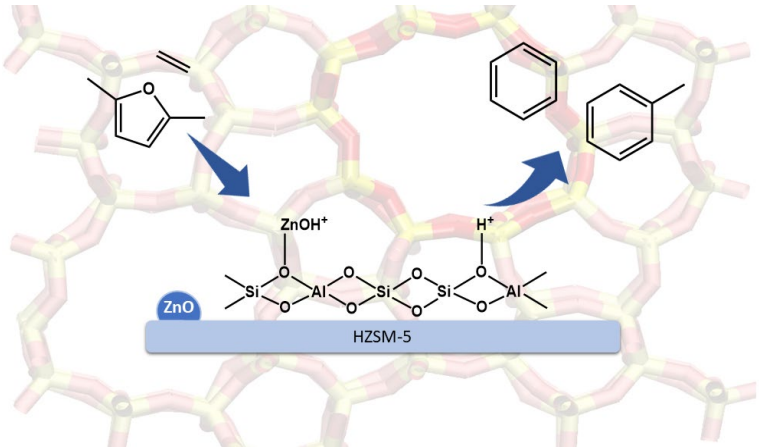

Abstract

The renewable bulk aromatics Benzene, Toluene and Xylenes (BTX) can be synthesized via the aromatization of biobased 2,5-dimethylfuran (DMF) in the presence of ethylene. In this Chapter, we report a set of Zn-promoted ZSM-5 zeolite catalysts as efficient catalysts for this reaction. The incorporation of Zn adds dehydrogenation activity to the HZSM-5 zeolites, thereby influencing the aromatization efficiency of the catalysts. Incorporation of Zn (1.5-3 wt.%) by incipient wetness impregnation to microporous only as well as hierarchical HZSM-5 zeolites led to a homogeneous dispersion of zinc over the zeolite crystals, as shown by SEM-EDX mapping, with no or little occlusion of the zeolite's micropores, as revealed by Ar physisorption. A decrease of the number of Brønsted Acid Sites (BAS) was observed by pyridine-probed FT-IR spectroscopy as a result of Zn^{2+} cation exchange. ZnO clusters were also formed on the external surface area, partly blocking access to the micropores, but only for the highest Zn loadings (3 wt.%). This resulted in up to a 40% acidity decrease for 3Zn-H15 compared to the benchmark catalyst (H15). Aromatization of DMF was studied at 500 °C with and without ethylene co-feeding, with the highest BTX selectivity (73.5% compared to 55.9% with H15 at 90% conversion) shown by the Zn/HZSM-5 catalyst with the highest Zn content and in the presence of ethylene. Zn addition thus did improve BTX selectivity, but at the expense of increased coke formation, possibly by condensation of the aromatics formed on the Zn sites.

5.1 Introduction

The aromatization of furan derivatives towards benzene, toluene and xylenes (BTX) over HZSM-5 zeolites has been widely investigated in the last decades as part of the efforts aimed at biomass valorization. In a more general sense, this particular reaction is part of the ZSM-5 catalyzed oxygenate-to-aromatics family of processes, such as the well-studied Methanol-to-Hydrocarbons (MTH) process. As also often seen with other oxygenates, the 2,5-dimethylfuran (DMF) conversion route still suffers from low carbon efficiency and rapid catalyst deactivation and thus, requires further attention[1,2]. Indeed, high temperature, gas-phase processes for the aromatization of biomass-derived oxygenates, such as DMF, given their high oxygen content (and resulting low H/C_{eff} ratio), show much faster deactivation than when using oxygen-free feedstocks, mainly because of the fast production of carbonaceous deposits[3]. It has also been shown that BTX production can be enhanced by the addition of light olefins, such as ethylene, to the feed. This increase in efficiency has been proposed to be the result of Diels-Alder (D-A) cycloaddition aromatization[4,5], while more recent studies suggest the olefins to play a more complex role than solely participating in the D-A mechanism. These last investigations suggest that different reaction pathways might be taking place (i.e., a hydrocarbon pool mechanism is involved, as is commonly accepted for the MTH process)[6]. Several recent studies also revealed that a combination of both Lewis Acid Sites (LAS) and medium-weak Brønsted Acid Sites (BAS) improves aromatization rates, while at the same time lowers the formation of carbon deposits[7–10]. When located within the micropores and channels as cations, gallium, for example, adds Lewis acidity to the zeolite, contributing positively to the aromatization of furan derivates. This has been discussed in more detail in Chapter 4 of this PhD Thesis[9]. Introducing Ga cations with dehydrogenation activity comes at the expense of a reduction in the number of Brønsted acid sites, which together results in an enhanced BTX selectivity. More specifically, for the aromatization of 2,5-dimethylfuran (DMF) in the presence of ethylene, Ga-promoted ZSM-5 zeolites resulted in improved BTX yields by improving the selectivity mostly towards the formation of benzene, while the selectivity for the more valuable alkylated aromatics, such as toluene and xylenes, remained the same[6,9,11].

Another method to modify Lewis acidity in zeolites is by the incorporation of Zn as promotor. Zn-containing ZSM-5 zeolites (Zn/ZSM-5) catalyst have been used widely for the aromatization of light hydrocarbons, exploiting their high dehydrogenation activity[12–16]. They have also been tested during the conversion of organic oxygenates, such as alcohols[17–20]. Zn speciation in ZSM-5 zeolite has been extensively studied, e.g. as function of the impregnation

method used[21–23]. As demonstrated by Hensen *et al.,* introduction of cationic Zn species, the nature of which depends on the deposition method, leads to a decrease in the number of BAS, thus inhibiting the strong cracking properties of ZSM-5 zeolites and favoring ring-closure reactions[24]. The suggested mechanism involving Zn-containing zeolites is known to occur via the activation of C-H bonds resulting in the formation of a strong molecular complex between the adsorbed carbon substrate and the Zn-based Lewis acid sites, which subsequently leads to the production of H_2 and an alkene[25]. Kazansky *et al.* suggested that an exchange of the BAS can be achieved by single Zn^{2+} cations and by bridging zinc oxide moieties $[Zn\text{-}O\text{-}Zn]^{2+}$. Further investigations suggested not only the presence of isolated Zn^{2+}, but pointed at the formation of $ZnOH^{+}$ cations as active Zn dehydrogenation sites, species formed at the expense of external silanol groups[20,24]. Later theoretical studies performed by Li *et al.*[26], noted that different oxo-, hydroxy-, and isolated Zn cations can be responsible for the dehydrogenation activity. However, as reported in previous studies, increase in activity brought by introduction of these Zn species is typically accompanied by a more rapid deactivation, as the highly active Zn species cause polyaromatic coke to form more rapidly than with the unmodified ZSM-5 catalysts[20,27–29]. As reported previously, the introduction of mesopores to a microporous system containing Zn can attenuate catalyst deactivation[30–32]. Unlike for the aromatization of alcohols, to the best of our knowledge, only very few investigations about the effect of Zn promotors for the aromatization of other oxygenates have been reported[33–35], dealing in particular with carbohydrates, furfural and furan, but not dimethylfuran.

As the nature and degree of furan substitution is known to strongly affect the outcome of catalytic aromatization[6], in this Chapter we have studied the catalytic performance of a series of Zn-promoted HZSM-5 zeolites with different Zn loading (1.5-3 wt.%) during DMF aromatization. The two different Zn loadings investigated modify the Brønsted and Lewis acidity of the catalyst to different extents and hence, catalyst performance. We report a positive effect of Zn promotion on the selectivity to aromatics, in particular, to alkylated aromatics. Moreover, by incorporating zinc promotors within a hierarchical zeolite system, we were able to further boost aromatics production. Furthermore, in some cases the incorporation of mesopores enhanced accessibility, thereby reducing diffusion limitations and hence improving the lifetime and stability of the zeolite-based catalysts.

5.2 Experimental Part

5.2.1 Catalyst Preparation and Reagents

The H^+ form of ZSM-5 zeolites with Si/Al = 15 and 40 was obtained by calcination of the commercial (NH_4^+)ZSM-5 zeolite (CBV 8014 and CBV 3024E, Zeolyst) at 550 °C for 5 h under air. Hierarchical zeolites (H15-A and H40-A) were prepared following the alkaline treatment, already described in Chapter 2 of this PhD Thesis[36]. The H^+ form samples with Si/Al = 15, and 40 were labelled as H15 and H40, while the alkaline-treated materials were labelled as H15-A and H40-A, respectively.

Zinc impregnated samples (with 1.5 and 3 wt. % Zn) were prepared by incipient wetness impregnation of the proton form and alkaline treated zeolites (H15 and H15-A) with an aqueous solution containing $Zn(OAc)_2 \cdot 2H_2O$ (98%, Sigma Aldrich) as precursor. Subsequently, samples were dried at 120 °C for 16 h and calcined at 550 °C for 4 h at a rate of 5 °C/min under air[24]. The obtained zinc-containing zeolite materials are labelled as 1.5Zn-H15, 3Zn-H15 and 3Zn-H15-A.

2,5-dimethylfuran (98+%, Alfa Aesar) was purchased and used as feedstock without any treatment. Ethylene was purchased and directly used from a steel cylinder without further treatment (> 99.95% purity, Linde).

5.2.2 Catalyst Characterization

The crystallinity before and after zinc impregnation of the zeolite materials was investigated by X-ray diffraction (XRD) using a Bruker-AXS D2 Phaser powder X-ray diffractometer in Bragg-Brentano mode equipped with a Lynxeye detector. The radiation used was a CoKα (λ = 1.79026 Å) source. The XRD patterns were collected in the 2θ range from 5° to 50° at a scanning speed of 0.02°/min and an acquisition time of 1 s per step.

The specific surface area and porosity of the zeolite materials were determined by Ar physisorption using a Micrometric TriStar Analyzer at -196 °C. Before the experiments were performed, all samples were degassed under a N_2 flow at 300 °C for 16 h to remove any physiosorbed impurities. The micropore volume and the surface area were determined by the *t*-

plot method and the Brunauer-Emmett-Teller (BET) theory, respectively. External surface area was determined by subtraction of the micropore volume area from the BET surface area.

The Si, Al and Zn content of the zeolites was determined by Inductive Coupled Plasma – Optical Emission Spectrometry (ICP-OES) elemental analysis in the Mikroanalytisches laboratorium Kolbe in Oberhauser (Germany). Prior to analysis, all the samples were digested in acid solutions.

Temperature programmed desorption (TPD) with NH_3 as probe molecule was performed with a Micromeritics AutoChem II 2920 equipped with a thermal conductivity detector (TCD) to determine the strength and amount of the acid sites within the zeolite materials. 100 mg of sample was placed within the chamber and pre-treated up to 600 °C under a He flow. The chamber was cooled down and kept at 100 °C before to start the NH_3 dosing. A 25 ml/min flow of 10% NH_3 in He was fed into the chamber using a pulse wise manner until saturation. Afterwards, the temperature was ramped to 600 °C at 10 °C/min and kept at that temperature for 25 min more.

For the Fourier transform-infrared (FT-IR) spectroscopy measurements with pyridine as probe molecule, the samples were grounded and pressed into thin self-supported wafers (~ 25 mg sample). The wafers were placed in a sealed FT-IR cell equipped with a vacuum system and a heating system. The wafers were pre-treated under vacuum (~10^{-3} mbar) at 550 °C for 2 h to remove all adsorbates, then was cooled down to 40 °C where pyridine vapor was introduced into the cell for 30 min until complete saturation. The weakly adsorbed pyridine was removed by evacuation for 1 h. Afterwards, the temperature was ramped from 40 to 150 °C at 2.5 °C/min and kept at 150 °C for 30 min, after which a spectrum was recorded. As described in ref.[37], this step is done to calculate the amount of Lewis acid sites (LAS) and Bronsted acid sites (BAS). In a next step, the temperature was ramped up to 550 °C to remove all pyridine from the sample. All spectra were recorded between 4000-1000 cm^{-1} using a Perkin-Elmer System 2000 instrument.

Fourier transform-infrared (FT-IR) spectroscopy with CO as probe molecule was also performed to investigate both the strength of the acid sites and the nature of the Zn^{2+} species present in the Zn/HZSM-5 zeolites. Approximately 30 mg of zeolite material was grounded and pressed into thin self-supported wafers. Then, the wafer was placed in a sealed FT-IR cell equipped with a vacuum system and a heating system. Prior to CO adsorption, the wafer was pre-treated under vacuum (~10^{-5} mbar) at 500 °C for 2 h to remove all adsorbates. Subsequently,

the wafer was cooled down to -188 °C with liquid N_2 before the dosing of CO (up to 4 mbar) to favor the adsorption of CO on our material ($CO_{b.p.}$= -191.5 °C).

Scanning electron microscopy (SEM)-energy dispersive X-ray analysis (EDX) was carried out to determine the degree of dispersion of zinc within the zeolite material. Prior to the SEM-EDX measurements, all samples were coated with a Pt/Pd layer (~ 4 nm) to reduce charging and increase conductivity. SEM images were performed with a FEI Helios Nanolab 600 FIB-SEM instrument operating at 15.0 kV acceleration voltage. For acquiring the EDX maps, the acceleration voltage was decreased to 2.0 kV while a Silicon Drift Detector (SDD) X-MAX from Oxford Instruments, coupled to the Helios Nanolab microscope, was used.

Thermogravimetric analyses (TGA) under O_2 flow were performed with a Perkin Elmer Pyris 1 TGA analyzer connected to an online mass spectrometer (MS) (OmniStar Pfeiffer). TGA experiments were carried out with ~ 10 mg spent zeolite material, which was kept at 50 °C under 20 mL/min oxygen flow and heated up to 700 °C at 10 °C/ min. The CO_2 (m/z = 44), CO (m/z = 28) and H_2O (m/z = 18) signals monitored by MS allowed to elucidate the degree of coking as well as the nature of the carbon deposits present in the spent catalysts.

5.2.3 Catalyst Testing

The aromatization of 2,5-dimethylfuran (DMF) with or without ethylene was performed in a custom-made reactor setup, as shown in Figure 5.1. For every catalytic test, ~ 55 mg catalyst was placed inside the reactor. All reagents and gases were fed into the reactor using calibrated mass-flow controllers (Bronkhorst). Activation of the catalyst was performed at the reaction temperature (500 °C) for 60 min under O_2/N_2 flow. Subsequently, the reactor was purged with N_2 for 30 min before starting the reaction test. DMF was fed into the reactor (0.78 bar) by means of a saturator using Ar as carrier gas with a WHSV = 0.7 h^{-1}. For the ethylene co-feeding experiments, a calibrated mass-flow controller for ethylene (Bronkhorst) was used. The reaction products were analyzed using an online compact gas chromatograph (GC) (Interscience) equipped with three 25 µl sample loops mounted on a six-way valve. The GC was equipped with three different columns and two different detectors. The C1-C3 products were analyzed with a Rt-QBond column of 3 m length and 0.32 mm diameter equipped with a flame ionization detector (FID). C4-C8/aromatic products were analyzed on a MXT-5 column of 15 m length and 0.28 mm diameter equipped with a FID detector. Non-condensable gases,

such as O_2, H_2, N_2 and CO_2, were analyzed with a Carboxen 1010 column of 10 m length and 0.32 mm diameter equipped with a thermal conductivity detector (TCD).

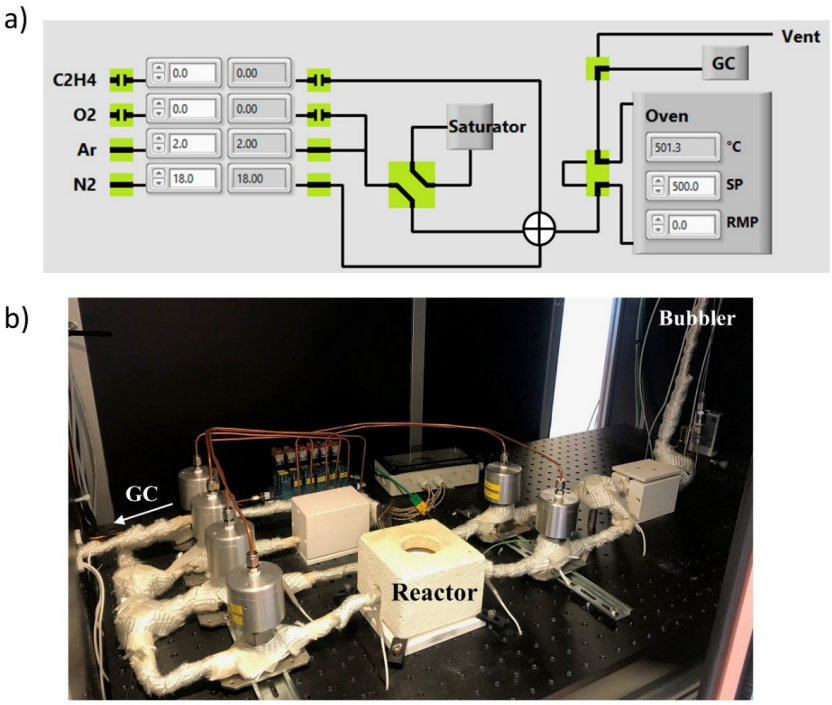

Figure 5.1. (a) Schematic obtained from the LabVIEW program used for running the reactions, depicting the experimental setup configuration used for performing the catalytic experiments and (b) Picture of the setup used for the aromatization of 2,5-dimethylfuran (DMF) in the absence and presence of ethylene over HZSM-5 zeolite-based catalysts.

Conversion, selectivity and yield (carbon-based) for the aromatization of DMF (which is represented as A) with co-feeding of ethylene (which is represented as B) were calculated using the following equations[38]:

$$X_{A,B}(t=x) = \frac{n_{A,B}^{in} - n_{A,B}^{out}}{n_{A,B}^{in}} = 1 - \frac{n_{A,B}^{out}}{n_{A,B}^{in}} \quad \text{(eq. 5.1)}$$

$$S_P(t=x) = \frac{n_P^{out} - n_P^{in}}{n_{A,B}^{in} - n_{A,B}^{out}} \times \left|\frac{\mu_p}{\mu_{A,B}}\right| \quad \text{(eq. 5.2)}$$

$$Y_P(t=x) = \frac{n_P^{out} - n_P^{in}}{n_{A,B}^{in}} = X_{A,B} \times S_P; \quad \text{(eq. 5.3)}$$

where $n^{in}_{A,B}$ and $n^{out}_{A,B}$ represent number of mols of DMF (A) and ethylene (B) entering the reactor and in the outlet, respectively. μ_p and $\mu_{A,B}$ represent the number of carbons of a product p and of the starting reagents A and B (DMF and ethylene), respectively. For the selectivity, conversion and yield calculations of the co-feeding tests, ethylene was included in all calculations together with DMF as starting reagent.

5.3 Results and Discussion

5.3.1 Catalyst Characterization

The physicochemical and structural characterization data of the parent and hierarchical zeolites, namely (H15, H40, H15-A and H40-A) samples, are discussed in detail in Chapter 2 of this PhD Thesis. Zinc-containing zeolites with different amount of Zn (1.5 and 3 wt. %) were synthesized by incipient wetness impregnation (IWI) and thoroughly characterized to assess how the incorporation of zinc affected the zeolite properties. As shown in previous studies, the method of zinc incorporation strongly influences the type of species formed[24]. The IWI method chosen is most commonly used in literature to favor the incorporation of Zn in the channels and porous space.

It is important to note that the crystallinity of the zeolite-based samples was not altered upon incorporation of zinc, as demonstrated by the XRD patterns, shown in Figure 5.2a. Furthermore, within the detection limits of the XRD method crystalline ZnO or zinc acetate precursor peaks were not observed for any of the Zn/ZSM-5 samples (Figure 5.2b), suggesting that ZnO is either highly dispersed over the zeolite crystals or amorphous[16,19,39].

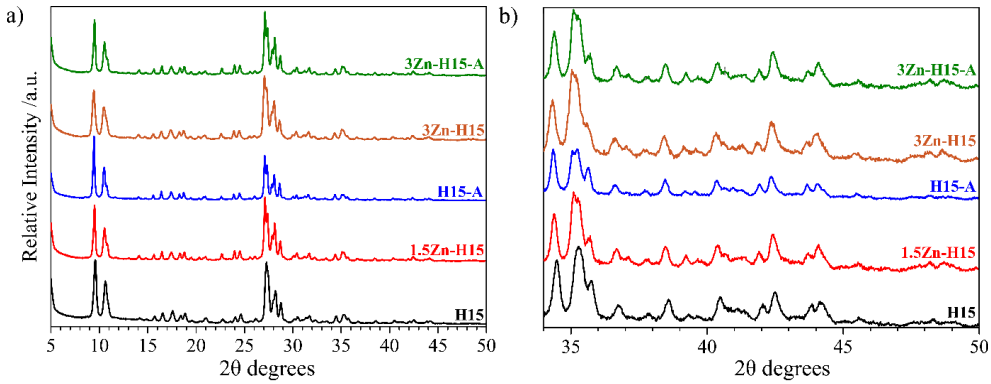

Figure 5.2. X-ray diffraction (XRD) patterns of the different Zn/ZSM-5 catalyst materials under study measured between (a) 5° to 50° and (b) from 34° to 50°.

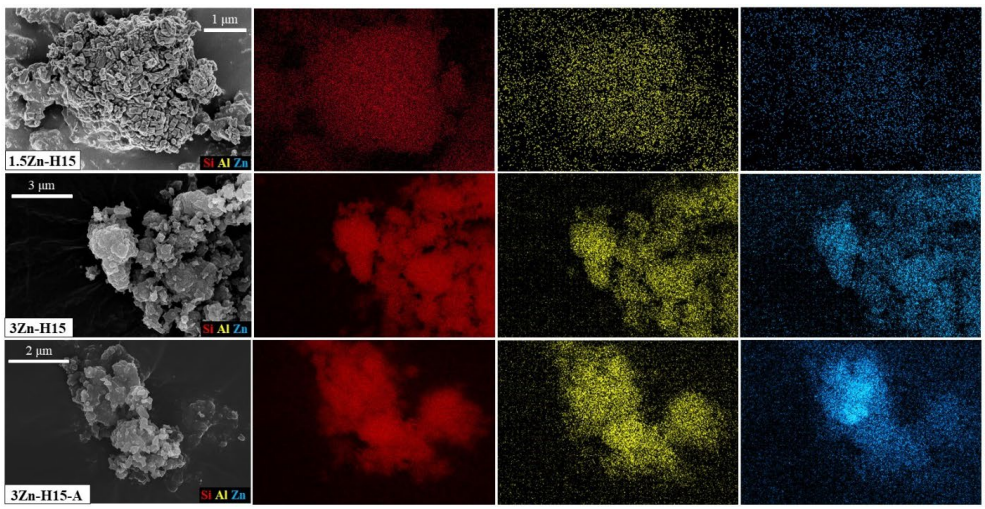

Figure 5.3. Scanning electron microscopy (SEM) images of the different Zn/ZSM-5 catalyst materials under study with Si (red), Al (yellow) and Zn (blue) measured with energy-dispersive X-ray (EDX) analysis.

The distribution of Zn over the zeolite sample was further examined by means of SEM-EDX. The SEM-EDX images in Figure 5.3 show that there is within the limits of the spatial resolution of the analytical methods a homogeneous distribution of Zn over the zeolite crystals in the 1.5Zn-H15 sample. The 3Zn-H15 sample image revealed small clusters of Zn on the zeolite crystals, which are too small and/or amorphous to be observed by XRD. Interestingly, 3Zn-

H15-A displayed much less ZnO agglomerations than its 3 wt. % analogue (3Zn-H15), suggesting that the presence of mesopores favored a better dispersion of Zn[31].

Physicochemical properties of the Zn/ZSM-5 catalysts under study are summarized in Table 5.1. The different results, obtained by ICP-OES and SEM-EDX, for the Zn content of the samples suggest that Zn was preferentially incorporated in the intra-zeolitic framework most probably as cations, rather than as agglomerates/clusters on the external surface or in the pore mouths. After incipient wetness impregnation, we have achieved Zn/Al ratios of 0.4 (1.5 wt. %) and 0.8 (3 wt. %), the latter being above the exchange capacity threshold (i.e., the zeolite material is over-exchanged)[24]. Based on our Ar physisorption studies, the micropore volume and surface area were only slightly affected upon Zn incorporation, confirming the high degree of Zn exchange achieved. Regarding the external surface area, a low percentage of zinc was also deposited at high Zn loading, with 3Zn-H15-A material showing a 40% decrease of the external surface area compared to the parent H15-A material. Moreover, as observed in previous studies[31], a considerable decrease in the mesopore volume and the external surface area was observed for the alkaline-treated sample, suggesting that Zn may be preferentially present in the mesopores. In general, the location and dispersion of Zn were thus found to depend on the differences in the Si/Al ratio and porosity between the diverse parent zeolites[40].

Table 5.1. Physicochemical properties of the HZSM-5 and Zn/HZSM-5 catalyst materials investigated in this Chapter, as determined with [a] inductively coupled plasma-optical emission spectroscopy (ICP-OES), [b] scanning electron microscopy-energy dispersive X-ray (SEM-EDX) analysis, [c] Ar physisorption, [d] NH_3 temperature programmed desorption (TPD) and [e] Fourier transform-infrared (FT-IR) spectroscopy with pyridine as probe molecule. Details of other physicochemical properties for H15 and H15-A samples are given in Chapter 2.

Materials	H15	1.5Zn-H15	3Zn-H15	H15-A	3Zn-H15-A
Si/Al ratio[a]	16	13	13	11	16
Zn/Al ratio[a]	-	0.4	0.8	-	0.8
Zn content[a] wt. %	-	1.1	2.1	-	1.6
Zn content[b] wt. %	-	0.9	1.3	-	2.1
BET area[c] $m^2\ g^{-1}$	462	430	420	394	305
External area[c] $m^2\ g^{-1}$	53	49	45	70	40
(Micro)Pore volume[c] $cm^3\ g^{-1}$	0.14	0.13	0.13	0.11	0.09
Total pore volume[c] $cm^3\ g^{-1}$	0.20	0.19	0.18	0.19	0.15
(Meso)pore volume $cm^3\ g^{-1}$	0.06	0.06	0.05	0.08	0.06
Total acid sites[d] $\mu mol\ g^{-1}_{cat}$	942	970	913	1050	977
Weak acid sites[d] T_{max}, °C	232	218	224	232	214
Strong acid sites[d] T_{max}, °C	421	398	415	418	397
Lewis acid sites[e] $\mu mol\ g^{-1}_{cat}$	100	210	157	128	88
Brønsted acid sites[e] $\mu mol\ g^{-1}_{cat}$	363	118	25	350	34

After the incorporation of zinc, the overall acidity slightly decreased for all samples This can be inferred from the data, obtained by NH_3-TPD, summarized in Table 5.1. As the Zn content increased, new weak-medium acid sites (250-350 °C) were observed in the 3Zn-H15 and 3Zn-H15-A samples (Figure 5.4a and 5.4b), revealing that the Zn^{2+} ions located in the pores and channels space, generate a new type of acid site[16,40]. A clear decrease in the number of BAS upon increasing Zn content is observed for all zeolites by NH_3-TPD. Seemingly, the impregnation method used allows the formation of both ZnO clusters, as suggested by the SEM-EDX measurements, and Zn^{2+} cations at the higher metal loading[18]. The desorption temperature of weak and strong acid sites decreased as compared to the non-promoted zeolites. Pyridine-probed FT-IR spectroscopy revealed that the number of Lewis Acid Sites (LAS) increased with increasing Zn content (Figure 5.5b), which is in accordance with the corresponding NH_3-TPD desorption profile. The NH_3-TPD results for the 3Zn-H15 sample (Figure 5.4a) display a shoulder, which develops at ~ 300 °C and becomes broader for higher Zn loadings. This again suggests that the addition of Zn to the HZSM-5 zeolite-based catalysts generates a new type of acid sites with weak-medium strength and their number increases with increasing Zn content. It is important to remark that with the applied impregnation method, Zn^{2+} cations will be exchanged at the expense of the available H^+ and hence, BAS are converted into LAS by the formation of e.g. $[Z^-Zn^{2+}Z^-]$ (with Z = zeolite) and $ZnOH^+$ species. At higher Zn loadings, Zn oxide clusters are instead known to form preferentially in the zeolite pore mouth and external surface area[20,24]. For hierarchical zeolites, the opposite trend was observed and according to FT-IR spectroscopy

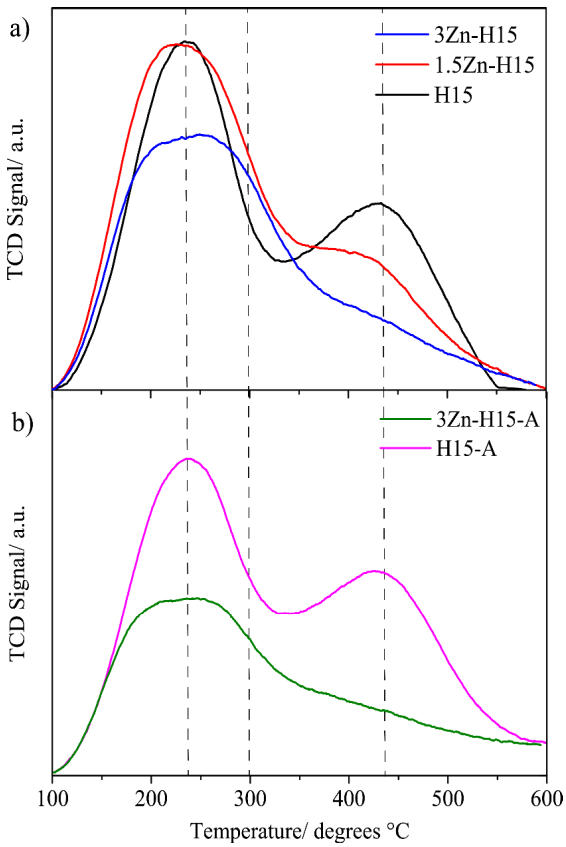

Figure 5.4. Temperature programmed desorption (TPD) for the non-promoted and Zn-promoted HZSM-5 zeolite-based catalysts.

with pyridine as probe molecule, the number of LAS sites decreased with increasing amount of Zn (see Table 5.1)[31,41]. The FT-IR spectra are shown in Figure 5.5b and confirm a high degree of ion exchange, in line with previous work[18,24]. Zinc ion exchange is suggested because the micropore volume values of the obtained materials hardly decreased after zinc impregnation. That H^+ are indeed exchanged for Zn^{2+} can be concluded after examination of the hydroxyl region of the FT-IR spectra, shown in Figure 5.5a. It was found that the peak intensity at ~ 3610 cm^{-1} slightly decreased with increasing zinc loading and ~ 3745 cm^{-1} slightly decreased after Zn impregnation, in line with the formation of $ZnOH^+$ cations[42]. Strikingly, the peak intensity corresponding to OH groups from extra-framework Al (EFAl) species decreased with increasing Zn content, suggesting the possible formation of zinc aluminate clusters (Zn(AlO=)), as previously reported in the literature[43].

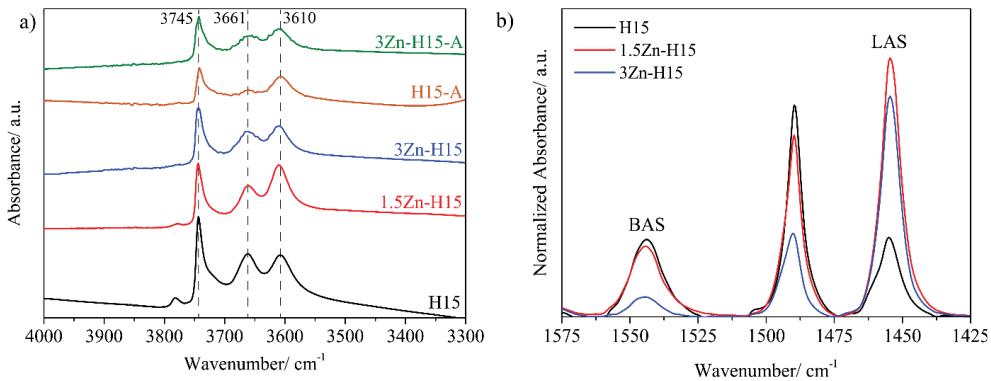

Figure 5.5. (a) Fourier transform-infrared (FT-IR) spectra of the OH region (4000-3300 cm^{-1}) of the fresh catalyst after drying at 500 °C under vacuum (10^{-5} mbar). (b) FT-IR spectra of H15, 1.5Zn-H15 and 3Zn-H15 samples after pyridine desorption at 150 °C. The Bronsted acid sites (BAS) are characterized by the band at ~ 1545 cm^{-1}, while the band at ~ 1445 cm^{-1} shows the presence of Lewis acid sites (LAS). FT-IR spectra were normalized to the structural Si-O stretching vibration peak at 1875 cm^{-1}.

Figure 5.6 highlights the decrease of the overall number of acid sites (Figure 5.6a) as well as of BAS (Figure 5.6b) upon introduction of Zn. The FT-IR spectra of adsorbed CO on HZSM-5 and Zn-promoted HZSM-5 zeolites are displayed in Figure 5.7. Similar to the pyridine-probed FT-IR spectra, a decrease in the intensity of the peak corresponding to BAS was noted upon increasing Zn content, while showing a similar shift for all samples after CO adsorption (shifted from 3610 cm^{-1} to 3273 cm^{-1} for non-promoted HZSM-5 zeolites, and to 3284 cm^{-1} and 3278 cm^{-1} for the promoted Zn/HZSM-5 zeolites)[44].

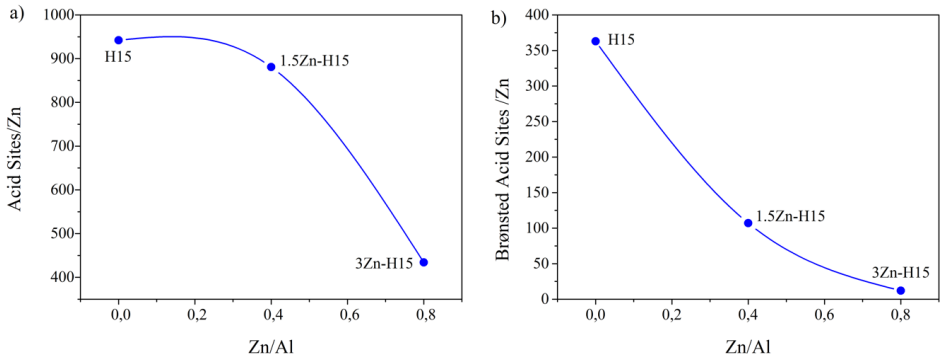

Figure 5.6. Relationship between (a) the decrease of the number of acid sites and increase of Zn loading, as obtained from the temperature programmed desorption (TPD) measurements with NH_3. (b) The decrease of the number of Bronsted acid sites (BAS) and increase of Zn loading.

This difference in red shift is possibly due to the difference in Si/Al ratios (i.e., Si/Al = 13 for H15 and Si/Al = 16 for Zn-promoted HZSM-5) and Zn content from each sample (1.5 wt. % and 3 wt.%). The bands at ~ 3743 cm^{-1} and ~ 3661-3667 cm^{-1} correspond to OH stretching from external silanol groups and extra-framework alumina moieties, which after CO adsorption are shifted to ~ 3586-3595 cm^{-1} and ~ 3487-3490 cm^{-1}, respectively. Furthermore, the FT-IR spectra of adsorbed CO did not show any change in acid strength of the remaining BAS, as no shift was observed for the 2175 cm^{-1} peak that is associated with CO adsorbed on BAS (see Figure 5.7d, 5.7e and, 5.7f)[45]. However, a shoulder did develop at ~ 2165 cm^{-1} upon increasing Zn loading, which is assigned to the interaction of CO with low acidic (extra-framework) Al-OH moieties[42].

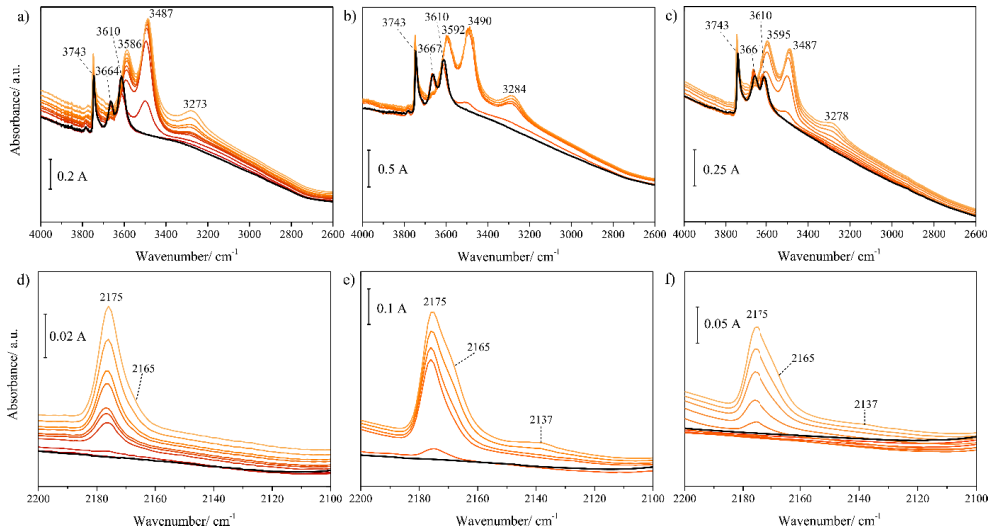

Figure 5.7. Fourier transform-infrared (FT-IR) spectra of CO adsorbed (from 0 to 3 mbar CO adsorbed at -188 °C) on fresh HZSM-5 zeolites (a and d) and promoted 1.5Zn-H15 (b and c) and 3Zn-H15 (e and f) zeolites.

The FT-IR spectra after CO adsorption of the Zn-promoted zeolites also showed bands in the 2200 to 2300 cm^{-1} region, as a result of adsorption of CO on different type of Lewis acid sites (Figure 5.8)[42]. The interpretation of these bands in terms of which Zn species are involved, is still under debate and will be further discussed in this Chapter. According to the current literature, the band at ~ 2210 cm^{-1} can be assigned to Zn^{2+} cations[46,47]. For the 1.5Zn-H15 and the hierarchical 3Zn-H15-A samples, a lower intensity and a small blue shift is exhibited for the 2210 cm^{-1} band (up to 2206 cm^{-1}). The actual Zn loadings of these two samples are 1.1 wt. % Zn for 1.5Zn-H15 and 1.6 wt. % Zn for 3Zn-H15-A, respectively, as determined by ICP-OES. This indicates that the ion exchange is limited by the amount of acid sites available, hence the lower loading obtained. The discrepancies between the NH_3-TPD and pyridine adsorbed FT-IR results have been discussed in Chapter 2. In this particular case, this difference is also caused by the lower accessibility index (ACI) values obtained for the hierarchical H15 zeolites (see Table 2.3 in Chapter 2). That this ACI value is lower than expected from the literature is possibly the result of blockage of the zeolite pores upon desilication and partial dealumination as indicated by the change in the Si/Al ratio. This seems in line with the observed decrease in the FT-IR bands after pyridine adsorption, which indicate a lower zeolite accessibility rather than a higher degree of exchange by Zn^{2+}. The FT-IR band at ~ 2224 cm^{-1} can also be attributed to an interaction of CO with Zn^{2+} cations[20]. The peaks at 2230-2233 cm^{-1} correspond to the

adsorption of CO on different extra-framework aluminum (Lewis) acid sites, suggesting the possible formation of Zn(AlO=) species[42], which would be in line with partial dealumination taking place during desilication of the 3Zn-H15-A sample, since the relative intensity between 2230 and 2210 cm^{-1} is smaller for the 3Zn-H15-A sample than for the 1.5Zn-H15 sample.

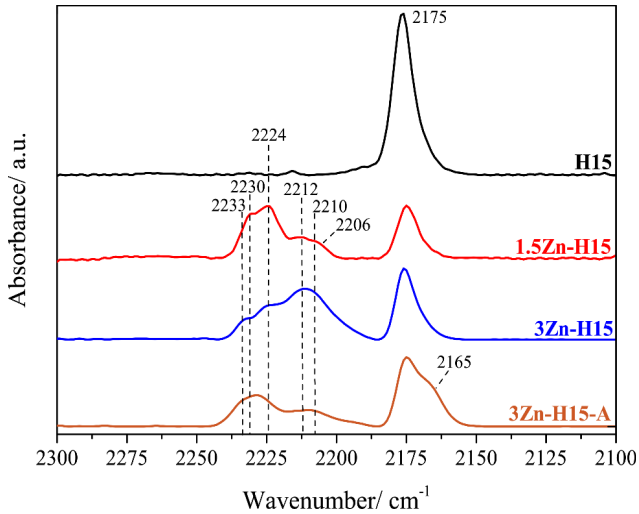

Figure 5.8. Fourier transform-infrared (FT-IR) spectra of fresh non-promoted and Zn promoted zeolites after adsorption of 2 mbar CO at -188 °C.

Taken together, these results suggest that the type of Zn species formed and the degree of ion exchange for the 1.5Zn-H15 and hierarchical 3Zn-H15-A samples are similar. Indeed, a similar number of acid sites was determined by NH_3-TPD, while the intensity and position of the FT-IR bands in the region 2200-2250 cm^{-1} after CO adsorption were also comparable (see Figure 5.8); furthermore, no large ZnO clusters could be observed by SEM-EDX. As previously mentioned, a possible explanation for the lower degree of exchange for the hierarchical 3Zn-H15-A sample could lie in its lower accessibility index. In contrast, for the 3Zn-H15 zeolite sample, ZnO clusters were detected, together with a higher degree of exchange by Zn^{2+} (i.e., a lower amount of remaining BAS), as determined by NH_3-TPD and pyridine-probed FT-IR spectroscopy. The higher intensity of the band ~ 2210 cm^{-1} further confirmed the higher degree of Zn ion exchange.

5.3.2 Catalyst Testing

In a second stage of our study, the well-characterized HZSM-5 zeolite samples, differing in their Si/Al ratio, mesoporosity and Zn loading, were tested in the aromatization of DMF at 500 °C in the absence and presence of ethylene. It was found that, regardless of the Si/Al ratio and porosity, all non-promoted HZSM-5 zeolite catalysts gave similar conversion values after 10 min time-on-stream (Figure 5.9b), although each HZSM-5 sample did show a different deactivation rate. All catalyst materials displayed a linear deactivation rate. The trend in decrease in conversion shown here for the conversion of DMF does not fully correspond to what has been previously reported for this type of reactions[9,48]. The reactor configuration and how the catalysts is placed in the catalyst bed might be a reason of this difference (for clarity see Figure 5.1b). The reactor employed during these studies was designed for performing *operando* spectroscopic studies with a tilted orientation of the catalyst bed, resulting in the unavoidable presence of dead volume. As the catalyst bed is in a tilted position in the reactor to allow for spectroscopic measurements, part of the gas flow bypasses the bed, resulting in the conversion values obtained. The lower acidity of the H40 and H40-A samples is reflected in slower deactivation compared to the H15-based samples. However, the mesoporosity of H40-A and H15-A did further reduce deactivation compared to H40 and H15. In other words, reduction in acidity did reduce deactivation rates, while the incorporation of mesoporosity did not slow down the deactivation rate of the HZSM-5 zeolite samples. A more severe alkaline treatment (i.e., longer post-treatment times or higher concentrations of NaOH solution) would lead to larger mesopores and improved accessibility, possibly resulting in a lower deactivation rate[49].

When comparing the effect of Zn loading, hardly any difference was observed in the deactivation rates between the non-promoted and Zn-promoted zeolites (Figure 5.9d), with the 3Zn-H15 sample giving the highest conversion after 10 min TOS. As reported previously by other authors, the catalysts with the highest Zn loadings deactivated only slightly faster (3Zn-H15 and 3Zn-H15-A), when comparing their results with the benchmark catalyst[20,28,29]. The amounts of coke formed after 125 min of reaction are given in Table 5.2. The results show that more coke is produced on the hierarchical zeolites than on the pristine zeolites. Furthermore, the addition of Zn also led to an increased formation of coke deposits. Although it is known that hierarchical systems should enhance diffusion and are, hence, expected to limit deactivation by coke buildup, higher amount of coke deposits were in fact preferentially formed in the hierarchical systems when compared to their unmodified analogous (H15 or H40)[49,50].

A summary of the product distribution obtained at 125 min reaction, as given in Table 5.2, shows that the DMF conversion dropped by 55% from the initial conversion, especially for the hierarchical and Zn-promoted zeolite material (i.e., 3Zn-H15-A). This drop in conversion is thought to be correlated with the decrease in number of BAS. Furthermore, the higher initial aromatization activity as a result of a high amount of Lewis acid sites, is also thought to contribute to catalyst deactivation, as these aromatics are also considered coke precursors.

The selectivity towards BTX at 90% conversion during the DMF reactions in the absence of ethylene are shown in Figure 5.9a and 5.9c. For the non-promoted zeolite catalysts, the highest BTX selectivity at 90% conversion was obtained by the hierarchical H15-A zeolite catalyst (56.7%), followed by the benchmark unmodified H15 zeolite catalyst. In line with previous investigations[19,51], the incorporation of Zn boosted the selectivity towards aromatics. When aromatization of DMF was performed over 1.5Zn-H15 catalyst, the highest BTX selectivity was obtained (72.4%). The selectivity to BTX as function of time when using non-promoted and Zn-promoted zeolite catalysts are shown in Figure 5.10 and 5.11., respectively. Among the non-promoted HZSM-5 zeolites, the hierarchical H15-A zeolite yielded the highest selectivity to BTX after 125 min (see Table 5.2), demonstrating a positive effect of mesoporosity after prolonged TOS (from 37.9% for the H15 sample to 44.8% for the H15-A sample). Regarding BTX distribution, the highest yield to benzene as function of TOS was obtained when using 3Zn-H15 zeolite as catalyst (Figure 5.12), while the highest mono- and di-alkylated yields as function of time were obtained with the hierarchical and non-promoted H15-A zeolite catalyst (up to 125 min TOS). This suggests that hierarchical systems do have a positive effect on the BTX selectivity. Zn-promoted zeolites yield a lower selectivity towards toluene and xylenes due to the lower number of BAS, which are thought to be responsible for the alkylation/trans-alkylation reactions to form alkylated aromatics. Thus, the results highlight that the right balance between both Zn metallic sites and Brønsted acid sites needs to be struck for an optimal aromatics distribution. Here, those bifunctional catalysts that have low Si/Al ratios and Zn loadings around 1.5 wt. %, were found to show the best catalytic performance toward aromatics[20]. Its worthy to note that in all cases, ethylene, propylene, methane, CO_2 and H_2O were also detected in the outlet stream, products that are formed by cracking and deoxygenation of DMF.

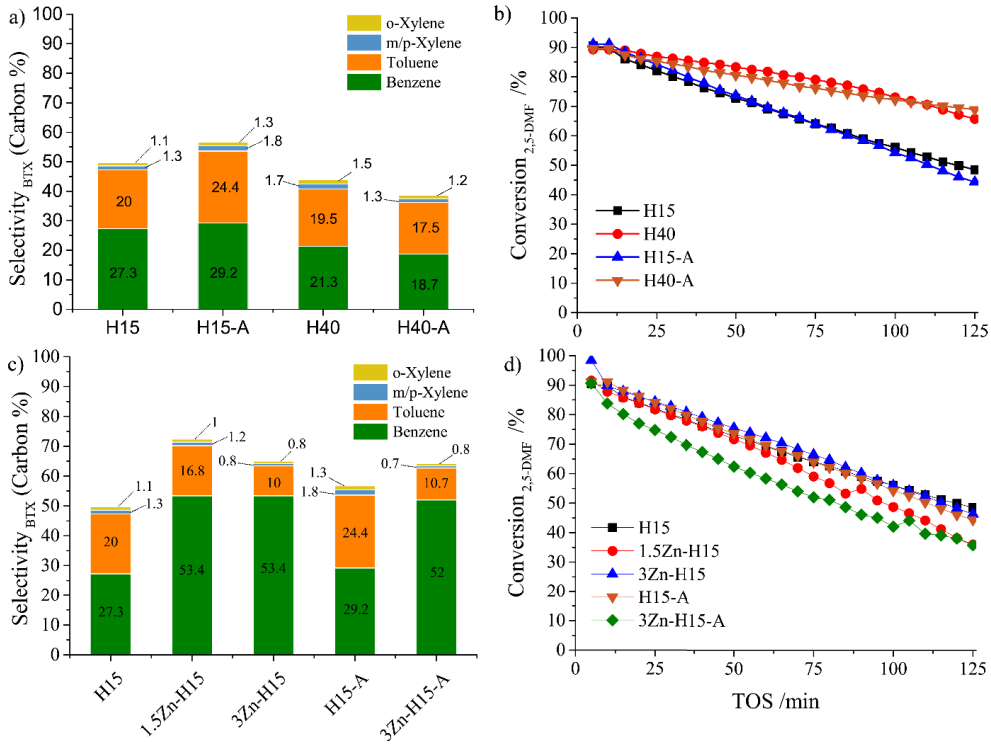

Figure 5.9. Selectivity towards benzene-toluene-xylenes (BTX) (at a conversion level of 90%) when using non-promoted (a) and Zn-promoted zeolites (c) and conversion of 2,5-dimethylfuran (DMF) over non-promoted (b) and Zn-promoted zeolites (d) as a function of time-on-stream (TOS, 125 min). Reaction conditions: $T_{reaction}$ = 500 °C, p(DMF) = 0.78 bar in 20 ml/min N_2 for 125 min reaction.

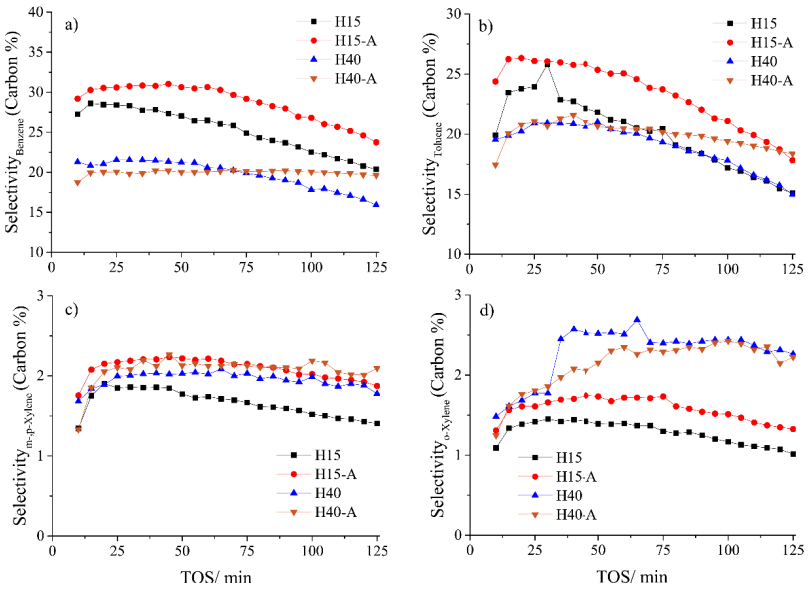

Figure 5.10. Selectivity obtained at different times-on-stream (TOS) for (a) Benzene, (b) Toluene, (c) *m*-, *p*-Xylene and (d) *o*-Xylene during the aromatization of 2,5-dimethylfuran (DMF) when using non-Zn-promoted HZSM-5 catalysts.

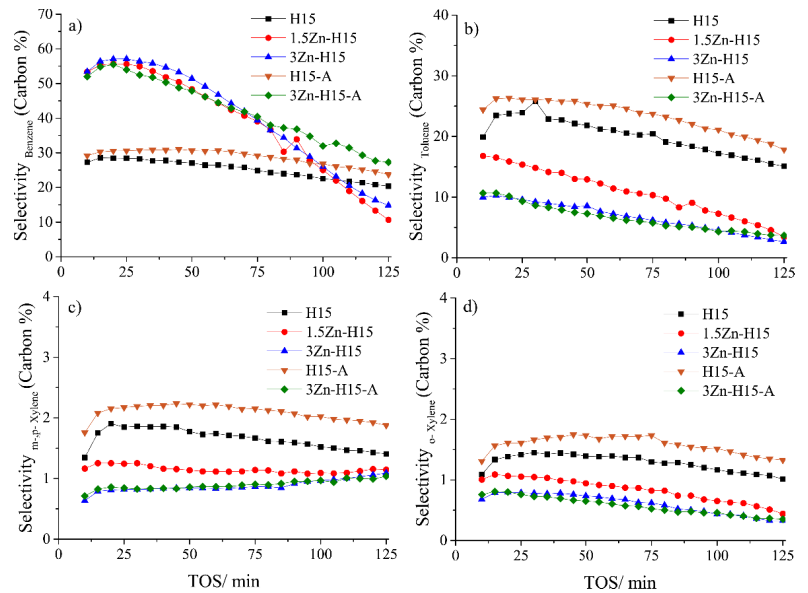

Figure 5.11. Selectivity obtained at different times-on-stream (TOS) for a) Benzene, (b) Toluene, (c) *m*-, *p*-Xylene and (d) *o*-Xylene during the aromatization of 2,5-dimethylfuran (DMF) when using Zn-promoted HZSM-5 catalysts.

Table 5.2. Conversion and selectivity values obtained for the conversion of 2,5-dimethylfuran (DMF) after 125 min time-on-stream (TOS). $T_{reaction}$ = 500 °C, p(DMF) = 0.78 bar in 18 ml/min N_2. WHSV = 0.7 h^{-1}

Materials	H15	H40	H15-A	H40-A	1.5Zn-H15	3Zn-H15	3Zn-H15-A
***Conversion** (C%)*							
DMF	48.5	65.8	44.3	68.9	36	46.3	35.8
***Selectivity** (C%)*							
BTX	37.9	34.9	44.8	42.3	16	19.4	32.6
Benzene	20.4	15.9	23.8	19.6	10.7	14.9	27.3
Toluene	15.1	15	17.8	18.4	3.4	2.6	3.7
***m*-, *p*-Xylene**	1.4	1.7	1.9	2.1	1.1	1.1	1
***o*-Xylene**	1	2.3	1.3	2.2	< 1	< 1	< 1
Total coke (wt. %)	10.6	10.1	12.2	16	12.3	12.4	13.4

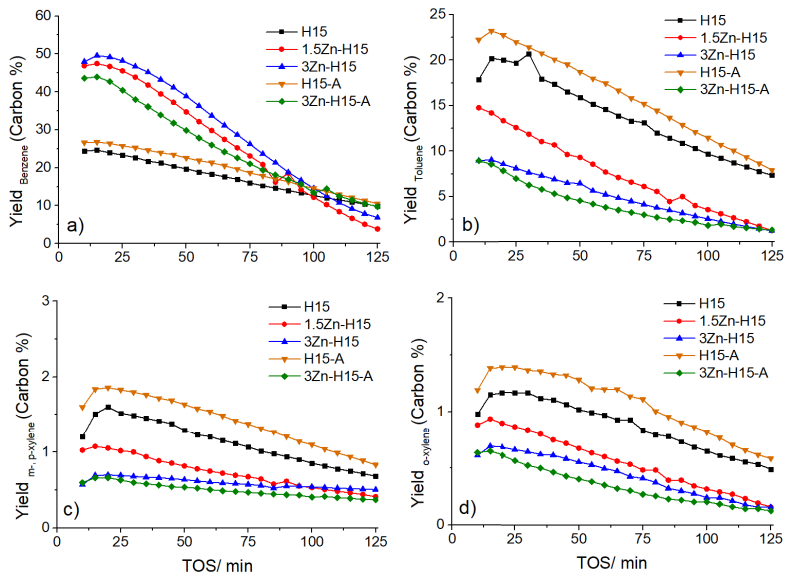

Figure 5.12. Yield obtained at different times-on-stream (TOS) for (a) Benzene, (b) Toluene, (c) m-, p-Xylene and (d) o-Xylene during the aromatization of 2,5-dimethylfuran (DMF) only when using non-promoted and Zn-promoted HZSM-5 catalysts.

DMF aromatization with ethylene co-feeding was performed under the same reaction conditions but with the addition of 0.5 molar equivalents of ethylene (p(ethylene) = 0.39 bar). The catalytic data for the conversion of DMF over the non-promoted and Zn-promoted zeolite catalyst materials at different TOS are shown in Figure 5.13b and 5.13d, respectively. When co-feeding ethylene, a rather similar linear rate of deactivation was observed for all catalysts, with the slowest deactivation again shown by the H15 benchmark catalyst. This catalyst gave less than a 15% decrease after 125 min TOS (Table 5.3). For the hierarchical zeolites, faster deactivation is again observed followed by the Zn-promoted zeolites, which deactivate even faster, as shown in Table 5.3.

The selectivity towards BTX (at 90% conversion) during the co-feeding of ethylene for non-promoted and Zn-promoted zeolites is shown in Figure 5.13a and 5.13b, respectively. The presence of ethylene in the feed, as in other aromatization processes, is known to improve the overall selectivity towards BTX[9,52,53]. For example, for H15 zeolite selectivity improved from 49% to 56% at 90% conversion, by the addition of ethylene to the feed. Furthermore, the introduction of a hierarchical zeolite system apparently does not improve DMF aromatization, neither in the presence of ethylene. Overall, when co-feeding ethylene, the selectivity towards benzene was in all cases lower than without ethylene (Figure 5.13a), while selectivity toward alkylated products, i.e., toluene and xylenes, was higher (Figure 5.13b). Overall, the highest BTX selectivity at 90% conversion was 73.5%, which was attained by the 3Zn-H15 zeolite catalyst (Figure 5.13c). These results are in line with the catalytic data reported in literature for light hydrocarbons when using Zn/ZSM-5 catalysts under similar reaction conditions[41]. The BTX selectivity obtained at different TOS under the same reaction conditions almost doubled when the 3Zn-H15 sample is compared to the unmodified H15 sample (Figure 5.15). Figure 5.16 shows the BTX yields obtained at different TOS when using Zn-promoted zeolites, highlighting that the combination of ethylene co-feeding and Zn-promoted zeolites enhances the yield towards alkylated aromatics. Such improvements have been previously reported for other oxygenates and non-oxygenated hydrocarbons upon introduction of Zn-based Lewis acid sites[9,41,54]. They report that the enhanced catalytic activity is attributed to the C-H bond activation capability of the Zn sites. In order to make a better comparison between the two series of catalytic experiments, we have also performed ethylene only conversion experiments with the parent H15 and 3Zn-H15 samples. These results, summarized in Figure 5.17, show that there is a rather linear and constant conversion value of up to 60% and 45% for the parent H15 and 3Zn-H15 samples, respectively, in line with previous reports at similar temperatures[27].

With ethylene only, the amount of ethylene converted per Zn/BAS active site is higher than when performing the DMF aromatization with co-fed ethylene. During the conversion of oxygenated aromatics, such as DMF, the performance of Zn-promoted zeolites is lowered as furan derivatives first need to undergo cracking at the BAS to form small olefins[55,56], which later on will be activated (C-H bond) on the Zn sites[27,41], to subsequently undergo oligomerization and aromatization on the BAS[54].

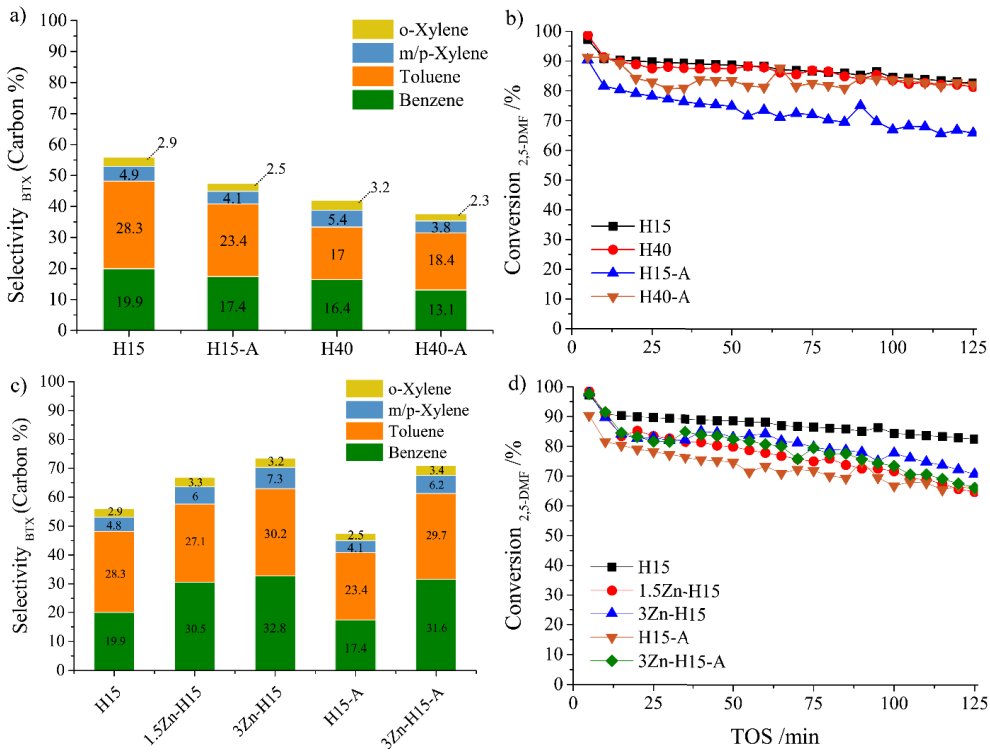

Figure 5.13. Selectivity towards benzene-toluene-xylenes (BTX) (at a conversion level of 90%) when using non-promoted (a) and Zn-promoted zeolites (c) and conversion of 2,5-dimethylfuran (DMF) with ethylene co-feeding over non-promoted (b) and Zn-promoted zeolites (d) as a function of time-on-stream (TOS). Reaction conditions: $T_{reaction}$ = 500 °C, p(DMF) = 0.78 bar with 0.5 molar equivalents of ethylene in 16 ml/min N_2.

Although coke formation is also observed during ethylene co-feeding tests, much less carbon deposits were produced for all catalysts than within the DMF only tests. The lowest amount of coke deposits was obtained with the benchmark H15 zeolite catalyst. In this case, hierarchical systems did attenuate coke formation, while when using Zn-promoted zeolites in combination with hierarchical systems, the amount of coke deposits produced increased, revealing that

neither the enlargement of the pores nor the reduction of the number of BAS after Zn exchange helped to attenuate the formation of carbon deposits (Table 5.3).

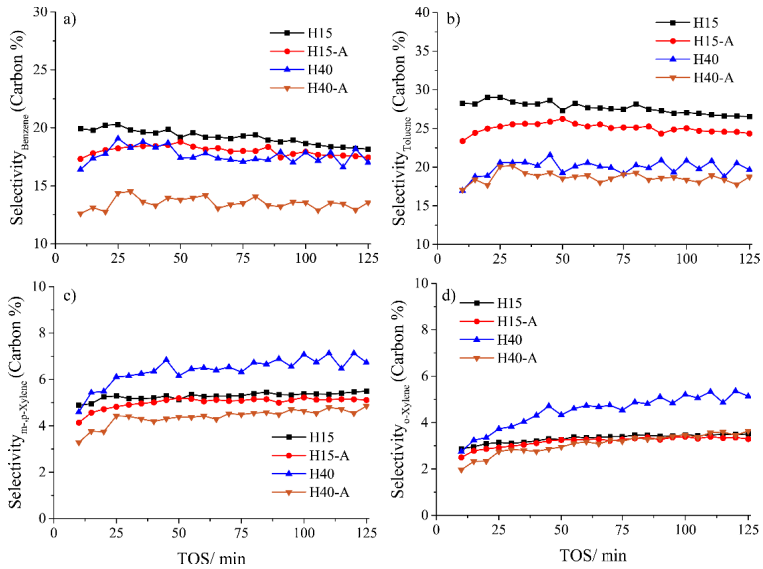

Figure 5.14. Selectivity obtained at different time-on-stream (TOS) for (a) Benzene, (b) Toluene, (c) *m*-, *p*-Xylene and (d) *o*-Xylene during the aromatization of 2,5-dimethylfuran (DMF) with ethylene co-feeding when using non-Zn-promoted HZSM-5 catalysts.

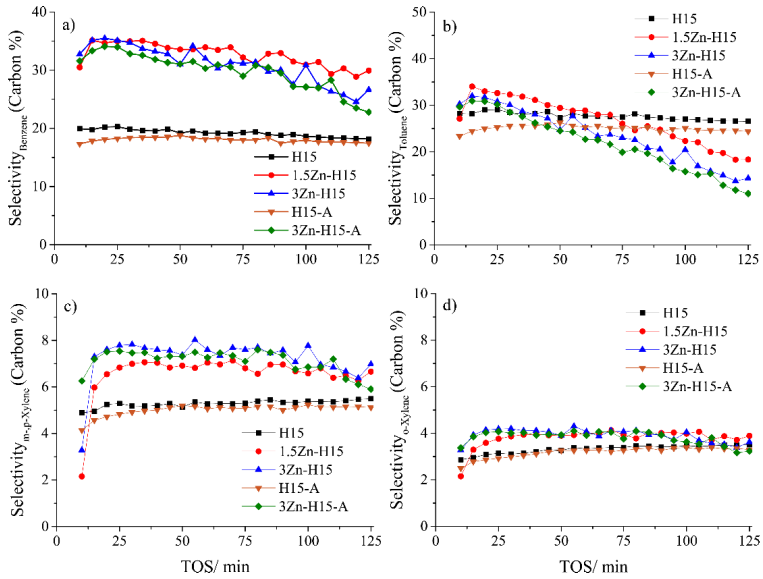

Figure 5.15. Selectivity obtained at different time-on-stream (TOS) for (a) Benzene, (b) Toluene, c) *m*-, *p*-Xylene and (d) *o*-Xylene during the aromatization of 2,5-dimethylfuran (DMF) with ethylene co-feeding when using Zn-promoted HZSM-5 catalysts.

Table 5.3. Conversion and reaction products distribution obtained for the conversion of 2,5-dimethylfuran (DMF) with ethylene after 125 min time-on-stream (TOS). $T_{reaction}$ = 500 °C, p(DMF) = 0.78 bar with 0.5 molar equivalent of ethylene in 16 ml/min N_2. WHSV = 0.7 h^{-1}

Materials	H15	H40	H15-A	H40-A	1.5Zn-H15	3Zn-H15	3Zn-H15-A
				Conversion (%)			
DMF	82.6	81.3	65.8	82.2	64.8	70.8	66.2
Ethylene	46.6	8.3	36.9	21.5	6.2	5.6	5.4
				Selectivity (%)			
BTX	53.8	48.4	50.3	40.8	58.9	51.5	42.9
Benzene	18.2	17	17.5	13.6	29.9	26.6	22.7
Toluene	26.6	19.6	24.4	18.7	18.4	14.3	11
***m*-, *p*- Xylene**	5.5	6.7	5.1	4.9	6.7	7	6
***o*-Xylene**	3.5	5.1	3.3	3.6	3.9	3.6	3.2
Total coke (wt. %)	7.9	9.2	9.7	8.2	11.3	10.7	11.1

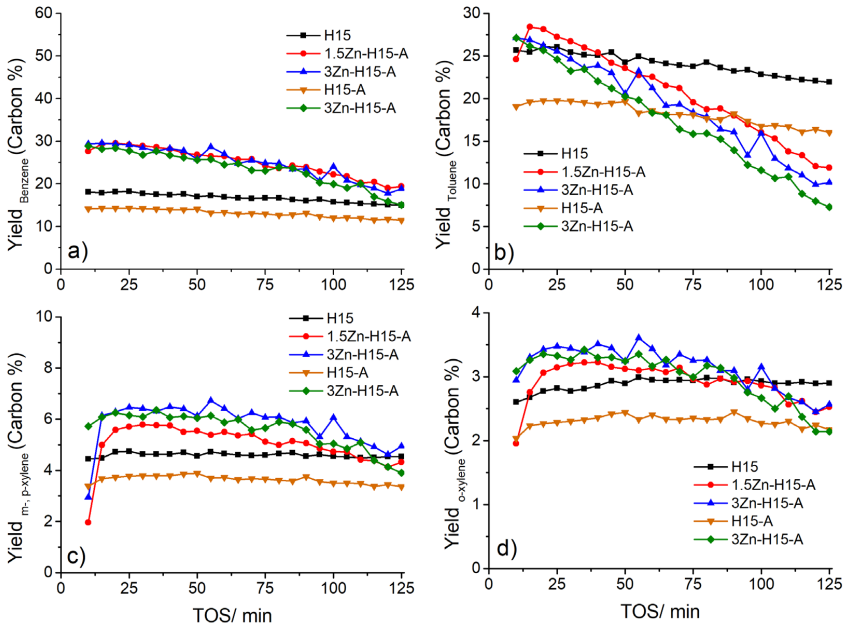

Figure 5.16. Yield obtained at different times-on-stream (TOS) for (a) Benzene, (b) Toluene, (c) *m-, p-*Xylene and (d) *o*-Xylene during the aromatization of 2,5-dimethylfuran (DMF) when using non-promoted and Zn-promoted HZSM-5 catalysts.

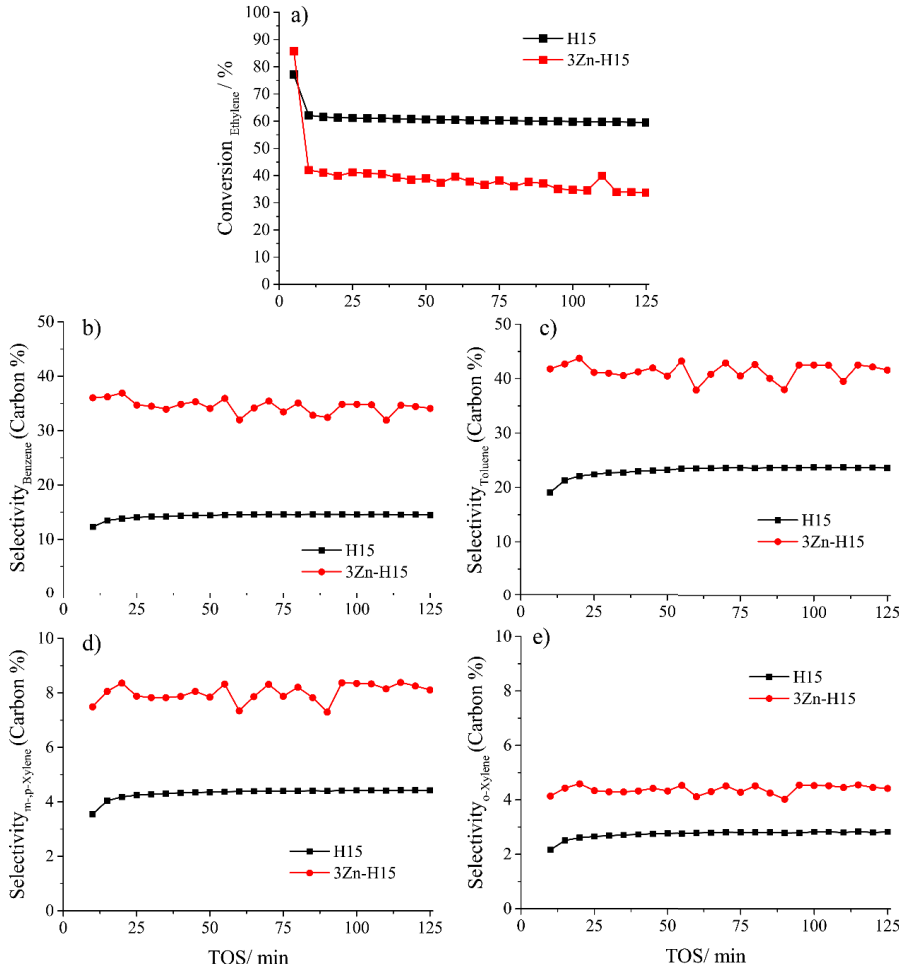

Figure 5.17. (a) Conversion of pure ethylene at the same reaction conditions ($T_{reaction}$ = 500 °C and p(ethylene) = 0.39 bar) when using the H15 and 3Zn-H15 zeolites as catalyst materials for the aromatization of 2,5-dimethylfuran (DMF). Selectivity obtained at different time-on-stream (TOS) for (a) Benzene, (b) Toluene, (c) *m-, p*-Xylene and (d) *o*-Xylene during the conversion of pure ethylene.

In Figures 5.18a and 5.18b, the selectivity values towards benzene and alkylated aromatics are shown as a function of Zn loading. It was found that the BTX selectivity increases with increasing Zn content, with benzene being the dominant product. Co-feeding ethylene causes a shift to the methylated products, with the selectivity towards benzene decreasing and the selectivity towards toluene and xylenes increasing. Both ethylene co-feeding and Zn metal sites thus favor the formation of alkylated aromatics. In contrast, the presence of only Zn has a negative effect on DMF aromatization, since Zn sites favor predominantly the formation of

dehydrogenated/non-alkylated product. The selectivity to benzene or alkylated aromatics as function of mesoporosity or Zn incorporation are displayed in Figure 5.18c and 5.18d. Regarding benzene selectivity, the hierarchical system, which has a higher porosity and BAS acidity, gave a higher benzene selectivity compared to the parent H15 zeolite. Upon Zn incorporation, benzene selectivity improved slightly more. Alkylated aromatics selectivity improved upon incorporation of mesopores but decreased after the addition of Zn compared to the benchmark H15 catalyst. When co-feeding ethylene, the BTX distribution shifted towards the formation of alkylated aromatics, showing its relevance during alkylation reactions.

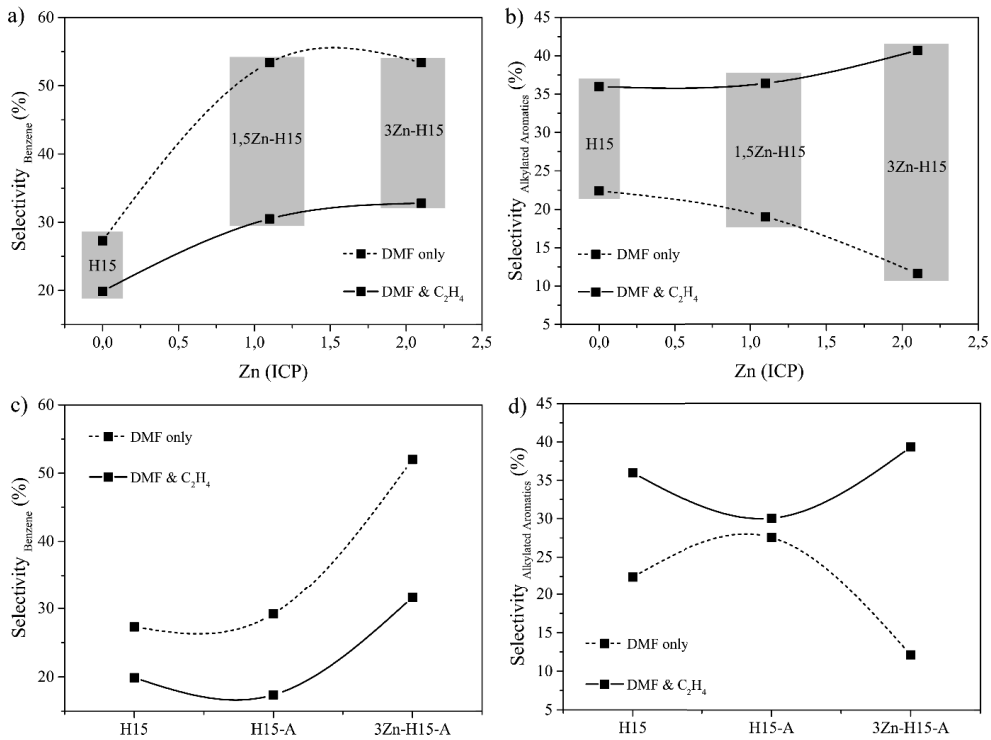

Figure 5.18. Selectivity towards benzene (a), and alkylated aromatics (b) such as toluene and xylenes versus the amount of Zn loading (as determined by ICP-OES) after the aromatization of 2,5-dimethylfuran (DMF) only (dashed lines) and after the aromatization of DMF with co-feeding of ethylene (solid lines). The influence in selectivity to benzene (c) and alkylated aromatics (d) versus mesoporosity and the content of Zn loading and after the aromatization of 2,5-dimethylfuran (DMF) only (dashed lines) and after the aromatization of DMF with co-feeding of ethylene (solid lines). The catalytic selectivity data are obtained at conversion levels of 90%.

Our results suggest that ethylene co-fed during DMF aromatization partially competes for the available active sites (i.e., the Zn sites and BAS). To form aromatics, DMF has to undergo first cracking at the BAS, with the cracking fragments subsequently undergoing aromatization at the BAS as well. However, ethylene is preferentially activated by the Zn sites, and subsequent aromatization reactions take place at the BAS. This may indicate that aromatization of DMF with ethylene co-feeding, in the presence of Zn metal sites may not (only) involve a co-aromatization between both reagents to yield BTX as stated in previous Chapters, but rather a competitive reaction between each reagent at the BAS must also be considered.

It has been suggested that the formation of aromatics during the catalytic conversion of oxygenates, such as methanol in the so-called, Methanol-to-Aromatics (MTA) process[57], is the result of an arene cycle mechanism. The observations made for the aromatization of DMF co-fed ethylene, suggest a similar catalytic reaction pathway to what is proposed for MTA reaction. For example, during the aromatization of DMF only, which seems to go through cracking to form alkenes followed by oligomerization and aromatization reactions, the formation of alkylated aromatics proceeds via a slower rate. Only with the presence of another source of carbon, i.e., ethylene, the selectivity towards alkylated aromatics is boosted. Thus, we suggest that a dual-cycle mechanism similar to the MTA process also takes place within the zeolite pores during DMF aromatization with ethylene co-feeding. This concept is illustrated in Scheme 5.1.

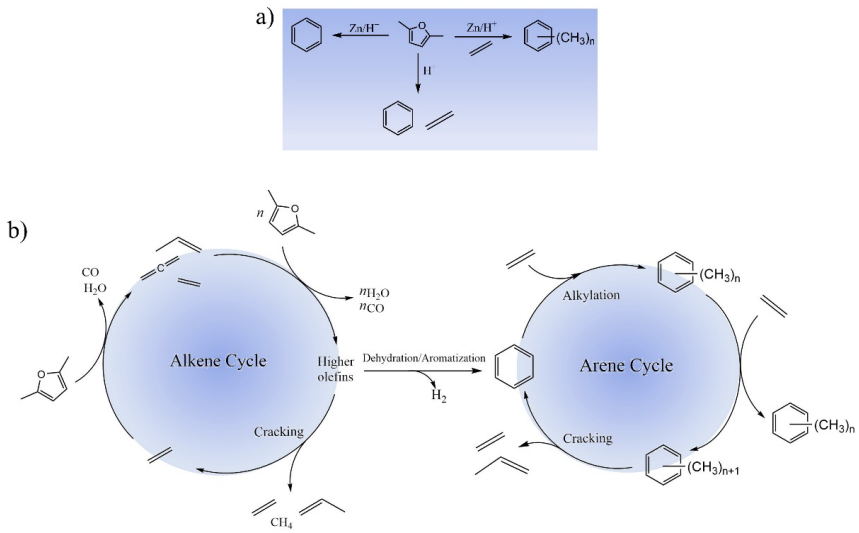

Scheme 5.1. (a) Proposed preferential reaction pathways taking place within the zeolite pores when using bifunctional Zn^{2+}/H^{+}-ZSM-5 zeolite catalysts for the aromatization of 2,5-dimethylfuran (DMF). (b) Possible alkene and arene cycles that take place within the zeolite pores. When co-feeding ethylene, we push the equilibrium to the arene cycle, thereby favoring the formation of alkylated aromatics.

5.4 Conclusions

It was found that Zn-promoted HZSM-5 zeolite-based catalysts, which were synthesized by the incipient wetness impregnation method, show an enhanced selectivity towards benzene, toluene and xylenes (BTX) in the aromatization of DMF, especially when ethylene is co-fed. The applied preparation method resulted in a homogeneous dispersion of Zn over the zeolite crystals and small ZnO clusters were only observed with 3 wt. % Zn loadings (3Zn-H15). Upon increasing the Zn loading a decrease in the number of Bronsted acid sites (BAS) was observed, implying a high degree of ion exchange and incorporation of Zn^{2+} cations. Moreover, after the Zn sites are introduced, a new type of weak-medium acid sites was detected, e.g., via TPD.

The presence of well-dispersed $ZnOH^{+}$ and ZnO clusters introduced enhanced dehydrogenation character, resulting in improved BTX selectivity during the aromatization of DMF with or without ethylene co-feeding. The BTX selectivity was only enhanced when using 1.5Zn-H15 as catalyst (up to a 20% increase) in the absence of ethylene, whilst the highest selectivity towards BTX was obtained when using 3Zn-H15 as catalyst (up to a 73.5% increase) in the presence of ethylene. The introduction of mesoporosity slightly improved the selectivity

towards BTX formation during the aromatization of only DMF, while it did not decrease the rate of deactivation, possibly due to the faster formation of carbon deposits by the higher number of BAS. Also, larger amounts of coke deposits were observed for all Zn-promoted HZSM-5 catalysts as compared to the benchmark HZSM-5 catalysts, this time due to the higher number of LAS known to favor dehydrogenation reactions. Moreover, the faster aromatization rates observed for the Zn-promoted HZSM-5 catalyst materials demonstrate that coke deposits are formed by condensation and dehydrogenation reactions, e.g. of aromatics. Thus, deactivation is directly related with the aromatization rate. Ethylene co-feeding leads to less coke deposition and improved the aromatization rates to alkylated aromatics. These results are in line with a dual-cycle mechanism, similar to the one proposed for the Methanol-to-Aromatics reaction, in which alkylated aromatics are formed during the DMF aromatization in the presence of ethylene via an arene cycle.

5.5 Acknowledgements

Nikos Nikolopoulos and Iris ten Have, both from Utrecht University (UU), are thanked for performing the SEM-EDX measurements. Dennie Wezendonk (UU) is acknowledged for performing the TGA measurements.

5.6 References

(1) Cheng, Y. T.; Huber, G. W. Chemistry of Furan Conversion into Aromatics and Olefins over HZSM-5: A Model Biomass Conversion Reaction. *ACS Catal.* **2011**, *1*, 611–628. https://doi.org/10.1021/cs200103j.

(2) Huber, G. W.; Corma, A. Synergies between Bio- and Oil Refineries for the Production of Fuels from Biomass. *Angew. Chem. Int. Ed.* **2007**, *46*, 7184–7201. https://doi.org/10.1002/anie.200604504.

(3) Prasertcharoensuk, P.; Bull, S. J.; Phan, A. N. Gasification of Waste Biomass for Hydrogen Production: Effects of Pyrolysis Parameters. *Renew. Energy* **2019**, *143*, 112–120. https://doi.org/10.1016/j.renene.2019.05.009.

(4) Cheng, Y.-T.; Huber, G. W. Production of Targeted Aromatics by Using Diels–Alder Classes of Reactions with Furans and Olefins over ZSM-5. *Green Chem.* **2012**, *14*, 3114–3125. https://doi.org/10.1039/c2gc35767d.

(5) Chang, C.-C.; Green, S. K.; Williams, C. L.; Dauenhauer, P. J.; Fan, W.; Climent, M. J.; Corma, A.; Iborra, S.; Huber, G. W.; Iborra, S.; et al. Ultra-Selective Cycloaddition of Dimethylfuran for Renewable p-Xylene with H-BEA. *Green Chem.* **2014**, *16*, 585–588. https://doi.org/10.1039/C3GC40740C.

(6) Uslamin, E. A.; Kosinov, N. A.; Pidko, E. A.; Hensen, E. J. M. Catalytic Conversion of Furanic Compounds over Ga-Modified ZSM-5 Zeolites as a Route to Biomass-Derived Aromatics. *Green Chem.* **2018**, *20*, 3818–3827. https://doi.org/10.1039/C8GC01528G.

(7) Li, J.; Yu, Y.; Li, X.; Wang, W.; Yu, G.; Deng, S.; Huang, J.; Wang, B.; Wang, Y. Maximizing Carbon Efficiency of Petrochemical Production from Catalytic Co-Pyrolysis of Biomass and Plastics Using Gallium-Containing MFI Zeolites. *Appl. Catal. B Environ.* **2015**, *172–173*, 154–164. https://doi.org/10.1016/j.apcatb.2015.02.015.

(8) Cheng, Y. T.; Wang, Z.; Gilbert, C. J.; Fan, W.; Huber, G. W. Production of *p*-Xylene from Biomass by Catalytic Fast Pyrolysis Using ZSM-5 Catalysts with Reduced Pore Openings. *Angew. Chem. Int. Ed.* **2012**, *51*, 11097–11100. https://doi.org/10.1002/anie.201205230.

(9) Uslamin, E. A.; Luna-Murillo, B.; Kosinov, N.; Bruijnincx, P. C. A.; Pidko, E. A.; Weckhuysen, B. M.; Hensen, E. J. M. Gallium-Promoted HZSM-5 Zeolites as Efficient Catalysts for the Aromatization of Biomass-Derived Furans. *Chem. Eng. Sci.* **2018**. https://doi.org/10.1016/j.ces.2018.09.023.

(10) Song, S.; Wu, G.; Dai, W.; Guan, N.; Li, L. Diels-Alder and Dehydration Reactions of Furan Derivatives with Ethylene Catalyzed by Liquid Brønsted Acids and Lewis Acids. *J. Mol. Catal. A Chem.* **2016**, *420*, 134–141. https://doi.org/10.1016/j.molcata.2016.04.023.

(11) Song, C.; Gim, M. Y.; Lim, Y. H.; Kim, D. H. Enhanced Yield of Benzene, Toulene, and Xylene from the Co-Aromatization of Methane and Propane over Gallium Supported on Mesoporous ZSM-5 and ZSM-11. *Fuel* **2019**, *251*, 404–412. https://doi.org/10.1016/j.fuel.2019.04.079.

(12) Lubango, L. M.; Scurrell, M. S. Light Alkanes Aromatization to BTX over Zn-ZSM-5 Catalysts: Enhancements in BTX Selectivity by Means of a Second Transition Metal Ion. *Appl. Catal. A Gen.* **2002**, *235*, 265–272. https://doi.org/10.1016/S0926-860X(02)00271-5.

(13) Kazansky, V. B.; Subbotina, I. R.; Rane, N.; van Santen, R. A.; Hensen, E. J. M. On Two Alternative Mechanisms of Ethane Activation over ZSM-5 Zeolite Modified by Zn^{2+} and Ga^{+} Cations. *Phys. Chem. Chem. Phys.* **2005**, *7*, 3088. https://doi.org/10.1039/b506782k.

(14) Tshabalala, T. E.; Scurrell, M. S. Aromatization of n-Hexane over Ga, Mo and Zn Modified H-ZSM-5 Zeolite Catalysts. *Catal. Commun.* **2015**, *72*, 49–52. https://doi.org/10.1016/j.catcom.2015.06.022.

(15) Li, Q.; He, P.; Jarvis, J.; Bhattacharya, A.; Mao, X.; Wang, A.; Bernard, G. M.; Michaelis, V. K.; Zeng, H.; Liu, L.; et al. Catalytic Co-Aromatization of Methane and Heptane as an Alkane Model Compound over Zn-Ga/ZSM-5: A Mechanistic Study. *Appl. Catal. B Environ.* **2018**, *236* , 13–24. https://doi.org/10.1016/j.apcatb.2018.05.006.

(16) Gao, J.; Wei, C.; Dong, M.; Wang, G.; Li, Z.; Qin, Z.; Wang, J.; Fan, W. Evolution of Zn Species on Zn/HZSM-5 Catalyst under H 2 Pretreated and Its Effect on Ethylene Aromatization. *ChemCatChem* **2019**, *11*, 3892–3902. https://doi.org/10.1002/cctc.201900596.

(17) Yu, L.; Huang, S.; Zhang, S.; Liu, Z.; Xin, W.; Xie, S.; Xu, L. Transformation of Isobutyl Alcohol to Aromatics over Zeolite-Based Catalysts. *ACS Catal.* **2012**, *2*, 1203–1210. https://doi.org/10.1021/cs300048u.

(18) Tamiyakul, S.; Ubolcharoen, W.; Tungasmita, D. N.; Jongpatiwut, S. Conversion of Glycerol to Aromatic Hydrocarbons over Zn-Promoted HZSM-5 Catalysts. *Catal. Today* **2015**, *256*, 325–335. https://doi.org/10.1016/j.cattod.2014.12.030.

(19) Xu, C.; Jiang, B.; Liao, Z.; Wang, J.; Huang, Z.; Yang, Y. Effect of Metal on the Methanol to Aromatics Conversion over Modified ZSM-5 in the Presence of Carbon Dioxide. *RSC Adv.* **2017**, *7*, 10729–10736. https://doi.org/10.1039/C6RA27104A.

(20) Pinilla-Herrero, I.; Borfecchia, E.; Holzinger, J.; Mentzel, U. V.; Joensen, F.; Lomachenko, K. A.; Bordiga, S.; Lamberti, C.; Berlier, G.; Olsbye, U.; et al. High Zn/Al Ratios Enhance Dehydrogenation vs Hydrogen Transfer Reactions of Zn-ZSM-5

Catalytic Systems in Methanol Conversion to Aromatics. *J. Catal.* **2018**, *362*, 146–163. https://doi.org/10.1016/j.jcat.2018.03.032.

(21) Biscardi, J. A.; Meitzner, G. D.; Iglesia, E. Structure and Density of Active Zn Species in Zn/H-ZSM5 Propane Aromatization Catalysts. *J. Catal.* **1998**, *179*, 192–202. https://doi.org/10.1006/jcat.1998.2177.

(22) Kazansky, V. B.; Serykh, A. I. Unusual Localization of Zinc Cations in MFI Zeolites Modified by Different Ways of Preparation. *Phys. Chem. Chem. Phys.* **2004**, *6* (13), 3760–3764. https://doi.org/10.1039/b401853b.

(23) Kolyagin, Y. G.; Ordomsky, V. V.; Khimyak, Y. Z.; Rebrov, A. I.; Fajula, F.; Ivanova, I. I. Initial Stages of Propane Activation over Zn/MFI Catalyst Studied by in Situ NMR and IR Spectroscopic Techniques. *J. Catal.* **2006**, *238*, 122–133. https://doi.org/10.1016/j.jcat.2005.11.037.

(24) Almutairi, S. M. T.; Mezari, B.; Magusin, P. C. M. M.; Pidko, E. A.; Hensen, E. J. M. Structure and Reactivity of Zn-Modified ZSM-5 Zeolites: The Importance of Clustered Cationic Zn Complexes. *ACS Catal.* **2012**, *2*, 71–83. https://doi.org/10.1021/cs200441e.

(25) Kazansky, V. B.; Serykh, A. I.; Pidko, E. A. DRIFT Study of Molecular and Dissociative Adsorption of Light Paraffins by HZSM-5 Zeolite Modified with Zinc Ions: Methane Adsorption. *J. Catal.* **2004**, *225*, 369–373. https://doi.org/10.1016/j.jcat.2004.04.029.

(26) Li, G.; Pidko, E. A. The Nature and Catalytic Function of Cation Sites in Zeolites: A Computational Perspective. *ChemCatChem* **2019**, *11*, 134–156. https://doi.org/10.1002/cctc.201801493.

(27) Hagen, A.; Roessner, F. Ethane to Aromatic Hydrocarbons: Past, Present, Future. *Catal. Rev. - Sci. Eng.* **2000**, *42*, 403–437. https://doi.org/10.1081/CR-100101952.

(28) Xin, Y.; Qi, P.; Duan, X.; Lin, H.; Yuan, Y. Enhanced Performance of Zn-Sn/HZSM-5 Catalyst for the Conversion of Methanol to Aromatics. *Catal. Lett.* **2013**, *143*, 798–806. https://doi.org/10.1007/s10562-013-1031-5.

(29) Müller, S.; Liu, Y.; Kirchberger, F. M.; Tonigold, M.; Sanchez-Sanchez, M.; Lercher, J. A. Hydrogen Transfer Pathways during Zeolite Catalyzed Methanol Conversion to Hydrocarbons. *J. Am. Chem. Soc.* **2016**, *138*, 15994–16003.

https://doi.org/10.1021/jacs.6b09605.

(30) Li, Y.; Liu, S.; Zhang, Z.; Xie, S.; Zhu, X.; Xu, L. Aromatization and Isomerization of 1-Hexene over Alkali-Treated HZSM-5 Zeolites: Improved Reaction Stability. *Appl. Catal. A Gen.* **2008**, *338*, 100–113. https://doi.org/10.1016/j.apcata.2007.12.026.

(31) Li, Y.; Liu, S.; Xie, S.; Xu, L. Promoted Metal Utilization Capacity of Alkali-Treated Zeolite: Preparation of Zn/ZSM-5 and Its Application in 1-Hexene Aromatization. *Appl. Catal. A Gen.* **2009**, *360*, 8–16. https://doi.org/10.1016/j.apcata.2009.02.039.

(32) Lago, C. D.; Decolatti, H. P.; Tonutti, L. G.; Dalla Costa, B. O.; Querini, C. A. Gas Phase Glycerol Dehydration over H-ZSM-5 Zeolite Modified by Alkaline Treatment with Na_2CO_3. *J. Catal.* **2018**, *366*, 16–27. https://doi.org/10.1016/j.jcat.2018.07.036.

(33) Haniff, M. I.; H. Dao, L. Deoxygenation of Carbohydrates and Their Isopropylidene Derivatives over ZSM-5 Zeolite Catalysts. *Appl. Catal.* **1988**, *39*, 33–47. https://doi.org/10.1016/S0166-9834(00)80937-9.

(34) Fanchiang, W. L.; Lin, Y. C. Catalytic Fast Pyrolysis of Furfural over H-ZSM-5 and Zn/H-ZSM-5 Catalysts. *Appl. Catal. A Gen.* **2012**, *419–420*, 102–110. https://doi.org/10.1016/j.apcata.2012.01.017.

(35) Espindola, J. S.; Gilbert, C. J.; Perez-Lopez, O. W.; Trierweiler, J. O.; Huber, G. W. Conversion of Furan over Gallium and Zinc Promoted ZSM-5: The Effect of Metal and Acid Sites. *Fuel Process. Technol.* **2020**, *201*, 106319. https://doi.org/10.1016/j.fuproc.2019.106319.

(36) Groen, J. C.; Peffer, L. A. A.; Moulijn, J. A.; Pérez-Ramírez, J. Mesoporosity Development in ZSM-5 Zeolite upon Optimized Desilication Conditions in Alkaline Medium. *Colloids Surfaces A Physicochem. Eng. Asp.* **2004**, *241*, 53–58. https://doi.org/10.1016/j.colsurfa.2004.04.012.

(37) Emeis, C. A. Determination of Integrated Molar Extinction Coefficients for Infrared Absorption Bands of Pyridine Adsorbed on Solid Acid Catalysts. *J. Catal.* **1993**, *141*, 347–354.

(38) Hanefeld, U.; Lefferts, L. *Catalysis: An Integrated Textbook for Students*, Wiley-VCH.; Hanefeld, U., Lefferts, L., Eds.; Weinheim, **2018**, 370.

(39) Lin, C. C.; Li, Y. Y. Synthesis of ZnO Nanowires by Thermal Decomposition of Zinc Acetate Dihydrate. *Mater. Chem. Phys.* **2009**, *113*, 334–337. https://doi.org/10.1016/j.matchemphys.2008.07.070.

(40) Niu, X.; Gao, J.; Miao, Q.; Dong, M.; Wang, G.; Fan, W.; Qin, Z.; Wang, J. Influence of Preparation Method on the Performance of Zn-Containing HZSM-5 Catalysts in Methanol-to-Aromatics. *Microporous Mesoporous Mater.* **2014**, *197*, 252–261. https://doi.org/10.1016/j.micromeso.2014.06.027.

(41) Zhang, C.; Kwak, G.; Lee, Y. J.; Jun, K. W.; Gao, R.; Park, H. G.; Kim, S.; Min, J. E.; Kang, S. C.; Guan, G. Light Hydrocarbons to BTEX Aromatics over Zn-Modified Hierarchical ZSM-5 Combined with Enhanced Catalytic Activity and Stability. *Microporous Mesoporous Mater.* **2019**, *284*, 316–326. https://doi.org/10.1016/j.micromeso.2019.04.041.

(42) Gabrienko, A. A.; Danilova, I. G.; Arzumanov, S. S.; Freude, D.; Stepanov, A. G. Does the Zn^{2+} Species Introduced into H-ZSM-5 Zeolite Affect the Strength of Brønsted Acid Sites? *ChemCatChem* **2019**, 478–487. https://doi.org/10.1002/cctc.201901637.

(43) Kamarudin, N. H. N.; Jalil, A. A.; Triwahyono, S.; Mukti, R. R.; Aziz, M. A. A.; Setiabudi, H. D.; Muhid, M. N. M.; Hamdan, H. Interaction of Zn^{2+} with Extraframework Aluminum in HBEA Zeolite and Its Role in Enhancing n-Pentane Isomerization. *Appl. Catal. A Gen.* **2012**, *431–432*, 104–112. https://doi.org/10.1016/j.apcata.2012.04.020.

(44) Kotrel, S.; Lunsford, J. H.; Knözinger, H. Characterizing Zeolite Acidity by Spectroscopic and Catalytic Means: A Comparison. *J. Phys. Chem. B* **2001**, *105*, 3917–3921. https://doi.org/10.1021/jp002161v.

(45) Nesterenko, N. S.; Thibault-Starzyk, F.; Montouillout, V.; Yuschenko, V. V.; Fernandez, C.; Gilson, J. P.; Fajula, F.; Ivanova, I. I. Accessibility of the Acid Sites in Dealuminated Small-Port Mordenites Studied by FTIR of Co-Adsorbed Alkylpyridines and CO. *Microporous Mesoporous Mater.* **2004**, *71*, 157–166. https://doi.org/10.1016/j.micromeso.2004.03.028.

(46) Liu, J.; He, N.; Zhou, W.; Shu, M.; Lin, L.; Wang, J.; Si, R.; Xiong, G.; Xin, Q.; Guo, H. *Operando* Dual Beam FTIR Spectroscopy Unravels the Promotional Effect of Zn on HZSM-5 in Iso-Butane Aromatization. *Catal. Sci. Technol.* **2019**, *9*, 1609–1620.

https://doi.org/10.1039/c9cy00136k.

(47) Stepanov, A. G.; Arzumanov, S. S.; Gabrienko, A. A.; Toktarev, A. V.; Parmon, V. N.; Freude, D. Zn-Promoted Hydrogen Exchange for Methane and Ethane on Zn/H-BEA Zeolite: In Situ ^{1}H MAS NMR Kinetic Study. *J. Catal.* **2008**, *253*, 11–21. https://doi.org/10.1016/j.jcat.2007.11.002.

(48) Pavlov, V. S.; Konnov, S. V.; Kots, P. A.; Ivanova, I. I. Deactivation of Silicoaluminophosphate SAPO-34 in Methanol Conversion to Lower Olefins in Different Types of Reactors. *Pet. Chem.* **2019**, *59*, 739–744. https://doi.org/10.1134/S0965544119070132.

(49) Bleken, F. L.; Barbera, K.; Bonino, F.; Olsbye, U.; Lillerud, K. P.; Bordiga, S.; Beato, P.; Janssens, T. V. W.; Svelle, S. Catalyst Deactivation by Coke Formation in Microporous and Desilicated Zeolite H-ZSM-5 during the Conversion of Methanol to Hydrocarbons. *J. Catal.* **2013**, *307*, 62–73. https://doi.org/10.1016/j.jcat.2013.07.004.

(50) Bai, R.; Song, Y.; Li, Y.; Yu, J. Creating Hierarchical Pores in Zeolite Catalysts. *Trends Chem.* **2019**, *1*, 601–611. https://doi.org/10.1016/j.trechm.2019.05.010.

(51) Lok, C. M.; Van Doorn, J.; Aranda Almansa, G. Promoted ZSM-5 Catalysts for the Production of Bio-Aromatics, a Review. *Renew. Sustain. Energy Rev.* **2019**, *113*, 109248. https://doi.org/10.1016/j.rser.2019.109248.

(52) Cheng, Y. T.; Jae, J.; Shi, J.; Fan, W.; Huber, G. W. Production of Renewable Aromatic Compounds by Catalytic Fast Pyrolysis of Lignocellulosic Biomass with Bifunctional Ga/ZSM-5 Catalysts. *Angew. Chem. Int. Ed.* **2012**, *51*, 1387–1390. https://doi.org/10.1002/anie.201107390.

(53) Cheng, Y. T.; Huber, G. W. Production of Targeted Aromatics by Using Diels-Alder Classes of Reactions with Furans and Olefins over ZSM-5. *Green Chem.* **2012**, *14*, 3114–3125. https://doi.org/10.1039/c2gc35767d.

(54) Xiang, Y.; Wang, H.; Cheng, J.; Matsubu, J. Progress and Prospects in Catalytic Ethane Aromatization. *Catal. Sci. Technol.* **2018**, *8*, 1500–1516. https://doi.org/10.1039/c7cy01878a.

(55) Lee, H. W.; Park, S. H.; Jeon, J. K.; Ryoo, R.; Kim, W.; Suh, D. J.; Park, Y. K. Upgrading

of Bio-Oil Derived from Biomass Constituents over Hierarchical Unilamellar Mesoporous MFI Nanosheets. *Catal. Today* **2014**, *232*, 119–126. https://doi.org/10.1016/j.cattod.2013.12.015.

(56) Cheng, Y.-T.; Huber, G. W. Chemistry of Furan Conversion into Aromatics and Olefins over HZSM-5: A Model Biomass Conversion Reaction. *ACS Catal.* **2011**, *1*, 611–628. https://doi.org/10.1021/cs200103j.

(57) Yarulina, I.; Chowdhury, A. D.; Meirer, F.; Weckhuysen, B. M.; Gascon, J. Recent Trends and Fundamental Insights in the Methanol-to-Hydrocarbons Process. *Nat. Catal.* **2018**, *1*, 398–411. https://doi.org/10.1038/s41929-018-0078-5.

PART B

Chapter 6 Technical Zeolite ZSM-5-based Catalysts for Catalytic Fast Pyrolysis: Effect of Different Biomass Pyrolysis Vapors on their Catalytic Performance

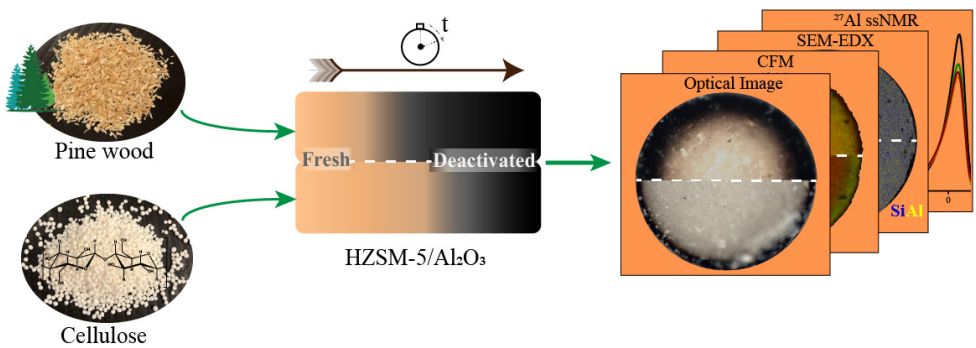

This Chapter is based on the following publication: B. Luna-Murillo, M. Pala, A. Lucini Paioni, M. Baldus, F. Ronsse, W. Prins, P.C.A. Bruijnincx, B.M. Weckhuysen, Catalytic fast pyrolysis of biomass: Catalyst characterization reveals the feed-dependent deactivation of technical ZSM-5-based catalyst extrudates, *submitted for publication.*

Abstract

Rapid catalyst deactivation due to coke formation is a major challenge in the catalytic fast pyrolysis of biomass. The extent and mechanism of deactivation will be dependent on the composition and shape of the catalyst used and on the type of biomass processed. In this Chapter, a multi-technique investigation of a technical Al_2O_3-bound ZSM-5-based catalyst extrudate is presented for the catalytic fast pyrolysis of pine wood and cellulose. Extensive characterization of fresh, spent and regenerated catalysts at both the bulk and catalyst particle level, provided insight into the effects of extrusion and the catalytic pyrolysis and the regeneration processes on catalyst structure and performance. The activity of the technical catalyst was found to decrease drastically with increasing time on stream (TOS), as evidenced by the decrease in aromatics yields (from 81 g kg^{-1} at TOS = 10 min to 8 g kg^{-1} at TOS = 180 min). This decrease correlated with reduction in catalyst acidity and surface area as observed by temperature programmed desorption of NH_3 and Ar physisorption for both feedstocks. Strikingly, confocal fluorescence microscopy of the shaped catalyst particles showed that cellulose-derived vapors and pine wood-derived vapors coke differently at the level of a single catalyst particle, likely due to the presence of lignin-derived oligomeric species in the latter. While lignin-derived species lead mainly to the blockage of the external surface area of the catalyst, larger carbon deposits were formed inside the catalyst's micropores upon catalytic fast pyrolysis of cellulose. The acidity and surface area of the catalyst material could not be restored completely after regeneration. These irreversible changes, observed by solid-state NMR and pyridine-probed FT-IR spectroscopy, occurred likely due to partial zeolite dealumination. Consequently, a loss of performance in terms of aromatic yields was observed upon reuse of the catalyst. On basis of our spectroscopic and catalytic studies, the usage of lignin-free biomass feedstocks yields improved BTX selectivity while contributes for longer catalyst lifetime.

6.1 Introduction

As outlined in Chapter 1 of this PhD Thesis, catalytic fast pyrolysis (CFP) is a thermochemical upgrading technology that enables the production of BTX (Benzene, Toluene and Xylenes) aromatics, polycyclic aromatic hydrocarbons (e.g., naphthalene and derivatives) and C_2-C_3 olefins from lignocellulosic biomass[1,2]. The prospect of producing hydrocarbons from renewable lignocellulosic biomass ready to be integrated into the existing chemical infrastructure, led to a considerable amount of research on CFP of biomass over the last few decades[3–13]. The intention is to use the produced hydrocarbons either as gasoline-range blend components, or as base chemicals for the production of high-volume plastics (e.g., polyurethane, polystyrene, polyester). Zeolite ZSM-5 generally show superior performance towards the upgrading of oxygenate-containing vapors[14,15] and are therefore, typically the catalyst materials of choice for the production of BTX from biomass. Despite the promising advances shown by this technology, the CFP process is also characterized by low carbon yields and rapid catalyst deactivation as a result of excessive coke formation, hampering commercialization efforts[16,17].

Two distinct operating modes (i.e. *in-situ* and *ex-situ*) can be employed during biomass CFP. *Ex-situ* CFP, which uses two separate reactors for the initial pyrolysis and subsequent catalytic vapor upgrading, is preferred because in that case the contact of biomass minerals (e.g. alkali and alkaline earth metals) and the catalyst particles is avoided[18,19]. Such inorganic materials accumulating on the catalyst would affect the activity of the catalyst and cannot be removed as easily as burning off the coke deposits. Another advantage of the ex situ CFP technology is that it allows for reactor configurations that enable integrated regeneration of the spent catalysts to deal with the rapid catalyst deactivation[20].

The mechanism of biomass CFP is thought to proceed through a hydrocarbon-pool mechanism[21] and according to this view, oxygenated pyrolysis vapors follow a series of cracking and dehydration reactions that produce small olefins inside the micropore channels of the zeolite which will undergo subsequent aromatization reactions[22–24]. Therefore, the hypothesized mechanism for the CFP of biomass resembles to that of the more advanced Methanol-to-Hydrocarbons (MTH) process. In the MTH process, highly methylated mono-aromatics are produced through the dual-cycle mechanism[25], which eventually lead to the formation of condensed coke precursors[26]. However, the complexity of the feedstock along with the rapid catalyst deactivation observed with biomass pyrolysis vapors[17], compared to MTH

process[27], implies that more complex phenomena play a role during biomass CFP with respect to coke formation on the catalyst.

From a feedstock perspective, fragments of the original polymeric components of lignocellulose present in the pyrolysis vapors (i.e., those derived primarily from the lignin fraction) are too large[28] to be able to diffuse into the micropores of the zeolite. Wang *et al.*[29] indeed reported that the yield of aromatic hydrocarbons decreased in the order of cellulose > hemicellulose >> lignin. They also found that the yield of catalytic coke was the highest with cellulose (30% on carbon basis), while with lignin, thermal production of coke by condensation, seemed to contribute more to the generation of solid carbonaceous residue. Stanton *et al.*[30] recently showed that the contribution of lignin-derived vapors to catalyst deactivation by irreversible changes in technical zeolite ZSM-5-based catalysts is substantially lower than that of cellulose-derived vapors, as evidenced by the higher amounts of acid sites (76%) and micropore area (93%) retained on the catalyst following regeneration after the CFP of lignin. Together, these studies suggest that lignin-derived monomers and oligomers coke on the external surface of the catalyst, while cellulose-derived vapors coke via successive aromatization reactions taking place inside the micropores of the catalyst. A previous work by Hernando *et al.* related the physicochemical properties from a technical ZrO_2-promoted ZSM-5-based catalyst particle with its catalytic performance. Hernando and co-workers gave further insight in the importance of properly choosing a promotor and catalyst binder to obtain improved catalytic performance[31]. In short, their investigation allowed a direct correlation between feedstock used and the effect this has on local catalyst functionality, demonstrating that the promoted ZSM-5-based extrudates that showed an outstanding accessibility and acid-base physicochemical properties during the characterization experiments resulted to be the most efficient catalysts to convert both the bulky molecules and the smaller oxygenates present in the bio-oil feedstock into valuable chemicals. In addition, more recent investigations performed by Heracleous *et al.* relating the *ex-situ* CFP of biomass with the formation and location of carbon deposits within technical ZrO_2-promoted ZSM-5-based catalyst extrudates, gave us a closer look to the investigations at the single catalyst particle level of spent and regenerated catalyst particles[32] obtained after CFP of biomass. After a regeneration process (e.g. 500 ºC, under air) and comparison of the characterization results from spent and regenerated catalysts, physicochemical properties were utterly restored. However, their investigations were performed for ZSM-5-based catalysts with alterations in the zeolite crystals, different matrix

composition (clays were used as binders), and pre-treated biomass feedstock (e.g. Alkali and alkaline earth metals were removed).

Previous studies[29,33] have shown that the bulk zeolite material is far too active for oxygenates-to-hydrocarbon conversions, giving extensive coke formation instead. The use of shaped catalysts, consisting of other components than the active zeolite phase, rather than the pure phases is a typically applied industrial practice to achieve optimal physical and chemical performance. The application of such technical catalysts offers important advantages, for example by providing mechanical strength and/or by avoiding pressure drops inside the reactor vessels[34,35]. Therefore, the use of binders is essential for the real-life industrial reactors whether is a fluidized bed or an *ex-situ* fixed-bed reactor. Accordingly, building on the knowledge gained with powdered samples, it is therefore of paramount importance to also study the performance of such shaped catalyst materials in CFP of biomass. Binders such as alumina (Al_2O_3), silica (SiO_2) or clays are typically used to support the active zeolite phase, generally altering the overall catalytic activity of the composite materials as well of zeolites by giving robustness and, in some cases, extra catalytic activity to the catalyst composites (i.e. pre-catalytic activity taking place in the binder matrix). Previous reports, revealed that the presence of mesoporous Al_2O_3 binders gave improved robustness and certain pre-cracking activity during diverse catalytic processes, when compared to technical catalysts without alumina or with inert SiO_2 binders[36–38]. Improved catalytic performance was attributed to the pre-cracking of larger oligomers within the alumina matrix. Investigations performed at the single particle catalyst level provided critical information on the accessibility, predominant active sites and possible deactivation pathways of zeolite ZSM-5-based catalyst materials in different complex matrices including fluid catalytic cracking and CFP catalysts by means of (micro)spectroscopic characterization[38–40]. Heracleous *et al.*[32] reported on the nature and location of carbon deposits formed within technical ZSM-5-based catalyst extrudates upon CFP of biomass. However, a novel catalyst formulation (i.e. ZrO_2 incorporated nanocrystalline ZSM-5, agglomerated with attapulgite) has been used in that work. As such, it may not be straightforward to decouple the influence of individual components (ZrO_2, nanocrystalline zeolite, and the attapulgite clay) on coke formation.

Literature dealing with a detailed characterization of the catalyst properties along with bench scale CFP testing, is scarce. A multi-technique characterization approach covering multiple length scales, analogous to what was used in previous investigations[31], will enable us to bridge the gap between catalytic activity and catalyst structural properties of HZSM-5/Al_2O_3 catalyst

extrudates, and to reveal the structure-performance relations governing zeolite ZSM-5-based catalysts for the CFP of biomass.

In this Chapter, Al_2O_3-bound ZSM-5 based catalysts have been prepared in a technical form (such as extrudates), and their performance is assessed for the CFP of biomass using pine wood and cellulose as feedstock. Bench-scale experiments were performed in a continuously fed fast pyrolysis system that enabled *ex-situ* upgrading of pyrolysis vapors over a fixed-bed of catalyst. Yields and bio-oil compositions were determined for the fresh and the regenerated catalyst to investigate the effect of reaction and regeneration. Catalyst performance could thus be correlated with the (spatially resolved) physicochemical properties. The advantages of the multi-technique catalyst characterization are amplified by performing the experiments in an industrially relevant setup using technical catalysts which are composed of commercially available components. Because, the characterization of such technical catalysts could potentially serve as a benchmark case for future research. The extensive analysis of the catalysts revealed the mismatch between the biomass pyrolysis vapors and the catalyst system due to a complex interplay of mass transfer limitations and chemistry. Also, despite the similarities between pine wood and cellulose derived vapors, different catalytic mechanisms seem to govern the CFP reaction and will be further discussed.

6.2 Experimental Part

6.2.1 Biomass Origin and Composition

Pine wood (Bemap Houtmeel B.V., Bemmel, The Netherlands) with a particle size range of 1.0 – 2.0 mm and cellulose (Cellets® 1000, Pharmatrans Sanaq AG, spherical pellets) with a particle size range of 1.0 – 1.4 mm were used as feedstock materials in the catalytic and non-catalytic fast pyrolysis experiments. The pine wood feedstock had an elemental composition of 0.47 g g^{-1} C, 0.06 g g^{-1} H, and 0.46 g g^{-1} O on dry basis. The biochemical composition of the pine wood used is 0.35 kg g^{-1} cellulose, 0.29 g g^{-1} hemicellulose and 0.28 g g^{-1} lignin (on dry biomass basis). The cellulose feedstock contained 0.42 g g^{-1} C, 0.06 g g^{-1} H and 0.52 g g^{-1} O. Both feedstocks used within this study, pine wood and cellulose, are denoted as PW and CELL, respectively.

6.2.2 Catalyst Synthesis

HZSM-5/Al_2O_3 composites (HZSM-5/Al_2O_3) were prepared by mixing alumina powder (PURAL SB from Sasol), ZSM-5 powder (CBV 2314 from Zeolyst, with SiO_2/Al_2O_3 = 23), water and an aqueous acid solution in a kneader for about 60 min at room temperature. Subsequently, the obtained paste is passed through an extruder to obtain the extrudates in a spaghetti-like structure. Afterwards, extrudates were dried at room temperature overnight. The catalyst extrudates were then crushed to obtain a particle size between (1.0 – 3.0 mm), which was followed by a calcination sequence, first at 350 °C for 16 h and then at 600 °C for 16 h. The composites obtained contained 50% zeolite ZSM-5 and 50% alumina by weight. While fresh catalyst extrudates are denoted as HZSM-5/Al_2O_3 throughout the manuscript, the individual zeolite and binder powders are denoted as HZSM-5 and Al_2O_3, respectively. Prior to any characterization, the individual components of the extrudates, HZSM-5 and Al_2O_3, were also subjected to the same two-step calcination procedure mentioned above.

Spent catalyst extrudates were collected at 10, 60, and 180 min time-on-stream after catalytic pyrolysis tests and they were analyzed without further treatment, unless otherwise stated. Regenerated catalyst extrudates were obtained after calcining the spent extrudates at 250 °C for 40 min with a heating ramp of 4.5 °C·min^{-1} under static air atmosphere followed by a second calcination at 600 °C for 5 h with a heating ramp of 5 °C·min^{-1} under air atmosphere[41]. Spent and regenerated catalyst extrudates are further denoted following the *feedstock*-TOS and *feedstock*-TOSr sequences, respectively. The feedstock indicates the feed (either CELL or PW for cellulose and pinewood, respectively) used in catalytic pyrolysis tests and TOS indicates the time-on-stream the sample is collected at. For example, spent and regenerated extrudates obtained at TOS = 10 min from the CFP of cellulose and pine wood are represented as CELL-10 and CELL-10r, and as PW-10 and PW-10r, respectively.

6.2.3 Catalyst Characterization

X-ray diffraction (XRD) patterns have been recorded on a Bruker-AXS D2 Phaser 2nd generation powder X-ray diffractometer, in Bragg-Brentano mode, equipped with a Co Kα (operation at 30 Kev, 10 mA, λ = 1.79026 Å) and a Lynxeye detector. All samples were measured over a 2θ range of 5° to 50° with 0.02° as scanning step size.

Porosity and surface area of the materials were determined by argon physisorption, carried out at -196 °C using a Micromeritics TriStar 3000. The samples were degassed under vacuum at 300 °C for 16 h prior to measurement. The micropore volume and the surface area were determined by the *t*-plot method and the Brunauer-Emmett-Teller (BET) theory, respectively. External surface area was determined by subtraction of the micropore volume area from the BET surface area.

NH_3 temperature programmed desorption (TPD) experiments were carried out in a Micromeritics AutoChem II equipped with a TCD detector. Approximately 100 mg sample was placed in the reaction chamber and the sample was dried up at 600 °C in a He flow. Then, the chamber was cooled to 100 °C in a He flow and held at 100 °C for 2 h. A flow of 10 ml/min of 10 vol. % NH_3/He was fed into the chamber to saturate the sample with NH_3. Thereafter, the sample was kept at 100 °C in a He flow for 2 h, followed by heating to 600 °C at 10 °C min^{-1}. For spent catalyst, a drying step at 400 °C in He flow was applied instead. After NH_3 dosing, sample was kept at 100 °C in a He flow for 2 h, followed by heating to 400 °C at 10 °C min^{-1}.

For the Fourier transform-infrared (FT-IR) spectroscopy measurements with pyridine as probe molecule, the samples were grounded and pressed into thin self-supported wafers (~ 25 mg sample). The wafers were placed in a sealed FT-IR cell equipped with a vacuum system and a heating system. The wafers were pre-treated under vacuum (~10^{-3} mbar) at 550 °C for 2 h to remove all adsorbates, then was cooled down to 40 °C where pyridine vapor was introduced into the cell for 30 min until complete saturation. The weakly adsorbed pyridine was removed by evacuation for 1 h. Afterwards, the temperature was ramped from 40 to 150 °C at 2.5 °C/min and kept at 150 °C for 30 min, after which a spectrum was recorded. As described in ref. [42], this step is done to calculate the amount of Lewis acid sites (LAS) and Bronsted acid sites (BAS). In a next step, the temperature was ramped up to 550 °C to remove all pyridine from the sample. All spectra were recorded between 4000-1000 cm^{-1} using a Perkin-Elmer System 2000 instrument.

Scanning electron microscopy (SEM) and energy dispersive X-ray analysis (EDX) were performed in bi-sectioned samples. Measurements were carried out with a FEI Helios NanoLab G3 UC (FEI Company) instrument at 15.0 kV acceleration voltage. Energy Dispersive Spectroscopy (EDS) was performed using a Silicon Drift Detector (SDD) X-MAX from Oxford Instruments coupled to the Helios Nanolab. Focused-Ion-Beam Scanning-Electron-Microscopy (FIB-SEM) images were taken on the same instrument aforementioned. The sample was

supported on an aluminum SEM stub with a carbon sticker. A small carbon strip tape was connecting the aluminum stub with the sample to ensure electrical conductivity. A protective layer of Pt was deposited on top of the region of interest before performing the measurements. For the FIB experiments, a trench was made by milling perpendicularly to the surface, next to the Pt-deposited area. After milling the trench, a cleaning step with Ga ions was performed before imaging. SEM images of the cross section were recorded in backscatter electron (BSE) mode (2 kV, 50 pA).

^{27}Al magic angle spinning (MAS) solid-state nuclear magnetic resonance (ssNMR) experiments were performed at 11.7 T (500 MHz proton frequency) on a Bruker Avance III spectrometer equipped with a 3.2 mm MAS probe. Spectra were recorded at ambient temperature using 16 kHz MAS. A radiofrequency (RF) field of 50 kHz was used for the ^{27}Al $\pi/12$ pulse followed by 6.5 ms acquisition. 10240 scans were accumulated using an inter-scan delay of 1s. The ^{27}Al chemical shift was externally referenced to an aqueous aluminum nitrate solution. The spectra were processed with the software Topspin3.5 using a line-broadening of 75 Hz. A zero-quantum (ZQ) filtered multiple-quantum magic angle spinning (MQ-MAS) pulse-sequence was used to correlate the ^{27}Al isotropic chemical shift (F1) with the quadrupolar line-shape (F2)[43]. The excitation and conversion pulses were applied with a RF field of 50 kHz, instead for the soft, selective pulse following the Z-filter delay a RF field of 6.5 kHz was used. 1024 scans were accumulated using an inter-scan delay of 1 s. Acquisition times of 6.5 ms and 1.3 ms were used for the direct and indirect dimensions, respectively. MQ-MAS data were Fourier transformed and sheared, using the software of Bruker Topspin3.5, and 75 Hz line-broadening was applied in both dimensions. For all the measurements the rotors were filled with the same amount of sample (35 mg).

Confocal Fluorescence Microscopy (CFM) measurements were carried out using a Nikon Eclipse 90i confocal fluorescence microscope equipped with a 50×0.55 NA dry objective lens and a pin hole and a dichroic mirror. Fluorescence microphotographs were collected by a Nikon A1-SHR A1 R scan head connected to a Melles Griot laser after illuminating the extrudates surface with 488 nm and 561 nm lasers. The emission was measured by the A1R scanning head equipped with a spectral detection unit consisting of a diffraction grating and a 32-photomultiplier tube array.

Thermogravimetric Analysis (TGA) of the samples in presence of oxygen (TPO) have been performed in a Perkin Elmer TGA8000 analyzer hyphenated with a Hiden HPR-20 Mass

Spectrometer (TGA-MS). 10 mg sample was placed in a ceramic pan on a thermo-balance under 20 ml/min 20 % O_2/Ar flow and heated from 30 °C to 700 °C at a heating rate of 10 °C·min^{-1}. CO_2 and H_2O masses (m/z 44 and 18, respectively) have been recorded during all the analyses in order to give insights about the nature of the carbonaceous deposits.

6.2.4 Catalyst Testing

Catalytic Fast Pyrolysis (CFP) experiments were performed in a continuously operated fast pyrolysis system employing auger reactor technology for the pyrolysis part, and a fixed-bed reactor for the integrated *ex-situ* catalytic upgrading. The biomass (either pine wood or cellulose) was fed at a rate of *ca.* 0.2 kg h^{-1}, while the catalyst bed contained 0.04 kg of catalyst. In this way, a weight-hourly space velocity (WHSV) of 5 h^{-1} on feed basis for each feedstock was achieved. The temperature of the pyrolysis reactor and the catalytic reactor were kept at 500 °C during the experiments. The reactor scheme (Figure 6.1), with a detailed explanation of the experimental procedure, and the product analysis are shown below.

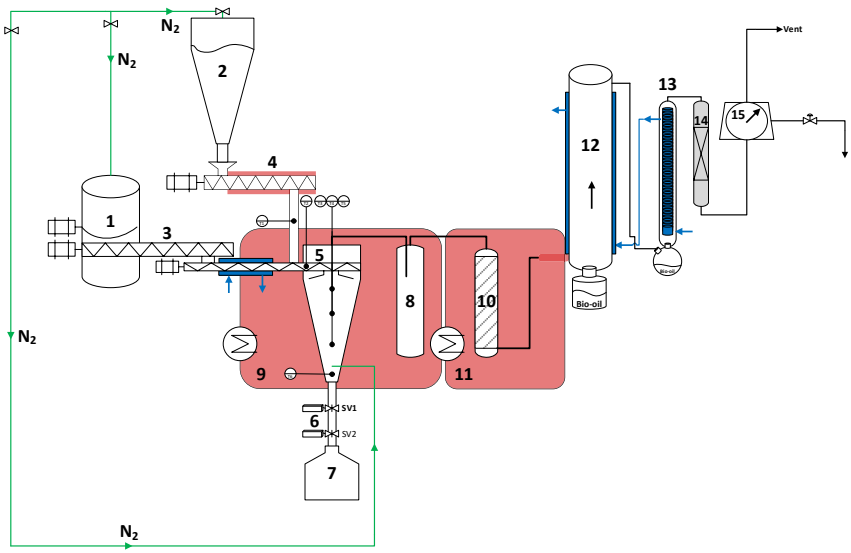

Figure 6.1. Schematic drawing of the catalytic fast pyrolysis (CFP) system used in the catalytic and non-catalytic fast pyrolysis experiments. (1) biomass hopper, (2) sand hopper, (3) feed conveyor, (4) sand conveyor, (5) auger reactor, (6) sluice valve system, (7) solid collection vessel, (8) knock-out

vessel, (9) pyrolysis reactor oven, (10) fixed-bed catalytic reactor, (11) catalysis reactor oven, (12) electrostatic precipitator, (13) glass condenser, (14) cotton filter and (15) gas meter.

Catalytic and non-catalytic fast pyrolysis experiments were performed in a fully controlled, continuously operated catalytic fast pyrolysis system (Figure 6.1). The bench-scale system, described previously in detail elsewhere[95], was slightly modified with the addition of a sluice valve system (6) and an electrostatic precipitator (12). The sluice valve system was operated in an automated way to facilitate the removal of sand/char particles from the hot reactor system in a controlled manner while maintaining an optimal solid residence time inside the reactor, thereby enabling the complete pyrolysis of biomass particles. And the electrostatic precipitator was added to the system to ensure proper condensation of condensable pyrolysis vapors.

In a typical fast pyrolysis experiment, biomass particles in the storage hopper (1) were continuously fed to the hot pyrolysis reactor (at 500 °C) at a rate of 0.2 kg h^{-1} via the feed (3) and the auger reactor (5) conveyors. The experiments were performed under continuous nitrogen flow (72 L h^{-1}) to provide an inert reaction atmosphere and to minimize the vapor residence time in the hot reaction zone. The pyrolysis reaction started when the biomass particles were in contact with the hot sand particles carried to the auger reactor via the heated sand conveyor (4). Following the auger reactor, the charred biomass particles were kept in the hot part of the pyrolysis reactor with the help of the sluice valve system (6) long enough to ensure a complete devolatilization of the particles. The pyrolysis vapors were then purged out of the pyrolysis reactor with the continuously flowing nitrogen gas. The fine char / sand particles that could entrain with the pyrolysis vapors were trapped inside the knock-out vessel (8). The fixed-bed catalytic reactor (10) was left empty in case of non-catalytic pyrolysis experiments, while it was filled with the HZSM-5/Al_2O_3 catalyst extrudates (0.04 kg) prior to the experiment in case of catalytic pyrolysis experiments. The condensable pyrolysis vapors are condensed underneath the water-cooled (2 °C) electrostatic precipitator (12) and the tap-water cooled (15 °C) glass condenser (13). The liquids collected underneath the condensers are collectively called the bio-oil, the liquid product of the pyrolysis reaction. The non-condensable vapors are counted with a wet gas meter (15) and sampled throughout the experiment to acquire data for gas yield and gas composition calculations.

I. Product Analysis

In this work, the lumped product yields of char, bio-oil (organics + water) and non-condensable gas fractions are all defined on as-received (a.r.) biomass basis.

The char yields (Y_c) on a.r. basis were calculated following the equation;

$$Y_c = \frac{m_c}{m_{ar}} \quad \text{(eq.6.1)}$$

where m_{ar} denotes the biomass fed to the reactor and m_c denotes the char collected from the solid collection vessel (7). The char is mixed with the sand inside the solid collection vessel. So, the amount of the char is determined by burning off the char at the end of an experiment. This was done for three experiments for each feedstock used in this work and the average value is assumed for all the remaining experiments.

The NCG product yields (Y_{gas}) were calculated on the basis of flow rate data measured continuously during the experiment as well as the gas composition data (CO, CO_2, CH_4, H_2, C_2H_4, C_2H_6, C_3H_6, C_3H_8) determined using gas chromatography (Varian micro-GC 490-GC)[95].

$$Y_{gas} = \frac{\int_{t_0}^{t_{end}} (\phi_{out} - \phi_{in}) \times \sum_j (V_j \times \rho_j)\, dt}{m_{daf}} \quad \text{(eq.6.2)}$$

where ϕ_{out} and ϕ_{in} represent total gas flow measured at the outlet and the inlet of the reactor throughout the experiment, V_j is the volume fraction of the individual gas components (excluding N_2) and ρ_j is the corresponding density of the individual gas components at 20 °C.

The pyrolysis oil yields (Y_{liq}) for the fast pyrolysis experiments were calculated with the following equation:

$$Y_{liq} = \frac{m_{liq}}{m_{ar}} \quad \text{(eq.6.3)}$$

The total amount of liquids (m_{liq}) include the liquids collected underneath the ESP and the glass condenser. The yield of organics (Y_{org}) in the bio-oils was calculated by:

$$Y_{org} = \frac{m_{liq} \times (1 - f_w)}{m_{ar}} \quad \text{(eq.6.4)}$$

The term, f_w, represents the water mass fraction of the bio-oils produced. By knowing the water content of the bio-oils, the yield of water (Y_w) is also calculated:

$$Y_{\mathrm{w}} = \frac{(m_{\mathrm{liq}} \times f_{\mathrm{w}})}{m_{\mathrm{ar}}} \qquad \text{(eq.6.5)}$$

The coke yields for the catalytic pyrolysis experiments were calculated by thermogravimetric analysis following the procedure described in section 6.2.3:

$$Y_{\mathrm{coke}} = \frac{m_{coke}}{m_{\mathrm{ar}}} \qquad \text{(eq.6.1)}$$

And the mass balance closure is defined as the sum of Y_{c}, Y_{gas}, Y_{org}, Y_{w} and Y_{coke}.

The non-condensable gas fraction was sampled through a sampling port downstream of gas meter during the experiments and subsequently analyzed for CO, CO_2, CH_4, H_2, C_2H_4, C_2H_6, C_3H_6 and C_3H_8 by gas chromatography using a Varian micro-GC 490-GC, equipped with 10 m molsieve 5 Å (with backflush) and 10 m PPQ analytical columns and TCD detectors.

The water content of the bio-oils was determined by Karl Fischer titration (Mettler Toledo V20 automatic titrator, using Merck Combi Titrant 5 Keto as the titrant and Merck Combi Solvent 5 Keto as the solvent). The elemental composition of the bio-oils was determined by a Thermo Scientific Flash 2000 Organic elemental analyzer for carbon and hydrogen. And oxygen contents are determined by difference.

A set of volatile compounds, selected on the basis of abundancy in the pyrolysis liquids, were quantified following the calibration of a GC/MS (Thermo Fischer ISQ) system equipped with a Restek DB-1701 column. Fluoranthene was used as the internal standard. The calibrated compounds and the corresponding functional groups assigned to them can be seen in Table 6.1. The response factors obtained for the compounds listed in Table 6.1 were also used to quantify the non-calibrated compounds with similar structure. For instance, the response factor used for naphthalene was also used for substituted naphthalene derivatives.

T**able 6.1.** The list of calibrated compounds that are used for the quantification of the abundant volatile compounds produced in this work.

Calibrated compounds	Functional groups
Acetaldehyde, hydroxy-	oxygenates
Acetic acid	oxygenates
2-Propanone, 1-hydroxy-	oxygenates
Furfural	oxygenates
2-Furancarboxaldehyde, 5-methyl-	oxygenates
1,2-Cyclopentanedione, 3-methyl-	oxygenates
Levoglucosan	oxygenates
Phenol	phenols
Guaiacol	phenols
4-methyl guaiacol	phenols
Eugenol	phenols
Vanillin	phenols
Benzene	aromatics
Toluene	aromatics
o-Xylene	aromatics
m-Xylene	aromatics
p-Xylene	aromatics
Naphthalene	aromatics

The concentrations of individual compounds (C_i) are calculated on dry bio-oil basis following:

$$C_i = \frac{A_i}{RF_i} \times \frac{C_{IS}}{A_{IS}} \times \frac{(w_{\text{liq}} + w_{\text{s}})}{w_{\text{liq}}} \times \frac{1}{w_{\text{liq}} \times (1 - f_w)} \quad \text{(eq.6.7)}$$

where A_i denotes the integrated peak area of the individual compound, RF_i represents the response factor of the respective compound. C_{IS} and A_{IS} represent the concentration and the area of the internal standard, respectively. The concentrations of individual compounds are then reported on a dry bio-oil basis following the correction due to the dilution of the bio-oil sample (w_{liq}) with the solvent (w_{s}).

II. Py/GC-MS Experiments

A set of catalytic pyrolysis experiments using the cellulose feedstock were carried out at micro-scale to see the effect of individual components (the zeolite HZSM-5 and the Al_2O_3 binder) of the catalyst extrudates on the composition of the bio-oil product. The experiments were performed using a micro-pyrolysis unit (multi-shot pyrolyzer, Frontier Labs, EGA/PY-3030D) coupled to a GC/MS system (Thermo Fisher Scientific Trace GC Ultra and Thermo ISQ MS). The zeolite (ZSM-5, CBV 2314 from Zeolyst) and the alumina (Al_2O_3, PURAL SB from Sasol) powders were subjected to a calcination sequence, first at 350 °C for 16 h and then at 600 °C for 16 h, prior to the catalytic pyrolysis experiments. Briefly, samples of approx. 200 µg cellulose (particle size between 100 – 250 µm) were mixed with approx. 4000 µg of either the zeolite (HZSM-5) or the binder (Al_2O_3) in a cup of deactivated stainless steel (Frontier Laboratories Eco-cup, 80 µl). The loaded cup was released with the aid of the double-shot sampler into a vertical stainless-steel tube (pyrolysis reactor tube) placed in a furnace which was held at 500 °C. The (catalytic) pyrolysis reaction products (i.e. vapors) were evacuated from the reactor tube with the helium gas stream (ca. 100 mL·min^{-1}). The pyrolysis vapors were transferred into the GC via a split/splitless injection port (split ratio = 1:100, injector temperature = 250 °C). And then the chromatographic separation of the pyrolysis vapors was achieved using a Restek capillary column (RTX-1701, 60 m, 0.25 mm, 0.25 µm) with a constant column gas flow of 1 mL·min^{-1}. The GC oven temperature program was set to hold at 40 °C for 3 min, followed by a ramp up at 5 °C·min^{-1} to 280 °C and finally to hold constant at 280 °C for 1 minute. Following the separation on the GC column, the pyrolysis compounds were identified using an MS (a single quadrupole mass spectrometric detector, Thermo ISQ MS). The MS transfer line temperature and the ion source temperature were kept at 280 °C and 230

°C, respectively. The peak areas were collected from the integration of the total ion current (TIC) signals gathered from MS chromatograms. The scanning was performed within a m/z range of 29–300 (recorded at every 0.2 s) employing an ionization energy of 70 eV. The identification of compounds was achieved based on the comparison of the mass spectra recorded with those in the National Institute of Standards and Technology (NIST) database library.

6.3 Results and Discussion

6.3.1 Catalyst Characterization

Figure 6.2a shows the X-ray diffraction (XRD) patterns of the individual components and fresh catalyst extrudates. The XRD diffraction patterns for the HZSM-5/Al_2O_3 catalyst extrudates show the characteristic reflections of zeolite ZSM-5. The alumina component displays no crystalline phase being purely amorphous.

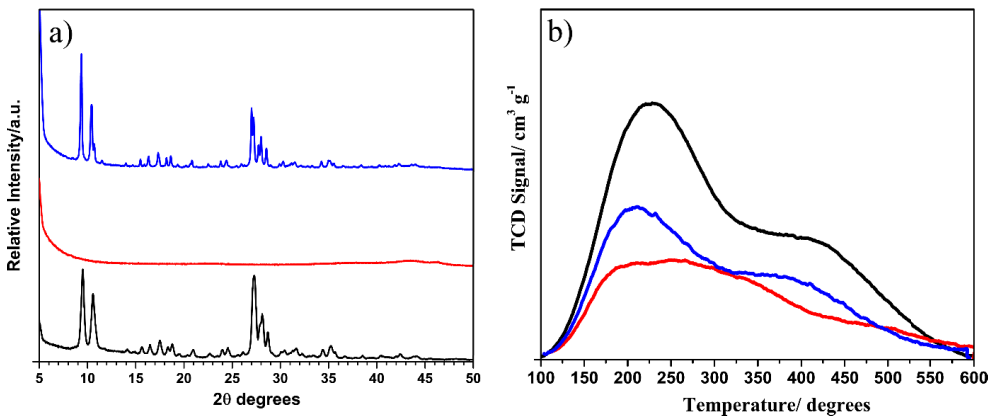

Figure 6.2. (a) XRD patterns and (b) NH_3-TPD profiles of fresh HZSM-5 and Al_2O_3 individual components, and fresh HZSM-5/Al_2O_3 extrudates. In both graphs, **black** line represents HZSM-5 zeolite, **red** line represents Al_2O_3 binder and **blue** line represent the fresh HZSM-5/Al_2O_3 extrudates.

Textural properties of catalyst extrudates, such as porosity and crystallinity, are mainly dictated by the percentages of binder and active phase, and the preparation method used. Pore size distributions obtained after Hg porosimetry and Ar physisorption at -196 °C are shown in Figure 6.3a and 6.3b, respectively. Zeolite HZSM-5 expectedly showed the presence of micropores,

while alumina (Al_2O_3) showed mesopores with a rather broad distribution of pore sizes (up to 15 nm), confirming the highly amorphous nature of the material. The technical HZSM-5/Al_2O_3 materials also showed the presence of mesopores (14 nm and ~ 45 nm), corresponding to both the mesopores from Al_2O_3 and the formation of interparticle domains upon extrusion. These domains are known to accommodate larger feedstock molecules[44].

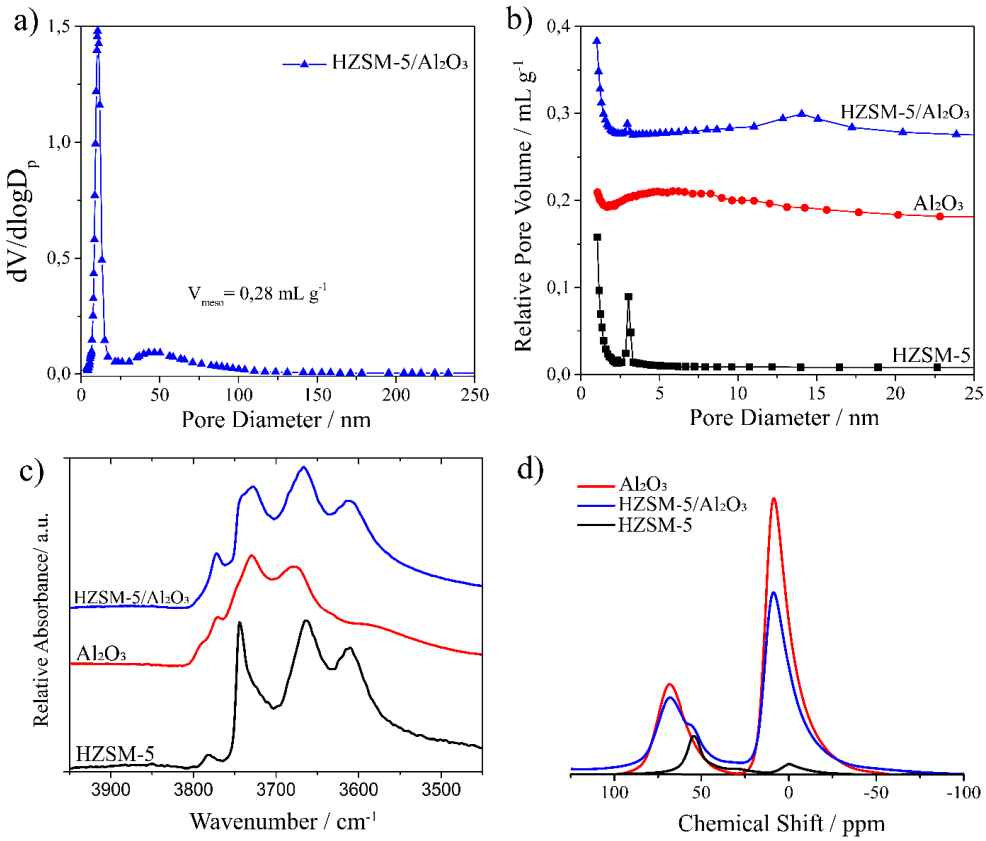

Figure 6.3. Pore size distribution graphs after (a) Hg porosimetry and (b) Ar physisorption at -196 °C. (c) Fourier transform-infrared (FT-IR) spectra of the OH-stretching region. Terminal silanols (3745 cm^{-1}) are assigned in the graph. (d) ^{27}Al solid-state nuclear magnetic resonance (ssNMR) spectra of fresh, individual components, and the HZSM-5/Al_2O_3 catalyst extrudates. The intensities in the ssNMR spectra were normalized by weight.

As expected, the physicochemical properties of the fresh extrudates are a weighted combination of the individual components (50:50) and show no major deviations. Figure 6.3c shows the Fourier transform-infrared (FT-IR) spectra from the OH-stretching region for HZSM-5, Al_2O_3

and HZSM-5/Al_2O_3 materials. For clarity, the assignments of the FT-IR bands from the OH region are provided in Table 6.2. The FT-IR spectrum of the HZSM-5/Al_2O_3 catalyst extrudates shows similar vibrations as for the HZSM-5 and Al_2O_3 isolated phases revealing that no new sites were formed after extrusion.

Regarding the FT-IR spectra, we have labelled the three different types of OH groups as terminal, bridging or triply bridging and the different possible Al coordination as IV, V and VI (i.e., tetra-, penta- and octahedral coordinated aluminum sites). HZSM-5 shows the presence of terminal OH (3744 cm^{-1}) and bridged hydroxyl groups or Brønsted acid site (3611 cm^{-1})[87], as expected. According to Bordiga *et al.*, the shoulder going to lower frequencies at 3744 cm^{-1} corresponds to internal OH groups. A certain degree of dealumination in the HZSM-5 phase is revealed by the presence of the 3782 cm^{-1} and 3665 cm^{-1} bands which correspond to OH stretching of extra-framework Al (EFAl) species[88–90]. For the Al_2O_3 component, five different OH frequencies are shown. The bands at 3795 cm^{-1}, 3777 cm^{-1} and 3730 cm^{-1} are assigned to terminal OH groups coordinated to a single octahedral, single tetrahedral and single pentahedral Al sites, respectively[51,91]. Bridging OH groups coordinated to two and three Al cations sites are also present as seen in the IR spectrum between 3740 – 3745 cm^{-1} and 3590 – 3650 cm^{-1}, respectively[51,92].

^{27}Al solid-state nuclear magnetic resonance (ssNMR) spectra of the zeolite, alumina and the fresh composites are displayed in Figure 6.3d. All NMR signals, which correspond to the individual components, are also present in the fresh HZSM-5/Al_2O_3 extrudates. This indicates that no new aluminum sites are formed after extrusion while all NMR peaks shown in the fresh extrudates spectrum represent a spectroscopic superposition of the individual components. The spectrum of the alumina binder showed two main peaks at 68 and 9 ppm, which correspond to calcined and dehydrated boehmite-alumina[45,46]. The chemical shifts observed for the zeolite phase corresponds to extra-framework octa- (0 ppm) and pentahedral (30 ppm) Al sites[47] and tetra-coordinated framework Brønsted acidic aluminum sites (55 ppm)[48,49,50], respectively.

Table 6.2. Fourier transform-infrared (FT-IR) bands present in the OH-stretching region of the HZSM-5 and Al_2O_3 individual phases. T = Terminal; B = Bridging.

Sample	Coordination Site	Type of Site	Wavenumber (cm^{-1})	Ref.
HZSM-5	Si – OH	Silanol (T)	3744 – 3747	87
	Al – OH – Si	Brønsted Acid (B)	3611	87
	Al - OH	EFAl (T)	3782 3665	88,89,93
Al_2O_3	Al - OH	Al(VI) (T)	3760 – 3780	92
			3722	94
		Al(IV) (T)	3785 – 3800	92,93
		Al(V) (T)	3730 – 3736	92,93
	Al - OH - Al	Al(VI)/Al(VI) (B)	3740 – 3745	91,93
			3675 – 3680	94
	OH (- Al)$_3$	Al(VI)/Al(VI)/Al(VI) (Triply B)	3590 - 3650	92,94

Table 6.3 shows a summary of the physicochemical properties of the individual components and HZSM-5/Al_2O_3 catalyst extrudates. HZSM-5/Al_2O_3 showed a larger external surface area value than the HZSM-5 component after the addition of alumina. This might facilitate the condensation of larger oligomeric species in pyrolysis vapors on the external surface compared with the precursor zeolite HZSM-5 material.

Acidity in the catalyst extrudates was evaluated by temperature programmed desorption (TPD) of NH_3 (Figure 6.2b) and pyridine FT-IR spectroscopy. After adsorption of pyridine on the HZSM-5/Al_2O_3 catalyst extrudates, the amount of Brønsted and Lewis acid sites was calculated[51] (see Table 6.3). The observed acidity of the HZSM-5/Al_2O_3 catalyst extrudates again was found to be a roughly mixed contribution of acid sites from each individual component. In short, no dealumination was observed to occur during the synthesis-extrusion process of the catalyst extrudates. Expectedly, both individual components contain Lewis acid sites (LAS) while only the zeolite has Brønsted acid sites (BAS). Upon mixing and extrusion, the amount of both the Lewis and Brønsted acid sites in the HZSM-5/Al_2O_3 extrudates were slightly higher than expected. This may be related to the higher external surface area values

enabling an improved accessibility and diffusion of the basic probe molecules. Accordingly, there is no evidence indicating extra dealumination taking place or neutralization of BAS by Al migration from the binder to the zeolite. This reveals that the intrinsic activity of the zeolite HZSM-5 individual component remains intact after extrusion. Therefore, the only effect of extrusion appears to be a dilution of the highly active zeolite HZSM-5 phase with the alumina binder. However, the contribution of additional LAS, introduced by the Al_2O_3 binder, to the overall catalytic activity of the extrudates cannot be neglected (*vide infra*, section 6.3.2).

Table 6.3. Physicochemical properties of the individual components and the fresh HZSM-5/Al_2O_3 catalyst extrudates. Acidity values were calculated from NH_3 temperature programmed desorption (TPD) and Fourier transform-infrared (FT-IR) after pyridine desorption at 423 K (extinction coefficients were 1.67 and 2.22 cm μmol^{-1} to calculate Brønsted and Lewis acid sites, respectively).

Materials		HZSM-5	Al_2O_3	HZSM-5/Al_2O_3
S_{BET} $m^2 \cdot g^{-1}_{cat}$	Ar physisorption	460	188	273
S_{micro} $m^2 \cdot g^{-1}_{cat}$		405	-	166
S_{ext} $m^2 \cdot g^{-1}_{cat}$		55	208	107
S_{micro} $m^2 \cdot g^{-1}_{cat}$		0.14	-	0.06
V_{micro} $cm^3 \cdot g^{-1}_{cat}$		0.05	0.52	0.27
Acid Properties				
Total amount of acid sites [a] $\mu mol \cdot g^{-1}$	NH_3-TPD	862	408	620 (635)
Desorption temperature of strong acid sites [a] °C		380	-	358
Lewis acid sites [b] $\mu mol \cdot g^{-1}_{cat}$	Pyridine FT-IR spectroscopy	94	237	129 (165)
Brønsted acid sites [b] $\mu mol \cdot g^{-1}_{cat}$		144	-	79 (72)

Between brackets, the theoretical acidity values calculated for an ideal 50:50 wt. % mixing of zeolite and alumina are shown.

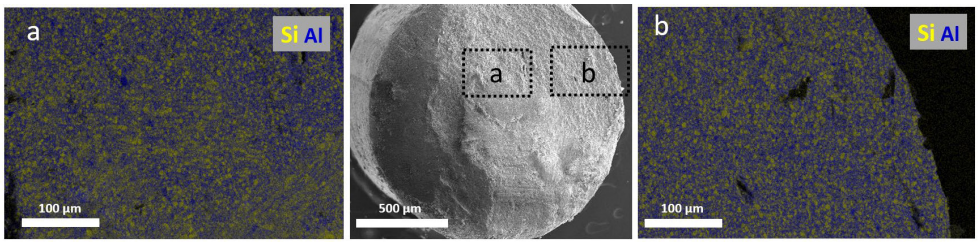

Figure 6.4. Scanning electron microscopy (SEM) and energy-dispersive X-ray (EDX) analysis images of (a) center and (b) edge of the cross section of a fresh HZSM-5/Al_2O_3 catalyst extrudate.

The morphology and distribution of the zeolite and alumina domains over the composite catalysts were analyzed by scanning electron microscopy – energy-dispersive X-ray (SEM-EDX) (Figure 6.4)[38,52]. The Si signal could be used as a marker to identify the zeolite domains, also taking into account that the amount of aluminum present in the zeolite domains is much lower than that of the alumina binder. In both EDX images, either at the center (Figure 6.4a) or edge (Figure 6.4b), we can roughly observe a homogeneous distribution of both active phase and binder within the cross section of the extrudate.

Focused ion beam – scanning electron microscopy (FIB-SEM) experiments allowed the distribution of each phase within the catalyst extrudate to be visualized in detail (Figure 6.5). The SEM electron image (Figure 6.5a) reveals an irregular and dotted pattern which clearly corresponds to the zeolite (darker domains as they coincide with the Si-rich yellow parts) and alumina phases as indicated in the EDX images (Figure 6.5b).

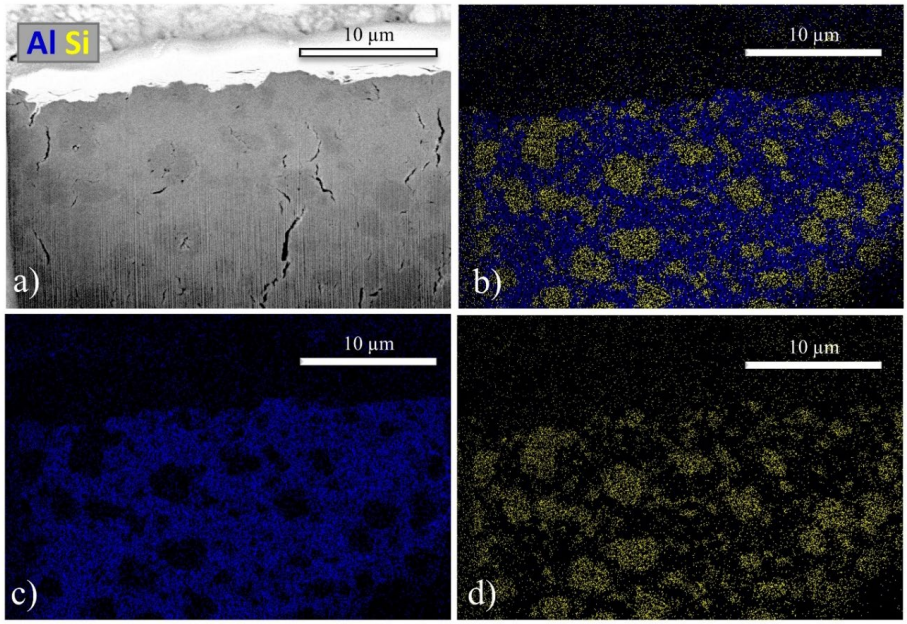

Figure 6.5. (a) Scanning electron microscopy (SEM) and energy-dispersive X-ray (EDX) images of (b) Al and Si, (c) Al and (d) Si obtained after the focused ion beam (FIB) milling in the center of the cross section of a fresh HZSM-5/Al_2O_3 catalyst extrudate.

Moreover, voids can be seen (~ 0.1 µm) thus constituting a macropore interparticle network between the zeolite and alumina agglomerations as also suggested by the porosimetry experiments[44,53,54]. However, even these relatively large-sized pore networks may not be suitable for the aerosols produced upon pyrolysis of cellulose and lignin biopolymers. Because the particle diameter of these aerosols is reported to be between 0.5 – 10 µm, majority of them being close to 1.0 µm. Therefore, the reported average particle diameter of aerosols exceeds even the largest pore diameters observed for the catalyst extrudate (see Figure 6.3a).

6.3.2 Catalytic Fast Pyrolysis

Catalytic fast pyrolysis (*ex-situ*) of pine wood and cellulose using HZSM-5/Al_2O_3 extrudates as catalyst yielded char, non-condensable gas, bio-oil (water and condensable organics) and coke as products. The product yields are summarized in Figure 6.6. For comparison, non-catalytic (NC) pyrolysis product yields are also provided. At high catalyst-to-biomass ratios (i.e. low space velocities), the conversion of pyrolysis vapors to catalytic products are typically

very high[55,56]. However, such operating conditions prevent observing the long-term effects of reactants (pyrolysis vapors in this case) on the catalyst materials[57]. Therefore, a rather high space velocity (5.0 h^{-1}) was chosen in this work to clearly see the effects of pyrolysis vapors on the catalyst as well as on the evolution of catalytic products with increasing TOS.

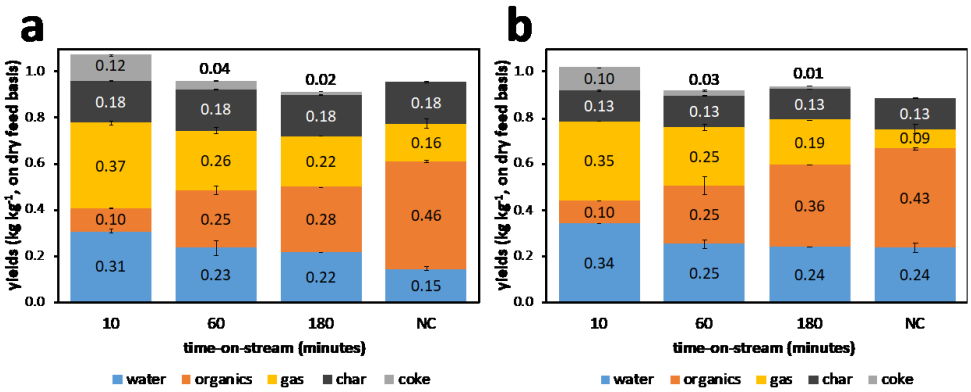

Figure 6.6. Product yields of catalytic pyrolysis of (a) pine wood, and (b) cellulose obtained at the experimental conditions of $T_{pyrolysis}$ = 500 °C, $T_{catalysis}$ = 500 °C and WHSV = 5.0 h^{-1}. Non-catalytic pyrolysis (NC) yields obtained from duplicate experiments (reaction time = 60 min) for each feedstock are also provided for comparison. Error bars represent standard deviation from the mean of duplicate experiments for all cases.

The product distribution changed significantly for both feedstocks with the applied *ex situ* catalysis, if compared to the non-catalytic pyrolysis tests. The strong changes in product yields are clearly an indication of the substantial catalytic activity of HZSM-5/Al_2O_3 catalyst extrudates. Overall, similar trends in product distribution were observed for pine wood and cellulose. The organic fractions produced upon pyrolysis are mostly converted to gas, water and coke, especially at the shortest time-on-stream (e. g. highest catalyst/biomass ratio) which is in agreement with literature[13,37,58]. Dehydration reactions are known to be the primary pathway of deoxygenation during catalytic pyrolysis of biomass[59], particularly when using acidic zeolite ZSM-5-based catalysts materials. When the catalyst is at its most active state (10 min TOS), very similar water yields of 0.31 kg kg^{-1} and 0.34 kg kg^{-1} (on dry feed basis) are obtained for pine wood and cellulose, respectively. However, these values also contain the thermally produced water during pyrolysis (see Figure 6.6. for the thermal (non-catalytic) water yields). Therefore, the catalytically produced water values at 10 min TOS would be 0.16 kg kg^{-1} and 0.10 kg kg^{-1} for pine wood and cellulose, respectively. This observation suggests that

hemicellulose and lignin fractions of pine wood contribute to catalytic dehydration reactions considerably. However, the relatively strong C-O bond between the benzene ring and the phenolic-OH would make lignin-derived phenolic structures less susceptible to acid catalyzed dehydration reactions, if compared to aliphatic alcohols for instance. Therefore, it is more likely that the hemicellulose-derived vapors are contributing to a larger extent to the dehydration reactions. On the other hand, decarbonylation and decarboxylation reactions are the other forms of deoxygenation observed during biomass CFP. The formation of non-condensable gases (NCG), in particular that of CO and CO_2, during the catalytic pyrolysis of pine wood seems to primarily originate from the reactions of cellulose-derived vapors over the catalyst. This is evidenced by the substantial increase in the catalytic NCG yields of cellulose compared to the thermal NCG yields. Wang *et al.*[29] showed that the catalytic CO_x formation is more prominent for cellulose, if compared to lignin and hemicellulose, in accordance with the results obtained in this work. In terms of coke formation, a slightly higher fraction of feed intake is converted to coke with pine wood compared to cellulose. The slight increase may be attributed to lignin-derived vapors coking on the external surface of the catalyst[30]. With increasing TOS, the product distribution and the yields of individual product streams converge to the non-catalytic case, indicating the (partial) deactivation of the catalyst.

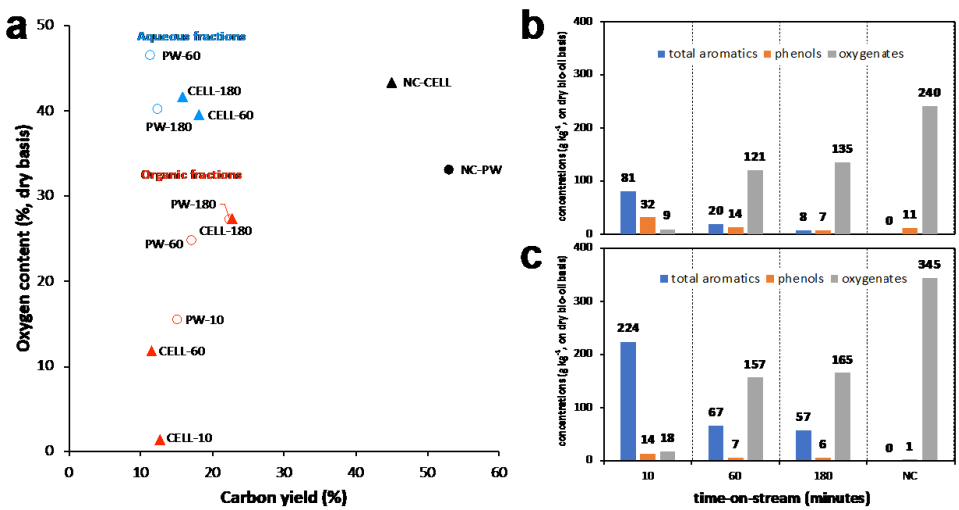

Figure 6.7. (a) Oxygen content (dry basis) and carbon yield of bio-oil fractions obtained upon *ex-situ* catalytic pyrolysis of pine wood and cellulose. Aqueous fractions at 10 min TOS are not included in the plot as they contain mostly water (>0.97 g g^{-1}). PW-NC (●) and CELL-NC (▲) values in the plot represent the non-catalytic pyrolysis yields of pine wood and cellulose, respectively. Conditions; $T_{pyrolysis}$

= 500 °C, $T_{catalytic}$ = 500 °C**,** WHSV = 5.0 h^{-1}. The composition of catalytic and non-catalytic bio-oils produced from (b) pine wood and (c) cellulose. Total aromatics = BTX and polycyclic aromatics (naphthalene, indene and their substituted forms). Phenols = phenol and substituted phenols; oxygenates = acids, aldehydes, ketones, furans and anhydrosugars, (typically non-catalytic pyrolysis products of biomass).

An important parameter to assess the feasibility of biomass-to-fuels (or chemicals) processes is to check the carbon yields on feed basis in the desired product[16,60]. The oxygen contents (on dry basis) versus the carbon yields of the liquid product streams (aqueous and organic fractions) obtained via CFP are plotted in Figure 6.7a, which highlights the two shortcomings of the CFP process. Firstly, the loss of C in the products of catalytic pyrolysis is obvious, if compared to the non-catalytic case. And unfortunately, the deoxygenation levels obtained do not justify the loss of C for most cases. Secondly, catalytic water production during CFP leads to phase separation in the bio-oil product resulting in aqueous and organic fractions. The aqueous fractions obtained were primarily composed of water-soluble oxygenates (products of pyrolysis reaction). And the organic fraction produced was composed of aromatic hydrocarbons and water-insoluble oxygenates. The phase separation induced upon CFP will likely increase the downstream processing costs if both aqueous and organic streams are to be utilized. The valorization of the aqueous fractions will be of importance in particular at higher TOS (60 and 180 min), considering that the C yields of these aqueous fractions are in the same range with the corresponding organic fractions. The composition of catalytic and non-catalytic bio-oils, as analyzed by GC/MS, is shown in Figures 6.7b and 6.7c for pine wood and cellulose, respectively. Lower aromatic hydrocarbon yields were obtained than reported in the literature which may be attributed to the high WHSV employed in this work[1,56,61]. Besides, as a result of Lewis acid sites present on Al_2O_3 (see Table 6.3), the catalytic effect of the binder cannot be neglected and were reported to have a pre-cracking effect[36,61–63]. Indeed, the catalytic effect of

the binder on the pyrolysis vapors was also corroborated with py-GC/MS tests using a mixture of only the Al_2O_3 binder and cellulose (see Figure 6.8).

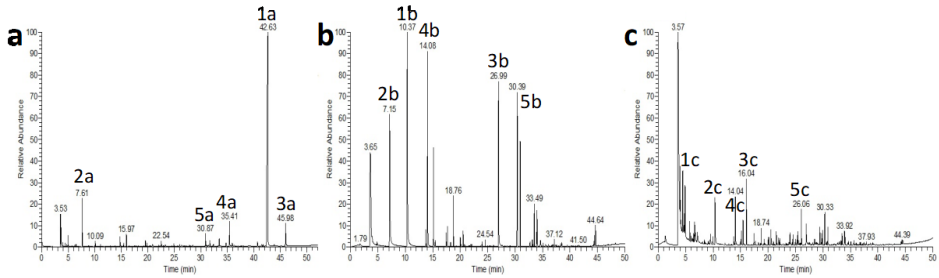

Figure 6.8. Pyrograms obtained upon py-GC/MS of (a) cellulose (200 µg), (b) cellulose (200 µg) mixed with HZSM-5 (4000 µg), (c) cellulose (200 µg) mixed with Al_2O_3 (4000 µg). The most abundant five compounds sorted by relative peak areas (%) for each test are as follows; (1a) levoglucosan (74.26%), (2a) glycolaldehyde (3.90%), (3a) 1,6-Anhydro-α-d-galactofuranose, (4a) unidentified (2.67%), (5a) unidentified (1.23%), (1b) toluene (20.83%), (2b) benzene (15.00%), (3b) naphthalene (13.19%), (4b) (*p-, m-*) xylenes (11.78%), (5b) 2-methyl-naphthalene (9.80%), (1c) furan (8.82%), (2c) toluene (6.41%), (3c) furfural (4.99%), (4c) (*p-, m-*) xylenes (4.91%), (5c) azulene (3.05%). The pyrolysis test performed with Al_2O_3 shows the catalytic effect of the individual alumina component on cellulose derived pyrolysis vapors.

While the aromatic hydrocarbons (monoaromatics and polycyclic aromatics) dominate the liquid product spectrum at short time-on-stream, the composition of organics produced starts to resemble the non-catalytic cases with increasing TOS as a result of (partial) deactivation of the catalyst. An increased selectivity towards aromatics production was observed for cellulose-derived vapors, if compared to that of derived from pine wood. Compared to the non-catalytic results, a higher quality liquid product (i.e., lower oxygen content, more hydrocarbons) is obtained but with inferior carbon yields; obviously a significant fraction of carbon in the feed is converted into coke and CO_x. The formation of CO_x is inevitable for the CFP process when the objective is to deoxygenate the pyrolysis vapors. Therefore, the formation of coke on the

catalyst appears to be the primary obstacle for the CFP process. Because it leads not only to the loss of C but also deactivates the catalyst at the same time.

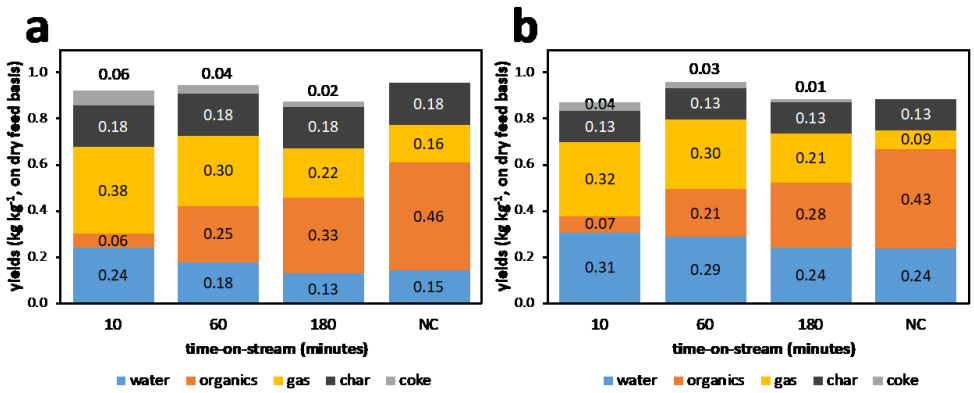

Figure 6.9. Product yields of catalytic fast pyrolysis (CFP) of (a) pine wood and (b) cellulose obtained with the regenerated catalysts at the experimental conditions of $T_{pyrolysis}$ = 500 °C, $T_{catalysis}$ = 500 °C and WHSV = 5.0 h^{-1}. Non-catalytic pyrolysis yields are also provided for comparison.

The catalyst activity after regeneration was examined as well, and the catalytic pyrolysis product yields are shown in Figure 6.9. Although the organic product yields seem to be lower with regenerated catalysts (specifically at the shortest TOS), it should be noted that the mass balance closures are not as good as those obtained with the fresh catalysts (see Figure 6.6). From experiments with pine wood, a clear decrease in dehydration reactions is observed by increasing TOS, possibly due to the loss in acid sites following regeneration (see Figure 6.9a).

Additionally, lower coke yields were obtained, which may be directly attributed to the decrease in Brønsted acid sites.

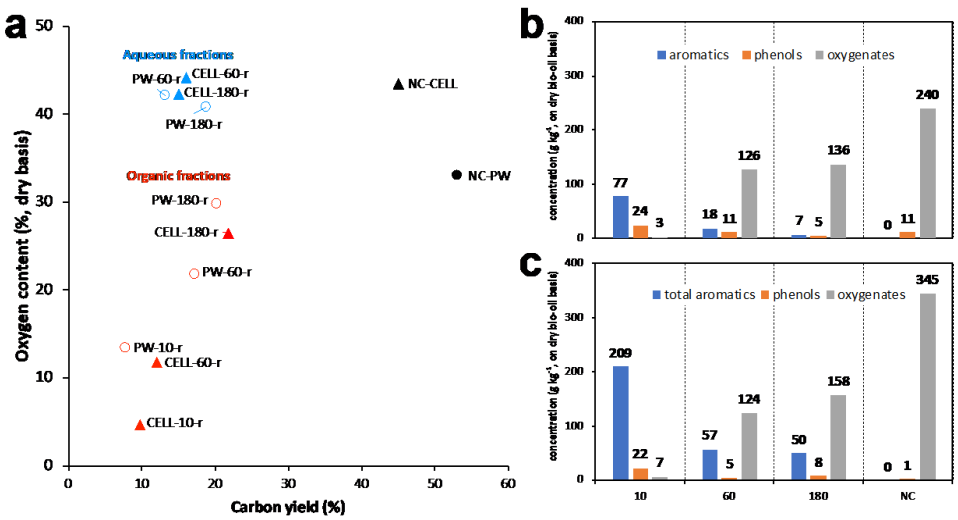

Figure 6.10. (a) Oxygen content (dry basis) and carbon yield of bio-oil fractions obtained upon *ex-situ* catalytic fast pyrolysis (CFP) of pine wood and cellulose with regenerated catalysts. Aqueous fractions at 10 min TOS are not included in the plot as they contain mostly water (>0.97 g g^{-1}). PW-NC (●) and CELL-NC (▲) values in the plot represent the non-catalytic pyrolysis yields of pine wood and cellulose, respectively. Conditions; $T_{pyrolysis}$ = 500 °C, $T_{catalytic}$ = 500 °C**,** WHSV = 5.0 h^{-1}. The composition of catalytic and non-catalytic bio-oils produced from (b) pine wood and (c) cellulose. Total aromatics include benzene, toluene, xylene and polycyclic aromatics such as naphthalene, indene and their substituted forms. Phenols include phenol and substituted phenols and the oxygenates include acids, aldehydes, ketones, furans and anhydrosugars which are typical non-catalytic pyrolysis products of biomass.

Carbon yield and oxygen content of the liquid products shown in Figure 6.10a, suggest that the loss of acid sites observed after one reaction/regeneration cycle do not affect the overall product composition drastically. In short, the trends observed with the fresh catalysts seem to prevail with the regenerated catalysts. The organic fractions obtained with the regenerated catalysts materials (shown in Figure 6.10b and 6.10c) reveal that the aromatic hydrocarbons were produced at 5 – 15% lower concentrations relative to the values produced with fresh catalysts. Small decreases in the production of the aromatic hydrocarbons following catalyst regeneration have been reported previously in the literature as well[41,64]. The reduced catalyst performance observed even after one reaction / regeneration cycle suggests that a frequent addition of fresh

make-up catalyst to the reactor would be required during long-term operation. However, such operating conditions would make the CFP process unsustainable.

6.3.3 Characterization of Spent Catalysts

As shown in the previous section, formation of carbon deposits on catalysts during CFP is directly correlated with the reaction conditions and feedstock used[65], leading to a temporary deactivation of the catalyst materials. And even after regeneration, the deactivation by coke formation still affects catalyst performance to a certain extent[64,65]. Here, the differences between the pine wood-derived and cellulose-derived vapors should be highlighted to facilitate the interpretation of the catalyst characterization results. Obviously, the pine wood vapors would be comprised of molecules derived from the carbohydrate (cellulose and hemicellulose) and the lignin fractions of the whole biomass whereas cellulose-derived vapors would contain only the molecules from the decomposition of cellulose. The fast pyrolysis of cellulose primarily produces levoglucosan and other small oxygenates (e.g. glycolaldehyde) in the bench-scale set-up employed. The kinetic diameter of levoglucosan (0.67 nm) is reported to be slightly larger than the pore diameter of ZSM-5 (0.63 nm). But levoglucosan may undergo dehydration reactions on the surface of the catalyst to produce smaller furan compounds which could easily diffuse into the pores of the catalyst[29]. In the case of pine wood vapors, the hemicellulose-derived vapors would be composed of monomeric sugars and their defragmentation products which can also diffuse easily to the pore network of the catalyst. However, the lignin-derived fraction of the vapors, which could correspond up to 15 % of pine wood vapors, would also contain oligomeric species next to the phenolic monomers. It is these relatively small fraction of oligomeric lignin species that could cause differences between the behavior of pine wood and cellulose vapors upon contact with the catalyst. Because these molecules, likely ejected as aerosols from the biomass particle during pyrolysis, are larger than the pore diameters of the catalyst. And they could be condensed and/or cracked on the external surface of the catalyst.

In addition, previous studies have demonstrated that increase in coke contents correlates linearly with a decrease of acidity and porosity[68,69]. In Figure 6.11, the coke content, the acidity and the porosity of the spent extrudates are plotted as a function of TOS.

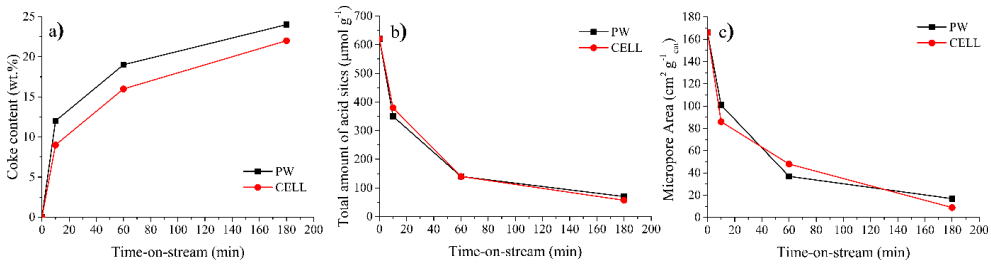

Figure 6.11. (a) coke content, (b) total number of acid sites and (c) micropore area from spent catalyst obtained at different time-on-stream (TOS) after catalytic fast pyrolysis (CFP) of pine wood (PW) and cellulose (CELL).

The spent catalyst extrudates obtained after pine wood CFP show a larger quantity of coke deposits formed over time (12 wt. %, 19 wt. % and 24 wt. %) than the spent catalyst extrudates obtained after using cellulose as feed (8 wt. %, 16 wt. % and 22 wt. %), values which are in accordance with the quantity of coke produced as depicted in Figure 6.6. Independently of the quantity of coke formed for each feedstock, decrease in the amount of acid sites occurs at a similar pace (Figure 6.11b). However, the micropores (Figure 6.11c) seem to be blocked faster for the CFP of cellulose, in particular at the shortest TOS. The coke content of the sample CELL-10 is ca. 30 % lower than that of PW-10. In contrast, a higher percentage of original micropore area is retained with the sample PW-10 (61 %) when compared to the sample CELL-10 (52 %). Additionally, the final values for the remaining micropore area and acid sites are lower in the CELL-180 than in PW-180. Therefore, it seems that lignin-derived oligomers present in the pine wood vapors block the external surface of the catalyst, restricting the access of small-sized cellulose vapors to the micropores. And during the CFP of cellulose, coke deposits appear to predominantly form in the zeolite micropores due to the unrestricted access of the small-sized cellulose-derived monomers to the micropores. predominantly coke the external surface area of the catalyst. Similar results have also been reported in another study[30] recently. Together, these results support the hypothesis that the primary cause of deactivation with cellulose vapors is due to the coke growth reactions occurring on the acid sites inside the micropores of the catalyst. Therefore, suppressing coke formation by cellulose-derived vapors, if possible, should be a priority of future catalyst designs. Because that would accelerate the development of CFP technology for the actual lignocellulosic biomass[67,69–71].

All spent catalysts were subjected to Temperature Programmed Oxidation (TPO) analysis to reveal information about the nature and location of the carbonaceous deposits on and in the catalyst extrudates, and are summarized in Figure 6.12. As shown in previous studies, CO_2 formation profiles may be used to determine either the composition[17,71–76] or the location[73–75,77] of the coke in the catalyst. By monitoring the desorption of H_2O over time by mass spectrometry (MS), a more accurate estimation about the nature of the carbon deposits can be obtained[1,72]. Such information is useful, especially during the scale-up of the process because it would help to determine the regeneration conditions (e.g. temperature, time) of the catalysts. For example, soft (thermal) coke species are more easily removed (i.e. at lower regeneration temperatures) compared to hard (catalytic) coke species. While the soft coke species were observed in all spent samples, their share in overall coke species seemed to increase with increasing TOS which is consistent with the literature[32]. At first, the MS profiles of all the samples display a similar pattern, revealing that the coke desorbed does not depend on the feedstock used, but on time on stream. The main water desorption corresponds to excess of water produced during the pyrolysis, which was absorbed by the catalyst, since the samples have not been pre-dried before the TPO experiments. The H_2O profiles revealed two main regions; H_2O desorption at low temperatures (<200 °C) and at higher temperatures (400 °C to 650 °C, roughly) which match with the CO_2 desorption profiles. H_2O desorption occurring at higher temperatures gives information on how aromatic or aliphatic are the coke deposits (i.e. the H-content), allowing us to distinguish between thermal coke (whether there is H_2O desorption), and catalytic coke. CO_2 desorption around 400 °C indicates a mainly aliphatic character of the coke because of a large desorption of H_2O takes place as well. This sort of carbon deposits are known as soft or thermal and are formed from condensation of oxygenated compounds[71,74]. Additionally, after curve fitting of the CO_2 desorption profiles, we could clearly distinguish three desorption regions revealing information about the location of the coke species on and in the catalyst extrudates. The primary CO_2 desorption peak (above 400°C) can be divided into two secondary desorption peaks that indicate different coke locations inside the catalyst extrudates (green and light blue curves). The former desorption is assigned to coke located either on the alumina binder or on the external surface area of the zeolite crystals[75], while the second sharp CO_2 desorption at ~ 500 °C is assigned to the carbon deposits formed at the pore mouth of the zeolite micropores[77]. The last CO_2 desorption peak (red curve in Figure 6.12) has predominantly an aromatic character due to the lower intensity or absence of H_2O detected by mass spectrometry. This region is assigned to coke deposits retained on the catalytic sites of the micropores of the zeolite, which is also known as hard or catalytic coke (graphite-like coke)[69,74,77]. It is noteworthy that

at higher TOS, the ratio between thermal coke and catalytic coke seems to increase. When catalysts remain for longer time-on-stream, the amount of catalytic coke formed is limited since it depends on the active sites being available.

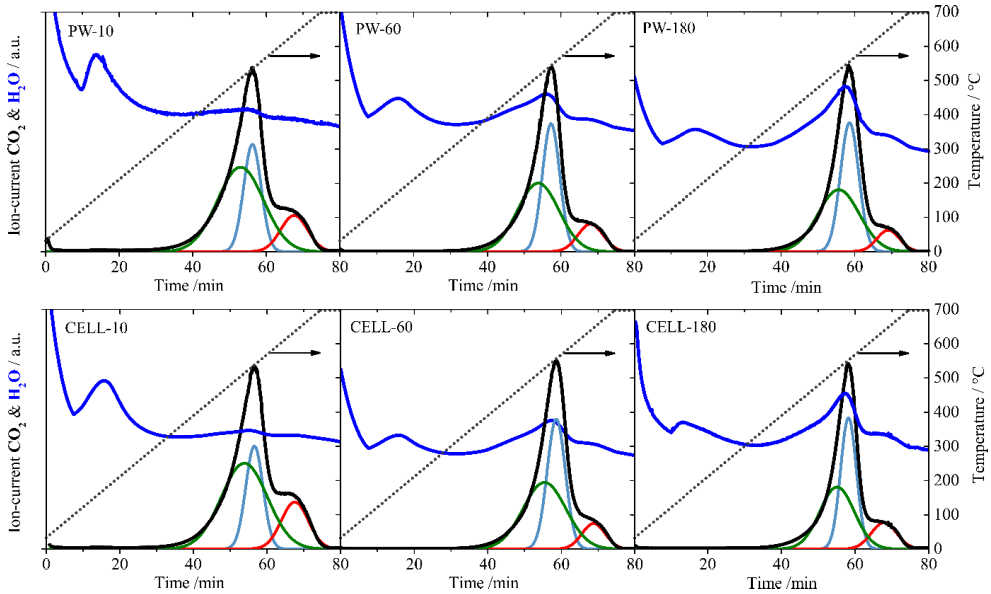

Figure 6.12. The mass spectra (MS) profiles of CO_2 (black line) and H_2O (dark blue line) of pine wood (top) and cellulose (bottom) spent extrudates after 10 min, 60 min and 180 min time-on-stream (TOS). Deconvolution from CO_2 desorption resulted in three secondary desorption peaks (curves) which correspond to soft or thermal coke located in the external surface area (green line), in the pore mouth of the zeolite crystals (light blue line), and hard or catalytic coke located on the catalytic sites (red line).

In Figures 6.13a and 6.13b, the ssNMR spectra of the spent samples after CFP of pine wood and cellulose are displayed, respectively. In all acquired spectra, a general decrease in intensity and a slight shift towards lower chemical shifts is observed for the 68 ppm and 55 ppm resonances with increasing TOS. In particular, the signal at 55 ppm, which corresponds to Brønsted acid sites (BAS), shows a significant decrease in intensity as a function of increasing TOS. Furthermore, a small shift of the 68 ppm peak towards lower chemical shifts is Visible. This signal originates from the Al (IV) sites of the alumina binder. The shift and overall broadening of both peaks may be attributed to a structural change in the environment of Al sites caused by the formation of the coke species in the proximity, especially species with an

aromatic character[78]. In short, the decrease in intensity and the shift to lower values demonstrate the partial poisoning and dealumination of the Al (IV) sites occurring over increasing TOS and caused by the carbon deposits.

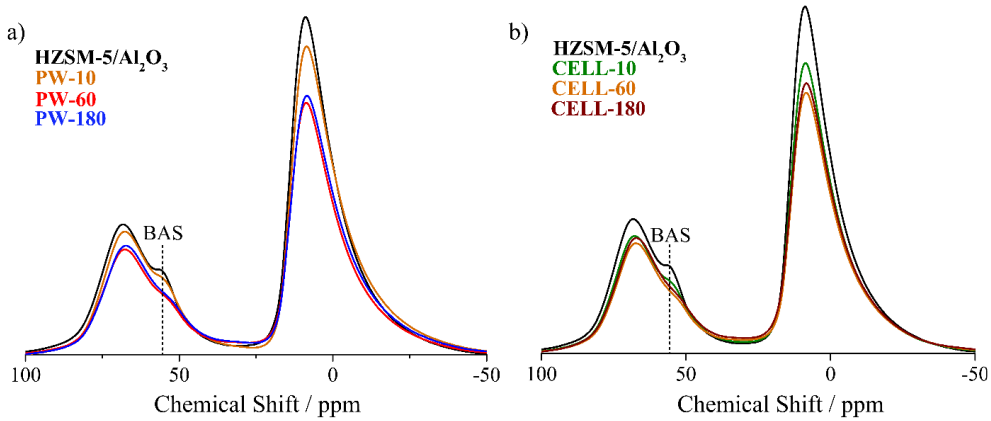

Figure 6.13. ^{27}Al solid-state nuclear magnetic resonance (ssNMR) spectra of (a) spent extrudates obtained after catalytic fast pyrolysis (CFP) of pine wood and (b) spent extrudates obtained after CFP of cellulose.

Figure 6.14a shows a schematic representation of the confocal fluorescence microscopy (CFM) approach used within this work to visualize the coke formation processes within catalyst extrudates. Clearly, the PW-10 catalyst extrudate displayed larger amount of highly condensed coke species in the outer phase than the CELL-10 extrudates, as was confirmed by thermogravimetric analysis (TGA). Before choosing these CFM images, several catalyst extrudates were analyzed to ensure that the CFM images shown are representative for the larger group of the spent catalyst extrudates.

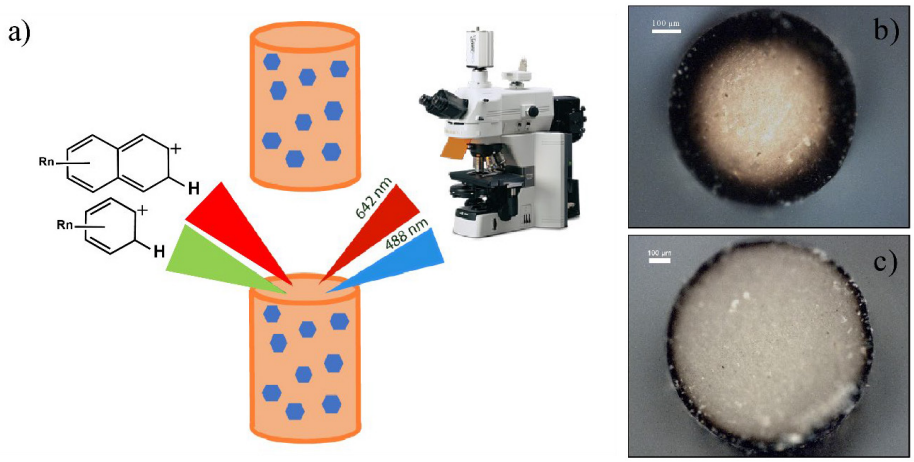

Figure 6.14. (a) Schematic of confocal fluorescence microscopy (CFM) approach used to analyze the cross section of the spent catalyst extrudates. The carbocationic species excited upon illumination with 488 and 642 nm lasers correspond to benzylic (green fluorescence) and naphthalene (red fluorescence) species and their corresponding methylated versions, respectively. Optical images of the cross section of (b) PW-10 and (c) CELL-10 spent extrudates.

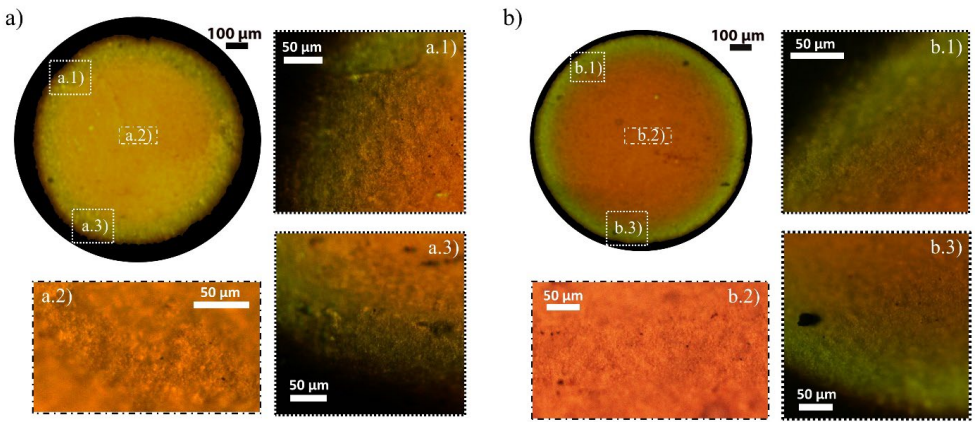

Figure 6.15. Confocal fluorescence microscopy (CFM) images obtained after irradiating the cross section of spent catalyst after 10 min time-on-stream (TOS) with 488 nm and 642 nm lasers after catalytic fast pyrolysis (CFP) of (a) pine wood and (b) cellulose.

The confocal fluorescence microscopy (CFM) approach (Figure 6.14a) enables the visualization of the location of different carbon deposits on the extrudate's cross section[79–81]. Fluorescence microscopy images of the cross section of PW-10 and CELL-10 spent catalysts materials and the corresponding magnifications are shown in Figure 6.15a and 6.15b. Almost no fluorescence was emitted from the cross-section of spent extrudates obtained at higher TOS (i.e., 60 or 180 min), because of the higher concentration of condensed graphite-like coke species throughout the extrudate. For emission spectra see Figure 6.16. The carbon deposits are distinguished according to their size and nature[82,83] when illuminated with 488 nm and 642 nm lasers, simultaneously in the cross section of PW-10 and CELL-10 (Figures 6.14b and 6.14c). According to previous works[54,84], the 488 nm laser only excites small aromatic species emitting green fluorescence (simple conjugated systems/rings; e. g. single aromatic carbocationic rings), while the 642 nm laser excites larger aromatic species emitting red fluorescence (≥2 aromatic carbocationic rings). Larger conjugated species (e.g. >3 aromatic carbocationic rings) cannot be detected in the range of emissions above 700 nm because the size of these species is much larger than the zeolite internal structure[85,86].

For both spent extrudates an external layer of coke which does not emit fluorescence can be observed. It corresponds to a graphite-like coke type. In Figure 6.15a (PW-10), smaller species are predominantly more abundant all along the cross-section of the catalyst body than in the case of CELL-10 (Figure 6.15b). The picture of CELL-10 also indicates a larger intensity of bigger aromatic carbon species in the core of the extrudate particle.

Regarding Figure 6.15a, when going from the edge to the center of the extrudate, a first thin green layer followed by a pale orange domain located in the center are observed which corresponds to small conjugated species (benzene and/or naphthalene carbocations) and larger conjugated species (naphthalene and/or pyrene carbocations), respectively. The pale orange fluorescence region corresponds to a mixture of small and large conjugated species in which the small ones are more abundant[54]. For the CELL-10 (Figure 6.15b), a similar pattern of green fluorescence in the edge and a more intense orange/red fluorescence in the center of the extrudate compared to the PW-10 was observed, indicating a higher presence of larger carbocations Apparently, cellulose vapors diffuse easier through the extrudate pores due to their smaller size. They react and form larger aromatics, which later on constitute the larger coke deposits. As a consequence, the fluorescence of the extrudate's interior becomes deep orange. In the case of pine wood, the presence of an external layer of condensed coke indicates that the pine wood vapors, being larger in molecular size, condensate and oligomerize already at

external surface of the extrudates. They are unable to further enter into the extrudate/zeolite pores. These observations suggest a close relation between the types of biopolymers present in the biomass vapors and the size and location of the coke deposits formed[30].

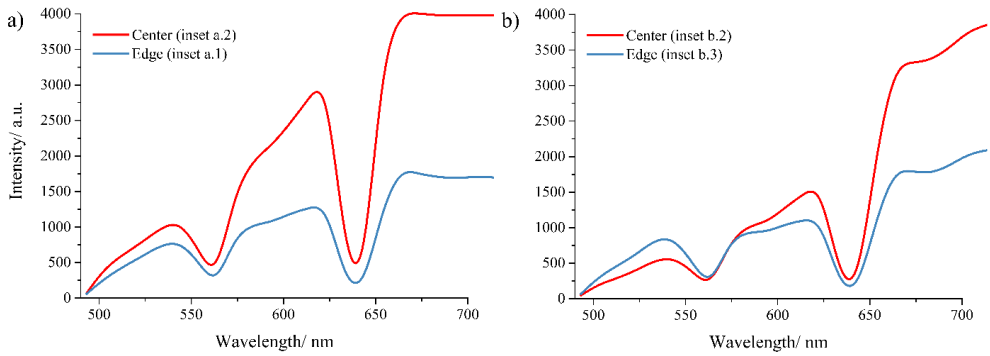

Figure 6.16. Emission spectra at different location of the cross-section from (a) PW-10 and (b) CELL-10 spent samples. The intensity valleys observed in all the spectra at 488, 562 and 642 nm correspond to the dichroic mirrors used for each of the laser wavelengths that were selected.

The emission spectra collected from the edge and center for PW-10 and CELL-10 spent extrudates (Figure 6.14b and 6.14c) are shown in Figure 6.16a and Figure 6.16b, respectively. A larger fluoresce intensity within the 600-700 nm range (i.e. obtained from larger carbocationic species) is observed, which is in accordance with both CFM images (Figure 6.15a.2 and Figure 6.15b.2). For the CFM image of CELL-10 material (Figure 6.15b.1 and Figure 6.15b.3), a much larger fluorescence intensity for the small carbocationic species (500-600 nm) is shown, which is in accordance with the emission spectra of CELL-10 material. The CFM images of PW-10 (Figure 6.15a.1 and Figure 6.15a.3) show overall a lower fluorescence intensity, which is also in accordance to with the emission spectra.

According to the observations made by Whiting *et al.*[54], molecules enter the catalyst pores and as they diffuse through the catalyst extrudate, they undergo cracking and oligomerization reactions over time to form poly-aromatic or conjugated species. If a transport barrier is present at a certain location inside the extrudate (e.g. pore narrowing), these enlarged species will be unable to diffuse out of the interior again. Instead, they will accumulate in the central part of the catalyst body. As shown in SEM-EDX images (Figure 6.4 and 6.5), both zeolite and alumina domains are distributed evenly over the entire volume of the catalyst particle, suggesting that the intrinsic catalytic activity must be the same and comparable all along the catalyst extrudates.

Diffusion limitations of the various pyrolysis vapors (size-dependent barrier) are therefore most likely the main reason for the observed circular fluorescent microscopy patterns.

6.3.4 Characterization of Regenerated Catalysts

Table 6.4 shows a summary of the physisorption values of the regenerated catalysts. After regeneration, the textural properties of the catalyst used after the CFP of pine wood were restored completely. The surface area of the catalyst after the CFP of cellulose was not, however completely restored. After regeneration, the textural properties of the catalyst used during the CFP of pine wood were restored completely. However, the surface area of the catalyst used during the CFP of cellulose was not completely restored.

Table 6.4. Physisorption values of the regenerated samples.

	Ar physisorption		
Materials	S_{BET} $m^2 \cdot g^{-1}$	S_{ext} $m^2\ g^{-1}$	V_{micro} $cm^3 \cdot g^{-1}$
HZSM-5/Al_2O_3	273	107	0.06
PW-10-r	270	104	0.06
PW-60-r	273	106	0.06
PW-180-r	269	105	0.06
CELL-10-r	257	115	0.06
CELL-60-r	251	115	0.05
CELL-180-r	270	117	0.05

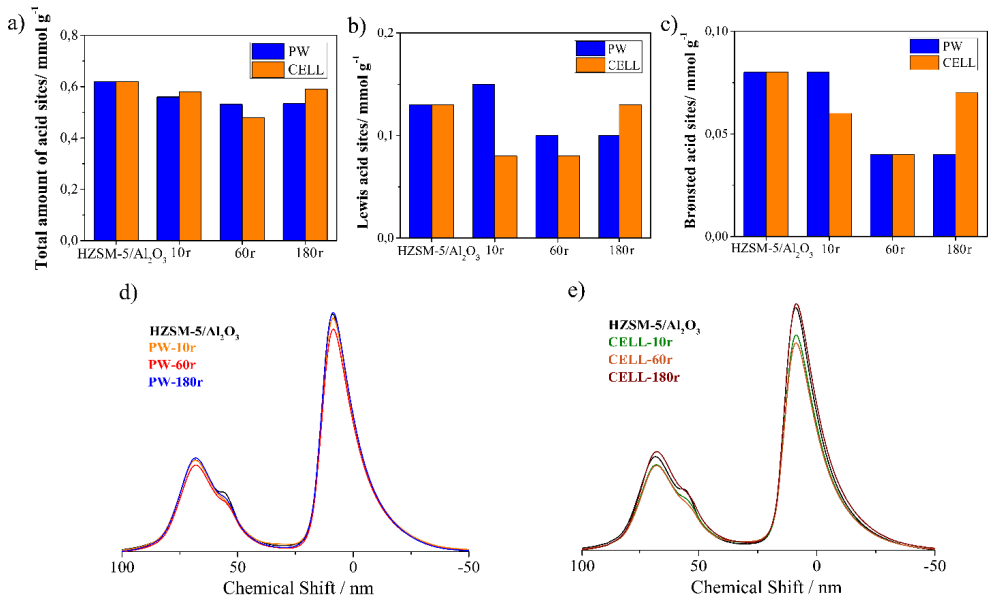

Figure 6.17. The total number of acid sites of (a) the regenerated extrudates was obtained by temperature programmed desorption of NH_3 (NH_3-TPD). (b) The total number of Lewis acid sites and (c) Brønsted acid sites available after regeneration were calculated after pyridine adsorption and FT-IR spectroscopy. ^{27}Al ssNMR spectra of the regenerated catalyst after one cycle for d) the CFP of pine wood and e) the CFP of cellulose.

NH_3-TPD and pyridine FT-IR analyses show that the total acidity could not be completely restored by the applied regeneration process, showing a slight drop in acidity for all samples (Figure 6.17a, 6.17b and 6.17c). A more pronounced loss of Lewis acid sites (LAS) is seen for the regenerated CELL extrudates, as also evidenced by a decrease in intensity shown in the ss-NMR spectra for the Al (VI) sites at 0 ppm (Figure 6.17e). In contrast, for Brønsted acidity, a larger drop is observed for the CELL batch than for the PW batch at short TOS, likely as a result of partial dealumination of the zeolite. The NMR spectra of the regenerated extrudates still shows a lower intensity for the peak at 55 ppm compared to the fresh extrudates. In this case, dealumination is most likely taking place and can be both the result of the CFP process (500 ºC) and of the regeneration process itself (600 ºC). All three characterization techniques confirm that the loss of catalyst acidity by dealumination is dependent on a) the type of pyrolysis feedstock (either being pine wood or cellulose) and b) the time on stream during CFP.

6.4 Conclusions

In this Chapter, the performance of an Al_2O_3-bound ZSM-5-based technical catalyst has been assessed in the *ex-situ* CFP of pine wood and cellulose. Although after extrusion meso- and small macropore domains were observed within the catalyst extrudates, their size might not be sufficiently large to accommodate the large aerosols ejected during pyrolysis of biomass. Moreover, the physicochemical properties observed in the technical catalyst extrudates such as acid density and porosity, were expected to reduce overall catalytic activity. Acidity measurements revealed that the acidity of the catalyst extrudates were a dilution of the physicochemical properties of the HZSM-5 and Al_2O_3 individual components. Catalytic pyrolysis product yields and composition showed similar trends as observed in the literature, converging to non-catalytic pyrolysis yields with increasing time-on-stream (higher biomass-to-catalyst ratios) as a result of catalyst deactivation. The lower total aromatic yields obtained (ca. 2 % on feed basis with cellulose feedstock), consistent with similar and previous works reported in literature, was attributed to the rapid catalyst deactivation known to occurs during the CFP of biomass. Strikingly, the Lewis acid sites present in the alumina binder also exhibited catalytic activity. The low selectivity to aromatics can be attributed to the loss of carbon as CO_x and carbon deposits. However, as identified in previous reports, coking is the primary challenge that needs to be overcome since it leads to both loss of carbon and catalyst deactivation. The slightly larger amount of coke was produced during the CFP of pine wood, likely because lignin-derived fraction of pine wood vapors contribute considerably to the formation of coke deposits. Irreversible and reversible structural changes were found to occur on the catalysts following the CFP reaction. Two types of carbon deposits were formed; thermal coke (aliphatic character) and catalytic coke (aromatic and graphite-like character). The thermal coke was located in the pores of the alumina structure (binder) and at the external surface of the zeolite domains. Thermal coke is accumulating with time-on-stream due to the progressing condensation reactions. The catalytic coke was formed on the Brønsted acid sites of the zeolite domains and its formation is limited to the catalytic sites available. CFM experiments revealed that larger coke species occur in the spent catalysts obtained from the CFP of cellulose. Cellulose-derived vapors consist of smaller molecules (oxygenates) than those of pine wood-derived vapors, which also include lignin and hemicellulose-derived vapors. While cellulose vapors are able to reach the extrudate core forming larger coke species, lignin-derived vapors present in the pine wood vapors form coke predominantly on the external surface area of the extrudates. Irreversible chemical changes in the catalyst structure (e. g. decrease in the

aluminum content) were observed for both feedstocks after catalyst regeneration. Progressing dealumination causes an ongoing loss of activity in subsequent cycles of CFP and catalyst regeneration. Overall, the structure of the state-of-the-art ZSM-5 based catalysts is unsuitable for accommodating the conversion of pyrolysis vapors, either from pine wood or from cellulose, to desirable fuel components or chemicals in sufficient quantities. Although it is not possible to decouple the effect of cellulose-derived vapors in the CFP of pine wood, the contribution of cellulose (and hemicellulose) derived vapors could be greater than lignin-derived vapors, due to the share of the latter being low in biomass pyrolysis vapors. In addition, the presence of lignin and/or hemicellulose generates a large buildup of condensed coke in the outer phase of the extrudate, not allowing the pyrolysis vapors from cellulose to enter the pores and reach the zeolite active phase. Therefore, modification of the catalyst system or the pyrolysis vapors prior to contacting with the zeolite-based catalysts is required to improve carbon yields obtained via CFP of lignocellulosic biomass. Moreover, if further developments on future catalyst designs are pursued to effectively tackle the coking with cellulose-derived vapors, a rigorous approach should be taken with respect to the selection of binder materials.

6.5 Acknowledgements

The authors thank Nikolaos Nikolopoulos (Utrecht University, UU) for the (FIB)SEM-EDX measurements. Dennie Wezendonk (UU) is also acknowledged for performing the TPO measurements. This work was also supported by the SBO proposal “Bioleum: Fuels and chemicals by fast pyrolysis of biomass” (grant no: 130039), supported by the Institute for promotion of Innovation through Science and Technology in Flanders (IWT).

6.6 References

(1) Carlson, T. R.; Cheng, Y.-T.; Jae, J.; Huber, G. W. Production of Green Aromatics and Olefins by Catalytic Fast Pyrolysis of Wood Sawdust. *Energy Environ. Sci.* **2011**, *4*, 145–161. https://doi.org/10.1039/C0EE00341G.

(2) Dickerson, T.; Soria, J. Catalytic Fast Pyrolysis: A Review. *Energies* **2013**, *6*, 514–538. https://doi.org/10.3390/en6010514.

(3) Sharma, R. K.; Bakhshi, N. N. Catalytic Upgrading of Pyrolysis Oil. *Energy & Fuels* **1993**, *7*, 306–314. https://doi.org/10.1021/ef00038a022.

(4) Horne, P. A.; Nugranad, N.; Williams, P. T. Catalytic Coprocessing of Biomass-Derived

Pyrolysis Vapours and Methanol. *J. Anal. Appl. Pyrolysis* **1995**, *34*, 87–108. https://doi.org/10.1016/0165-2370(94)00877-4.

(5) Williams, P. T.; Horne, P. A. The Influence of Catalyst Type on the Composition of Upgraded Biomass Pyrolysis Oils. *J. Anal. Appl. Pyrolysis* **1995**, *31*, 39–61. https://doi.org/10.1016/0165-2370(94)00847-T.

(6) Samolada, M. C.; Papafotica, A.; Vasalos, I. Catalyst Evaluation for Catalytic Biomass Pyrolysis. *Energy & Fuels* **2000**, *14* , 1161–1167. https://doi.org/10.1021/ef000026b.

(7) Lappas, A. A.; Samolada, M. C.; Iatridis, D. K.; Voutetakis, S. S.; Vasalos, I. A. Biomass Pyrolysis in a Circulating Fluid Bed Reactor for the Production of Fuels and Chemicals. *Fuel* **2002**, *81*, 2087–2095. https://doi.org/10.1016/S0016-2361(02)00195-3.

(8) Vitolo, S.; Bresci, B.; Seggiani, M.; Gallo, M. G. Catalytic Upgrading of Pyrolytic Oils over HZSM-5 Zeolite: Behaviour of the Catalyst When Used in Repeated Upgrading-Regenerating Cycles. *Fuel* **2001**, *80*, 17–26. https://doi.org/10.1016/S0016-2361(00)00063-6.

(9) Aho, A.; Kumar, N.; Eranen, K.; Salmi, T.; Hupa, M.; Murzin, D. Y. Catalytic Pyrolysis of Woody Biomass in a Fluidized Bed Reactor: Influence of the Zeolite Structure. *Fuel* **2008**, *87*, 2493–2501. https://doi.org/10.1016/j.fuel.2008.02.015.

(10) Carlson, T. R.; Vispute, T. P.; Huber, G. W. Green Gasoline by Catalytic Fast Pyrolysis of Solid Biomass Derived Compounds. *ChemSusChem* **2008**, *1*, 397–400. https://doi.org/10.1002/cssc.200800018.

(11) Carlson, T. R.; Tompsett, G. A.; Conner, W. C.; Huber, G. W. Aromatic Production from Catalytic Fast Pyrolysis of Biomass-Derived Feedstocks. *Top. Catal.* **2009**, *52*, 241–252. https://doi.org/10.1007/s11244-008-9160-6.

(12) Engtrakul, C.; Mukarakate, C.; Starace, A. K.; Magrini, K. A.; Rogers, A. K.; Yung, M. M. Effect of ZSM-5 Acidity on Aromatic Product Selectivity during Upgrading of Pine Pyrolysis Vapors. *Catal. Today* **2015**, *269*, 175–181. https://doi.org/http://dx.doi.org/10.1016/j.cattod.2015.10.032.

(13) Iisa, K.; French, R. J.; Orton, K. A.; Yung, M. M.; Johnson, D. K.; ten Dam, J.; Watson, M. J.; Nimlos, M. R. *In Situ* and *Ex Situ* Catalytic Pyrolysis of Pine in a Bench-Scale

Fluidized Bed Reactor System. *Energy & Fuels* **2016** *30*, 2144–2157. https://doi.org/10.1021/acs.energyfuels.5b02165.

(14) Puertolas, B.; Veses, A.; Callen, M. S.; Mitchell, S.; Garcia, T.; Perez-Ramirez, J. Porosity-Acidity Interplay in Hierarchical ZSM-5 Zeolites for Pyrolysis Oil Valorization to Aromatics. *ChemSusChem* **2015**, *8*, 3283–3293. https://doi.org/10.1002/cssc.201500685.

(15) Lee, H. W.; Park, S. H.; Jeon, J. K.; Ryoo, R.; Kim, W.; Suh, D. J.; Park, Y. K. Upgrading of Bio-Oil Derived from Biomass Constituents over Hierarchical Unilamellar Mesoporous MFI Nanosheets. *Catal. Today* **2014**, *232*, 119–126. https://doi.org/10.1016/j.cattod.2013.12.015.

(16) Venderbosch, R. H. A Critical View on Catalytic Pyrolysis of Biomass. *ChemSusChem* **2015**, *8*, 1306–1316. https://doi.org/10.1002/cssc.201500115.

(17) Mukarakate, C.; Zhang, X.; Stanton, A. R.; Robichaud, D. J.; Ciesielski, P. N.; Malhotra, K.; Donohoe, B. S.; Gjersing, E.; Evans, R. J.; Heroux, D. S.; et al. Real-Time Monitoring of the Deactivation of HZSM-5 during Upgrading of Pine Pyrolysis Vapors. *Green Chem.* **2014**, *16*, 1444–1461. https://doi.org/10.1039/c3gc42065e.

(18) Yildiz, G.; Ronsse, F.; Venderbosch, R.; Duren, R. van; Kersten, S. R. A.; Prins, W. Effect of Biomass Ash in Catalytic Fast Pyrolysis of Pine Wood. *Appl. Catal. B Environ.* **2015**, *168–169*, 203–211. https://doi.org/10.1016/j.apcatb.2014.12.044.

(19) Yung, M. M.; Stanton, A. R.; Iisa, K.; French, R. J.; Orton, K. A.; Magrini, K. A. Multiscale Evaluation of Catalytic Upgrading of Biomass Pyrolysis Vapors on Ni- and Ga-Modified ZSM-5. *Energy and Fuels* **2016**, *30*, 9471–9479. https://doi.org/10.1021/acs.energyfuels.6b01866.

(20) Yildiz, G.; Ronsse, F.; Duren, R. Van; Prins, W. Challenges in the Design and Operation of Processes for Catalytic Fast Pyrolysis of Woody Biomass. *Renew. Sustain. Energy Rev.* **2016**, *57*, 1596–1610. https://doi.org/10.1016/j.rser.2015.12.202.

(21) Stöcker, M. Methanol-to-Hydrocarbons: Catalytic Materials and Their Behavior. *Microporous Mesoporous Mater.* **1999**, *29*, 3–48. https://doi.org/10.1016/S1387-1811(98)00319-9.

(22) Park, H. J.; Heo, H. S.; Jeon, J. K.; Kim, J.; Ryoo, R.; Jeong, K. E.; Park, Y. K. Highly Valuable Chemicals Production from Catalytic Upgrading of Radiata Pine Sawdust-Derived Pyrolytic Vapors over Mesoporous MFI Zeolites. *Appl. Catal. B Environ.* **2010**, *95*, 365–373. https://doi.org/10.1016/j.apcatb.2010.01.015.

(23) Carlson, T. R.; Jae, J.; Huber, G. W. Mechanistic Insights from Isotopic Studies of Glucose Conversion to Aromatics over ZSM-5. *ChemCatChem* **2009**, *1*, 107–110. https://doi.org/10.1002/cctc.200900130.

(24) Kelkar, S.; Saffron, C. M.; Andreassi, K.; Li, Z.; Murkute, A.; Miller, D. J.; Pinnavaia, T. J.; Kriegel, R. M. A Survey of Catalysts for Aromatics from Fast Pyrolysis of Biomass. *Appl. Catal. B Environ.* **2015**, *174–175*, 85–95. https://doi.org/10.1016/j.apcatb.2015.02.020.

(25) Yarulina, I.; Chowdhury, A. D.; Meirer, F.; Weckhuysen, B. M.; Gascon, J. Recent Trends and Fundamental Insights in the Methanol-to-Hydrocarbons Process. *Nat. Catal.* **2018**, *1*, 398–411. https://doi.org/10.1038/s41929-018-0078-5.

(26) Whiting, G. T.; Nikolopoulos, N.; Nikolopoulos, I.; Chowdhury, A. D.; Weckhuysen, B. M. Visualizing Pore Architecture and Molecular Transport Boundaries in Catalyst Bodies with Fluorescent Nanoprobes. *Nat. Chem.* **2019**, *11*, 23–31. https://doi.org/10.1038/s41557-018-0163-z.

(27) Müller, S.; Liu, Y.; Vishnuvarthan, M.; Sun, X.; Van Veen, A. C.; Haller, G. L.; Sanchez-Sanchez, M.; Lercher, J. A. Coke Formation and Deactivation Pathways on H-ZSM-5 in the Conversion of Methanol to Olefins. *J. Catal.* **2015**, *325*, 48–59. https://doi.org/10.1016/j.jcat.2015.02.013.

(28) Yu, Y.; Li, X.; Su, L.; Zhang, Y.; Wang, Y.; Zhang, H. The Role of Shape Selectivity in Catalytic Fast Pyrolysis of Lignin with Zeolite Catalysts. *Appl. Catal. A Gen.* **2012**, *447–448*, 115–123. https://doi.org/10.1016/j.apcata.2012.09.012.

(29) Wang, K.; Kim, K. H.; Brown, R. C. Catalytic Pyrolysis of Individual Components of Lignocellulosic Biomass. *Green Chem.* **2014**, *16*, 727. https://doi.org/10.1039/c3gc41288a.

(30) Stanton, A. R.; Iisa, K.; Mukarakate, C.; Nimlos, M. R. Role of Biopolymers in the Deactivation of ZSM-5 during Catalytic Fast Pyrolysis of Biomass. *ACS Sustain. Chem.*

Eng. **2018**, *6*, 10030–10038. https://doi.org/10.1021/acssuschemeng.8b01333.

(31) Hernando, H.; Hernández-Giménez, A. M.; Gutiérrez-Rubio, S.; Fakin, T.; Horvat, A.; Danisi, R. M.; Pizarro, P.; Fermoso, J.; Heracleous, E.; Bruijnincx, P. C. A. Weckhuysen B.M.; Scaling-Up of Bio-Oil Upgrading during Biomass Pyrolysis over ZrO_2/ZSM-5-Attapulgite. *ChemSusChem* **2019**, *12*, 2428–2438. https://doi.org/10.1002/cssc.201900534.

(32) Heracleous, E.; Pachatouridou, E.; Hernández-Giménez, A. M.; Hernando, H.; Fakin, T.; Paioni, A. L.; Baldus, M.; Serrano, D. P.; Bruijnincx, P. C. A.; Weckhuysen, B. M.; Characterization of Deactivated and Regenerated Zeolite ZSM-5-Based Catalyst Extrudates Used in Catalytic Pyrolysis of Biomass. *J. Catal.* **2019**, *380*, 108–122. https://doi.org/10.1016/j.jcat.2019.10.019.

(33) Wan, S.; Waters, C.; Stevens, A.; Gumidyala, A.; Jentoft, R.; Lobban, L.; Resasco, D.; Mallinson, R.; Crossley, S. Decoupling HZSM-5 Catalyst Activity from Deactivation during Upgrading of Pyrolysis Oil Vapors. *ChemSusChem* **2015**, *8*, 552–559. https://doi.org/10.1002/cssc.201402861.

(34) Mitchell, S.; Michels, N.; Pérez-Ramírez, J. From Powder to Technical Body: The Undervalued Science of Catalyst Scale Up. *Chem. Soc. Rev.* **2013**, *42*, 5981–6202. https://doi.org/10.1039/c3cs60076a.

(35) Vogt, E. T. C.; Weckhuysen, B. M. Fluid Catalytic Cracking: Recent Developments on the Grand Old Lady of Zeolite Catalysis. *Chem. Soc. Rev.* **2015**, *44*, 7342–7370. https://doi.org/10.1039/C5CS00376H.

(36) Zhang, H.; Xiao, R.; Jin, B.; Xiao, G.; Chen, R. Biomass Catalytic Pyrolysis to Produce Olefins and Aromatics with a Physically Mixed Catalyst. *Bioresour. Technol.* **2013**, *140*, 256–262. https://doi.org/10.1016/j.biortech.2013.04.094.

(37) Mante, O. D.; Dayton, D. C.; Carpenter, J. R.; Wang, K.; Peters, J. E. Pilot-Scale Catalytic Fast Pyrolysis of Loblolly Pine over -Al_2O_3 catalyst. *Fuel* **2018**, *214*, 569–579. https://doi.org/10.1016/j.fuel.2017.11.073.

(38) Whiting, G. T.; Meirer, F.; Mertens, M. M.; Bons, A. J.; Weiss, B. M.; Stevens, P. A.; De Smit, E.; Weckhuysen, B. M. Binder Effects in SiO_2- and Al_2O_3-Bound Zeolite ZSM-5-Based Extrudates as Studied by Microspectroscopy. *ChemCatChem* **2015**, *7*, 1312–

1321. https://doi.org/10.1002/cctc.201402897.

(39) Ruiz-Martínez, J.; Buurmans, I. L. C.; Knowles, W. V.; Van Der Beek, D.; Bergwerff, J. A.; Vogt, E. T. C.; Weckhuysen, B. M. Microspectroscopic Insight into the Deactivation Process of Individual Cracking Catalyst Particles with Basic Sulfur Components. *Appl. Catal. A Gen.* **2012**, *419–420*, 84–94. https://doi.org/10.1016/j.apcata.2012.01.016.

(40) De Winter, D. A. M.; Meirer, F.; Weckhuysen, B. M. FIB-SEM Tomography Probes the Mesoscale Pore Space of an Individual Catalytic Cracking Particle. *ACS Catal.* **2016**, *6*, 3158–3167. https://doi.org/10.1021/acscatal.6b00302.

(41) Yildiz, G.; Lathouwers, T.; Toraman, H. E.; Geem, K. M. Van; Marin, G. B.; Ronsse, F.; Duren, R. Van; Kersten, S. R. A.; Prins, W. Catalytic Fast Pyrolysis of Pine Wood : Effect of Successive Catalyst Regeneration. *Energy & Fuels* **2014**. https://doi.org/10.1021/ef500636c.

(42) Emeis, C. A. Determination of Integrated Molar Extinction Coefficients for Infrared Absorption Bands of Pyridine Adsorbed on Solid Acid Catalysts. *J. Catal.* **1993**, *141*, 347–354.

(43) Amoureux, J. P.; Fernandez, C.; Steuernagel, S. Z Filtering in MQMAS NMR. *J. Magn. Reson. - Ser. A* **1996**, *123*, 116–118. https://doi.org/10.1006/jmra.1996.0221.

(44) Michels, N. L.; Mitchell, S.; Pérez-Ramírez, J. Effects of Binders on the Performance of Shaped Hierarchical MFI Zeolites in Methanol-to-Hydrocarbons. *ACS Catal.* **2014**, *4*, 2409–2417. https://doi.org/10.1021/cs500353b.

(45) Samain, L.; Jaworski, A.; Edén, M.; Ladd, D. M.; Seo, D. K.; Javier Garcia-Garcia, F.; Häussermann, U. Structural Analysis of Highly Porous γ-Al_2O_3. *J. Solid State Chem.* **2014**, *217*, 1–8. https://doi.org/10.1016/j.jssc.2014.05.004.

(46) Paglia, G.; Buckley, C. E.; Rohl, A. L.; Hart, R. D.; Winter, K.; Studer, A. J.; Hunter, B. A.; Hanna, J. V. Boehmite Derived γ-Alumina System. 1. Structural Evolution with Temperature, with the Identification and Structural Determination of a New Transition Phase, -Alumina. *Chem. Mater.* **2004**, *16*, 220–236. https://doi.org/10.1021/cm034917j.

(47) Jiang, Y.; Huang, J.; Dai, W.; Hunger, M. Solid-State Nuclear Magnetic Resonance

Investigations of the Nature, Property, and Activity of Acid Sites on Solid Catalysts. *Solid State Nucl. Magn. Reson.* **2011**, *39*, 116–141. https://doi.org/10.1016/j.ssnmr.2011.03.007.

(48) Klinowski, J. Nuclear Magnetic Resonance Studies of Zeolites. *Prog. NMR Spectrosc.* **1984**, *16*, 237–309.

(49) Samoson, A.; Lippmaa, E.; Engelhardt, G.; Lohse, U.; Jerschkewitz, H. G. Quantitative High-Resolution ^{27}Al NMR: Tetrahedral Non-Framework Aluminium in Hydrothermally Treated Zeolites. *Chem. Phys. Lett.* **1987**, *134*, 589–592. https://doi.org/10.1016/0009-2614(87)87199-3.

(50) Wang, Z.; Jiang, Y.; Lafon, O.; Trébosc, J.; Duk Kim, K.; Stampfl, C.; Baiker, A.; Amoureux, J. P.; Huang, J. Brønsted Acid Sites Based on Penta-Coordinated Aluminum Species. *Nat. Commun.* **2016**, *7*, 13820. https://doi.org/10.1038/ncomms13820.

(51) Thibault-Staruk, F.; Francoise, M. *Characterization of Solid Materials and Heterogeneous Catalysts*; Che, M., Védrine, J. C., Eds.; Wiley-VCH, Weinheim, 2012, 1-48. https://doi.org/10.1002/9783527645329.

(52) Verkleij, S. P.; Whiting, G. T.; Esclapez, S. P.; Mertens, M. M.; Bons, A.-J.; Burgers, M.; Weckhuysen, B. M. *Operando* Micro-Spectroscopy on ZSM-5 Containing Extrudates during the Oligomerization of 1-Hexene. *Catal. Sci. Technol.* **2018**, *8*, 2175–2185. https://doi.org/10.1039/C7CY02460F.

(53) Mitchell, S.; Michels, N. L.; Kunze, K.; Pérez-Ramírez, J. Visualization of Hierarchically Structured Zeolite Bodies from Macro to Nano Length Scales. *Nat. Chem.* **2012**, *4*, 825–831. https://doi.org/10.1038/nchem.1403.

(54) Whiting, G. T.; Nikolopoulos, N.; Nikolopoulos, I.; Chowdhury, A. D.; Weckhuysen, B. M. Visualizing Pore Architecture and Molecular Transport Boundaries in Catalyst Bodies with Fluorescent Nanoprobes. *Nat. Chem.* **2019**, *11*, 23-31. https://doi.org/10.1038/s41557-018-0163-z.

(55) Aho, A.; Tokarev, A.; Backman, P.; Kumar, N.; Eränen, K.; Hupa, M.; Holmbom, B.; Salmi, T.; Murzin, D. Y. Catalytic Pyrolysis of Pine Biomass over H-Beta Zeolite in a Dual-Fluidized Bed Reactor: Effect of Space Velocity on the Yield and Composition of Pyrolysis Products. *Top. Catal.* **2011**, *54*, 941–948. https://doi.org/10.1007/s11244-011-

9716-8.

(56) Yang, H.; Coolman, R.; Karanjkar, P.; Wang, H.; Dornath, P.; Chen, H.; Fan, W.; Conner, W. C.; Mountziaris, T. J.; Huber, G. The Effects of Contact Time and Coking on the Catalytic Fast Pyrolysis of Cellulose. *Green Chem.* **2017**, *19*, 286–297. https://doi.org/10.1039/c6gc02239a.

(57) Kramm, U. I.; Marschall, R.; Rose, M. Pitfalls in Heterogeneous Thermal, Electro- and Photocatalysis. *ChemCatChem* **2019**, *11*, 2563–2574. https://doi.org/10.1002/cctc.201900137.

(58) Paasikallio, V.; Agblevor, F.; Oasmaa, A.; Lehto, J.; Lehtonen, J. Catalytic Pyrolysis of Forest Thinnings with ZSM-5 Catalysts: Effect of Reaction Temperature on Bio-Oil Physical Properties and Chemical Composition. *Energy & Fuels* **2013**, *27*, 7587–7601.

(59) Hernando, H.; Jiménez-Sánchez, S.; Fermoso, J.; Pizarro, P.; Coronado, J. M.; Serrano, D. P. Assessing Biomass Catalytic Pyrolysis in Terms of Deoxygenation Pathways and Energy Yields for the Efficient Production of Advanced Biofuels. *Catal. Sci. Technol.* **2016**, *6*, 2829–2843. https://doi.org/10.1039/C6CY00522E.

(60) Saraeian, A.; Nolte, M. W.; Shanks, B. H. Deoxygenation of Biomass Pyrolysis Vapors : Improving Clarity on the Fate of Carbon. *Renew. Sustain. Energy Rev.* **2019**, *104*, 262–280. https://doi.org/10.1016/j.rser.2019.01.037.

(61) Iisa, K.; French, R. J.; Orton, K. A.; Budhi, S.; Mukarakate, C.; Stanton, A. R.; Yung, M. M.; Nimlos, M. R. Catalytic Pyrolysis of Pine Over HZSM-5 with Different Binders. *Top. Catal.* **2016**, *59*, 94–108. https://doi.org/10.1007/s11244-015-0509-3.

(62) Hargreaves, J. S. J.; Munnoch, A. L. A Survey of the Influence of Binders in Zeolite Catalysis. *Catal. Sci. Technol.* **2013**, *3*, 1165–1171. https://doi.org/10.1039/c3cy20866d.

(63) Vogt, E. T. C.; Whiting, G. T.; Dutta Chowdhury, A.; Weckhuysen, B. M. Zeolites and Zeotypes for Oil and Gas Conversion. *Adv. Catal.* 1st ed.; Elsevier, Amsterdam, **2015**; *58*, 143-314 https://doi.org/10.1016/bs.acat.2015.10.001.

(64) Williams, P. T.; Horne, P. A. The Influence of Catalyst Regeneration on the Composition of Zeolite-Upgraded Biomass Pyrolysis Oils. *Fuel* **1995**, *74*, 1839–1851. https://doi.org/10.1016/0016-2361(95)80017-C.

(65) Gayubo, A. G.; Aguayo, A. T.; Atutxa, A.; Valle, B.; Bilbao, J. Undesired Components in the Transformation of Biomass Pyrolysis Oil into Hydrocarbons on an HZSM-5 Zeolite Catalyst. *J. Chem. Technol. Biotechnol.* **2005**, *80*, 1244–1251. https://doi.org/10.1002/jctb.1316.

(66) Cerqueira, H. S.; Caeiro, G.; Costa, L.; Ramôa Ribeiro, F. Deactivation of FCC Catalysts. *J. Mol. Catal. A Chem.* **2008**, *292*, 1–13. https://doi.org/10.1016/j.molcata.2008.06.014.

(67) Yang, H.; Coolman, R.; Karanjkar, P.; Wang, H.; Dornath, P.; Chen, H.; Fan, W.; Conner, W. C.; Mountziaris, T. J.; Huber, G. The Effects of Contact Time and Coking on the Catalytic Fast Pyrolysis of Cellulose. *Green Chem.* **2017**, *19*, 286–297. https://doi.org/10.1039/c6gc02239a.

(68) Gou, J.; Wang, Z.; Li, C.; Qi, X.; Vattipalli, V.; Cheng, Y.-T.; Conner, W. C.; Dauenhauer, P. J.; Mountziaris, T. J.; Fan, W.; et al. The Effect of ZSM-5 Mesoporotsity and Morphology on the Catalytic Fast Pyrolysis of Furan. *Green Chem.* **2017**, *19*, 286–297. https://doi.org/10.1039/c7gc01395g.

(69) Du, S.; Gamliel, D. P.; Giotto, M. V.; Valla, J. A.; Bollas, G. M. Coke Formation of Model Compounds Relevant to Pyrolysis Bio-Oil over ZSM-5. *Appl. Catal. A Gen.* **2016**, *513*, 67–81. https://doi.org/10.1016/j.apcata.2015.12.022.

(70) Gou, J.; Wang, Z.; Li, C.; Qi, X.; Vattipalli, V.; Cheng, Y. T.; Huber, G.; Conner, W. C.; Dauenhauer, P. J.; Mountziaris, T. J.; et al. The Effects of ZSM-5 Mesoporosity and Morphology on the Catalytic Fast Pyrolysis of Furan. *Green Chem.* **2017**, *19*, 3549–3557. https://doi.org/10.1039/c7gc01395g.

(71) Ibarra, Á.; Veloso, A.; Bilbao, J.; Arandes, J. M.; Castaño, P. Dual Coke Deactivation Pathways during the Catalytic Cracking of Raw Bio-Oil and Vacuum Gasoil in FCC Conditions. *Appl. Catal. B Environ.* **2016**, *182*, 336–346. https://doi.org/10.1016/j.apcatb.2015.09.044.

(72) Yung, M. M.; Starace, A. K.; Griffin, M. B.; Wells, J. D.; Patalano, R. E.; Smith, K. R.; Schaidle, J. A. Restoring ZSM-5 Performance for Catalytic Fast Pyrolysis of Biomass: Effect of Regeneration Temperature. *Catal. Today* **2019**, *323,* 76-85. https://doi.org/10.1016/j.cattod.2018.06.025.

(73) Guisnet, M.; Magnoux, P. Organic Chemistry of Coke Formation. *Appl. Catal. A Gen.* **2001**, *212*, 83–96. https://doi.org/10.1016/S0926-860X(00)00845-0.

(74) Valle, B.; Castaño, P.; Olazar, M.; Bilbao, J.; Gayubo, A. G. Deactivating Species in the Transformation of Crude Bio-Oil with Methanol into Hydrocarbons on a HZSM-5 Catalyst. *J. Catal.* **2012**, *285*, 304–314. https://doi.org/10.1016/j.jcat.2011.10.004.

(75) Du, S.; Valla, J. a.; Bollas, G. M. Characteristics and Origin of Char and Coke from Fast and Slow, Catalytic and Thermal Pyrolysis of Biomass and Relevant Model Compounds. *Green Chem.* **2013**, *15*, 3214. https://doi.org/10.1039/c3gc41581c.

(76) Liu, Y.; Kirchberger, F. M.; Müller, S.; Eder, M.; Tonigold, M.; Sanchez-Sanchez, M.; Lercher, J. A. Critical Role of Formaldehyde during Methanol Conversion to Hydrocarbons. *Nat. Commun.* **2019**, *10*, 1462. https://doi.org/10.1038/s41467-019-09449-7.

(77) Xian, X.; Ran, C.; Nai, C.; Yang, P.; Zhao, S.; Dong, L. Characterization of the Location of Coke Deposited on Spent HZSM-5 Zeolite by Special Temperature-Programmed Oxidation and Isothermal Oxidation Methods. *Appl. Catal. A Gen.* **2017**, *547*, 37–51. https://doi.org/10.1016/j.apcata.2017.08.023.

(78) Devaraj, A.; Vijayakumar, M.; Bao, J.; Guo, M. F.; Derewinski, M. A. Discerning the Location and Nature of Coke Deposition from Surface to Bulk of Spent Zeolite Catalysts. *Sci. Rep.* **2016**, *6*, 37586. https://doi.org/10.1038/srep37586.

(79) Kox, M. H. F.; Stavitski, E.; Groen, J. C. C.; Pérez-Ramírez, J.; Kapteijn, F.; Weckhuysen, B. M. Visualizing the Crystal Structure and Locating the Catalytic Activity of Micro- and Mesoporous ZSM-5 Zeolite Crystals by Using In Situ Optical and Fluorescence Microscopy. *Chem. Eur. J.* **2008**, *14*, 1718–1725. https://doi.org/10.1002/chem.200701591.

(80) Aramburo, L. R.; Karwacki, L.; Cubillas, P.; Asahina, S.; De Winter, D. A. M.; Drury, M. R.; Buurmans, I. L. C.; Stavitski, E.; Mores, D.; Daturi, M.; et al. The Porosity, Acidity, and Reactivity of Dealuminated Zeolite ZSM-5 at the Single Particle Level: The Influence of the Zeolite Architecture. *Chem. Eur. J.* **2011**, *17*, 13773–13781. https://doi.org/10.1002/chem.201101361.

(81) Ristanović, Z.; Kerssens, M. M.; Kubarev, A. V.; Hendriks, F. C.; Dedecker, P.;

Hofkens, J.; Roeffaers, M. B. J.; Weckhuysen, B. M. High-Resolution Single-Molecule Fluorescence Imaging of Zeolite Aggregates within Real-Life Fluid Catalytic Cracking Particles. *Angew. Chem. Int. Ed.* **2015**, *54*, 1836-1840. https://doi.org/10.1002/anie.201410236.

(82) Nordvang, E. C.; Borodina, E.; Ruiz-Martínez, J.; Fehrmann, R.; Weckhuysen, B. M. Effects of Coke Deposits on the Catalytic Performance of Large Zeolite H-ZSM-5 Crystals during Alcohol-to-Hydrocarbon Reactions as Investigated by a Combination of Optical Spectroscopy and Microscopy. *Chem. Eur. J.* **2015**, *21*, 17324–17335. https://doi.org/10.1002/chem.201503136.

(83) Castaño, P.; Ruiz-Martínez, J.; Epelde, E.; Gayubo, A. G.; Weckhuysen, B. M. Spatial Distribution of Zeolite ZSM-5 within Catalyst Bodies Affects Selectivity and Stability of Methanol-to-Hydrocarbons Conversion. *ChemCatChem* **2013**, *5*, 2827–2831. https://doi.org/10.1002/cctc.201300218.

(84) VanSpeybroeck, V.; Hemelsoet, K.; DeWispelaere, K.; Qian, Q.; VanderMynsbrugge, J.; DeSterck, B.; Weckhuysen, B. M.; Waroquier, M. Mechanistic Studies on Chabazite-Type Methanol-to-Olefin Catalysts: Insights from Time-Resolved UV/Vis Microspectroscopy Combined with Theoretical Simulations. *ChemCatChem* **2013**, *5*, 173–184. https://doi.org/10.1002/cctc.201200580.

(85) Mores, D.; Kornatowski, J.; Olsbye, U.; Weckhuysen, B. M. Coke Formation during the Methanol-to-Olefin Conversion: In Situ Microspectroscopy on Individual H-ZSM-5 Crystals with Different Brønsted Acidity. *Chem. Eur. J.* **2011**, *17*, 2874–2884. https://doi.org/10.1002/chem.201002624.

(86) Hemelsoet, K.; Qian, Q.; De Meyer, T.; De Wispelaere, K.; De Sterck, B.; Weckhuysen, B. M.; Waroquier, M.; Van Speybroeck, V. Identification of Intermediates in Zeolite-Catalyzed Reactions by in Situ UV/Vis Microspectroscopy and a Complementary Set of Molecular Simulations. *Chem. Eur. J.* **2013**, *19*, 16595–16606. https://doi.org/10.1002/chem.201301965.

(87) Bordiga, S.; Lamberti, C.; Bonino, F.; Travert, A.; Thibault-Starzyk, F. Probing Zeolites by Vibrational Spectroscopies. *Chem. Soc. Rev.* **2015**, *44*, 7262–7341. https://doi.org/10.1039/C5CS00396B.

(88) Penkova, A.; Dzwigaj, S.; Kefirov, W. R.; Hadjiivanov, K.; Che, M. Effect of the Preparation Method on the State of Nickel Ions in BEA Zeolites. A Study by Fourier Transform Infrared Spectroscopy of Adsorbed CO and NO, Temperature-Programmed Reduction, and X-Ray Diffraction. *J. Phys. Chem. C* **2007**, *111*, 8623–8631. https://doi.org/10.1021/jp071927p.

(89) Bernauer, M.; Tabor, E.; Pashkova, V.; Kaucký, D.; Sobalík, Z.; Wichterlová, B.; Dedecek, J. Proton Proximity – New Key Parameter Controlling Adsorption, Desorption and Activity in Propene Oligomerization over H-ZSM-5 Zeolites. *J. Catal.* **2016**, *344*, 157–172. https://doi.org/10.1016/j.jcat.2016.09.025.

(90) Holzinger, J.; Beato, P.; Lundegaard, L. F.; Skibsted, J. Distribution of Aluminum over the Tetrahedral Sites in ZSM-5 Zeolites and Their Evolution after Steam Treatment. *J. Phys. Chem. C* **2018**, *122*, 15595–15613. https://doi.org/10.1021/acs.jpcc.8b05277.

(91) H. Knözinger; P. Ratnasamy, Catalytic Aluminas: Surface Models and Characterization of Surface Sites, *Catal. Rev*., **2007**, 17, 31–70. https://doi.org/ 10.1080/03602457808080878.

(92) Digne, M.; Sautet, P.; Raybaud, P.; Euzen, P.; Toulhoat, H. Hydroxyl Groups on γ-Alumina Surfaces: A DFT Study. *J. Catal.* **2002**, *211* 1–5. https://doi.org/10.1006/jcat.2002.3741.

(93) Thibault-Staruk, F.; Francoise, M. Part One Molecular / Local Spectroscopies. *Charact. Solid Mater. Heterog. Catal. From Struct. to Surf. React.* **2012**, 1–48.

(94) Vigué, H.; Quintard, P.; Merle-Méjean, T.; Lorenzelli, V. An FT-IR Study of the Chlorination of γ-Alumina Surfaces. *J. Eur. Ceram. Soc.* **1998**, *18*, 305–309. https://doi.org/10.1016/S0955-2219(97)00142-8.

(95) Yildiz, G.; Pronk, M.; Djokic, M.; Van Geem, K. M.; Ronsse, F.; Van Duren, R.; Prins, W. Validation of a New Set-up for Continuous Catalytic Fast Pyrolysis of Biomass Coupled with Vapour Phase Upgrading. *J. Anal. Appl. Pyrolysis* **2013**, *103*, 343–351. https://doi.org/10.1016/j.jaap.2013.02.001.

Chapter 7 Summary, Concluding Remarks and Future Perspectives

I. Summary

Climate change and the ever-increasing energy and materials demand by a growing world population are two of the main challenges faced by society. They motivate the replacement of the commonly used fossil resources, by renewable and more sustainable feedstocks, such as biomass and municipal waste, for the production of fuels and commodity chemicals. As part of these efforts, the development of environmentally friendly routes to produce renewable platform compounds, such as Benzene-Toluene-Xylenes (BTX) and light olefins, became the subject of broad interest in both industry and academia.

The upgrading of biomass into building blocks can be performed by means of catalytic fast pyrolysis (CFP) technology, as outlined in more detail in **Chapter 1**. Despite its promise as an upgrading technology, CFP of biomass often suffers from low carbon yields due to CO_x and coke formation, which hampers commercialization efforts[1]. For the CFP of bio-derived oxygenates, such as furan derivatives, acidic zeolites with the MFI topology, e.g. ZSM-5, are the solid catalysts of choice to produce BTX. The superior performance of zeolite ZSM-5-based catalysts is attributed to their shape-selective topology[2] as well as the presence of the right amount and strength of Brønsted acid sites (BAS)[3,4]. In this PhD Thesis, the aromatization of diverse furan derivatives over a series of zeolite ZSM-5 catalysts (i.e., hierarchical and (metal-promoted catalysts) was investigated, with particular emphasis on their performance in terms of activity, selectivity and stability as well as their related reaction and deactivation mechanisms.

In **Chapter 2**, the conversion of alkylated and non-alkylated furan derivatives, such as furan, 2-methylfuran and 2,5-dimethylfuran, into BTX over highly acidic and hierarchical zeolite ZSM-5 catalysts was studied. During the aromatization of these bio-derived oxygenates, closely monitored by *operando* UV-Vis diffuse reflectance (DR) spectroscopy, the formation of diverse enyl and arenium ions were detected within the zeolite pores, which rapidly evolved to form light olefins and BTX. Inspired by the dual-cycle reaction mechanism operative during the Methanol-to-Aromatics (MTH) process as well as the occurrence of specific reaction intermediates and related coke precursor molecules, a similar mechanism was proposed for furan derivatives aromatization. The combination of several analytical techniques allowed us to identify some of the tentative intermediates and/or coke species, i.e., benzofuran, trapped within the zeolite micropores during the aromatization of furan derivatives. Our findings revealed that the Si/Al ratio and porosity of the zeolite catalyst are key parameters that

determine both the type and size of active species formed and thus, the final product distribution.

Detailed investigations in the catalytic performance of ZSM-5 catalysts modified with different promotors are described in Chapters 3-5. By combining catalytic testing with a large array of characterization tools, insights in their aromatization capabilities and deactivation rates were obtained. In **Chapter 3**, the effect of phosphorus as promotor was investigated on the aromatization of MF and DMF. Upon the introduction of new phosphorus sites, the amount of BAS and acidity strength were altered, with a new type of acid sites being formed within zeolite ZSM-5. As function of the synthesis method employed, the phosphor speciation was determined, revealing that extra washing and calcination steps improved the overall acidity and accessibility. Such additional washing led to the removal and hydrolysis of several extra-framework phosphate species, such as condensed polyphosphates, resulting in an upgraded PHZSM-5 catalyst material that performed better than the non-washed PHZSM-5 catalyst materials in MF and DMF aromatization. An improved selectivity towards (di)alkylated aromatics was seen compared to the pristine HZSM-5 zeolite. A study of the effect of co-feeding ethylene on phosphorus-modified HZSM-5 zeolites demonstrated that a larger amount of non-condensable gases was produced over the washed PHZSM-5 zeolite catalysts when compared to the pristine HZSM-5 zeolite during DMF aromatization. It was also found that BTX selectivity was lower over PHZSM-5 zeolites during the aromatization of DMF and MF in the presence of ethylene when compared to the pristine HZSM-5 zeolites. The results obtained showed that the positive effect seen for P-promotion in the liquid phase did not translate to the gas phase. Second, the boost in BTX formation, that is typically seen upon ethylene co-feeding, is the result of a complex combination of mechanisms and not solely from improved Diels-Alder cycloaddition activity.

Chapter 4 focuses on Ga-promoted HZSM-5 zeolites as DMF aromatization catalysts. The introduction of the dehydrogenation character of Ga favored aromatization considerably, boosting the Benzene-Toluene-Ethylbenzene-Xylenes (BTEX) yields. The sequential reduction and re-oxidation approach applied for the synthesis of a series of Ga/HZSM-5 zeolite catalysts, favored a high dispersion of Ga into the zeolite micropores, reaching nearly quantitatively exchange of the BAS with $(GaO)_x^{x+}$ ions, thus substituting BAS for Lewis acid sites (LAS). The BAS/LAS ratio was indeed found to be dependent on the amount of Ga introduced. The addition of ethylene to the aromatization of DMF resulted in enhanced BTEX yields, which we

speculate is again the result not (only) of Diels-Alder cycloaddition, but rather of increased alkylation and cyclization activity via the hydrocarbon pool mechanism.

Chapter 5 also emphasized the importance of metal promotors, specifically, of Zn-promoted HZSM-5 zeolite-based catalysts, to enhance the selectivity to BTX in DMF aromatization with ethylene co-feeding. The impregnation approach employed resulted in a homogeneous dispersion of Zn over the zeolite crystals, as well as in the formation of small ZnO clusters at higher loadings. It was found that Zn addition to zeolite ZSM-5 via incipient wetness impregnation (IWI) decreased the number of BAS, implying a high degree of ion exchange due to the incorporation of Zn^{2+} ions. The amount of LAS slightly increased, but not linearly with increasing Zn loading, with the newly introduced Zn sites generating a new type of weak-medium acid sites. In addition, a hierarchical Zn/ZSM-5 zeolite catalyst was also synthesized to further investigate the effect of mesoporosity and Zn. The use of a zeolite catalyst with a high dispersion of divalent Zn cations together with ethylene co-feeding gave outstanding BTX selectivities when compared with the pristine HZSM-5 catalyst. BTX yields could be further improved by combining mesoporosity and Zn addition. The higher BTX yields came at the expense of faster catalyst deactivation, though, and fairly rapid coking was observed for all Zn/ZSM-5 catalysts under study, including the hierarchical Zn/ZSM-5. The results clearly suggested that coke species are formed from condensation of aromatics, as shown in previous investigations. Mechanistic investigations on Zn/ZSM-5 again suggested the process to be dominated by a dual-cycle mechanism in which both olefins and aromatics are formed. Upon co-feeding of ethylene, the arene cycle is further promoted, resulting in a higher aromatization rates to alkylated aromatics. However, to further evaluate the performance of these catalyst materials for the production of BTX aromatics at a larger scale, catalyst shaping, and up-scaling studies will be needed.

Previous studies[5,6] showed that the bulk zeolite is often far too active for the oxygenates-to-hydrocarbon conversion reactions and that different catalyst configurations need to be explored. In **Chapter 6**, the performance of Al_2O_3-bound zeolite ZSM-5-based catalyst bodies was assessed in the *ex-situ* CFP of pine wood and cellulose using a bench scale reactor. The product yields and distribution as well as the catalyst deactivation rates depended on the biomass feedstock and the time-on-stream (TOS) chosen. The large amount of coke deposits produced led to reversible and irreversible structural changes in the catalyst extrudates. In addition to the difference in nature between the thermal and catalytic coke formed, each type of coke was also

found in different locations of the catalyst extrudates, as revealed by micro-spectroscopic methods.

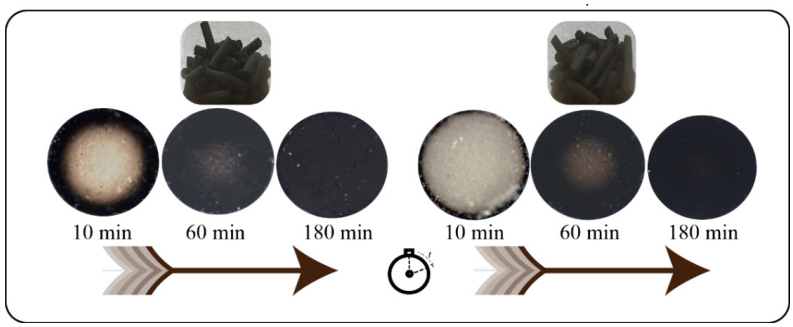

Figure 7.1. Cross-section of diverse spent catalyst extrudates at different times-on-stream (TOS) obtained during the catalytic fast pyrolysis (CFP) of pine wood (i.e., the three cross-sections on the left) and cellulose (i.e., the three cross-sections on the right).

For example, thermal coke was found to be preferentially located in the pores of the alumina structure (binder) and at the external surface of the zeolite domains, while catalytic coke, whose formation was dictated by the active catalytic sites, was indeed found on the BAS of the zeolite domains. Larger coke species were produced in the spent catalyst materials obtained after CFP of cellulose (Figure 7.1), revealing that the smaller sized cellulose-derived fragments in the vapors more easily enter the pores compared to the pine wood vapors, which predominantly condensed on the external surface of the extrudates. Irreversible chemical changes in the catalyst structure, such as a decrease in aluminum content, were observed for both feedstocks after regeneration. Overall, more extensive dealumination was observed for the spent catalyst materials after CFP of pine wood, as more (hot) water is produced with this feed than with cellulose.

Concluding Remarks and Future Perspectives

In this PhD Thesis different approaches to improve BTX selectivity from bio-derived feedstock were investigated making use of catalyst formulations based on zeolite ZSM-5. Modifications in the catalyst composition (i.e., with non-metals, metals promotors and binders) along with different reactor setup configurations were carried out to achieve such purpose. Zeolite ZSM-5 was selected for aromatics production based on its proven high shape-selectivity towards BTX and its tunable properties. The addition of metal promotors, such as Ga or Zn, provided the

zeolite ZSM-5-based catalysts with bifunctional characteristics that clearly boosted BTX formation. In particular, a right balance between BAS and LAS, or weak-medium acid sites in the case of Zn/ZSM-5 catalysts, is required to enhance the selectivity towards BTX formation. At a larger scale, such as in the performed bench scale experiments, the use of Al_2O_3 as binder for ZSM-5-based catalyst extrudates also revealed that the presence of LAS was responsible for some pre-cracking allowing a better diffusion of pyrolysis vapors into the zeolite micropores.

While catalytic performance of the synthesized catalyst materials improved in terms of, for example, BTX selectivity, other aspects of performance such, catalyst deactivation by coking was not sufficiently improved. Our efforts together with the large amount of literature on catalytic coke[7–9], suggest that coking may be an intrinsic property of the particular feed-zeolite-hydrocarbon pool combination and unfortunately, cannot be fully suppressed without simultaneously affecting other aspects of catalyst performance. Nevertheless, we have thoroughly characterized the different types of deactivated catalyst materials obtained, thus gaining further insight in the composition, nature and location of the different carbon deposits formed at diverse locations of the zeolite ZSM-5 crystals. Although comparable percentages of carbon deposits were obtained with the different catalysts tested (~ 10 wt.%), *ex-situ* spectroscopic techniques revealed that the composition and nature of these coke species vary and depend on the feedstock and reaction conditions used.

Mechanistic insights into the formation of aromatics within the micropores and channels of zeolite ZSM-5 during the aromatization of furan derivates were also presented and discussed, as provided by the use of microscopic and spectroscopic techniques under a combination of *in-situ*, *ex-situ* and *operando* conditions. Our different catalytic investigations (i.e., with and without ethylene co-feeding) are in line with the proposed dual-cycle mechanism, similar to the MTA process, for the aromatization of furan derivatives over ZSM-5 as catalyst. While the dual cycle mechanism is considered to dominate the reaction, Diels-Alder cycloaddition reactions, are also expected to contribute, as indicated, e.g., by the detection and conversion of benzofurans.

The investigations performed in this PhD Thesis demonstrated the potential of bio-derived oxygenated feedstocks to produce renewable aromatics in a more sustainable manner than the commonly applied fossil-based route without the use of complex catalytic processes or catalyst synthesis methods. Although this synthetic route (i.e., Furan-to-Aromatics, FTA) will not reach

commercialization for now, this PhD Thesis demonstrated the potential of different bio-derived feedstocks, such as furan derivatives or cellulose, to be converted into important platform compounds for the chemical industry. The results obtained thus highlight the general potential of ZSM-5 based materials for renewable oxygenates-to-aromatics processes.

II. Nederlandse Samenvatting

Grote maatschappelijke uitdagingen, zoals klimaatverandering en de steeds toenemende vraag van een groeiende wereldbevolking naar energie en materialen, vragen om de geleidelijke vervanging van veelgebruikte fossiele bronnen, zoals aardolie en aardgas, door hernieuwbare en duurzamere grondstoffen, zoals biomassa en huishoudelijk afval, voor de productie van brandstoffen en basischemicaliën. Om de huidige milieuproblemen te verzachten, wordt constant gezocht naar de ontwikkeling van meer milieuvriendelijke routes om hernieuwbare platformverbindingen te produceren. Een voorbeeld hiervan is het productie van aromaten (bv. benzeen, tolueen en xylenen, BTX) en korte alkenen (bv. etheen en propeen). Dit onderzoeksonderwerp heeft de afgelopen decennia heel wat aandacht gekregen.

De verwaardering van biomassa tot chemische bouwstenen kan worden uitgevoerd door middel van een techniek, die bekend staat als katalytische snelle pyrolyse (CFP). Ondanks de veelbelovende aspecten van deze technologie heeft CFP van biomassa nog vaak te lijden onder lage koolstofopbrengsten. De hoofdreden hiervan, zoals beschreven in **Hoofdstuk 1**, is de vorming van CO_x en koolstofafzettingen (ook wel cokes), wat de commercialisering van de CFP technologie sterk belemmert[1]. Een mogelijke manier om dit op te lossen is door verdere verbetering van de gebruikte katalysatoren, vaak zure zeolieten, voor de conversie van de biomassa zelf of van biomassa-afgeleide oxygenaten, zoals furaanderivaten. Meer specifiek wordt hiervoor vaak zeoliet ZSM-5 met de MFI-topologie gebruikt omdat dit katalysatormateriaal bij uitstek BTX produceert. De superieure katalytische prestaties van op zeoliet ZSM-5 gebaseerde katalysatoren worden toegeschreven aan hun vormselectieve topologie[2] en de aanwezigheid van voldoende sterke Brønsted zure plaatsen (BAS)[3,4]. In dit proefschrift werd de aromatisering van diverse furaan-derivaten over een reeks van zeoliet ZSM-5-gebaseerde katalysatoren (met en zonder het gebruik van promotoren en metalen) onderzocht. Hierbij lag de nadruk op het onderzoeken van het reactie- en deactiverings-mechanisme van het Furan-naar-Aromaten (FTA) proces.

In **Hoofdstuk 2** werd de conversie van gealkyleerde en niet-gealkyleerde furaan-derivaten, zoals furan, 2-methylfuran en 2,5-dimethylfuran, in BTX over zeer zure en hiërarchisch gestructureerde ZSM-5 zeolieten bestudeerd. Tijdens de aromatisering van deze uit biomassa verkregen oxygenaten, nauwlettend gevolgd door middel van operando UV-Vis diffuse reflectie (DR) spectroscopie, werd de vorming van diverse enyl- en areniumionen in de zeolietporiën geïdentificeerd, die snel evolueerden tot olefinen en BTX via het zogenaamde "hydrocarbon pool" mechanisme met twee in elkaar grijpende reactiecycli. Evenzo stelden we, net als bij het Methanol-tot-Aromaten (MTA) proces, door de evolutie en vorming van reactie-intermediairen en de gerelateerde cokes-voorlopers te volgen, een reactiemechanisme voor het FTA-proces. Bovendien stelde de combinatie van verschillende analytische technieken ons in staat om enkele van de intermediairen en/of cokes-soorten (d.w.z. benzofuran) te identificeren die vastzaten in de zeolietporiën na de aromatisering van furaan-derivaten. Onze bevindingen lieten zien dat zowel de Si/Al verhouding als de porositeit van het zeolietmateriaal sleutelparameters zijn die zowel het type als de grootte van de gevormde intermediairen en dus de uiteindelijke productverdeling bepalen.

In **Hoofdstukken 3-5** werden gedetailleerde onderzoeken verricht naar de prestaties van verschillende katalytische materialen. Door het combineren van katalytisch testen met een groot aantal karakteriseringsmethodes, werden nieuwe inzichten verkregen in hun FTA-activiteit en mate van deactivering. In **Hoofdstuk 3** is het effect van fosfor als promotor onderzocht tijdens methylfuran en dimethylfuran aromatisering. Bij de introductie van nieuwe fosforverbindingen veranderden de hoeveelheid BAS alsook de zuurtegraad van het katalytische materiaal, wat suggereert dat er een nieuw type zure site werd gevormd. Met behulp van een specifieke synthesemethode konden de meest geschikte fosforverbindingen worden geïntroduceerd in de zeoliet, waarbij het helder werd dat een extra was- en calcineringsstap het mogelijk maakte om de zuurtegraad en toegankelijkheid van het zeolietmateriaal substantieel te verbeteren. Bij dit wassen werden via hydrolyse verschillende fosfaatsoorten uit de zeolietporiën verwijderd (bv. gecondenseerde polyfosfaten), wat resulteerde in een verbeterde PHZSM-5 katalysator, die beter presteerde dan de niet-gewassen PHZSM-5 katalysatoren. Dit uitte zich onder meer in een hogere selectiviteit voor (di) gealkyleerde aromaten. Het toevoegen van ethyleen aan de aromatisering van DMF met de fosfor-gemodificeerde HZSM-5-zeolieten leidde slechts tot een grotere hoeveelheid niet-condenseerbare gassen geproduceerd over gewassen PHZSM-5 zeolietkatalysatoren en niet tot hogere BTX-opbrengsten. Verder suggereren de resultaten dat

het toevoegen van ethyleen niet (uitsluitend) de vorming van BTX via het Diels-Alder cycloadditie-mechanisme bevordert.

De rol van Ga-bevattende zeoliet ZSM-5 katalysatoren werd onderzocht in **Hoofdstuk 4** tijdens de aromatisering van DMF waarbij ethyleen werd bijgevoegd. Het dehydrogeneringskarakter van Ga was gunstig voor de aromatiseringsreactie en leidde tot sterk verhoogde opbrengsten van benzeen-tolueen-ethylbenzeen-xylenen (BTEX). De reductie- en re-oxidatiebenadering, die werd toegepast voor de synthese van Ga/HZSM-5 katalysatoren, bevorderde een hoge dispersie van Ga in de microporiën van het zeoliet en leidde tot bijna volledig kwantitatief uitgewisselde $(GaO)_x^{x+}$. Introductie van de Ga kationen resulteerde in een verlaging van de BAS en een toename van de Lewis-zure plaatsen (LAS). De juiste verhouding van deze zure plaatsen, belangrijk voor een hoge opbrengst, hangt af van de hoeveelheid aan Ga kationen. Hoewel in de aanwezigheid van ethyleen de aromatisering van DMF resulteerde in verbeterde BTEX-opbrengsten, is de Diels-Alder cycloadditie weer niet het dominerendedominante reactiemechanisme, maar vinden de alkylerings- en cycliseringsreacties eerder plaats via het “hydrocarbon pool” mechanisme.

Hoofdstuk 5 beschrijft het gebruik van Zn-bevattende HZSM-5 katalysatoren voor het FTA proces. De Zn-HZSM-5 materialen blijken een verhoogde selectiviteit naar BTX te vertonen tijdens de DMF aromatisering in aanwezigheid van ethyleen. De toegepaste katalysatorsynthesemethode resulteerde in een homogene dispersie van Zn-ionen in het zeolietmateriaal alsook in de vorming van kleine ZnO-clusters. Zn toevoeging aan zeoliet ZSM-5 door impregnatie verminderde het aantal BAS door ionenuitwisseling met Zn^{2+} kationen. De hoeveelheid LAS nam hierbij lichtjes toe, maar niet lineair met de hoeveelheid toegevoegd Zn. Dit suggereerde dat deze nieuwe Zn sites leiden tot de vorming van een nieuw type zwak-medium zure sites. Daarnaast werd ook een hiërarchische Zn/ZSM-5-zeolietkatalysator gesynthetiseerd om het effect van mesoporositeit en Zn verder te onderzoeken. Het gebruik van een zeolietmateriaal met hoge dispersie van Zn^{2+} en met ethyleen-bijvoeding gaf een uitstekende BTX selectiviteiten in vergelijking met het niet-gemodificeerde HZSM-5 katalysatormateriaal. De combinatie van mesoporositeit en Zn^{2+} zorgde voor nog meer BTX-vorming. Ondanks de hogere BTX-opbrengsten, werd ook een snellere katalysator-deactivering waargenomen voor alle Zn/ZSM-5-katalysatoren, inclusief de hiërarchische Zn/ZSM-5-katalysator. De oorzaak was cokes-vorming. Inderdaad, deze resultaten geven aan dat cokes-vorming vrijwel altijd ten koste gaat van de vorming van aromaten. Mechanistisch onderzoek van de Zn/ZSM-5-katalysator wees uit dat de reactie wordt gedomineerd door een mechanisme

met twee reactiecycli, één waarin olefines en één waarin aromaten worden gevormd. Het toevoegen van ethyleen bevordert dan de zogenaamde areencyclus, wat resulteert in de vorming van meer gealkyleerde aromaten. Eerdere studies[5,6] toonden aan dat het zeolietmateriaal op zichzelf veel te actief is voor de omzettingsreacties van oxygenaten naar koolwaterstoffen en dat verschillende katalysatorsamenstellingen moeten worden onderzocht. In **Hoofdstuk 6** werden de prestaties van op aluminiumoxide (Al_2O_3)-gebonden zeoliet ZSM-5-gebaseerde katalysator-extrudaten beoordeeld in de *ex-situ* katalytische snelle pyrolyse (CFP) van dennenhout en cellulose.

Ondanks dat de twee grondstoffen op elkaar lijken (d.w.z. de hoge aanwezigheid van zuurstofhoudende moleculen), waren productopbrengsten, productdistributie en deactiveringssnelheden van de katalysator sterk afhankelijk van de gekozen voeding en reactietijd. De grote hoeveelheid cokes-afzettingen die worden geproduceerd, leidden tot omkeerbare en onomkeerbare structurele veranderingen in de katalysator-extrudaten. Naast verschillen in aard tussen de gevormde thermische en katalytische koolstofafzettingen, werden deze ook gevonden op verschillende plaatsen binnen het katalysator-extrudaat. Zo bevond thermische cokes zich bij voorkeur in de poriën van het bindmiddel aluminiumoxide en aan het buitenoppervlak van zeolietdeeltjes, terwijl katalytische cokes, waarvan de vorming word bepaald door de katalytisch actieve sites, gevonden werd binnen de zeolietdeeltjes. Confocale fluorescentie microscopie liet verder zien dat er grotere cokes-verbindingen werden gevormd na CFP met cellulose dan met dennenhout. Dit is waarschijnlijk omdat bij gebruik van cellulose vluchtige moleculen eenvoudiger de microporiën van het zeoliet binnendringen dan bij gebruik van dennenhout; deze laatste grondstof leidde voornamelijk tot condensatie van deze vluchtige verbindingen op het buitenoppervlak van de katalysator-extrudaten. Na regeneratie van de katalysatoren werden voor beide voedingen onomkeerbare chemische veranderingen in de structuur van de katalysator waargenomen, zoals een afname van het aluminiumgehalte. Meer specifiek vertoonde een katalysator een sterkere dealuminering na CFP van dennenhout, waarschijnlijk als gevolg van een grotere hoeveelheid waterdamp die wordt gevormd met deze grondstof.

References

(1) Venderbosch, R. H. A Critical View on Catalytic Pyrolysis of Biomass. *ChemSusChem* **2015**, *8*, 1306–1316. https://doi.org/10.1002/cssc.201500115.

(2) Jae, J.; Tompsett, G. A.; Foster, A. J.; Hammond, K. D.; Auerbach, S. M.; Lobo, R. F.; Huber, G. W. Investigation into the Shape Selectivity of Zeolite Catalysts for Biomass Conversion. *J. Catal.* **2011**, *279*, 257–268. https://doi.org/10.1016/j.jcat.2011.01.019.

(3) Puertolas, B.; Veses, A.; Callen, M. S.; Mitchell, S.; Garcia, T.; Perez-Ramirez, J. Porosity-Acidity Interplay in Hierarchical ZSM-5 Zeolites for Pyrolysis Oil Valorization to Aromatics. *ChemSusChem* **2015**, *8*, 3283–3293. https://doi.org/10.1002/cssc.201500685.

(4) Lee, H. W.; Park, S. H.; Jeon, J. K.; Ryoo, R.; Kim, W.; Suh, D. J.; Park, Y. K. Upgrading of Bio-Oil Derived from Biomass Constituents over Hierarchical Unilamellar Mesoporous MFI Nanosheets. *Catal. Today* **2014**, *232*, 119–126. https://doi.org/10.1016/j.cattod.2013.12.015.

(5) Wang, K.; Kim, K. H.; Brown, R. C. Catalytic Pyrolysis of Individual Components of Lignocellulosic Biomass. *Green Chem.* **2014**, *16*, 727. https://doi.org/10.1039/c3gc41288a.

(6) Wan, S.; Waters, C.; Stevens, A.; Gumidyala, A.; Jentoft, R.; Lobban, L.; Resasco, D.; Mallinson, R.; Crossley, S. Decoupling HZSM-5 Catalyst Activity from Deactivation during Upgrading of Pyrolysis Oil Vapors. *ChemSusChem* **2015**, *8*, 552–559. https://doi.org/10.1002/cssc.201402861.

(7) Guisnet, M.; Magnoux, P. Organic Chemistry of Coke Formation. *Appl. Catal. A Gen.* **2001**, *212*, 83–96. https://doi.org/10.1016/S0926-860X(00)00845-0.

(8) Guisnet, M.; Magnoux, P. Coking and Deactivation of Zeolites. *Appl. Catal.* **1989**, *54*, 1–27. https://doi.org/10.1016/s0166-9834(00)82350-7.

(9) Collett, C. H.; McGregor, J. Things Go Better with Coke: The Beneficial Role of Carbonaceous Deposits in Heterogeneous Catalysis. *Catal. Sci. Technol.* **2016**, *6*, 363–378. https://doi.org/10.1039/c5cy01236h.

List of Abbreviations

AlPO	Aluminum Phosphate
BAS	Brønsted Acid Sites
BET	Brunauer-Emmett-Teller
BTX	Benzene-Toluene-Xylenes
BTEX	Benzene-Toluene-Ethylbenzene-Xylenes
CELL	Cellulose
CFM	Confocal Fluorescence Microscopy
CFP	Catalytic Fast Pyrolysis
CP	Cross-Polarization
DFT	Density Functional Theory
DMF	2,5-dimethylfuran
DR	Diffuse Reflectance
DRS	Diffuse Reflectance Spectroscopy
EDX	Energy-Dispersive X-ray
EFAl	Extra-framework Aluminum
F	Furan
FIB	Focused Ion Beam
FID	Flame Ionization Detector
FT-IR	Fourier Transform-Infrared
FTA	Furans-to-Aromatics
GC	Gas Chromatography
GCxGC	Tandem Gas Chromatography
HZSM-5	Proton form of ZSM-5
ICP-OES	Inductively Coupled Plasma with Optical Emission Spectrometry
IWI	Incipient Wetness Impregnation
LAS	Lewis Acid Sites
MAS	Magic Angle Spinning
MF	2-methylfuran
MFI	Mordenite Framework Inverted
MQ	Multi-Quantum
MS	Mass Spectrometry
MTA	Methanol-to-Aromatics
MTH	Methanol-to-Hydrocarbons

MTO	Methanol-to-Olefins
NCP	Non-Catalytic Pyrolysis
NCG	Non-Condensable Gases
PW	Pine Wood
P-Z	Phosphor-Zeolite
RF	Radiofrequency
SEM	Scanning Electron Microscopy
ssNMR	solid-state Nuclear Magnetic Resonance
TCD	Thermal Conductivity Detector
TFAl	Tetrahedral Framework Aluminum
TGA	Thermogravimetric Analysis
TMS	Trimethylsilane
TOS	Time-on-stream
TPD	Temperature Programmed Desorption
TPO	Temperature Programmed Oxidation
UV/Vis	Ultraviolet-Visible
WHSV	Weight Hourly Space Velocity
XRD	X-ray Diffraction
ZSM-5	Zeolite Socony Mobil-5
ZQ	Zero-quantum

List of Scientific Publications and Presentations

Scientific Publications

B. Luna-Murillo, D. Waard, A. Lucini Paioni, M. Baldus, P.C.A. Bruijnincx, B.M. Weckhuysen, Structure-performance relationships for the aromatization of furan derivatives over phosphorus-modified ZSM-5 zeolite, *in preparation.*

E.A. Uslamin, B. Luna-Murillo, N.A. Kosinov, P.C.A. Bruijnincx, E.A. Pidko, B.M. Weckhuysen, E.J.M. Hensen, Gallium-promoted HZSM-5 zeolites as efficient catalysts for the aromatization of biomass-derived furans. *Chem. Eng. Sci.* **2019**, *198*, 305-316.

B. Luna-Murillo, M. Pala, A. Lucini Paioni, M. Baldus, F. Ronsse, W. Prins, P.C.A. Bruijnincx, B.M. Weckhuysen, Catalytic fast pyrolysis of biomass: Catalyst characterization reveals the feed-dependent deactivation of technical ZSM-5-based catalyst extrudates, *submitted for publication.*

Oral Presentations

"Advanced characterization of ZSM-5-based extrudates after catalytic fast pyrolysis", 8th IUPAC International Conference on Green Chemistry, **2018**, Bangkok, Thailand.

"Unravelling the chemical changes of HZSM-5/Al_2O_3 extrudates after catalytic fast pyrolysis", Dutch Zeolite Association (DZA), **2018**, Amsterdam, The Netherlands.

"Advanced characterization of HZSM-5/Al_2O_3 extrudates after the catalytic fast pyrolysis of Biomass and Cellulose", 20th Netherlands Catalysis and Chemistry Conference (NCCC), **2019**, Noordwijkerhout, The Netherlands.

"Advanced characterization of HZSM-5/Al_2O_3 extrudates after the catalytic fast pyrolysis of Biomass and Cellulose", 14th European Congress on Catalysis (Europacat), **2019**, Aachen, Germany.

Acknowledgements

"*Life is not easy for any of us. But what of that? We must have perseverance and above all confidence in ourselves. We must believe that we are gifted for something and that this thing must be attained*"

Marie Skłodowska-Curie (1867-1934)

Finally, here I am, with a PhD Thesis and myself in one piece. Did I ever think about how all this was going to end when I started in 2015? Not by a long shot! So, I am going to thank everyone that help me in one way or another to make this possible.

First of all, I would like to thank my first promotor prof. **Bert** Weckhuysen for giving me the opportunity to do my PhD in a multidisciplinary and international team as the ICC group. Thanks for all your fruitful discussions and meetings along all these four years. Also, for all the support during my oral presentations and international trips.

I would like to also thank my second promotor prof. **Pieter** Bruijnincx, who was very much involved in daily tasks and supervision until the very end and completion of this booklet. Thanks for being so supportive and for your motivating and constructive speeches during all our meetings. Even during the most difficult and stressful periods, you always had a minute to discuss anything with me.

I would like to acknowledge also my collaborators and the people who contributed experimentally to the completion of this booklet. Firstly, I would like to thank **Evgeny Jr.** It was very nice to work with you. **Mehmet**, thanks for the very fruitful discussions, which allowed us to improve our chapter and paper. Thanks to **Davey** and **Dustin**. I never imagined that I would learn so much from you two. You demonstrated me that with hard work, perseverance and supportiveness you can arrive very far. I would also like to thank **Alessandra** and prof. **Marc Baldus,** for allowing and helping me on the performance of the NMR experiments. Alessandra, I very much enjoyed also our non-scientific conversations.

I would like to acknowledge all the technical and support staff from UU. Thanks to **Belen**, **Ilonka**, **Iris**, **Sandra** for being so helpful. I would like to especially thank **Dymph** for always be willing to answer my questions even outside the permitted office hours. Also, to the MCEC staff, **Emke** and **Nina** for making and organizing very fruitful and entertaining MCEC events.

Our technicians, **Herrick**, **Oscar**, **Pascal** and **Ramon**, for helping me in the design, build up and optimization of my setup. Thank you very much to our Ads, **Ad Mens** and **Ad van der Eerden**. Bedankt Ad van der Eerden, I will always remember with a smile how happy you were when I was able to maintain a conversation in Dutch. **Fouad** and **Pieter de Peinder**, thank you for all the discussions on IR spectroscopy. Also, thanks to **Deni** for measuring XRD and TGA for me, especially at the very last minute before going on holiday. Thanks **Jan Willem**, for helping me every time I needed a hand with the gases.

I would also like to thank **Florian Meirer** and prof. **Eelco Vogt** for their very useful suggestions during the development of my PhD Thesis. **Abhishek**, **Gareth**, **Joel** and **Zoran,** thank you very much for all the scientific discussions we had.

I am also grateful to all the people I met during my stage in ICC and got to share meetings, discussions, lunches and parties. Thanks to **Ahmed, Ana, Antonio, Ara, Anne-Eva, Bea, Baira, Bas, Caroline Versluis, Christa, Caroline Vis, Charlotte, Daan, Ellen, Erik, Fang, Federica, Florian, Francesco, Frank, Giorgio, Haissam, Ilse, Ina, Iris, Ivan, Jelle, Jeroen, Jessi, Jiadong, Jochem, Jogchum, Johan, Jongkook, Joris, Jose, Jovana, Katinka, Khaled, Koen, Kordula, Lars, Laurens, Laura Barberis, Lisette, Longfei, Özgun, Robert, Maarten, Mahnaz, Marisol, Marjolein, Martin, Mark, Matthias, Max, Michael, Nazila, Nienke, Nynke, Pasi, Petra, Peter Bramwell, Peter Ngene, Pierre, Rafael, Remco, Robin, Romy, Roozbeh, Ru-Pan, Savannah, Sandra, Sebastian, Shiyou, Shuang, Stijn, Tao, Thijs, Tom D., Tom van D. Wouter, Xiaohui, Xinwei, Yan, Yannick** and **Yuanshuai..**

Thanks to **Arjan**, **Egor**, **Ioannis**, **JX**, **Laura de Kort, Miguel** and **Suzanne**, my desk neighbors, for all the entertaining days and chats we had. As well, thanks to the neighbors and friends in the second and third coordination sphere: **Donglong, Carlos, Katarina, Lennart, Rolf, Thomas** and **Stano**. Guys, you made the evenings and second lunches at the ICC very memorable. Thanks also to my office mates during the last year, **Fei, Heba**, **Hongyu, Justine, Kang, Marianna, Nina** and **Wirawan**. I promise that our secret conversations in the office about conquering the world will always be safe with me. **Roxana**, **Richard** and sweet **Alondra**, thanks for all the nice weekends and events in Leuven.

Thank you, **Christia**, for being the sweetest and most beautiful girl from Lebanon I have ever met. **Ioannis** and **Sofi,** my dear and sweet friends, thank you for being always there and caring so much for me. My little Chinese mafia, **Donglong** and **Kang,** thank you for all the hotpots and activities we always enjoyed together.

Thanks to the *Dutchbasilio* gang (also temporarily known as *Covidbalisio*). **Egor, Guusje, Luke, Matteo, Nikos, Philippe, Silvia** and **Sophie**. You are great, guys! Thanks for taking care of me and for all the amazing times we spent, and will spend, together.

A **Judith** y **Dani**, mis amigos colombianos de aventuras. Esperando con ansias nuestro próximo viaje de ENSUEÑO por Sudamérica.

Judit i **Eric**, gràcies per estar al meu costat en tot moment. Sou els millors companys de la URV de l´història.

Gracias a **Álvaro, Jose** y **Luuk**, por hacer mis tardes en Enschede y Utrecht tan especiales.

I will always be grateful to my girls' squad, my *Shangri-la* girls, **Marianna** and **Katarina**. Anything I say here in words about you would never be enough. Thank you very much for being ALWAYS by my side.

Miguel, no sé cómo podré agradecerte todo lo que has hecho estos años por mí. Siempre has sido y serás un apoyo incondicional.

Y por último, quiero agradecer a toda mi familia este gran logro. Sin vosotros, esta tesis nunca habría llegado a su fin. **Mami**, gracias por darme ese empujoncito en aquella cafetería de El Vendrell, y alentarme a que aceptara esta maravillosa oportunidad. A mis abuelos **Bernabela y Santiago**, mis yayitos y mis segundos padres. ¡Qué cierto es eso de que los abuelos deberían ser eternos! Y como dice mi yaya Bernabela: -yo no digo na´ pero… ¡Qué os quiero un montón!-. A mi pequeña **Ainoa** ¡la mejor atleta que nadie ha visto jamás! Y a mi hermano **Óscar**; gracias por aportarme siempre una sonrisa con vuestras travesuras 😊. También a **Santi, mis tíos** y **Laura**. Ya estoy esperando con ganas nuestra próxima comida en familia. No os llegáis a imaginar la vitalidad y alegría que me dais durante nuestros eventos. Gracias, por quererme tal y como soy y por ser vuestra "*niña*" siempre, aunque esté cerca de los 30. Vuestro apoyo incondicional durante todos estos años ha sido el pilar más importante de mi vida. Os quiero muchísimo.

About the Author

Beatriz Luna Murillo was born in L´Hospitalet de Llobregat (Barcelona, Spain) on 27th January 1992. Afterwards, she moved to El Vendrell, a small town in Tarragona, were she finished her undergraduate studies. In 2009, she participated in the 33th ed. Chemistry Olympics in Barcelona. In 2009, she started her studies on Chemistry in Universitat Rovira I Virgili (URV). In 2014, she did her internship in Sekisui Specialty Chemicals. Her research topic was "*Digitalization of tools for the quality control of industrially produced polyvinyl alcohol (PVA)*". She obtained her Bachelor´s degree in 2014, and the same year, she started her Master´s study in Synthesis, Catalysis and Molecular Design, an academic joint program offered by URV and Institut Català d'Investigació Química (ICIQ). Her Master research project was entitled "*Supported bifunctional Ni/H^+ catalysts for the hydrogenolysis of glycidol*". In July 2015, she obtained her Master´s degree. The same year, she started her PhD studies on "*Bio-oil to chemicals and fuels: (in-situ) catalyst deactivation studies at multiple length scales*", sponsored by the Netherlands Center for Multiscale Catalytic Energy Conversion (MCEC) research program at Utrecht University (Utrecht, The Netherlands) under the supervision of prof. Bert Weckhuysen and prof. Pieter Bruijnincx. During her PhD period, Beatriz supervised two Master projects and two Bachelor projects. The majority of her research results are described in this PhD Thesis and were presented as oral and poster presentations at several national and international conferences. Together with her colleagues, Beatriz was also participating in the U-talent platform, an outreach program dedicated to reach out and propose short scientific projects to young and outstanding undergraduate students. Additionally, as member of the NIOK PhD Platform (NPP) from 2016 to 2018, she was in charge of organizing an international company trip to two international companies in Belgium; ExxonMobil and Total. Since April 2020, she continues her research career at the Total Research and Technology Feluy (TRTF) center (Feluy, Belgium). In TRTF, she will be working as a research engineer on CO_2 conversion projects. During her free time, she likes to do sports, play volleyball, dance salsa and to travel.